UNIVERSITÀ
DEGLI STUDI
FIRENZE

DOTTORATO DI RICERCA IN
SCIENZE CHIMICHE

CICLO XXXIII

COORDINATORE Prof. Piero Baglioni

The functionalization of nanostructured carbon materials for biological application

Settore Scientifico Disciplinare CHIM/06

Dottorando
Dott. (*Ligi Maria Cristina)*

Tutore
Prof. (*Cicchi Stefano)*

Coordinatore
Prof. (*Piero Baglioni)*

Anni 2017/2020

INDEX

1. Preface and objectives

The main subject of this PhD thesis belongs to the use of nanostructured carbon material for different goals. Graphene oxide (GO) and oxidized multiwalled carbon nanotubes (CNTs) have been exploited for covalent and adsorption decoration to achieve systems profitable in several areas, such as nanomedicine or organocatalysis. GO and CNTs represent good platform thanks to their deep versatility, as showed in **Figure 1** the nanostructured carbon material could be applied in the following studies.

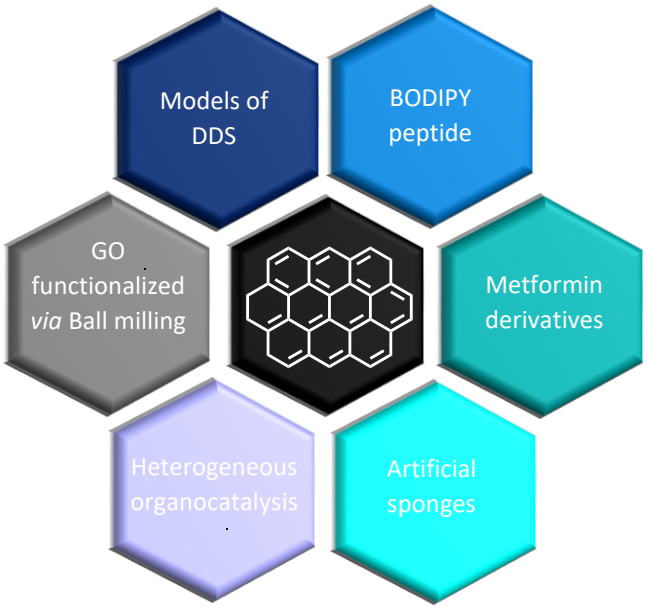

***Figure 1**. Different applications of CNTs and GO*

In the first part of my PhD I have been involved in a project concerning the design and synthesis of a Drug Delivery System.[1] This system was based on short oxidized multiwalled carbon nanotubes, as a device suitable for cancer treatment. A multimodal approach was chosen, targeting both metabolism and proliferation of tumor cells with two different drugs, in such a way to address cells of different sub-populations of the tumor: proliferative and staminal cancer cells (stem cells).

The synthetic approach, exploiting the chemical flexibility of carbon nanotubes, was planned in a way to decorate the delivery system with the highest quantities of two different drugs (metformin and doxorubicin), and a targeting component, a small molecule reported to increase tumor uptake (biotin). (**Figure 2**) Then, with minor changes to the synthetic protocol, the system was modified to study the pharmacokinetic in tumor bearing mice models The biological properties of these systems were studied thanks to the collaborations with the Department of Clinical and Experimental Biomedical Sciences, which carried out *in vitro* studies, and with the University of Texas MD Anderson Cancer Centre for the radio-labeling of the DDS and their *in vivo* studies.

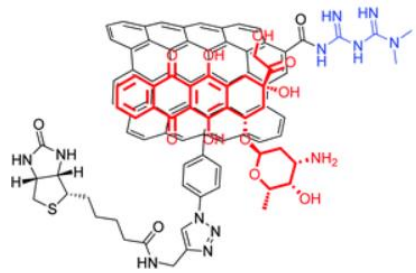

***Figure 2**. Structure of the designed DDS.*

The first cytotoxic drug, doxorubicin, was loaded on DDS exploiting the supramolecular chemistry, due to formation of π-π stacking interaction between the anthracycline moiety of doxorubicin and the π-system on the CNTs. Another chemical approach was exploited to load metformin. The drug was covalent bund to CNTs by exploiting the carboxyl groups on nanostructured material after their activation.

The major limitation observed for the described system consisted in the lack of metformin release after the internalization into cell, which caused a no combined effect.

To overcome this problematic two DRUG DELIVERY SYSTEM MODELS based on CNTs and GO were designed and synthesized. In these MODELS one or more cytotoxic drugs will be covalent attached on carbon material through disulfide linkers, labile in intracellular environment. These systems will afford a modulated release of molecular fragments (drugs) attached on CNTs or GO through the linkers. To verify the correct internalization into cells of our DDS and the efficiency in the use of disulfide linker we synthesized a MODEL SYSTEM decorated with two BODIPY dies, different in conjugation, one of which covalent attached through the linker to the carbon material, the other covalent bund to CNTs/GO. (**Figure 4**)

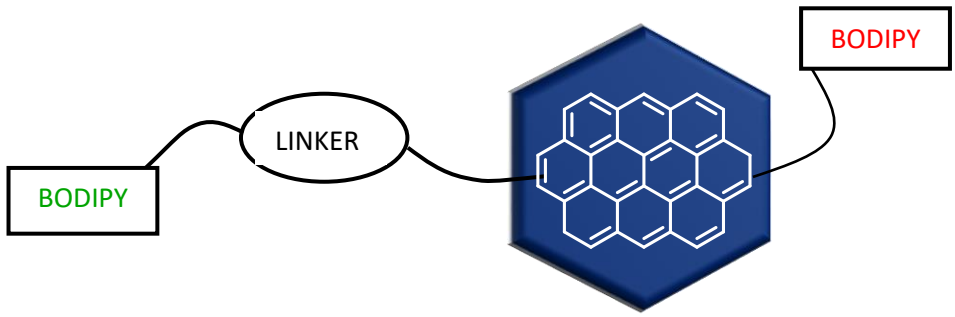

***Figure 4**: Structure of model of DDS*

BODIPY probes represent excellent substrates both for their fluorescence and for the possibility to modify their structure to achieve different purposes. We performed the modification of BODIPY dye through first amino acids conjugation, then peptides addition, such as the conjugation with RGD sequence. The final goal will be the use of BODIPY-PEPTIDES as selector for DDS, increasing the uptake of the system into cancer cells, and, at the same time, exploiting the fluorescence properties of BODIPY. This described system will be exploited for theranostic applications.

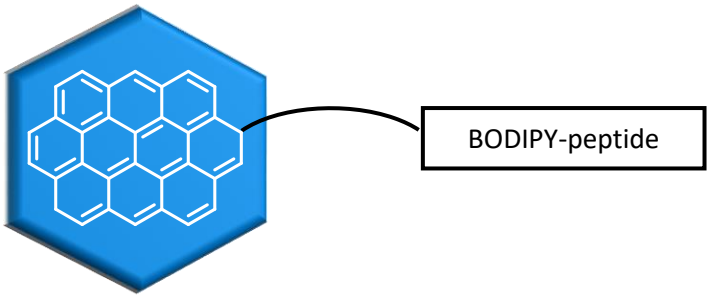

***Figure 5**: BODIPY conjugated with RGD sequence covalent bund on CNTs/GO.*

In addition to the use of a linker to bind the drug, an alternative possibility to overcome the lack of metformin release observed for our first DDS (**Figure 2**) may be a change in the chemical approach to decorate CNTs. Metformin could be adsorbed on CNTs instead of covalent bund to the material. To increase the interaction of drug with the carbon platform, the organic molecule should be modified, to afford a METFORMIN DERIVATIVE. (**Figure 6**).

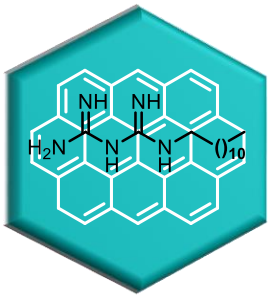

***Figure 6**: Biguanide derivative adsorbed on CNTs.*

The activity of the derivative will be studied and compared to metformin activity.

CNTs should be the base of our ARTIFICIAL SPONGES consisting of CNTs decorated with polycationic molecules able to form stable complexes with proteoglycans, inhibitory substrates for the regeneration of injured spinal cord tissue. These nano-platforms could be the channel to remove proteoglycans from the medium, thanks to the addition of magnetic nanoparticles the entire systems may be moved away the damaged tissue. (**Figure 7)**

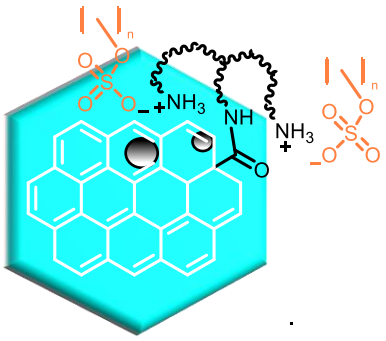

***Figure 7**: Representation of nano-sponges.*

Nanostructured carbon material, as previously presented, could be profitable support for DDS, useful in nanomedicine, but also versatile substrate for different purposes. The covalent decoration of CNTs with organophosphorus moieties afforded catalysts for chemical reactions in HETEROGENEOUS phase, such as Staudinger Ligation, Wittig Reaction and Mitsunobu Reaction. (**Figure 8**).

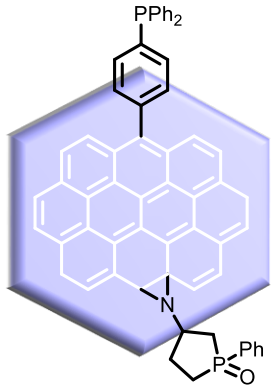

***Figure 8**: Example of catalysts based on CNTs decorated with organophosphorus moieties*

The FUNCTIONALIZATION of GO should be performed in liquid phase, as previously presented for DDS based on GO, but also by mechanical chemistry *via* Ball Milling. This procedure allowed to avoid the use of solvents, introducing amines or phenols onto GO surface. (**Figure 9**).

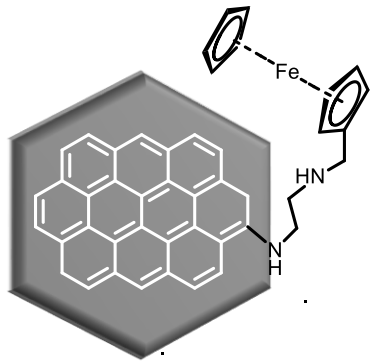

***Figure 9**: GO functionalization via Ball Milling.*

2. Fluorescent probes linked to carbon nanotubes and graphene oxide through a disulfide bridge: viability study for drug delivery

2.1 OBJECTIVES OF THIS CHAPTER (2)

This project has two main objectives that aim to design and synthesize two model systems for a viability studies for drug delivery systems. In particular, the first one is to develop a multifunctionalization procedure on oxide carbon nanotubes (CNTs) for future biomedical application. In addition to chemical strategies to reproduce the same designed system, but on graphene oxide (GO) have been investigated as second goal.

In Figure 1 was reported the desired system.

. A central backbone consisted in a nanostructured carbon material: oxidized carbon nanotubes (CNTs) for the first part of the project, GO for the second one.

. A BODIPY dye, with a maximum adsorption at 640 nm. This probe will be essential to verify the effective internalization of the system into cell.

. A BODIPY dye with a disulfide linker reactive in intracellular environment, due to the high concentration of endogenous thiols in cancer cells, such as glutathione. Maximum adsorption of the modified dye at 529 nm.

. Polyethylene glycol chain to improve cells uptake.

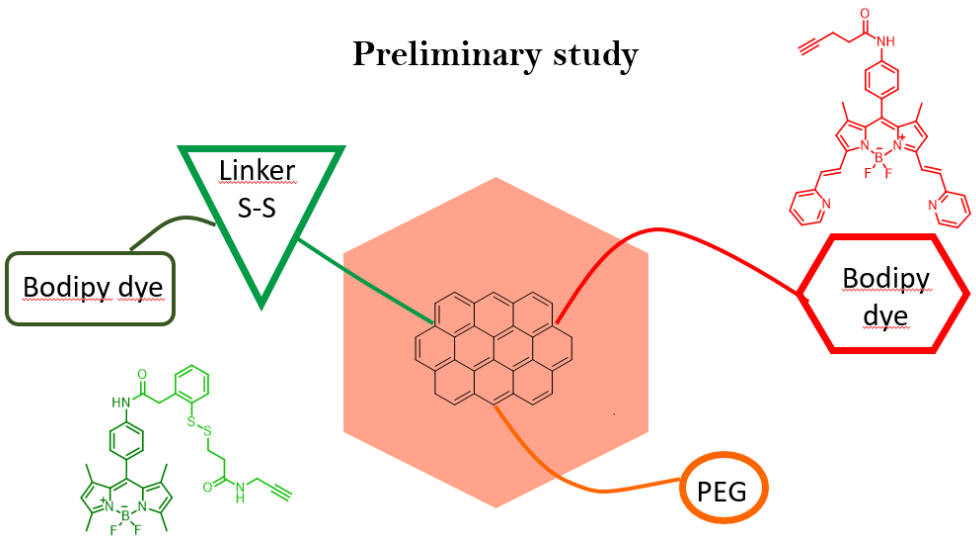

***Figure 1**. Model system for DDS.*

The first goal of this model system is to demonstrate that in the environment melanoma cancer cells, the molecular fragment attached through a disulfide bond could be released. This study represents a viability study to build systems of drug delivery (**Figure 2**) in which the drug is anchored to the

nanostructured material with a covalent bond that can only be broken after a cellular internalization. PEG chain will be bund to a specific selector, such as a peptide, useful to increase cell uptake of drug.

Due to the interest in their applications as drug nanocarriers, CNTs and GO were chosen. Their ability to cross cell membrane is independently of the kind of chemical groups on carbon surface, as well as the cell type selected.[2]

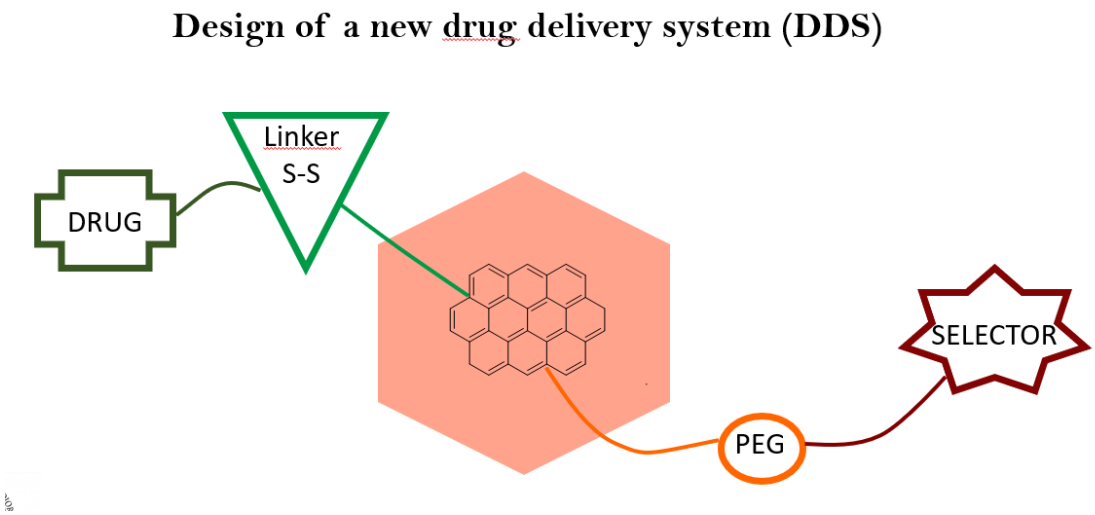

***Figure 2**. Future DDS.*

The second goal is a comparison of the preliminary models for DDS made of CNTs or GO. The loading degree of BODIPY dye and BODIPY-linker on nanostructured carbon material were investigated and compared.

2.2 INTRODUCTION

2.2.1 CARBON NANOMATERIAL

Difficulties in overcoming the limited control over biophysical and biochemical characteristics in traditional biomaterials have hampered their use in biomedical applications.[3] This pushed the research of novel materials showing multiple properties that allow advanced functionalities. In this respect, carbon nanostructures (CN) thanks to the multiple uncommon properties, have had an impressive impact on scientific research with important technological implications. Carbon is one of the prototypal elements showing an organization in different allotropic forms (as sketched in **Figure 3**), carbon nanostructures (CN) consist of sp^2 carbon atoms with different spatial arrangements:[4] from the zero-dimension fullerenes and carbon quantum dots, to the one dimensional CNTs, to the two-dimensional graphene atomic sheet, to the 3D bulk graphite or diamond crystals where atoms are pure sp^2 or sp^3 hybrids organized in the hexagonal or cubic lattice, respectively.

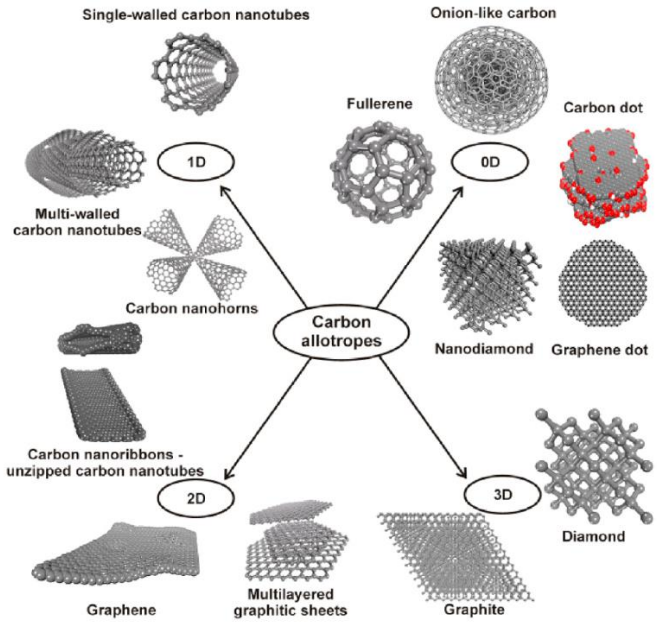

***Figure 3**. Carbon allotrpes*

Thanks to electrical, chemical, and mechanical properties of these systems, have led to a number of different types of applications. Concerning biology and biomedicine, the big potential of carbon nanomaterials is the possibility to tune the CNS dimensions, the capability to functionalize the surface, and the high chemical stability coupled to the optical and biomimetic properties. As an example, CNTs and fullerenes soon after their discovery have been studied for biosensing, drug delivery, and bioimaging. Recently they experienced a revival for their application in the regenerative medicine,[5] cancer therapy, and theranostic applications.[6]

2.2.2 CARBON NANOTUBES (CNTs)

Carbon Nanotubes (CNTs) are one kind of carbon allotrope which has a seamless hollow cylindrical shape. Like carbons in graphene, carbon atoms in CNTs are also bonded with three neighboring carbon atoms in a sp2 configuration forming the hexagonal units. Conceptually, CNTs are considered as rolled-up graphene sheets in certain directions. The rolling up of single-layer graphene and multi-layer graphene form single-wall CNTs (SWCNTs) and multi-wall CNTs (MWCNTs), respectively. Their structure makes them suitable for a wide variety of applications ranging from electronics to biomedical.[7],[8]

A list of properties of this carbon nanostructured material was reported below:

I. The high surface area and the hollow structure make CNT suitable for drug loading, but also as nano-adsorbents for the scavenging of metallic ions and organic compounds from aqueous solutions.

II. The ease functionalization of CNTs allow their modification and tailoring for several different applications.[9–11]

III. The excellent conductive profile offers a unique platform for the development of sensors and biosensors10 as well as a large number of applications in electronic devices.

IV. Their mechanical strength has promoted them as reinforcement additives in polymeric matrix, or in biology as surface for cell adhesion, proliferation and differentiation.[12]

The most preferred technique to produce CNTs was represented by chemical vapor deposition (CVD). This process involves the pyrolysis of hydrocarbons, or other carbon feedstock carried out in a stream of inert gas into a chamber with a metal catalyst (Ni, Fe and Co). Numerous parameters influence CVD; the control of these variables (temperature, gas pressure, presence of inert gas) allows to modify some CNTs feature such as diameter, length and alignment. Catalytic decomposition of methane at 680°C for 120', using nickel oxide–silica binary aerogels as catalyst was exploited to achieve MWCNTs. The diameter of synthesized CNTs was found to be dependent on the temperature; as the temperature increased, the diameter also increased. Essential is to remove metal catalyst impurities which could influence material's properties. [8] It is difficult to separate single CNTs and make stable biocompatible solutions in most solvents, especially not possible in water. Surface functionalization has provided efficient solutions to solve this problem.

Functionalization is fundamental to provide material suitable for widespread applications thanks also to the possibility to remove residues of metallic catalyst.

2.2.3 FUNTIONALIZATION OF CARBON NANOTUBES

Thanks to their unique properties, CNTs are expected to be versatile nanomaterials for biomedical application. As previously mentioned surface functionalization could also provide efficient intracellular uptake and increase the possibility of the attachment of different functional groups onto the surface of CNTs for biomedical applications.[13] CNTs functionalization can be generally divided into two groups: noncovalent functionalization, and covalent functionalization.

COVALENT APPROACH

The covalent functionalization process involves several chemical reactions, through which covalent chemical bonds are formed between CNTs and the entities for functionalization. They can be divided into two categories: (i) oxidation and end/defect functionalization, and (ii) side wall covalent functionalization.

The first step in the functionalization of CNTs is the oxidation of the material. This process cuts tubes into short pieces and removes impurities inside CNTs, such as amorphous carbon and metallic catalysts. At the same time, it opens the tube ends of CNTs and brings in tube-end oxygen functional groups, such as carboxylic acid, ketone, alcohol, and ester groups. Meanwhile the oxidation process generates defects on the tube wall, for example holes with oxygenated functional groups.[14]
A chemical method to achieve oxidized material is the addiction of an acid mixture (HNO_3/H_2SO_4).[15] **(Figure 4)** Successive modifications were reported in **Figure 4** through four reaction pathways. The first decoration consisted in the formation of CNTs-carboxylate zwitterion.[16,17] The second modification is the amidation reaction exploited to graft R-NH_2 on to CNTs. Before the synthesis of amide an activation of carboxyl groups is required by using $SOCl_2$ or coupling reagents. Lastly through an esterification process between the surface carboxylic groups on CNTs with ROH.

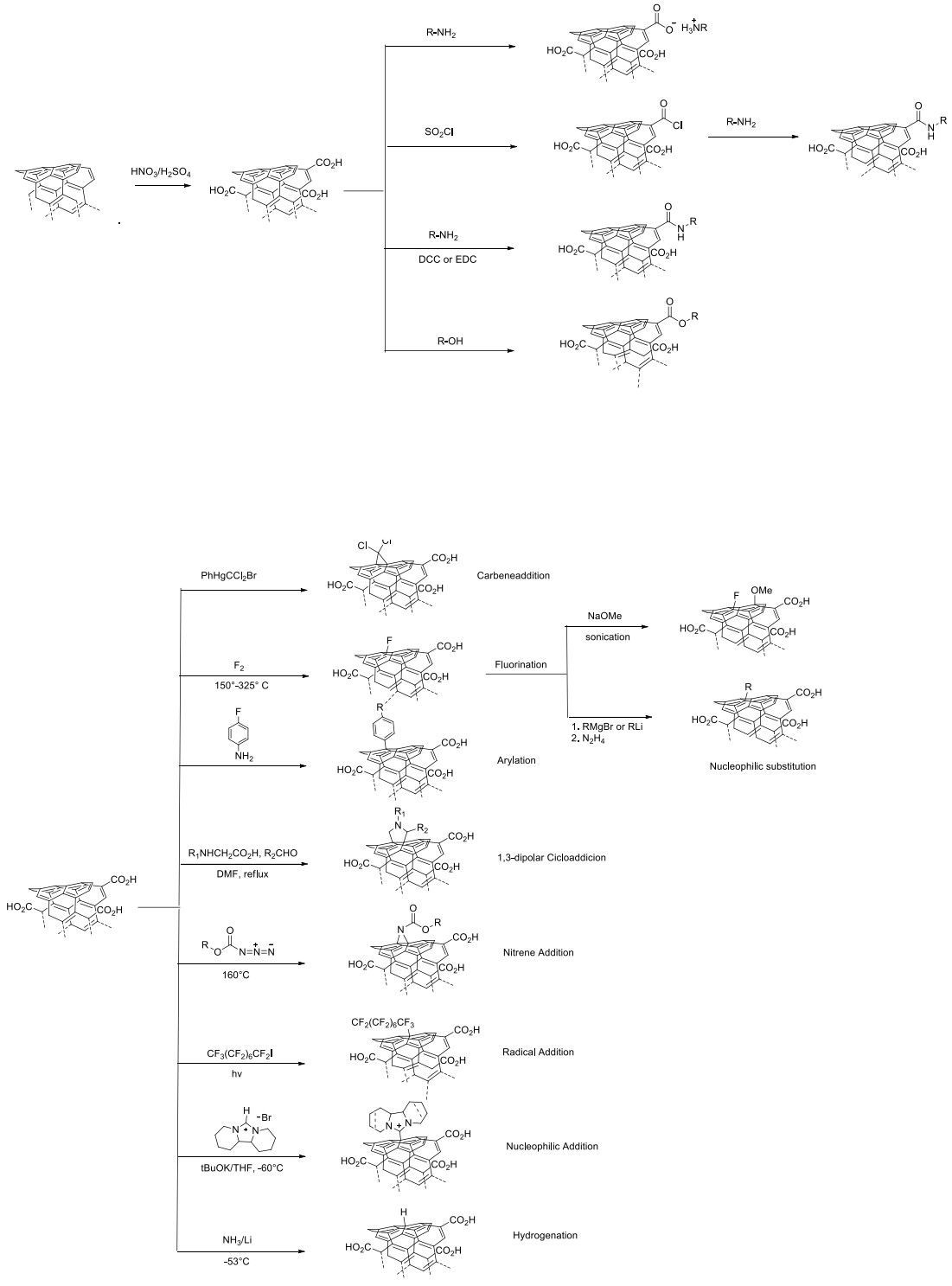

Figure 4. *Different chemical reactions for end functionalization of CNTs.*[4]

Side wall covalent functionalization of CNTs usually involves the breaking of sp^2 bonding networks to form sp^3 binding on CNT walls.

GRAPHENE SYNTHESIS

Several techniques have been established for graphene synthesis. However, mechanical cleaving (exfoliation),[18] chemical exfoliation[19], chemical synthesis,[20] and thermal chemical vapor deposition (CVD)[21] synthesis are most commonly used methods today. Some other techniques are also reported such as unzipping nanotube[22] and microwave synthesis; however, those techniques need to be explored more extensively. An overview of graphene synthesis techniques is shown in the flow chart in **Figure 5**. In 1975, few-layer graphite was synthesized on a single crystal platinum surface via chemical decomposition methods, but was not designated as graphene due to lack of characterization techniques or perhaps due to its limited possible applications.[23]

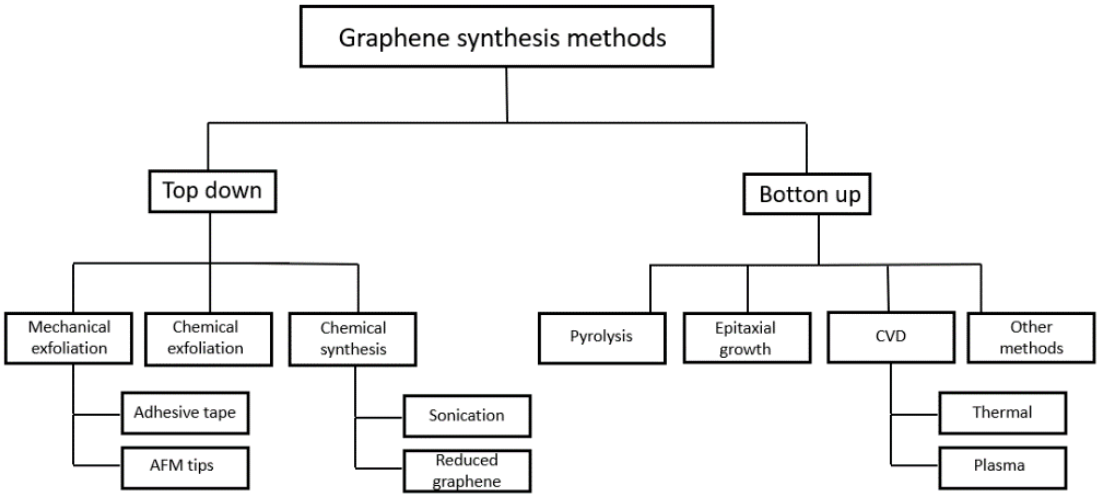

Figure 5. *Graphene synthesis methods.*

In 1999, mechanical cleaving of highly ordered pyrolytic graphite (HOPG) by atomic force microscopy (AFM) tips was first developed in order to fabricate graphene from a few layers down to a mono-atomic single layer.[24] Nevertheless, mono-layer graphene was first produced and reported in the year 2004, where adhesive tape was used to repeatedly slice down the graphene layers on a substrate.[18] This technique was found to be capable of producing different layers of graphene and is relatively easy to fabricate. Mechanical exfoliation using AFM cantilever was found equally capable of fabricating few-layer graphene, but the process was limited to producing graphene of a thickness 10 nm, which is comparable to 30-layer graphene. Chemical exfoliation is a method where solution-dispersed graphite is exfoliated by inserting large alkali ions between the graphite layers. Similarly, chemical synthesis process consists of the synthesis of graphite layers. Similarly, chemical synthesis process consists of the graphite oxide, dispersion in a solution, followed by reduction with hydrazine. Like carbon nanotube synthesis, catalytic thermal CVD has proved to be one of the best processes for large-scale graphene fabrication. Here, thermally dissociated carbon is deposited onto a catalytically active transition metal surface and forms a honeycomb graphite lattice at elevated temperature under atmospheric or low pressures. When the thermal CVD process is carried out in a resistive heating furnace, it is known as

thermal CVD, and when the process consists of plasma-assisted growth, it is called plasma enhanced CVD or PECVD. As a whole, all the above techniques are standard in their respective fields. However, all synthesis methods have their own advantages as well as disadvantages depending upon the final application of graphene. For example, the mechanical exfoliation method is capable of fabricating different layers of graphene (from monolayer to few-layer), but the reliability of obtaining a similar structure using this technique is quite low. Moreover, large-area graphene fabrication using mechanical cleaving is a serious challenge at this moment. From monolayer to few-layer graphene can easily be obtained by the adhesive tape exfoliation method, but extensive method, but extensive research is a prerequisite for further device fabrication, which limits the feasibility of this process for industrialization. Furthermore, chemical synthesis process (that involve the synthesis of graphite oxide and reducing it back to graphene in a solution dispersal condition) are low temperature processes that make it easier to fabricate graphene on various types of substrates at ambient temperature, particularly on polymeric substrates (those exhibit a low melting point). However, homogeneity and uniformity of large-area graphene synthesized from reduced graphene oxides often causes incomplete reduction of graphite oxide (which exhibits insulator characteristics) and results in the successive degradation of electrical properties depending on its degree of reduction. In contrast, thermal CVD methods are more advantageous for large-area device fabrication and favorable for future complementary metal-oxide semiconductor technology by replacing Si.[25] Epitaxial graphene, thermal graphitization of a SiC surface, is another method, but the high process temperature and inability to transfer on any other substrates limit this method's versatility. In this context, the thermal CVD method is unique because a uniform layer of thermally chemically catalyzed carbon atoms can be deposited onto metal surfaces and can be transferred over a wide range of substrates. However, graphene layer controllability and low-temperature graphene synthesis are challenges for this technique.

2.2.4 GRAPHENE OXIDE FOR BIOMEDICAL APPLICATION

Chemistry, material science, biology, medicine and nanotechnology are fields of applications of graphene and graphene oxide (GO). Brodie discovered in 1859 GO, but only recently its properties started to be fully exploited and studied. Later different procedures emerged to obtain GO from graphite thanks to the studyes of Staudenmaier and Hummers.[26]

GO is a two dimensional material made of sp^2 and sp^3 hybridized carbon atoms arranged in a hexagonal honeycomb pattern and of oxygen atoms present in the form of different functional groups (**Figure 6**). The type and amount of oxygenated species is still highly discussed today. This is due to a lack of sufficiently sensitive analytical techniques and to the amorphous and berthollide character of this material.[27]

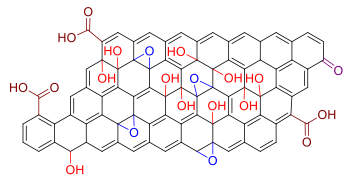

***Figure 6**. Schematized representation of GO*

GO's sheets are irregular. Modulating the size of this material is possible through an accurate post-sonication, centrifugation and filtration procedure.[28] But until today a complete control it is still no possible.

GO is a very hydrophilic material thanks to their oxygenated functional groups. This carbon material, compared to non-oxidized form graphene, is more chemically reactive due to the presence of defects. The mechanical properties of GO are lower, but it shows a higher optical transmittance.

Exploiting their hydrophilic aspects, GO finds many applications in the biomedical field. The large surface area allowed a high drug loading. Drugs and molecules can be covalently attached or can be adsorbed onto the surface of GO. GO proved to be an excellent structure for DDS or for combined strategies of targeting and imaging. Numerous studies were performed by using GO as delivery for anticancer drugs.[29]

The graphene surface with delocalized π electrons can be utilized for effective loading of aromatic anticancer drugs such as doxorubicin (DOX) via π- π stacking and hydrophobic interactions. The extremely large surface area of graphene, with every atom exposed on its two sides, is allowed for ultra-high drug-loading efficiency. [30]

CPT, a cytotoxic quinoline alkaloid, has been proved to be effective against a broad spectrum of tumors by inhibiting the DNA enzyme topoisomerase I (Topo1).[31] But CPT has a low bioavailability due to its poor water solubility which limits its clinical applications. The functionalized GO as a nanocarrier can help improving not only its solubility but also its cellular uptake by enhancing its ability to go across the target cell membrane. Dai and collaborators explored for the first time functionalized nanoscale GO (NGO) as a novel and efficient nanocarrier for delivery of SN38, a CPT analog into cells.[32]

Apart from cancer drugs, presently GO-based drug delivery is elaborated to other drugs for non-cancer diseases treatment. Rana et al. synthesized chitosan-functionalized graphene oxides (FGOCs) and studied the delivery of an anti-inflammatory drug, IBU.[33] The IBU drug was released up to ~ 19% in PBS from FGOCs. They showed that there was no serious toxicity of the CEM cell line for various concentrations of FGOCs GS without drug loading, which suggested that FGOCs sheets had a very good biocompatibility. But FGOCs/IBU samples showed higher cell killing effect compared with FGOCs.

2.2.5 STRUCTURAL PROPERTIES OF GRAPHENE OXIDE AND MAIN SYNTHESIS PROCEDURES

Brodie developed the first production procedure of this material: the treatment of graphite with an oxidation mixture made of potassium chlorate and fuming nitric acid. A modification in chemical procedure was introduced in 1898 by Staudenmaier who added to the oxidation mixture concentrated sulfuric acid, reduced the oxidation cycles to only one and introduced a two-step protocol.[26] This protocol thanks to Hummers and Offeman was improved obtaining a time-efficient synthetic route. New reagents were introduced such as potassium permanganate to oxidize substrates, with the cooperate effect of sodium nitrate and sulfuric acid. Later, due to the toxic gases produced by the oxidation, *Tour et al* proposed the use of phosphoric acid instead of sodium nitrate, removing the dangerous gases. Eigler *et al.* understood the importance of temperature during the synthesis process, decreasing from 45°C to 10°C. This method allowed to achieve a better quality GO, called oxo-G.[34]

Surface composition of GO was influenced by synthetic process, such as the oxidation reagent or the mentioned adopted temperature. Eng. *et al* investigated by using voltammetry analysis on GO material, obtained by adding permanganate or chlorate oxidation mixture. The results revealed that the use of permanganate mixture involved a majority of *ortho*-quinones followed by ketones. A small amount of carboxyl groups was found. Epoxides represent the major contribution on GO surface followed by a minor number of hydroxyl groups.[35] Chlorate oxidation mixture contributes to have a more uniform

distribution, but with a lower amount of oxygenated functional groups, ketones represent the major contribution. Carboxyl acids were not detected.

Because of the complexity of GO and difficulty in analytical techniques for characterization, many models to represent GO were proposed in literature. The first models, dated in the forties, suggested repeating groups of 1,2-epoxide or 1,3-epoxide and hydroxyl groups. Later ketones functional groups were introduced, such as quinones. Phenolic groups are mentioned to explain the acidity of GO.[36] All these improvements were provided by different analyses: magic angle spinning (MAS), transmission electron microscopy (TEM), elemental analyses, Fourier Transform (IR).

Today one of the plausible model was introduced by Tour and coworkers.[37] They proposed an unconventional view of GO chemistry and developed the corresponding "dynamic structural model" (DSM). In contrast to previously proposed models, the DSM considers GO as a system, constantly changing its chemical structure due to interaction with water. Using potentiometric titration, ^{13}C NMR, FTIR, UV-vis, X-ray photoelectron microscopy, thermogravimetric analysis, and scanning electron microscopy we showed that GO did not contain any significant quantity of preexisting acidic functional groups, but gradually generates them through interaction with water. This model explained also the reduction of GO under strong alkaline conditions, resulting in the formation of CO_2 and vacancies.

In spite of all the suggested models, until today the definitive structure of GO is till unknow.

2.2.6 FUNCTIONALIZATION OF GRAPHENE OXIDE

GO, without any surface functionalization, usually has sheet dimensions of hundreds of nm and tends to aggregate in physiological solutions with salts and proteins due to screening of electrostatic charges and non-specific binding of proteins. As a result, size control and individual separation are necessary for GO to suitably interact with a biological system in vitro and in vivo. As well, rational functionalization is essentially needed to offer GO with better compatibility and stability in the physiological environment.[38] To achieve these purposes, two strategies, covalent conjugation and non-covalent physisorption, have been reported.

COVALENT FUNCTIONALIZATION

Numerous oxygenated functional groups on GO allowed many possibilities of derivatization of this nanostructured material, but many side reactions could occur, hindering an easy selectivity degree. For this reason performing control reactions in the same conditions, but without an essential reagent is required.

The functional groups more exploited for covalent decorations of GO are epoxides, carboxyl groups and hydroxyl groups. Hydroxyl groups are localized on the core surface of GO, they were reacted through silanization,[39] etherification,[40] phosphorylation[41] and Ritter reaction.[42]

Silanization is a two-steps reaction: first the hydrolysis of the trialkoxy groups of the silane followed by the reaction between the Si-OH groups and the hydroxyl groups of GO (**Scheme 1**)

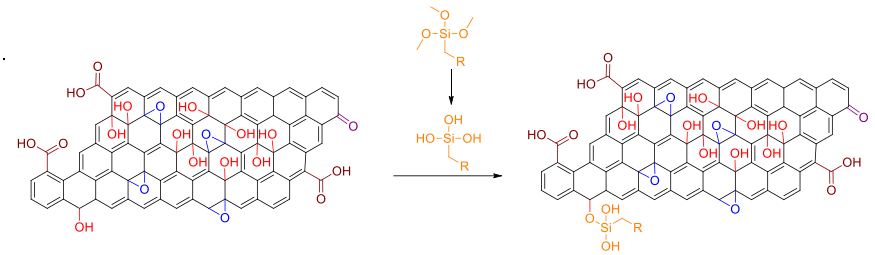

***Scheme 1**. Silanization reaction on GO. (The reaction has been drawn only on one functional group for clarity reasons. Side reactions were not considered).*

Phosphorylation was performed by mixing GO with concentrated phosphoric acid at 50°C. **Scheme 2**

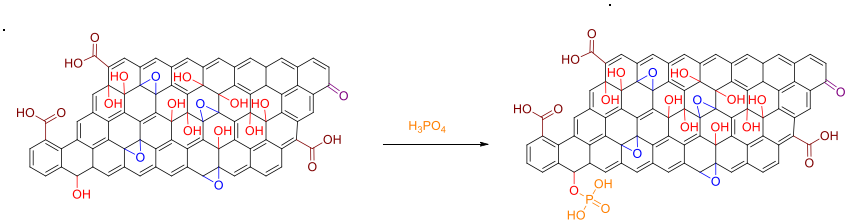

***Scheme 2**. Phosphorylation of GO. (The reaction has been drawn only on one functional group for clarity reasons. Side reactions were not considered).*

Ritter reaction: carbocations produced on the basal plane of GO underwent a nucleophilic attack by the nitrogen of a nitrile. After hydrolysis an amide is formed. This reaction has been performed with sulfuric acid and acetic acid at 70°C, conditions that brought to the reduction of GO to restore the conductivity of this material. (**Scheme 3**)

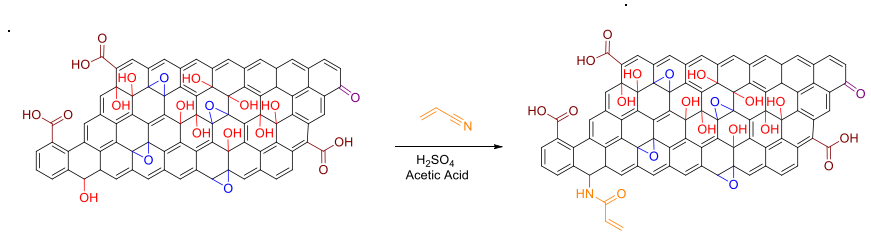

***Scheme 3**. Ritter reaction on GO. (The reaction has been drawn only on one functional group for clarity reasons. Side reactions were not considered).*

Epoxide groups are manly located on the basal plane of GO, the rings could be opened by addition of amine-terminated molecules or sodium azide (**Scheme 4**). Graphene azide could be synthesized from GO as precursor for click chemistry by *Halbig et al*.

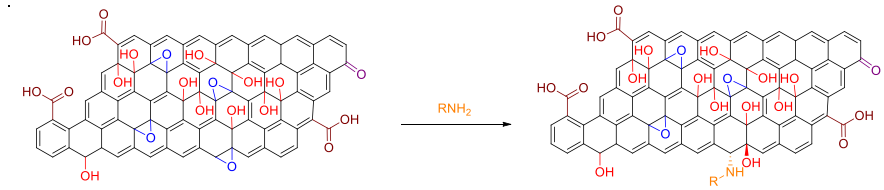

***Scheme 4**. Opening of epoxide ring on GO. (The reaction has been drawn only on one functional group for clarity reasons).*

After the activation of carboxyl acids located mainly at the edges of GO, esterification or amidation process could be performed. The activation was achieved by adding oxalyl chloride or thionyl chloride. However, these reagents can cause side reactions. (**Scheme 5**)

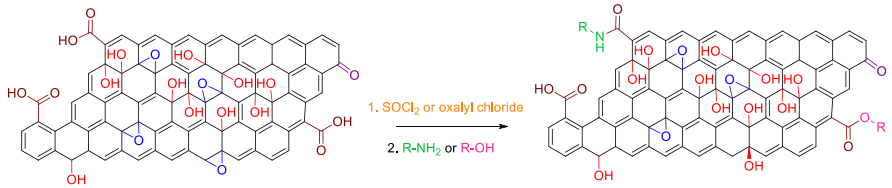

***Scheme 5**: Esterification and Amidation approaches on GO. Side reactions were not considered.*

2.2.7 CITOTOXICITY OF GO: BIOCOMPATIBILITY AND BIODEGRADATION

The cytotoxicity of GO and its derivatives must be extensively investigated in vitro and in vivo if they are employed as drug nanocarriers. Several research groups have deliberatively explored this critical issue.[30] Most of the in vitro experimental results to date have suggested that as-prepared GO was a safe material at low concentrations in a variety of cells such as human fibroblasts,[43] HeLa cells,[44] L929 cells,[45] human hepatoma HepG2 cells[46] and A549 human lung cancer cells.[47]

On the other hand, in vivo studies indicated severe chronic toxicity associated with GO, especially at a high dose. Zhang *et al.* systematically studied the distribution and biocompatibility of GO in mice by using radiotracer technique and a series of biological assays.[27] When mice were exposed to 1 mg/kg body weight of GO for 14 days, no pathological changes were observed in examined organs, indicating that GO might be non-toxic and suitable for biomedical applications at a low injection dose. However, it is revealed that GO at a relatively higher injection dose (10 mg/kg) showed dominant accumulations in the lungs after being intravenously injected into rats or mice and were hardly excreted for long periods of time, leading to serious toxic effects and significant pathological changes, such as inflammation cell infiltration, pulmonary edema and granuloma formation.

GO biocompatibility depends on the synthesis procedure and on the starting graphite used. The surface of GO plays an important role in the biological interaction of nanomaterial. A fundamental factor is the number of layers of material which is closely connected to the flexibility of GO. Multilayer GO could acquire the behavior of a rigid block interacting with cells. Many aspects are influenced by lateral dimension size such as uptake, renal clearance, blood brain barrier transport, cell internalization mechanism and other bio-phenomena.

The interaction with proteins in blood could determine the half-lives and biodistribution of the nanoparticles. Their hydrodynamic size could be influenced and improved. This effect facilitates recognition and clearance by macrophages and phagocytes. Interaction with proteins may also impact on the targetability of nanomedicines. Protein corona formation is a phenomenon consisting in serum protein adsorption onto the surface of GO. Proteins (albumin, apolipoprotein, immunoglobulins, complement, and fibrinogen) adsorb on various nanomaterial (polymeric nanoparticles, iron oxide nanoparticles, gold nanoparticles, liposomes, GO and CNTs) surfaces exhibit structural changes in the bloodstream (bioactivity). PEG is used to limit non-specific protein adsorption.[48]

A good dispersibility of GO can influence also the biodegradation of this material.[49]

Toxicity can derive also from some residues due to the production process of GO, such as from oxidation mixture previously mentioned. Considering that until now there are only a lot of studyes performed with different kinds of GO, without any standard, the analysis of the results of toxicity studyes is still inconclusive.

2.2.8 DISULFIDE LINKER

The final goal of this project is the synthesis of two models for a DDS based on the use of CNTs and GO which allow the release of the molecular fragment bound through the disulfide linker.
A DDS for the treatment of tumors should not exhibit systemic toxicity: the linker must be stable in the bloodstream, but in cell internalization the disulfide bridge should be broken to release the drug. For this purpose a simple molecule has been synthesized (**Figure 7).**

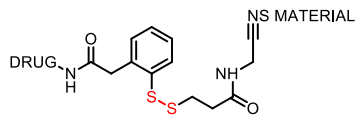

Figure 7: *linker that binds the drug to the CNT. In red the disulfide bridge cleaved into intracellular environment.*

The structure shows a stable disulfide bridge in the blood, but potentially cleavable from endogenous thiols typical of the intracellular environment of tumors, such as glutathione. (**Figure 8**)

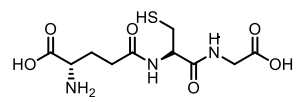

Figure 8*: Glutathione.*

GSH levels in cancer cells have been shown to be> 1000 higher compared to the amount in the blood plasma.[50] The presence of glutathione leads to the cleavage of disulfide bridge by forming a 5-membered thiolactone, releasing the drug free.
In this work any drug has been not used, but a BODIPY dye linked to CNTs via the linker. The internalization of the system can be monitored.

2.2.9 FLUORESCENT PROBES

Fluorescent probes are molecules that absorb light of a specific wavelength and emit light of a different, typically longer, wavelength (a process known as fluorescence), and are used to study biological samples. The molecules, also known as fluorophores, can be attached to a target molecule and act as a marker for analysis with fluorescence microscopy.

Experimentally they are used in different areas of interest such as in medical care, biochemistry, clinical diagnostical environment. Thanks to a remarkable advancement of imaging techniques, many of the previous technical-practical limits were overcome. The affirmation of confocal microscopy is now able to obtain images, even of complexes samples, with high contrast and resolution.

DESIGN CRITERIA

Design criteria include numerous parameters simultaneously required to ensure the effectiveness of the probe itself:

i. High selectivity and high fluorescence response for the desired analyte, without competitive reactions with other analytes in the same chemical environment;

ii. Probe's robustness to chemical agents and light;

iii. The fluorescence must be as intense as possible, requiring wide values of ε (λ) at the λ wavelength of excitation and quantum yield Φ very high;

iv. The associative-dissociative mechanism between receptor and analyte must be fast, such as to carry out a real-time investigation of the concentration (in the case of time-dependent response);

v. The fluorescence signal generated by the "starting/lighting" of the probe (e.g. fluorescence enhancement or length shifts wave of excitation and / or emission, must be favored on response of the type "shutdown" (for example, quenching of fluorescence), with a concomitant signal-to-noise ratio lower;

vi. The use of indicators that absorb and emit light in the visible or near infrared NIR (650-900 nm) was preferred, choosing this region numerous advantages, compared to UV region, were achieved: such as the absence of quartz optical equipment and less light scattering.

Primarily light-induced damage to the biological sample should be minimized, for this reason NIR (Near Infrared) is more used. In this wavelength interval, biological samples have a low fluorescence background, which consequently produces a high signal/noise ratio; furthermore, in this band, Rayleigh and Raman scatterings are reduced, allowing an important capacity penetration of light into biological tissues and cells. In biological environment, a certain water solubility, a permeability of membrane (closely connected to pH) and minimal toxicity towards samples are also required.

BODIPY dyes represent an important class of fluorescent probes. These compounds found many applications such as an imaging probes[51] or in chemosensing.[52] We decide to synthesize and modify the structure of this probe thanks to its versatility and its properties.

Many types of BODIPY are not soluble in water and only a few of these structures have been modified to increase their solubility. On the other hand, however, they are relatively insensitive to the polarity and pH of the environment, exploiting their related stability in physiological conditions. BODIPY represents an excellent investment as *building block*, although not meeting all the previously mentioned requirements.

2.2.10 BODIPY

STRUCTURE AND PROPERTIES

The basic structure, also called *"core"*, is shown in **Figure 9**. This structure is fundamental for the synthesis of the most complex BODIPY dyes.

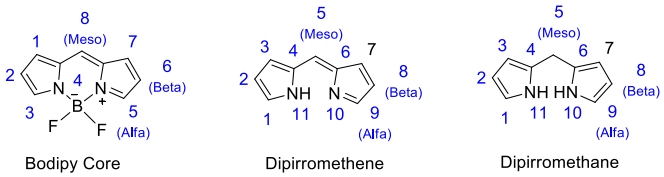

Figure 9: *BODIPY's structure.*

The pyrrole protons of the BODIPY Core, especially those in position 5 and 7, are relatively acidic and this leads to electrophilic attack, reason why this compound, without any substituent, has never been isolated. Analogously for the other two systems: dipyrrometene, for example, decomposes at temperatures above -40 °C.[53],[54]

The most basic structure of BODIPY is shown in **Figure 10**; compounds B and C are not presented in literature due to the synthetic limits:

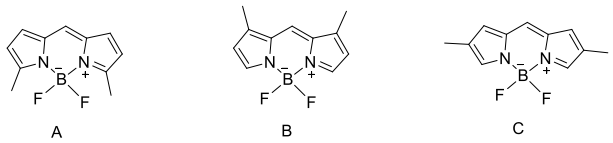

Figure 10. *BODIPY 3,5 Dimethyl substituted A. EtOH, φ=0.81; $\lambda_{Max\ Abs}$=506 nm, $\lambda_{Max\ Emis}$= 520 nm; B e C not isolated.*

The synthesis of tera-, esa-, epta- substituted compounds **Figure 11** reveled a shift of fluorescence close to the red region directly proportional to the number of substituents.

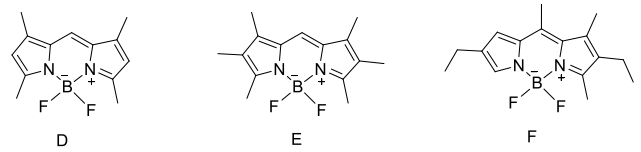

Figure 11. D, *EtOH, φ = 0.80; $\lambda_{Max\ Abs}$= 505 nm, $\lambda_{Max\ Emis}$= 516 nm;* ***E****, EtOH, φ= 0.56; $\lambda_{Max\ Abs}$= 528 nm, $\lambda_{Max\ Emis}$=535 nm;* ***F****, EtOH, φ=0.70; $\lambda_{Max\ Abs}$= 517 nm, $\lambda_{Max\ Emis}$= 546 nm.*

The substitutions in *meso* position are not associated with relevant change in absorption or emission wavelength, but considerable variation in quantic yields (*φ*) are collected, as shown in **Figure 12**.

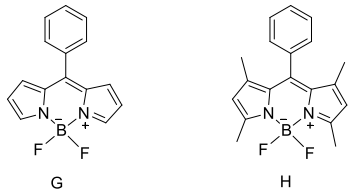

Figure 12*. G, MeOH, φ= 0.19; $\lambda_{Max\ Abs}$= 508 nm, , $\lambda_{Max\ Emis}$= 519 nm; H, MeOH, φ=0.65; $\lambda_{Max\ Abs}$= 498 nm, , $\lambda_{Max\ Emis}$=508 nm.*

The difference in quantic yields between the compounds in FIGURE are associated to a major rigidity due to the presence of methyl groups in position 1 or 7 which prevent the free rotation of phenyl group. Less energy was lost from excited states (via non-radiative). Aromatic rings substituted in *orto* show analogous properties.

2.2.11 SYNTHESIS OF BODIPY

The synthetic procedures of this class of compounds are widely described in literature to obtain various derivative of the BODIPY Core.

SYNTHESIS FROM CARBOXYL ACIDS AND PYRROLES

BODIPY *meso*-substituted are synthesized from condensation of acidic chlorides and pyrroles **Figure 13** [55]

As synthetic intermediates dipirromethene chloridites constituted instable compounds. These salts, although they are easier to treat and purify, are generally never isolated during the process synthesis of BODIPY derivatives.

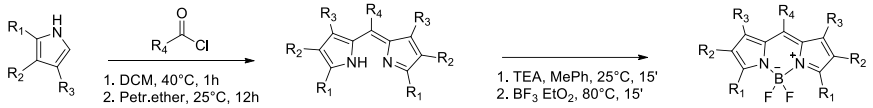

Figure 13. *Synthesis of BODIPY starting from acidic chloride and pyrroles.*

Otherwise, anhydrides can be used as an alternative to chlorides, as shown in **Figure 14**, in which derivative 4 is synthesized starting from glutaric anhydride.[56]

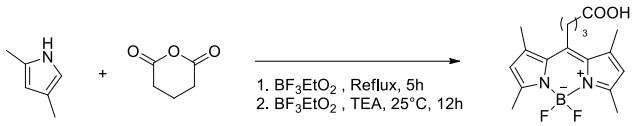

Figure 14. *Synthesis of BODIPY achieved from derivatives of carboxyl (glutaric anhydride).*

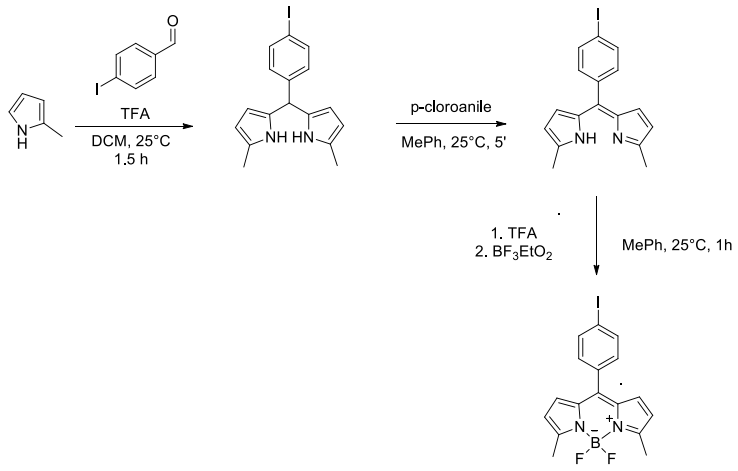

Figure 15. *Aromatic aldehyde was reacted with pyrrole to achieve dipirromethane, after a condensation process. The consecutive oxidation and complexation process allow to obtain the final BODIPY product.*

3-iodobenzaldehyde forms with pyrrole, by acid-catalyzed condensation, the substituted dipyrromethane. If unsubstituted pyrrole is used, the reaction should be carried out using the pyrrole as solvent to avoid polymerization. In Scheme 3 2-Methylpyrrole doesn't have any polymerization as competitive reaction, therefore it doesn't need to be in large excess. [57]
BODIPY compounds are sensitive to light, to air and acids, it must be immediately used for subsequent oxidation. This latter step occurred by using both para-chloroanile and 2,3-Dicloro-5,6-Diciano-*p*-benzochinone, to achieve dipirrometene. Many examples are presented in literature describing aromatic aldehydes, but any synthesis exploiting no aromatic aldehydes were reported. Finally this substrate reacted with a tertiary amine and BF_3EtO_2 to obtain the final product, in high yield.

CHANGES ON BODIPY's STRUCTURES

The family of BODIPY, thanks to its versatility in structural changes, is a molecule of relevant interest. it is an excellent building block, different positions that lead BODIPYs to nucleophilic or electrophilic attacks, as shown in **Figure 16**.

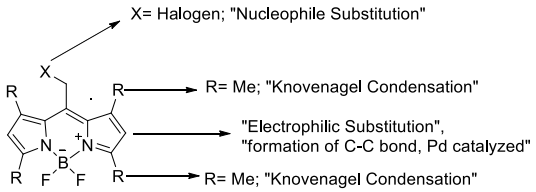

Figure 16. *Modifications of BODIPY structure.*

The structure shows that the two pyrrole rings are aromatic electron-poor systems resulting in the relative acidity of the two methyl groups (3 and 5 positions) providing excellent positions for electrophilic attacks, such as for Knovenagel Condensation with aromatic aldehydes (**Figure 17**). Usually the reaction is carried out under inert atmosphere (N_2), with the presence of a buffer, or by using a base-catalyzed system. Although the ease chemical procedure, the collected yields are often low with electron-poor aldehydes.

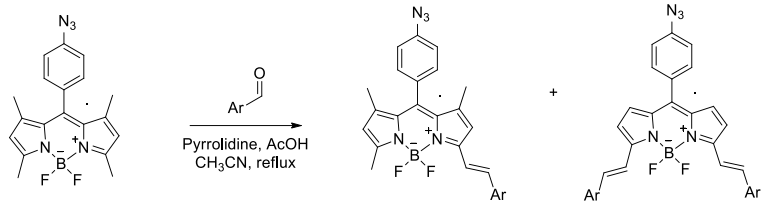

Figure 17. *Condensation of 3,5-dimethyl-BODIPY and aromatic aldehydes; changing the equivalents the synthesis produces mono- or di- substituted.*

The condensation process allows to increase the conjugation of BODIPY core. Electron donor substituents on aromatic aldehydes shift the absorption and emission wavelengths towards the red or even in the NIR. The substituents in 3 and 5 positions modify the properties of BODIPY, both for the spectra and fluorescence quantum yield of product. [11]

The above mentioned positions, thanks to their poverty of electrons, are excellent sites for aromatic nucleophile substitutions. **Figure 18**

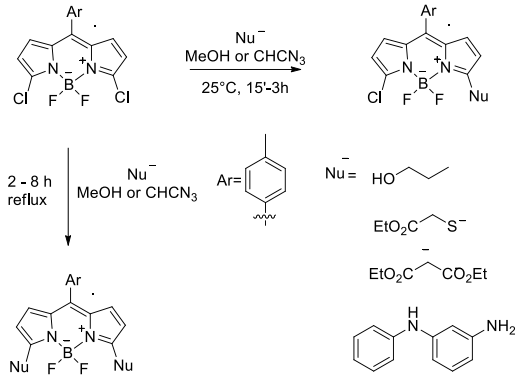

***Figure 18**. Synthetic pattern to obtain BODIPY*

The versatility of reaction of substitution allows to synthesize both *mono-* and *di- substituted*, modifying/stressing reaction conditions. Additional flexibility derives from a wide range of nucleophiles with different structures and properties, such as amines, alkoxides, thiolates etc. *Cross-coupling* reactions metal catalyzed on positions 3 and 5 are possible. Different reagents bring to various products, as shown in **Figure 19**.

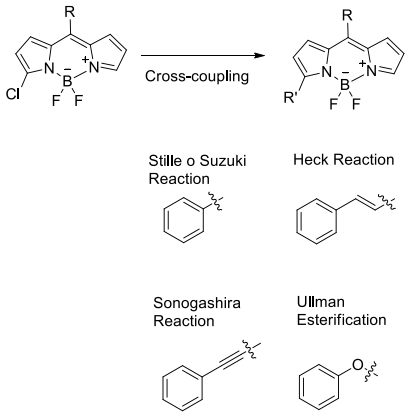

***Figure 20.** Functionalization of BODIPY-3-halogenated metal catalyzed.*

Recalling **Figure 16**, focusing on position 6 (or Beta) reaction Pd catalyzed occurred, exploiting a new bond C-C. (**Figure 21**). A direct functionalization of BODIPY is possible without resort to halogenated or metallized intermediates. [58]

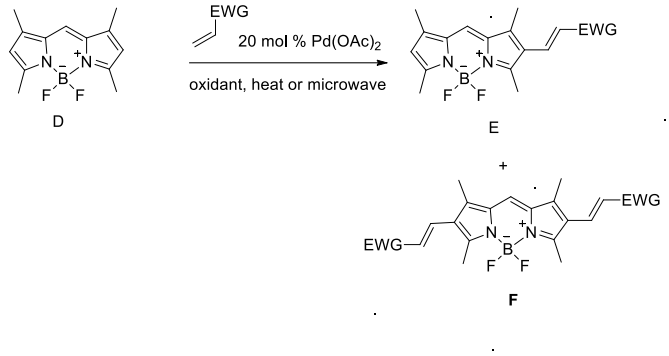

Figure 21. *Functionalization Palladium catalyzed of C-H (EWG=CO_2Me).*

As show in **Figure 21** two products could be obtained: mono- and di- substituted with different spectrophotometric properties, **Tab 1.**

	Solvent	λMax Abs	λMax Em	ϕ
E	MeOH	527 nm	549 nm	0.73
F	EtOAc	559 nm	580 nm	0.51

Tab 1

An additional reaction concerning BODIPY in position 6 is the electrophilic aromatic substitution, such as sulfonation, nitration and halogenation. Changing the reaction condition displayed in **Tab 2**, the synthesis provides numerous products.[59,60]

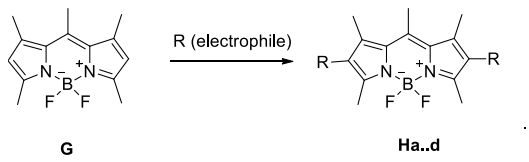

Figure 22*. Disubstituded BODIPY.*

	R	Reaction Conditions	λMax Abs (MeOH)	λMax Emis (MeOH)	Φ (MeOH)
G	-H	-	492 nm	504 nm	0.95
Ha	-SO_3Na	1.$ClSO_3H$, DCM, 50°C 2. NaOH	492 nm	533 nm	0.73 (H_2O)
Hb	-NO_2	HNO_3, 0°C, 15'	-	-	-
Hc	-Br	Br_2, DCM, 25°C	516 nm	546 nm	0.45 (DCM)
Hd	-I	I2, HNO_3 EtOH, H_2O, 60°C, 20'	534 nm	543 nm	0.02

Tab2

2.3 RESULTS AND DISCUSSION-fCNTs

2.3.1 OXIDATION OF CARBON NANOTUBES

The synthetic work started with the preparation of the carrier: pristine MWCNT needed to be treated to increase the water dispersibility of the material and to remove all impurities, like residues of the metallic catalysts and amorphous carbon. Such feature can be obtained through an oxidation process where CNTs are chopped at defect sites and oxygenated functionalities are created on their sidewall and edges. This process requires harsh conditions: concentrated oxidant acids, high energy sonication for prolonged time or heating at high temperatures.[61] To guarantee the highest purity and water dispersibility,

MWCNT (diameter 6-9 nm and 5 µm length) were treated with a refluxing 3:1 mixture of concentrated sulfuric acid and nitric acid for 30 minutes. (**Scheme 6**)

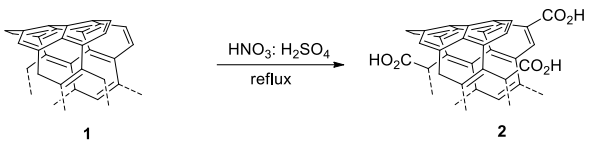

***Scheme 6**. Oxidation process to obtain compound 2.*

Accordingly to a previous procedure, oxidized material was recovered after quenching with demineralized water, two centrifugation cycles (replacing the supernatant with fresh water) and filtration followed by washing with water until the filtrated solvent was neutral.[11] The OxMWCNTs obtained have an average length ranging from 50 to 1000 nm and are dispersible in water. Considering that, as mentioned above, shorter OxCNTs are more biocompatible than longer ones, and are believed to be more easily internalized by tumor cells, we harvested the shortest fraction using a series of centrifugation cycles (**Figure 23**), (see experimental part for details).

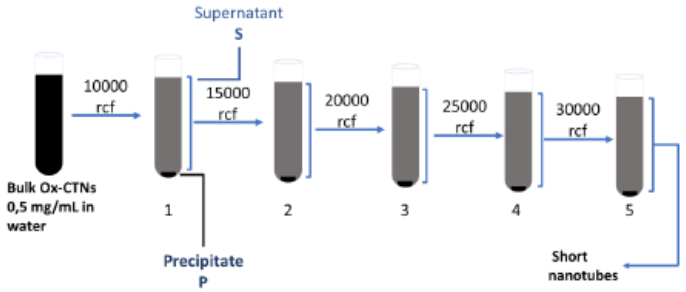

***Figure 23**:. Schematic representation of the separation process.*

The procedure allows to collect a fraction with highly oxidized short multi-walled CNTs (from now on called CNTs). The length measured by TEM (**Figure 24**) ranges from 50 to 200 nm with a mean value of 130.

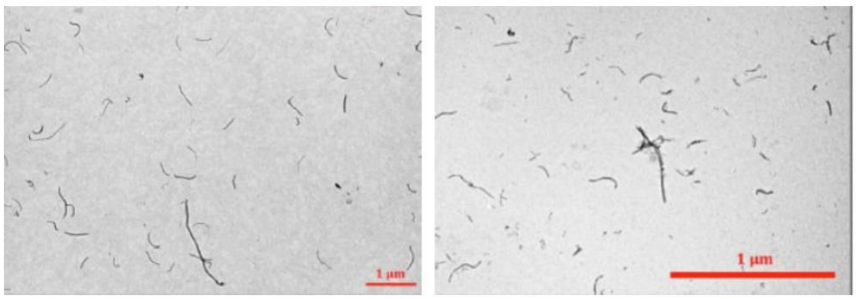

***Figure 24.**TEM images of CNTs bulk material on the left, collected short fraction on the right.*

2.3.2 DECORATION OF CNTs WITH 4-AZIDOANILINE

The nanostructured support chosen to realize the DDS model was oxidized carbon nanotubes (CNTs). The first kind of functionalization was the introduction of 4-azidoaniline through Tour reaction (**Scheme 7**). This radical process allowed to exploit an aniline to covalent bind a substrate with an azido group.

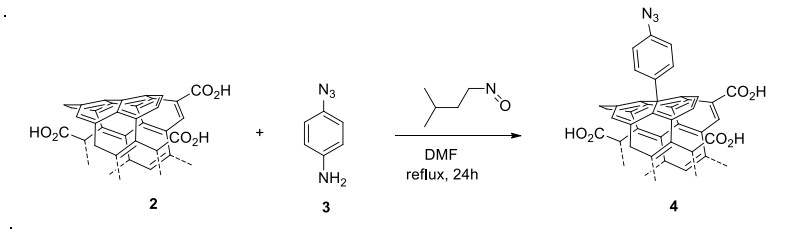

***Scheme 7**. Functionalization of CNTs (2) with 4-azidoaniline (3).*

Elemental analyses evaluated a loading degree equal to 1.4 mmol of azide /mg of material.

2.3.3 GO FUNCTIONALIZATION *via* PEG

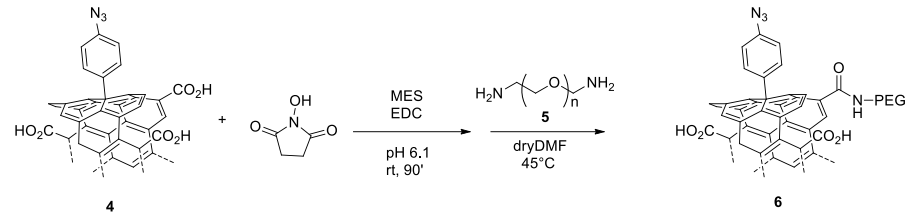

***Scheme 8**: PEG functionalization of GO*

A two steps process allowed to introduce PEG chains (**5**) covalent bound to CNTs by using 2-(N-morpholino)ethanesulfonic acid Buffer and EDC to activate carboxyl acids on carbon nanotubes, followed by an addition of PEG in dry DMF. After a filtration process the material was recovered as a black powder.

2.3.4 SYNTHESIS OF BODIPY CORE

The first part was the synthesis of BODIPY Core, which may be functionalized to bring two different fluorescent probes. The first synthetic pathway was presented in literature. [62] During the mechanochemical synthesis 4-Nitro benzaldehyde was reacted with 2,4-dimethylpyrrole in the presence of trifluoroacetic acid (TFA), with an excess of p-chloroanyl for the oxidation of meso carbon (**Scheme 9**)

Numerous extractions were required to obtain compound **7** (BODIPY-Nitro) due to the formation of triethyl amine salts, nevertheless after chromatography purification the yield was low. ^{1}H-NMR spectrum of compound **8** was synthesized in **Scheme 9**. and compared to ^{1}H-NMR of compound **7**, collected before the complexation process with BF_3Et_2O.

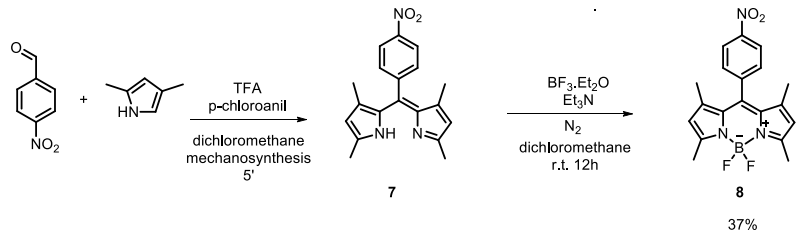

***Scheme 9:** Synthesis of BODIPY Core*

Moving from compound **7** to compound **8** by adding boron to bridge the two pyrrole rings, a shift of the signals to higher ppm was showed:

. The signal of the methyl protons has a shift of 0.22 ppm;

. The signal of the pyrrole hydrogens has a shift of 0.12 ppm;

. The signal of methyl hydrogens is shifted by 0.10 ppm;

. The signals of the protons of the benzene ring are essentially unchanged.

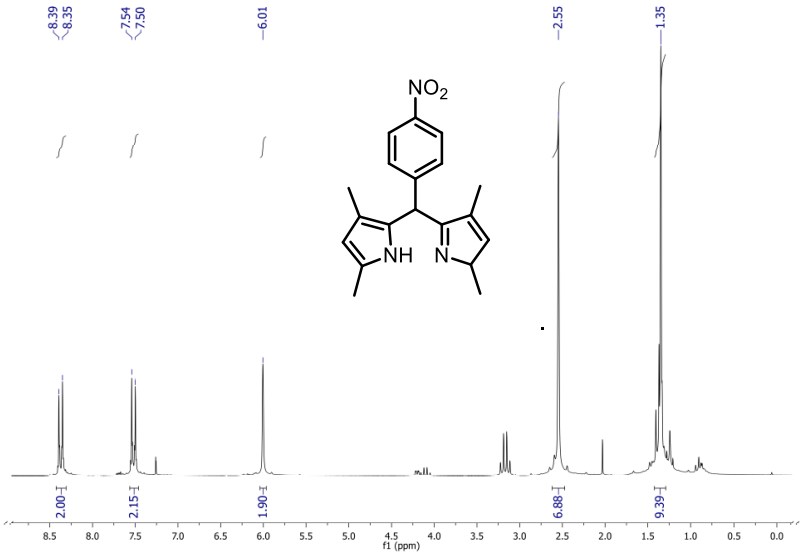

Figure 25. *^{1}H-NMR Spectrum of compound **7**.*

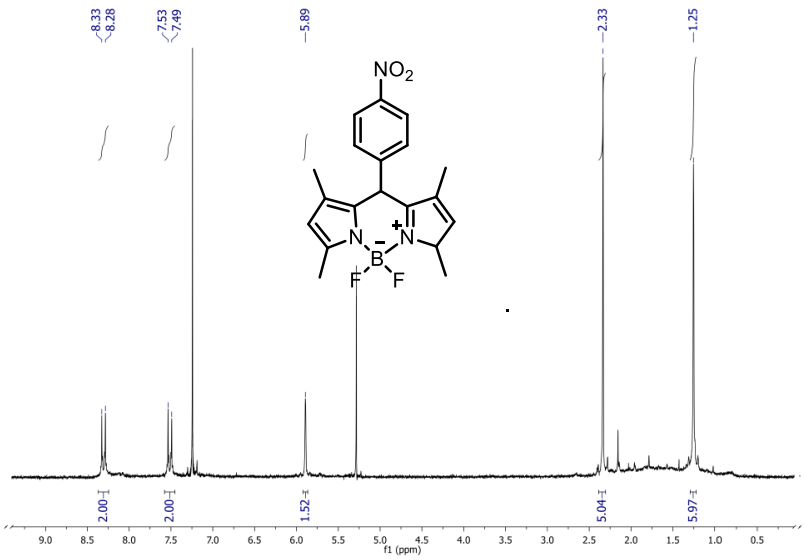

Figure 26. *^{1}H-NMR Spectrum of compound **8**.*

These two mentioned steps were limiting in yields. A different synthetic approach allowed to improve the yields and the ease workup. (**Scheme 10**).

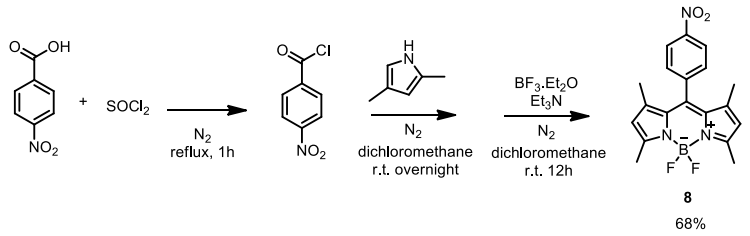

***Scheme 10**. Synthesis of BODIPY Core*

The adopted synthetic approach provided compound **8** through the reaction of 4-Nitro benzoic acid and thionyl chloride, followed by pyrrole addition and BF_3Et_2O complexation. This procedure was preferred compared to the previous mentioned.

The reduction of $-NO_2$ to $-NH_2$ group occurred by using Fe powder, H_2O and HCl in MeOH for 2.5 h in reflux condition.

^{1}H-NMR spectrum (**Figure 12**) showed:

. Signal at 6.90 ppm: dd of hydrogen atoms of benzene;

. Singlet at 5.97 ppm of pyrrole hydrogens;

. Signal of amino protons at 3.83 ppm;

. Two singlets of methyl hydrogens at 2.54 ppm and 1.29 ppm.

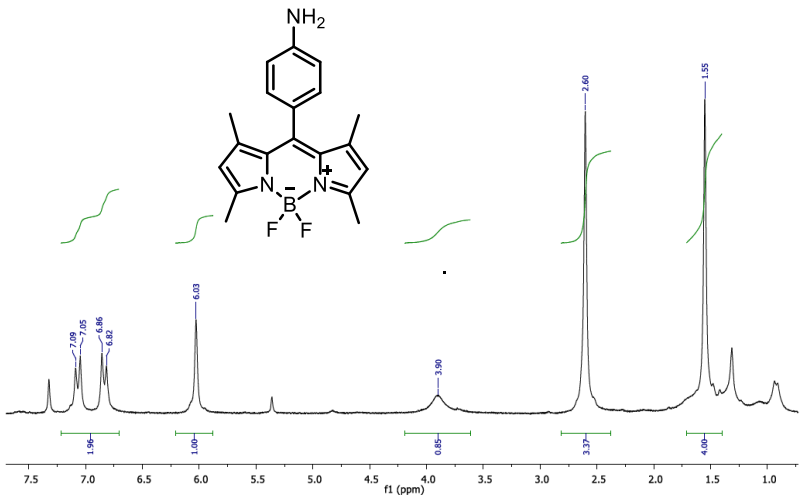

***Figure 27**: ^{1}H-NMR spectrum of compound **9**.*

A part of product **9** was modified by introducing an alkyne group thanks to a coupling with 4-pentynoic acid to introduce a triple bond to allow the grafting onto nanomaterial. Subsequently the extension of the conjugation in position 3 and 5 has been extended. The reaction was carried out on reflux, under nitrogen atmosphere and controlled by TLC. After 40' the reaction was stopped. The products of

reaction were mono and disubstituted compounds. **(Scheme 11)** Thanks to a chromatography column BODIPY-disubstituted was collected.

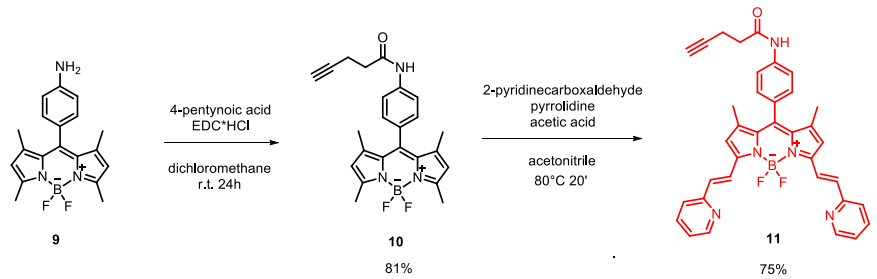

***Scheme 11**. Coupling Reaction and Knovenagel Reactio.*

In ^{1}H-NMR the appereance of signal at 2.07 ppm confirmed the occurred reaction, due to the presence of an alkyne proton.

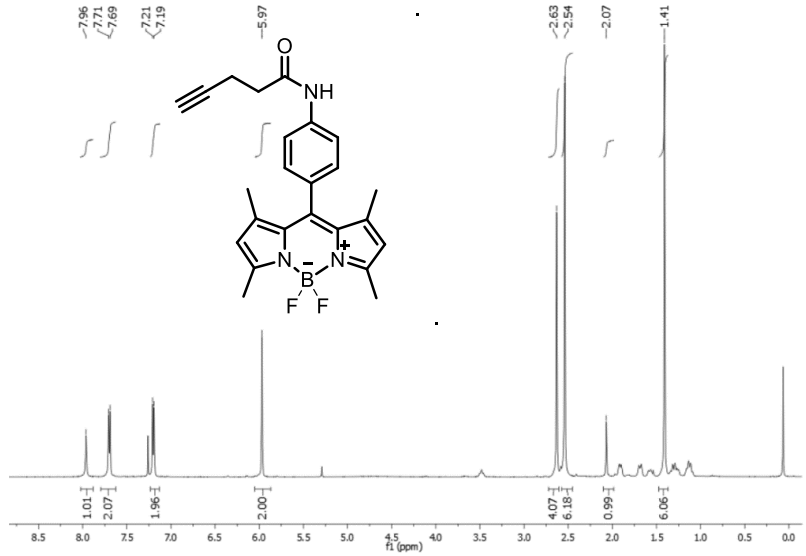

***Figure 28**: ^{1}H-NMR spectrum of compound **10**.*

The synthesis of BODIPY-disubstituted was showed in **Scheme 11**

. At 8.65 ppm a doublet that integrates two protons, which are those of pyridine adjacent to the N atom;

. Signal centered at 8.05 ppm, a doublet which integrates 2 protons, belonging to double bond that binds pyridine to BODIPY;

. A multiplet is included in the aromatic zone between 7.75 ppm and 7.65 ppm which integrates 7 protons of which 2 belong to the two pridiles, 4 belong to the benzene ring in the meso position of the BODIPY and the last is the H amide;

. A signal centered at 7.35 ppm is a doublet that integrates 2 belonging protons to the double bond between pyridyls and BODIPY;

. A signal centered at 7.27 ppm there is a doublet that integrates 2 belonging protons to pyridyls;

. A signal centered at 7.20 ppm a triplet integrates two protons belonging to the system of pyridyls;

. A signal centered at 6.69 ppm a singlet integrating 2 protons indicates the presence of 2 equivalent hydrogens of pyrroles;

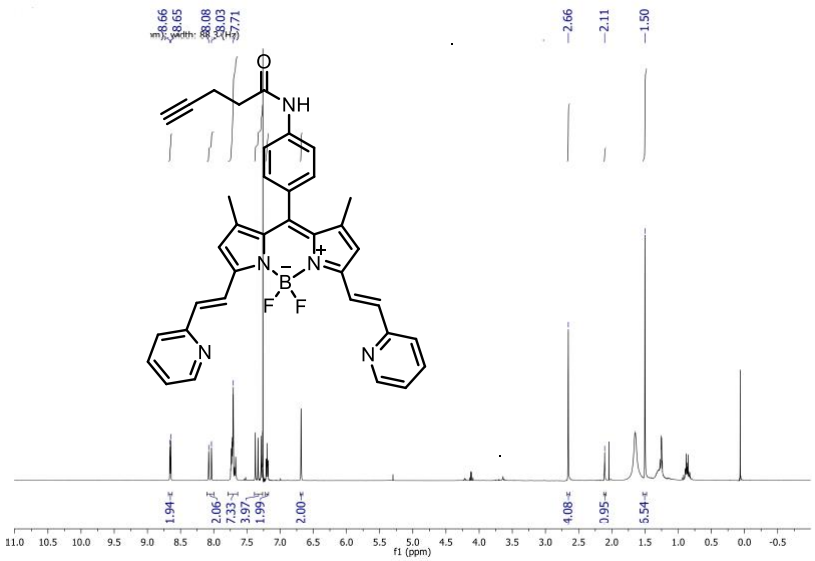

***Figure 29**: [1]H-NMR spectrum of compound **11**.*

2.3.5 SYNTHESIS OF THE LINKER

To synthesize the disulfide linker a known synthetic pattern was followed.[50]

SYNTHESIS OF tri-tert-butylsilyl 3-(pyridin-2-yldisulfanyl)propanoate

The first step is an exchange reaction between the 2,2-dipyridyl disulfide and the 3- acid mercaptopropionic, which occurred in methanol at room temperature. After 1:50 h a TLC analysis did not reveal the presence of residual acid. **(Scheme 12)**

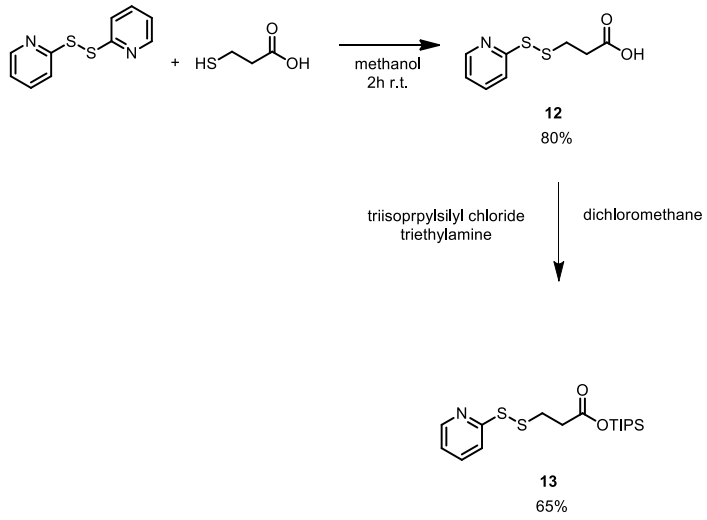

***Scheme 12**. Synthetic pattern to obtain compound **13**.*

Although ^{1}H-NMR spectrum of the crude showed overlapping signals of by products it presented also the signals of desired product **12**.

The obtained acid (**12**) was protected with TIPSCl, slowly added under nitrogen atmosphere at 0°C, in dry DCM in the presence of TEA dry. Such protection was necessary for a subsequent reaction, the selective reactivity of a carboxyl group is required.

The crude product **12** was washed with a saturated aqueous solution of NH_4Cl; then the product was further purified by flash chromatography with eluent EP-EtOAc (20: 1), obtaining a product with 65% of yield.

A ^{1}H-NMR spectrum of **12** was recorded, showing typical TIPS signals: a doublet at 1.06 ppm (18H) and a multiplet centered at 1.26 ppm (3H)(**Figure 30**).

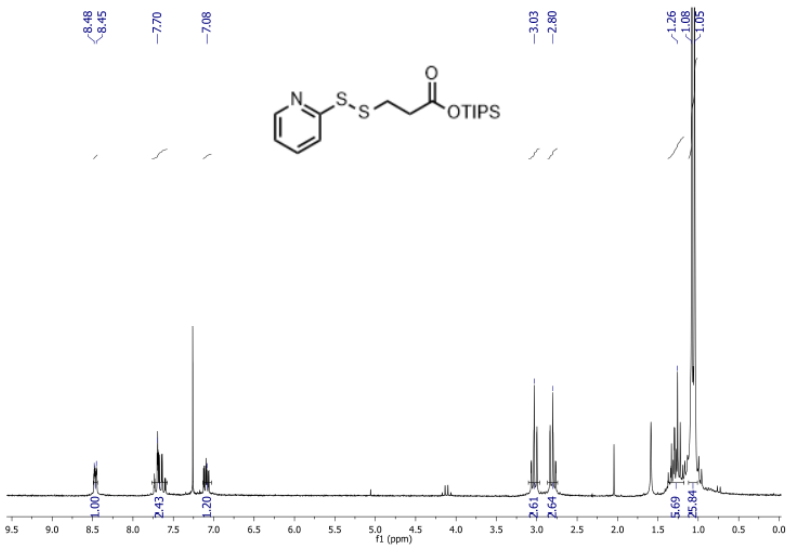

***Figure 30**. [1]H-NMR of product **13**.*

SYNTHESIS OF 2-(2-mercaptophenyl)acetic acid

The synthesis of compound **14** was achieved through the synthetic pathway shown in **Scheme 13**. Benzo[b]thiophen-2-ylboronic acid was reacted with H_2O_2 in ethanol at room temperature for 5h to obtain a thiolactone **14** (90% yield)

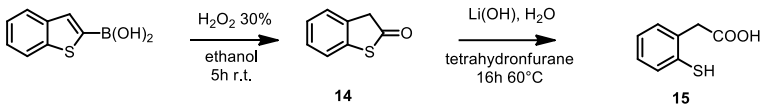

14

90%

15

97%

***Scheme 13**: Synthesis of compounds **14, 15**.*

At the end of reaction the solid product was characterized *via* [1]H-NMR **(Figure 31)**

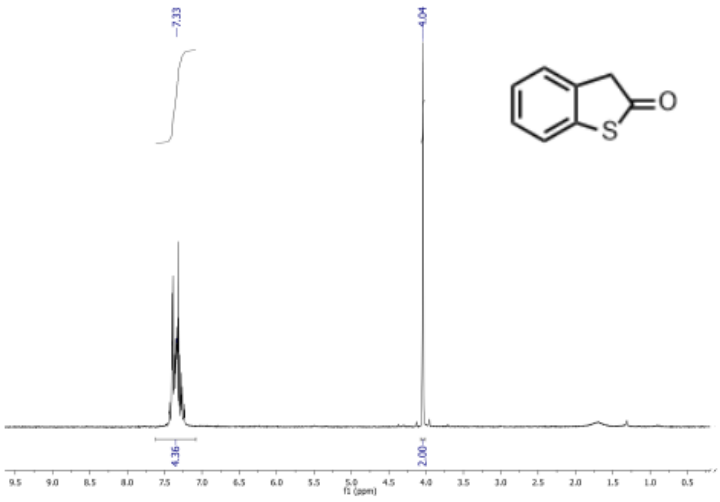

***Figure 31**. [1]H-NMR of compound **14**.*

Several overlapping signals are observed due to the protons of the benzene ring, centered at 7.33 ppm, which integrate 4 hydrogens. Finally, there is a singlet centered at 4.04 ppm connected with 2 protons, adjacent to carbonyl group. The spectrum confirmed the desired product.

The thiolactone was subsequently hydrolyzed with LiOH in H_2O and THF for 16 h at 60°C, to obtain a carboxylic acid **15** with a yield of 97%. [1]H-NMR spectrum confirmed the presence of 2-mercaptophenylacetic acid **(Figure 32)**:

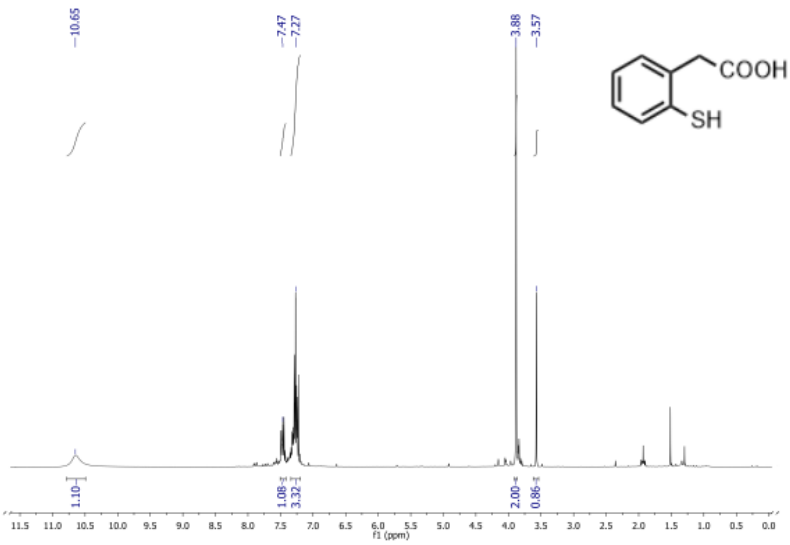

***Figure 32**: [1]H-NMR of compound **15**.*

. The signal at 10.65 ppm suggested the successful transformation into carboxylic acid;

. Two multiplets were generated at 7.20 ppm and 7.50 ppm (4 protons) connected with benzene ring of product;

. At 3.88 ppm a singlet (2 protons), diagnostic signal of 2 aliphatic hydrogens

. At 3.57 ppm there is a singlet, a proton, typical of the -SH of aromatic thiols;

SYNTHESIS OF 2-(2-((3-oxo-3-((tri-tertbutylsilyl)oxy)propyl)disulfanyl)phenyl)acetic acid (**16**)

In the following synthetic step, the desired disulfide linker was achieved through the reaction between compounds **11** and **13** previously prepared. The reaction was carried out in dry Et_2O under nitrogen atmosphere, for 48 hours, at -7 C° with the aid of a thermostat.

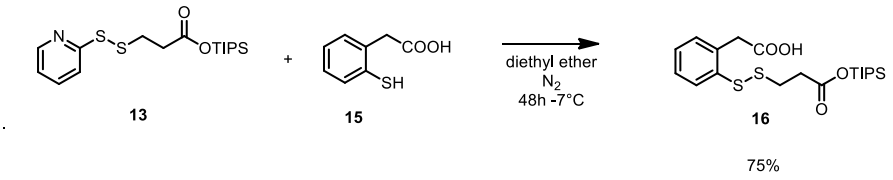

Scheme 14. *Synthetic path to achieve compound* ***16****.*

Through chromatography column byproducts were removed and the final compound was characterized by ^{1}H-NMR. **(Figure 33)**

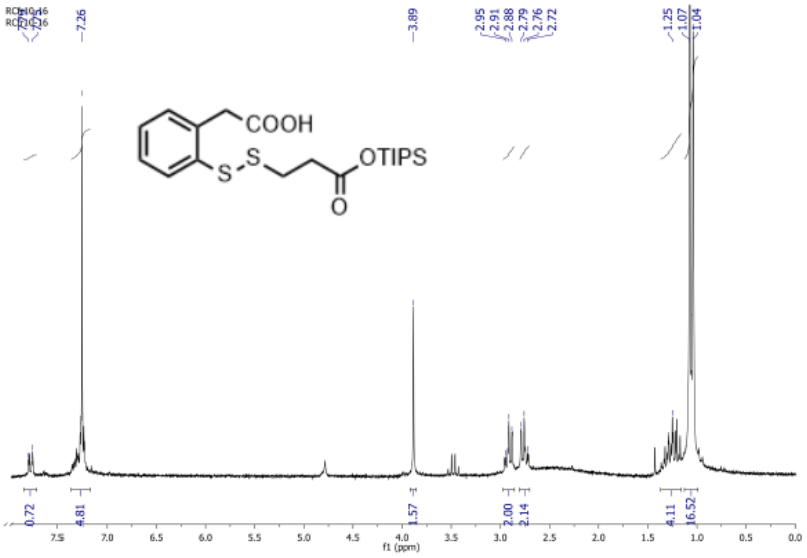

Figure 33*. ^{1}H-NMR of compound* ***16****.*

. Typical TIPS signals were localized between 1.0 ppm and 1.5 ppm;

. Two triplets centered at 2.82 ppm and 2.98 ppm (4 protons), confirmed the presence of the two aliphatic -CH_2- adjacent to the disulfide bridge;

. A singlet at 3.95 ppm (2 protons), indicates the presence of the 2 aliphatic hydrogens between -Ph and -COOH;

. The multiplet ranging from 7.20 ppm to 7.30 ppm and the doublet centered at 7.77 ppm, are correlated to the protons bound to the benzene ring

2.3.6 COUPLING OF BODIPY WITH LINKER

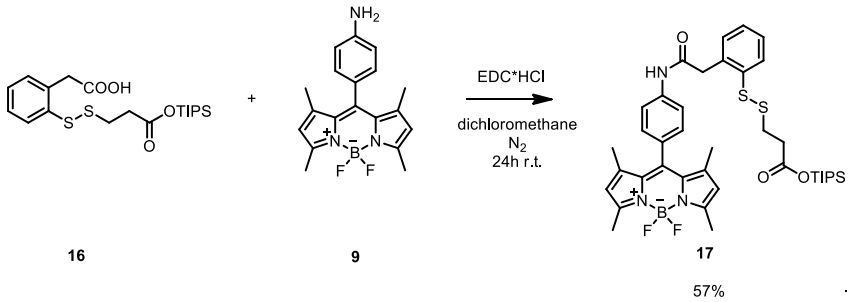

***Scheme 15**. Coupling of BODIPY Core with Linker*

This reaction allowed to bind the newly synthesized linker (compound 14) to the reduced BODIPY 3,5-dimethyl substituted (compound 8), by forming an amide. EDC was used as a coupling agent, to activate the carboxyl group. The reaction was carried out under nitrogen atmosphere for 24 h.

^{1}H-NMR showed signals confirming the presence of the BODIPY amide:

. Typical TIPS signals between 0.9 ppm and 1.30 ppm;

. Centered at 1.45 ppm and 2.47 ppm there are two singlets, due to the methyl groups of the BODIPY;

. At 2.74 ppm and 2.93 ppm two triplets, connected to 2 protons each, diagnostic of aliphatic hydrogens between S-S and -CO_2TIPS;

. A singlet (2 protons) at 3.99 ppm associated with the two protons between the amide group and the benzene ring;

. A singlet centered at 6.05 ppm which suggested the presence of the two hydrogens of pyrrole;

. The multiplet ranging from 7.20 ppm to 7.50 ppm and the doublet centered at 7.80 ppm, due to 4 protons connected to the benzene ring of the BODIPY in meso position and to the 4 protons of the benzene ring of the linker (the number of protons were 8);

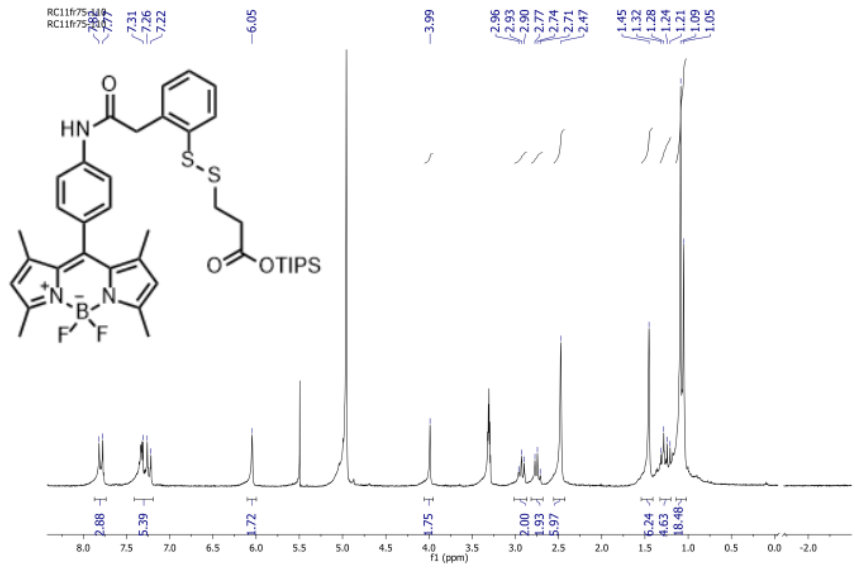

Figure 34**. [1]H-NMR Spectrum of compound **17

DEPROTECTION OF BODIPY AMIDE

The consecutive step was the deprotection of carboxyl group of the BODIPY amide to re-establish its reactivity. TIPS was removed by using TEA 3HF, at room temperature.

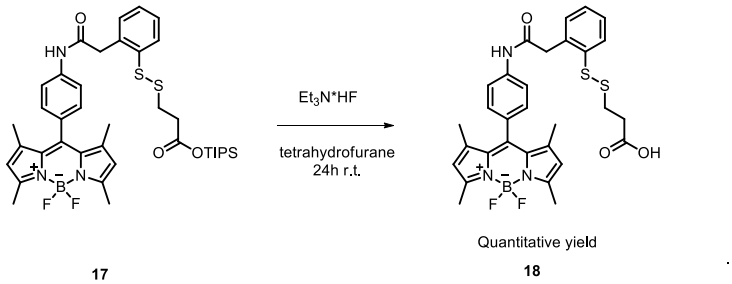

Scheme 16**. TIPS deprotection to afford compound **18

[1]H-NMR spectrum was recorded. The occurred deprotection process was confirmed thanks to the lack of signals connected to Triisopropyl groups as showed in **Figure 35**.

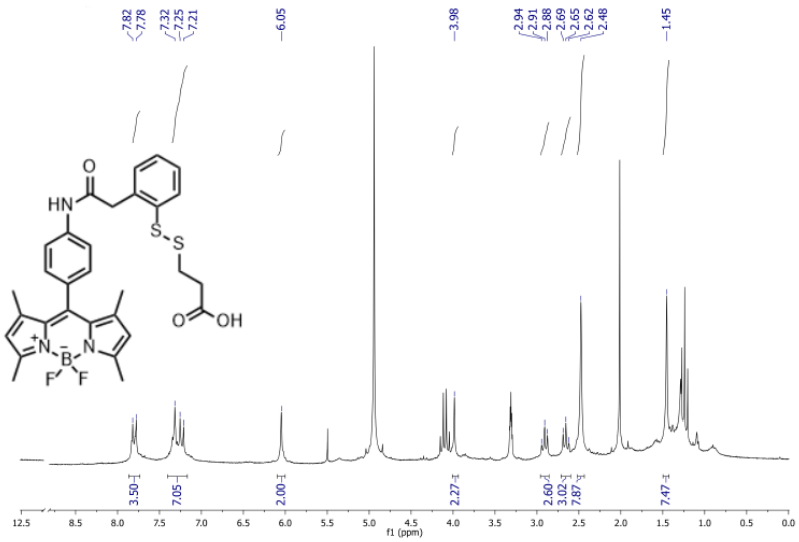

Figure 35. *^{1}H-NMR Spectrum of compound* ***18***

COUPLING BODIPY-LINKER

To attach the final system on CNTs the introduction of an alkyne group was required to exploit CuAAC chemistry. The introduction of propargylamine occurred by adding EDC HCl and HOBt to increase the reaction yield. After a purification through chromatography column a ^{1}H-NMR was showed in **Figure 36**.

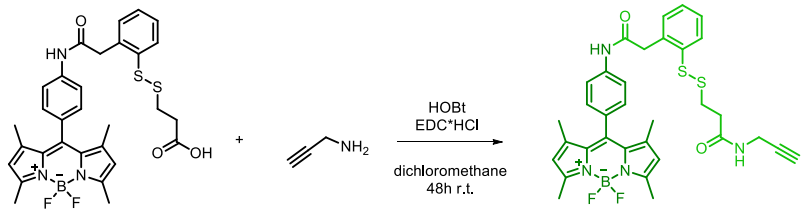

Scheme 17. *Coupling BODIPY with propargylamine*

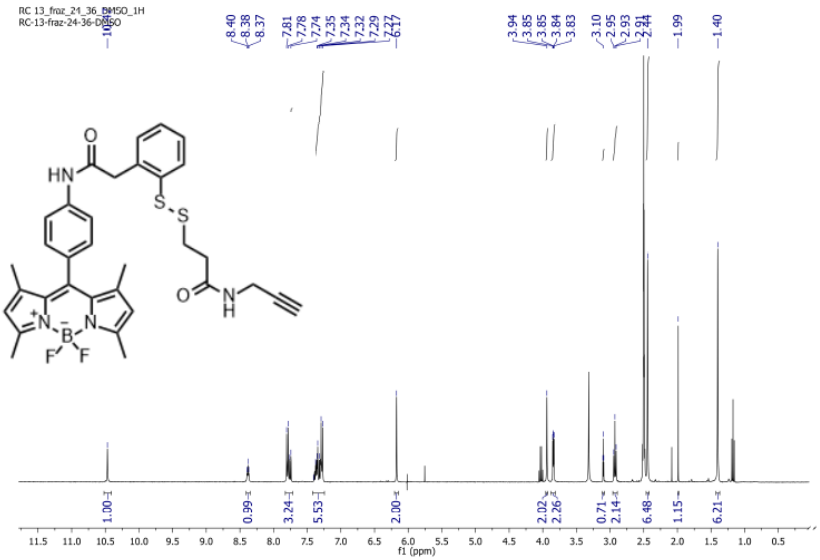

Figure 36**. [1]H-NMR Spectrum of compound **19

In this synthetic step the fluorescent probes 9 and 17 were bund on CNTs surface. The nanotubes are already functionalized with azide group and PEG chain. The azide groups on CNTs and the alkyne groups on the fluorescent probes were exploited to conduct a Cu (I) catalyzed cycloaddition reaction. CuIP $(OEt)_3$ was used as catalyst at 60°C for 48 h. (**Scheme 18**)

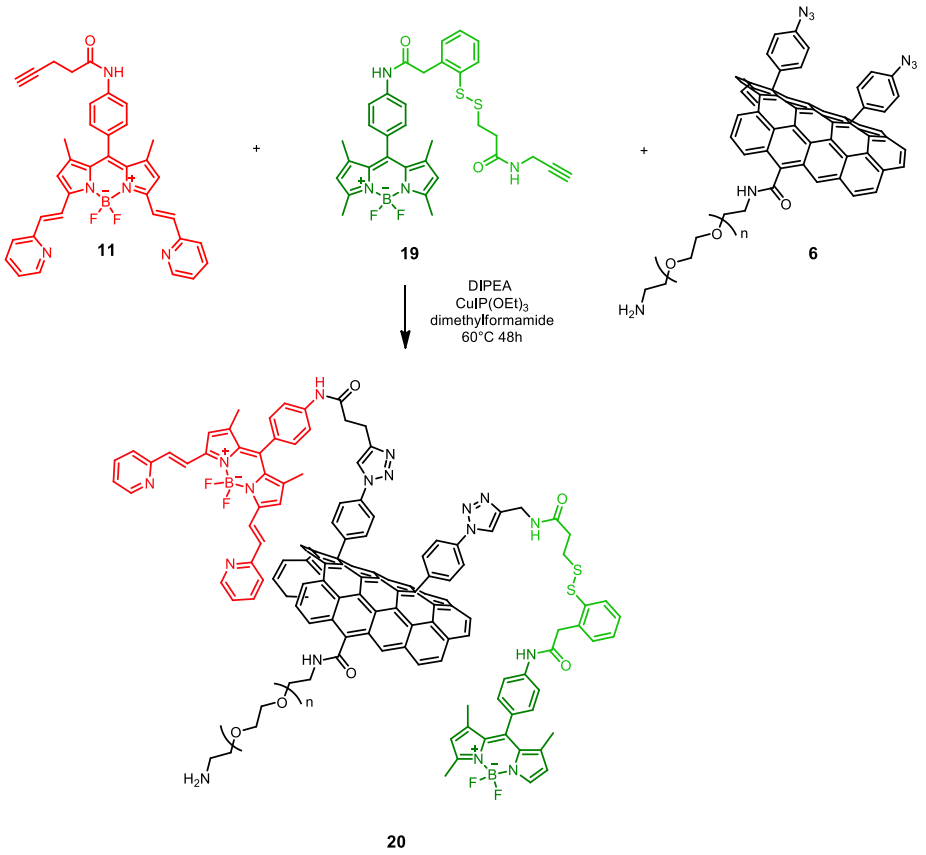

***Scheme 18**. Functionalization of CNTs with fluorescent probes.*

At the end of reaction functionalized CNT were filtered on nylon and washed several times with water and methanol. The collected workup waters were analyzed by UV spectroscopy to evaluate the complete removal of two dyes not bund on functionalized carbon material.

In **Figure 37** a UV Spectrum of **20** was reported. The absorption profile of synthesized compound suggested the occurred reaction. showing the two characteristic absorbance signals connected with the fluorescent molecules. In orange with maximum of absorption at 510 nm (BODIPY-Linker, **19**) and in blue with a maximum absorption at 623 nm (BODIPY **11**).

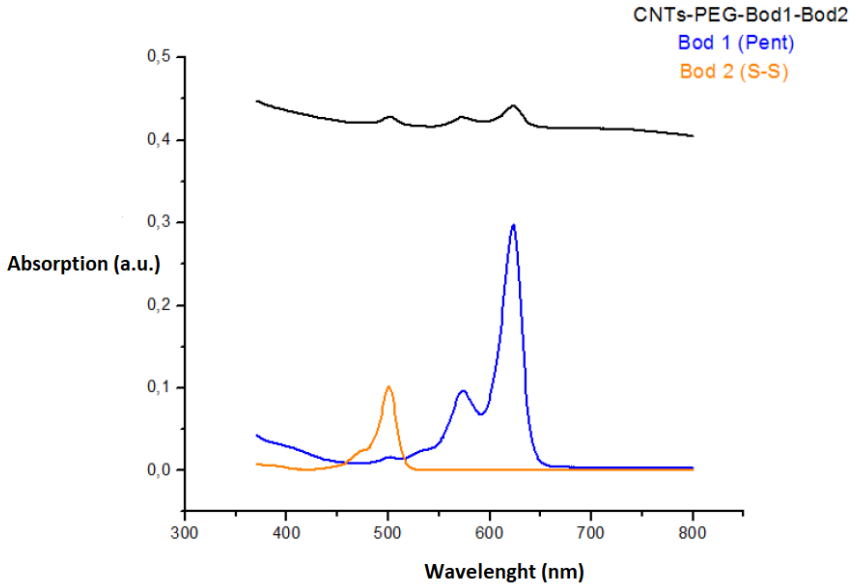

***Figure 37**. UV adsorption of compounds **20** (black), **11** (blue) and **19** (orange).*

Confocal microscopy images analysis performed on functionalized carbon nanotubes were acquired by using a laser with two wavelengths (**Figure 38**)

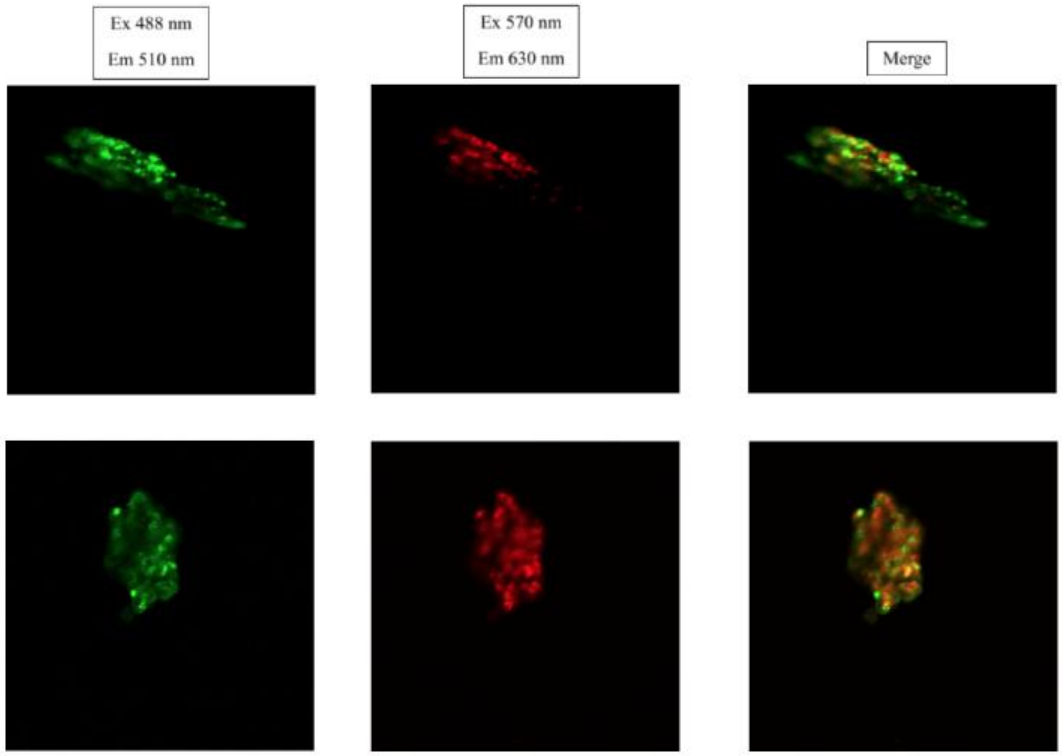

***Figure 38**. Images of functionalized CNTs provided by confocal microscope.*

First two columns of **Figure 38** showed the single fluorescence of two probes, confirming the occurred functionalization. The last column revealed the merge of the images of two dyes.

2.3.7 IN VITRO BIOLOGICAL ASSAYS

The desired model for DDS was objective of study about its cancer cells internalization. This study was carried out in cooperation with Professor Paolo Paoli. at Dipartimento di Scienze Biomediche Sperimentali e Cliniche dell'Università di Firenze.

Confocal microscopy images were acquired of both isolated models of DDS and models of DDS incubated for different period of time in melanoma cancer cell cultures (A375). The images showed the presence of both fluorescent probes by using two lasers with different wavelengths (488 nm and 570 nm). The two different fluorescence were connected to the two probes.

Different images were collected after 0 minutes, 5 minutes, 30 minutes, 6 hours and 24 hours of incubation. (**Figure 39, 40, 41, 42, 43**).

After 6 hours (**Figure 42**) the collected images showed small areas with a lack of a perfect overlapping of two fluorescence, suggesting a possible release of a BODIPY due to the break of disulfide bridge. This hypothesis was confirmed thanks to the images recorded after 24 hours: extended are

as with only green fluorescence were showed in **Figure 43**. The compound appears suitable for our proposal.

0' A375 Melanoma cells

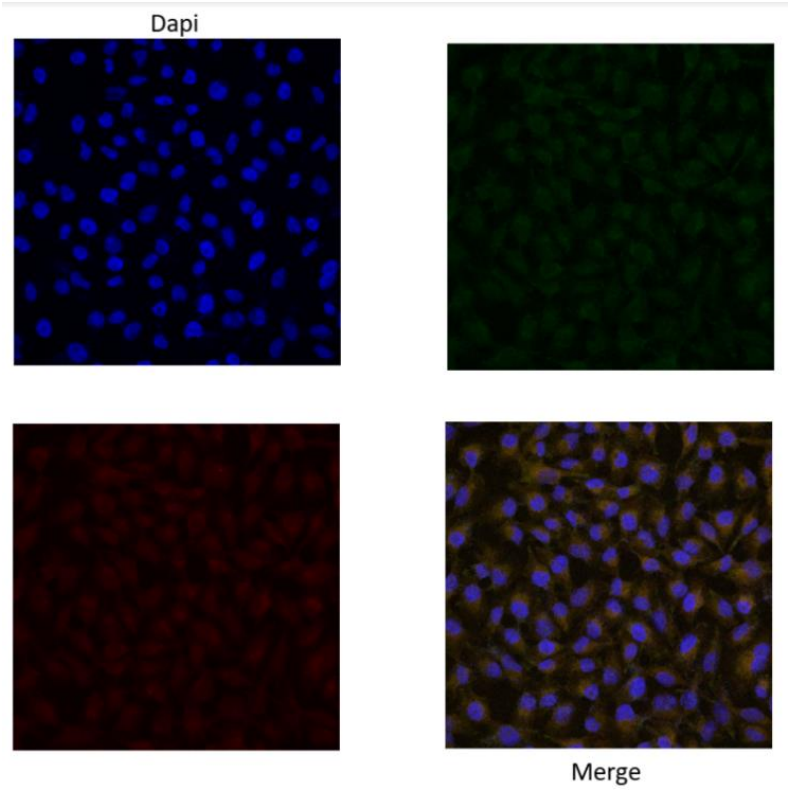

***Figure 39**. A375 cells incubated with product 18 at 0'. In A only the cell nucleus (DAPI dye). In B fluorescence of the probe S-S-linker (product 17). In C fluorescence of product 9. In D the merge of the two fluorescence.*

5’ A375 Melanoma cells

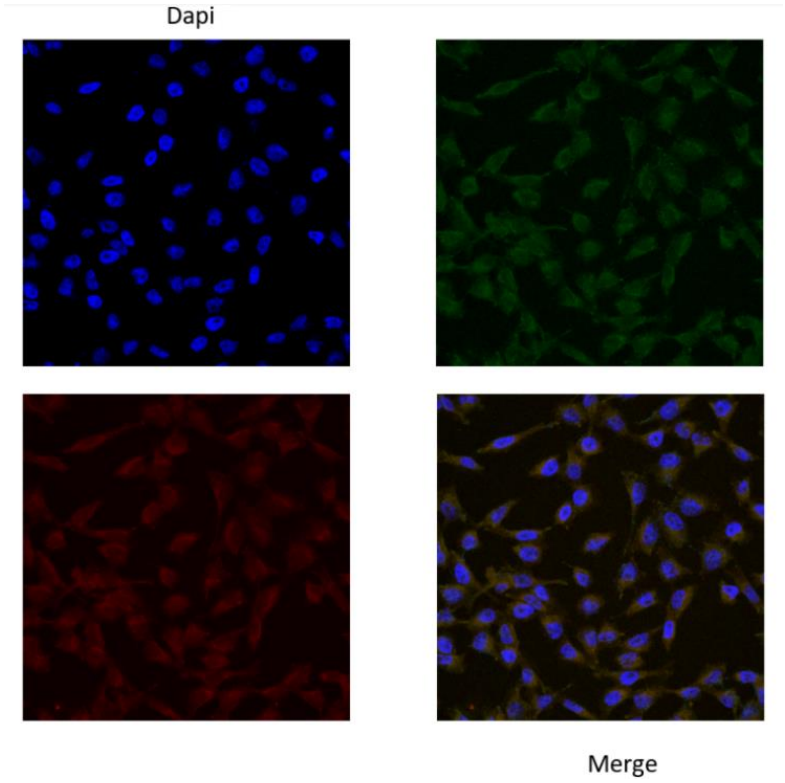

Figure 40. *A375 cells incubated with product 18 at 5’. In A only the cell nucleus (DAPI dye). In B fluorescence of the probe S-S-linker (product 17). In C fluorescence of product 9. In D the merge of the two fluorescence.*

30’ A375 Melanoma cells

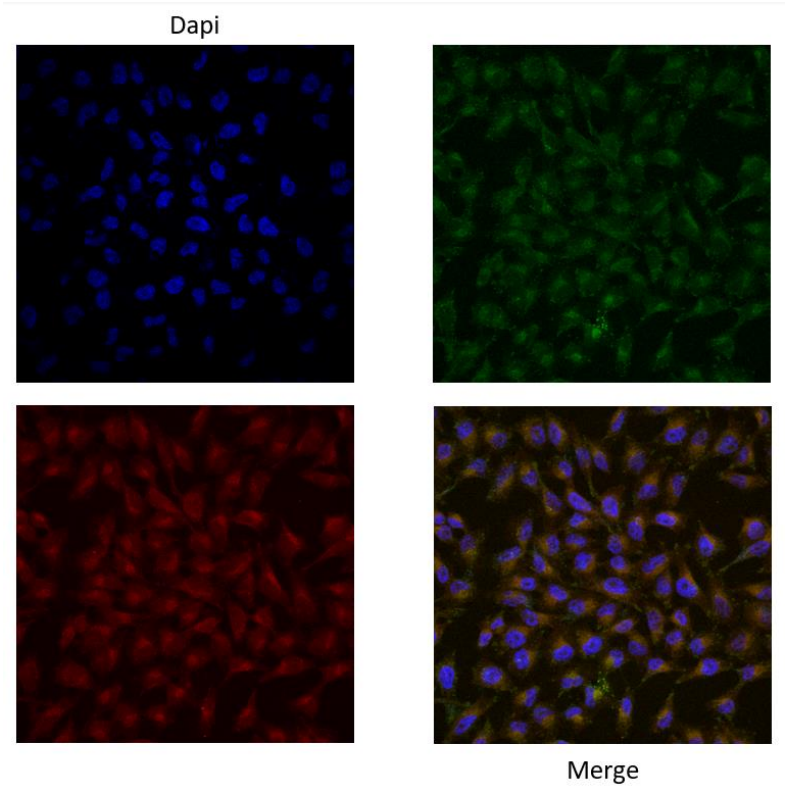

Figure 41*: A375 cells incubated with product 18 at 30’. In A only the cell nucleus (DAPI dye). In B fluorescence of the probe S-S-linker (product 17). In C fluorescence of product 9. In D the merge of the two fluorescence.*

6h A375 Melanoma cells

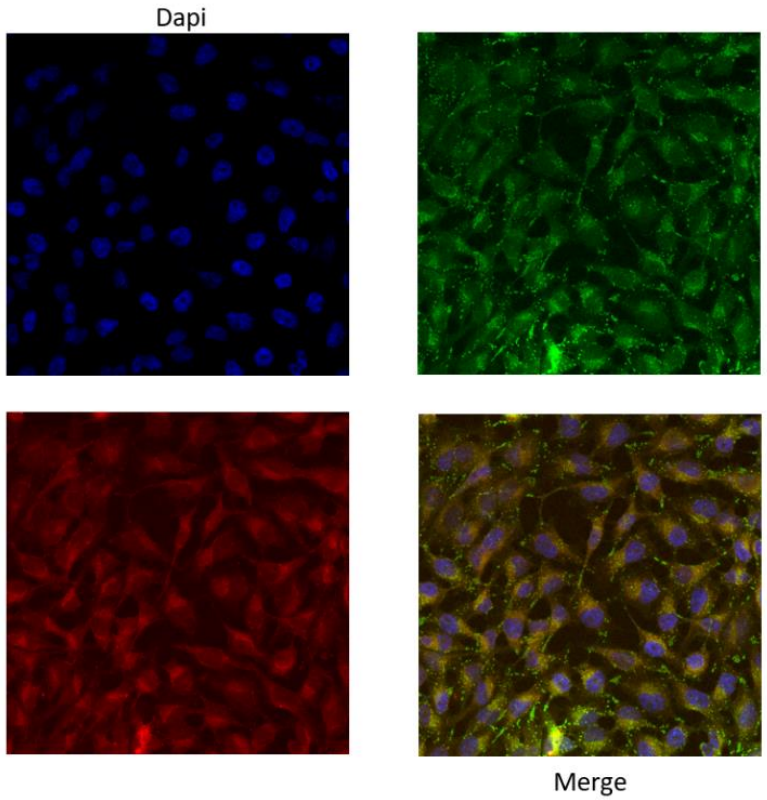

***Figure 42**: A375 cells incubated with product 18 at 6h. In A only the cell nucleus (DAPI dye). In B fluorescence of the probe S-S-linker (product 17). In C fluorescence of product 9. In D the merge of the two fluorescence.*

24h A375 Melanoma cells

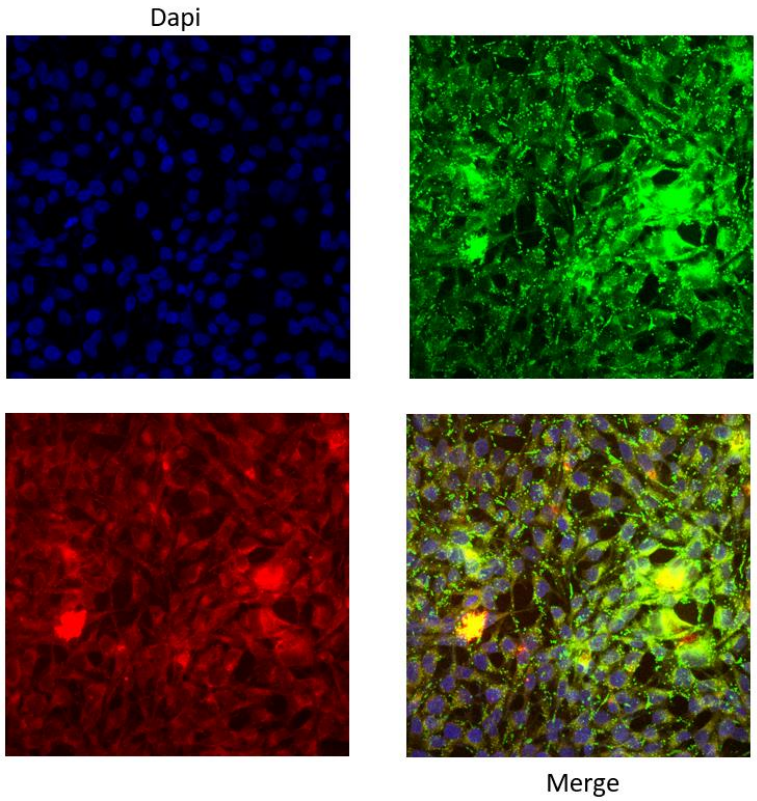

***Figure 43**: A375 cells incubated with product 18 at 24h. In A only the cell nucleus (DAPI dye). In B fluorescence of the probe S-S-linker (product 17). In C fluorescence of product 9. In D the merge of the two fluorescence.*

2.4 CONCLUSION AND PERSPECTIVES OF CNTs-MODEL OF DDS

This project was focused on the viability study of a drug delivery system. The drug was bund to multi walled carbon nanotubes through covalent bonds divisible in intracellular environment. The prepared system showed functionalized CNTs with two fluorescent probes of BODIPY family; the first BODIPY (maximum of absorption at 623 nm) directly to nanostructured material, the second BODIPY dye (maximum of absorption at 510 nm) through a disulfide bridge. This bond resulted cleavable in the environment of cancer cells, due to the higher concentration of endogenous thiols.

The ability of nanotubes to cross cell membranes and the selective release mechanism are interesting properties for a drug vectorization system (especially in the chemotherapy field, the lack of selectivity is one of the main problems). Since this project was a viability study, instead of a drug, a fluorescent probe was anchored to the CNTs.

One of the two dyes was then modified to form an amide bond with the linker disulfide molecule, previously synthesized. The other BODIPY conjugation was extended by Knoevenagel condensation, to modify also the emission frequency.

The functionalization of CNTs with these described molecules was carried out through a click-chemistry reaction catalyzed by a complex (CuIP (OEt) $_3$), exploiting the azide groups on nanotubes.

In collaboration with Professor Paolo Paoli, microscopy images of cell cultures (A375) incubated for different periods of time were acquired by confocal microscope. These analyses revealed a double

fluorescence of the tumor cells after the incubation and therefore the internalization of the model of DDS. The collected images suggested the release of the BODIPY dye. Future studies could quantify the release of compound bonded to carbon nanotubes via disulfide bridge.

2.5 RESULTS AND DISCUSSION-fGO

As previously showed in chapter **2.2**, a similar approach was exploited to achieve a model to build a DDS based on GO instead of CNTs. The synthetic approach was the same, first the decoration with a PEG chain which will exploit to bind a selector, later the introduction of a substrate with an azido group to anchor the fluorophores.

Thanks to Dr. Alberto Bianchi (Institut de biologie moleclulaire et céllulaire, Strasbourg) we have decided to extend the study by substituting carbon nanotubes with an other nanostructured carbon material such as graphene oxide since the higher biocompatibility and low toxicity compared to carbon nanotubes.

The first step allowed the introduction of PEG chain by exploiting the epoxide ring opening at room temperature in water. **(Scheme 19)**.

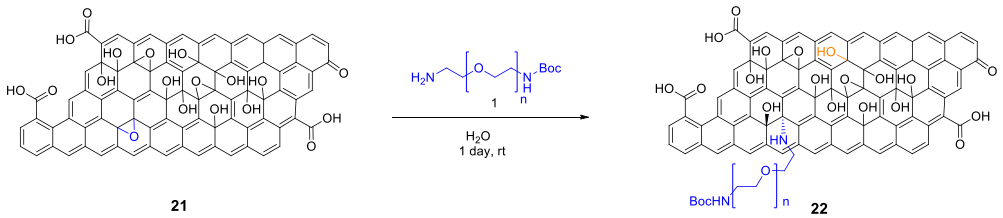

***Scheme 19**. Functionalization of GO via Epoxide Rings Opening.*

Few milligrams of compound **22** were used to remove BOC protecting group through an acidic reaction **Scheme 20**

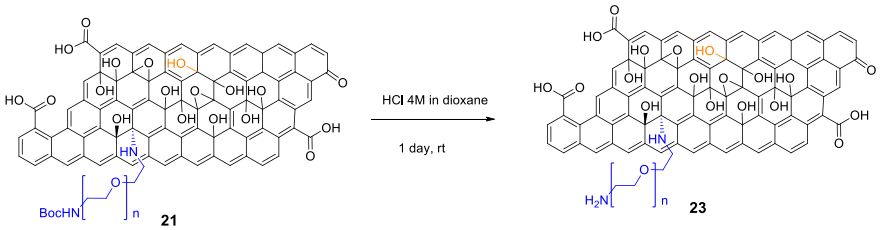

***Scheme 20**: BOC Deprotection of amine.*

To functionalize graphene oxide, amino-terminated chains were chosen because they can be easily functionalized for other purpose, such as bonds with selectors. Moreover, the presence of a primary amine makes it possible to evaluate the amount of molecules introduced on GO using a colorimetric

test, namely the Kaiser test (material methods). Kaiser test result revealed an amount of amine equal to 34 µg/g of material.

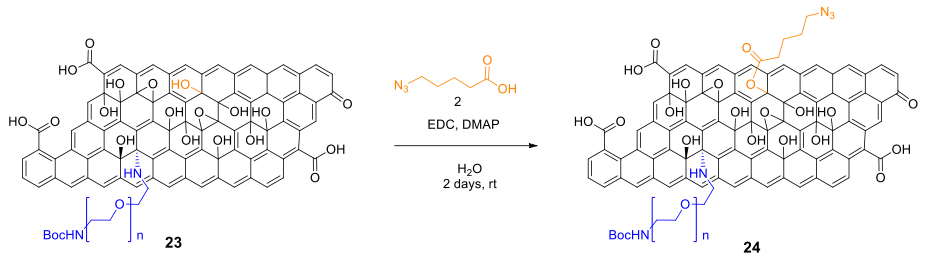

***Scheme 21**: Functionalization of GO via esterification*

Our strategy involved the addition of 5-azidopentanoic acid to introduce an azido group. This fragment allowed to bind the two dyes previously synthesized. (**Scheme 21**)

A control reaction was done, to verify if 5-azidopentanoic acid was adsorbed onto GO surface. This reaction was performed in the same conditions of **Scheme 21**, without adding the coupling reagents.

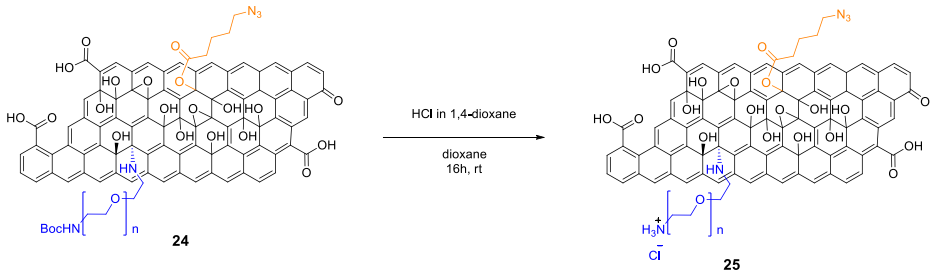

***Scheme 22**. Deprotection of BOC.*

Elemental analysis on GO of control reaction didn't establish any absorption of 5-azidopentanoic acid onto GO; consequently the organic molecule was covalent bound onto carbon material.

From these results, we can conclude the occurred functionalization of GO in two steps.

Once obtained the decorated system (**25**), a strategy of multifunctionalization was developed. Mild conditions were used to avoid the reduction of GO. In the presence of copper sulfate and sodium ascorbate at room temperature the two fluorophores were added to compound **25** in water. **(Scheme 23)**

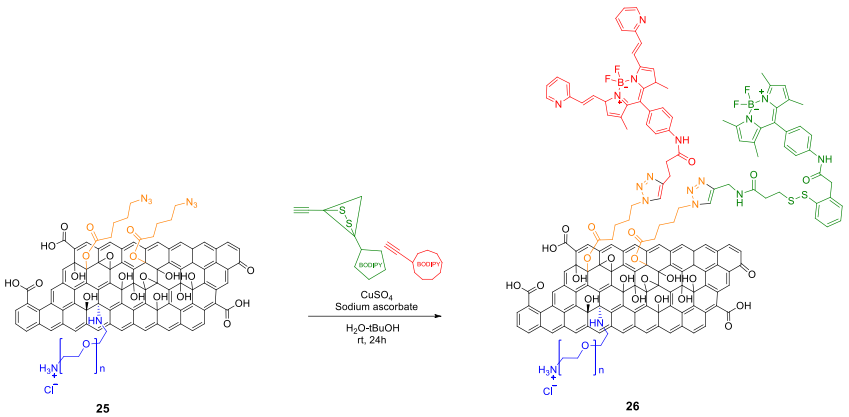

25 26

***Scheme 23**. CuAAC reaction to introduce fluorescent dyes.*

To evaluate the loading degree of two fluorophores, ICP (S, B) analyses were done to establish an amount of compound **11** equal to 0.42 mmol/g and **19** equal to 0.37 mmol/g.

Comparing the loading degree collected for the first described model, based on CNTs, to the second one, built with GO, **26** three times higher values for the second model (GO) were collected as compared to the model achieved by using CNTs **20**.

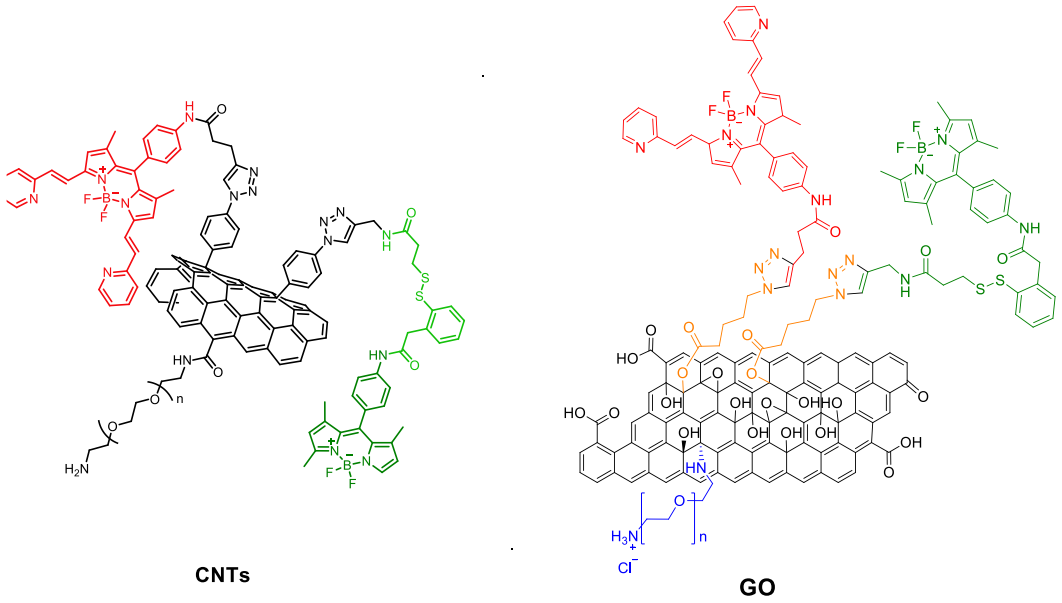

***Figure 44**. Loading degree of two models of DDS.*

ICP analyses S, B:

BODIPY 11: 0.15 mmol/g

BODIPY-Linker 19: 0.12 mmol/g

2.6 CONCLUSION AND PERSPECTIVES OF GO-MODEL OF DDS

A system made of functionalized GO was achieved. The previously synthesized BODIPY **11** and BODIPY-Linker **19** were covalent attached onto GO. A similar approach was carried out to bind PEG chain onto nanostructured carbon material.

Our hypothesis plans to exploit the properties of disulfide bridge to release the dye with a maximum adsorption at 510 nm.

In conclusion all the studyes mentioned used CNTs and GO samples with different characteristics, thus drawing a real conclusion appears to be a difficult task. A good functionalization of carbon materials has been possible. Analogous studyes with confocal microscope and in vitro studyes for the compound **26** will be done by reproducing the same experiments previously adopted for compound **20**.

2.7 MATERIAL AND METHODS

OXIDATION OF MULTIWALLED CARBON NANOTUBES **2**

Pristine nanotubes (500 mg) were dispersed in a 3:1 mixture of 95% sulfuric acid and 65% nitric acid (30 mL) and heated at 100°C under stirring for 30 minutes. The mixture was cooled at room temperature and quenched with 130 mL of MilliQ water, the obtained solution was centrifuged at 1500 rcf (relative centrifugal force) for 30 minutes, the supernatant was removed, and the precipitate dispersed with milliQ water (130 mL) and centrifuged again. The CNT slurry recovered from centrifugation (still acidic)

was filtered on a 0.2 µm polycarbonate membrane and washed with water until neutral pH of the filtered solution. The process provided 200 mg of oxidized material, elemental analysis: C 79.1%, N 0.15%, H 0.62% and O 20.3%. FT-IR showed the C=O absorption peak at 1700 cm-1.

SEPARATION OF OXIDE CARBON NANOTUBES BY LENGHT

Bulk oxidized CNT (140 mg) were dispersed using ultrasound bath in milliQ water (280 mL) to obtain a 0.5 mg/mL solution. The solution was centrifuged at 10k rcf for 1h and supernatant and precipitate were collected. The supernatant was centrifuged again at 15k rcf for 1h providing a new precipitate and a new supernatant. The procedure was repeated using the supernatant other 3 times using different G force (20, 25 and 30 K rcf) as reported in the figure 6. The supernatant of the 30 k rcf centrifuge was dried and 65 mg of material 2 were obtained, the length was measured with TEM (**Figure 45**) giving an average value of 130 nm.

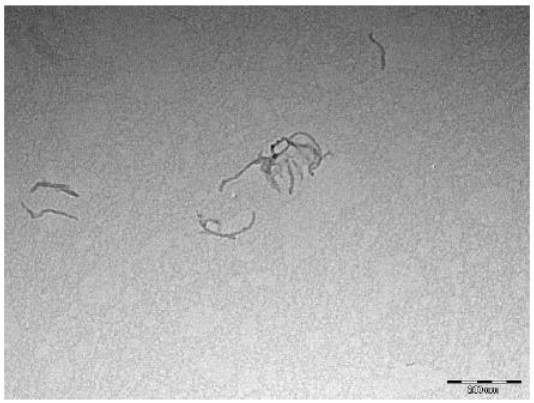

Figure 45*. TEM image of short oxidized carbon nanotubes*

SYNTHESIS OF 4-azidoaniline- **3**

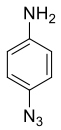

4-azidoaniline was synthesized from 4-bromoaniline in quantitative yield following a procedure reported in the literature.[63]

SYNTHESIS OF N_3-CNTs (Tour reaction)- **4**

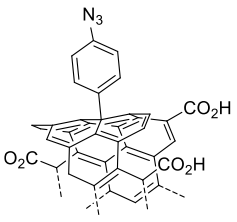

CNTs (**2**) (20 mg) was dispersed in dry DMF (2 mL) and sonicated for 15 minutes, then 4-azidoaniline (61.5 mg, 0.46 mmol) and isoamylnitrite (38.6 mg, 0.33 mmol) were added and the mixture stirred at 60°C under nitrogen for 24 h. CNT **5** was recovered by filtration on a 0.2 µm nylon membrane, washing with DMF until a colorless solution obtained and then with methanol to remove the unreacted materials. FT-IR peak at 2100 cm-1 confirmed the azide decoration (**Figure 46**).

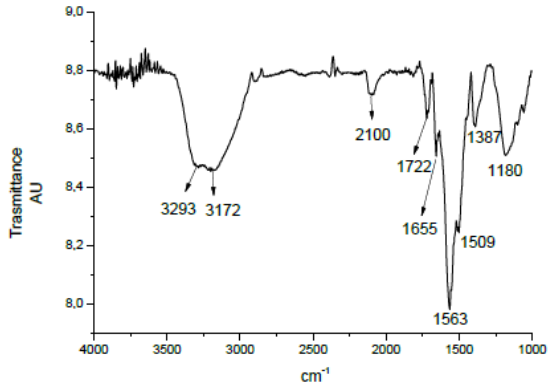

***Figure 46**. IR of compound 4*

SYNTHESIS OF N_3-CNTs-PEG **6**

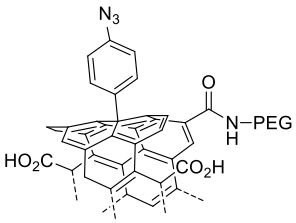

N_3CNTs (**4**) (15 mg) were dispersed in MES (50 mL) and sonicated for 15 minutes, then EDC-HCl (90 mg, 0.47 mmol) and N-Hydroxysuccinimide (375 mg, 3.26 mmol) were added and the mixture stirred at room temperature for 90'. Functionalized CNTs were recovered by filtration on a 0.2 µm nylon membrane, washing with water. The recovered material (12.7 mg) was dispersed in $_{dry}$DMF (2.5 mL). 100 mg of PEG 2K (**5**)were added and the mixture stirred at 45°C for 24h. CNTs (**6**) were filtered on a 0.2 µm nylon membrane washing first with DMF (10 mL) than water (30 mL).

SYNTHESIS OF BODIPY Core-**7**

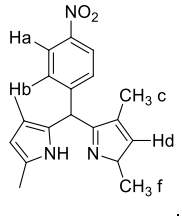

P-nitrobenzaldehyde (790 mg, 5 mmol, 1 eq.), 2,4-dimethylpyrrole (952 mg, 10 mmol, 2 eq.) were mechanical reacted with mortar and pestle; about 20 drops of TFA were added. DCM and p-chloroanyl (1844 mg, 7.5 mmol, 1.5 eq.) were added and homogenize with the pestle; the color of the substance varied from orange to dark purple. The product obtained was diluted with 250 mL and transferred in a separating funnel. The solution was washed with 200 mL of a saturated solution of Na_2CO_3 and then with 200 mL of BRINE. Each aqueous phase is then washed again with 100 mL of DCM to recover as much product as possible. The combined organic layers were anhydrified with Na_2SO_4, filtered on cotton and dried. 2.810 g of crude product were obtained.

^{1}H-NMR (CDCl3, 200 MHz) _(ppm): 8.31 (AA'BB', 2H, Ha); 7.51 (AA'BB', 2H, Hb); 5.89 (s, 2H, Hd); 2.33 (s, 6H, He); 1.25 (s, 6H, Hc)

SYNTHESIS OF BODIPY Core-**8**

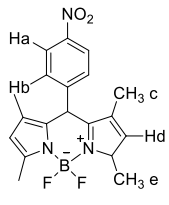

Product **7** (1606 mg, 5 mmol, 1 eq.) was put into a two-necked flask, under nitrogen atmosphere, diluted in 50 mL of anhydrous DCM and subsequently added first, fresh distilled TEA (6 mL, 42.9 mmol, 8.6 eq.), than BF_3 (previously distilled under a flow of N_2) at 0°C. After 12 h at room temperature the organic phase were diluted with 55 mL of DCM and washed with 3x50 mL of Na_2CO_3 and 3x50 mL of BRINE.Thn the organic layers were dried on Na_2SO_4 The crude product was purified through a flash chromatography column (EtP: DCM 1:1). 943 mg of product, or a yield of 37%.

^{1}H-NMR (CDCl δ 200 MHz) (ppm): 8.37 (AA'BB'2H, Ha); 7.52 (AA'BB'2H, Hb); 6.01 (s, 2H, Hd); 2.55 (s, 6H, He); 1.35 (s, 6H, Hc)

2.5 g (0.015 mmol, 1eq) of 4-Nitrobenzoic acid were dissolved in 3.3 mL (0.045 mmol, 3 eq) of thionyl chloride at 80°C for 1h, under nitrogen atmosphere. 75 mL of dichloromethane were added into the flask. Then 15 mL of fresh distilled triethyl amine and 15 mL of BF_3 Et_2O were added. At the end of reaction several extractions with waters were repeated after the dilution with dichloromethane (50

mL). The crude product was purified through a flash chromatography column (PEt: DCM 1:1). 1.73 g of product, or a yield of 68%.

SYNTHESIS OF BODIPY-amine-**9**

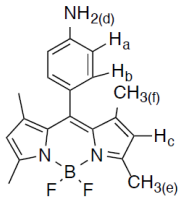

In a flask equipped with a magnetic stirrer, under N_2 atmosphere, compound **7** (500 mg, 1.35 mmol, 1eq) was placed with MeOH (21 mL). A solution of HCl in MeOH (0.4 mL of HCl 37% in 10 mL of MeOH) was added. The resulting mixture was heated to reflux, 8 mL of water were added and the reaction was monitored *via* TLC (R_f: 0.55, 4:1 DCM: Pet. E.). After 2.5 h the product was synthesized. After cooling to room temperature, the reaction mixture was diluted with dichloromethane and filtered to remove Fe. The mixture was washed with a solution of Na_2CO_3, the organic layers were combined, dried over anhydrous $MgSO_4$ and evaporated. Yield: 250 mg, 55%, solid red compound.

^{1}H-NMR ($CDCl_3$, 200Hz) δ (ppm): 7.03 (AA' of a system AA'-BB', 2H, J=8.0Hz, Ha); 6.78 (BB' of a system AA'-BB', 2H, J=8.0Hz, Hb); 5.97 (s, 2H, Hc); 3.88 (bs, 2H, Hd); 2.53 (s, 6H, He); 1.48 (s, 6H, Hf).

SYNTHESIS OF BODIPY-alkyne-**9**

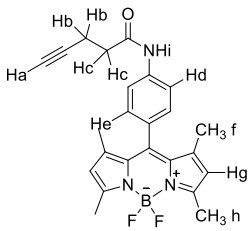

100 mg of product **8** (0.29 mmol, 1eq) were put in a flask. 4-Pentynoic acid (29 mg, 0.29 mmol, 1eq), Dicyclohexylcarbodiimide (87 mg, 0.44 mmol, 1.5 eq), 4-(Dimethylamino)pyridine (3.7 mg, 0.03 mmol, 0.1 eq) were added to the flask with 5.5 mL of dry dichloromethane. After 24h at room temperature the reaction was completed. The crude product was washed with 30 mL of 0.1M HCl solution (x3), 30 mL of a saturated solution of Na_2CO_3 (x3), 30 mL of a BRINE solution (x2). The crude product was purified by a flash chromatography column (DCM:Pet.Et. 4:1). 108 mg were collected with a yield of 91%.

^{1}H-NMR ($CDCl_3$, 200 MHz) δ (ppm): 7.96 (bs, 1H, Hi); 7.70 (dd, 2H, He); 7.20 (dd, 2H, Hf); 5.97 (s, 2H, Hg); 2.63 (s, 4H, Hb+Hc); 2.54 (s, 3Hf) 2.07 (s, 1H, Hi); 1.41 (s, 6H, Hc)

SYNTHESIS OF -BODIPY disubistuted-**11**

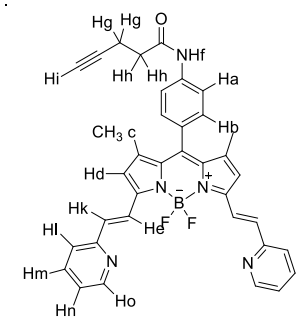

Compound **10** (80 mg, 0.19 mmol, 1 eq.) was put in a flask under nitrogen atmosphere in anhydrous CH_3CN and brought to reflux temperature.2-pyridincarboxaldehyde (102 mg, 0.95 mmol, 5 eq.), pyrrolidine (82 mg, 1.14 mmol, 6 eq.) and acetic acid (56 µL, 0.95 mmol, 6 eq). After 1 h of reaction the crude product was diluted with 50 mL of DCM. The organic phase was washed with 2x30 mL of Na_2CO_3, then 2x30 mL with MilliQ water and finally 2x40 mL with BRINE and dried on Na_2SO_4. The obtained compound was purified by flash chromatography with eluent PetEt-EtOAc (2: 1). 79.4 mg of BODIPY-disubstituted were recovered with a yield of 70%.

^{1}H-NMR ($CDCl_3$, 200 MHz) δ (ppm): 8.65 (d, 2H, Ho); 8.05 (d, 2H, He); 7.75-7.65 (m, 7H, Hm + Ha + Hb + Hf); 7.36 (d, 2H, Hk); 7.27 (d, 2H, H1); 7.20 (t, 2H, Hn); 6.69 (s, 2H, Hd); 2.66 (s, 4H, Hg + Hh); 2.11 (s, 1H, Hi); 1.50 (s, 6H, Hc).

SYNTHESIS OF (tert-butyl)-2,2,4,4-tetramethylsiletan-1-yl 3-(pyridin-2yldisulfanyl)propanoate-**13**

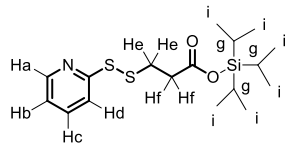

3-mercaptopropionic acid was added in a flask (130 µL, 1.49 mmol, 1 eq.) And it is solubilized in 1.4 mL of MeOH. Add the 2-2'-dipyridyldisulfide (503 mg, 2.29 mmol, 1.5 eq.) under magnetic stirring. After a reaction time of 4 h at room Temperature a ^{1}H-NMR spectrum of the crude is acquired to ensure the absence of 2-2'-dipyridyl disulfide.

To protect the carboxylic group TIPSCl was used.

The obtained crude (325.1 mg, 1.52 mmol, 1 eq.) was solubilized in a flask with 8.12 mL of dry DCM under nitrogen atmosphere, $_{dry}$ TEA (420.9 µL, 3.02 mmol, 2 eq.) was slowly added to the flask. At 0°C TIPSCl (387.7 µL, 1.81 mmol, 1.2 eq) was added drop by drop in 10' of time. 6mL of aqueous solution of NH_4Cl was used to wash the organic layers. The crude is purified by flash chromatography. Eluent Pet.Et-EtOAc (20: 1). 362.3 mg of product 11 were recovered with a yield of 65%.

^{1}H-NMR (CDCl3, 200 MHz) δ (ppm): 8.46 (d, 1H, Ha); 7.75-7.61 (m, 2H, Hb+Hd); 7.08 (t, 1H, Hc); 3.03 (t, 2H, He); 1.40-1.13 (m, 3H, Hg); 1.13-0.90 (d, 18H, Hi)

SYNTHESIS OF (2-mercaptophenyl)acetic acid-**15**

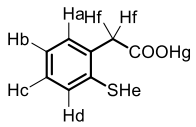

Benzo-b-thiophen boronic acid was added to a flask (417 mg, 2.34 mmol, 1 eq) and solubilized in 5 mL of EtOH; therefore 930 µL of H_2O_2 at 30% were added under magnetic stirring. After 5 h. the reaction mixture was diluted with 12 mL of H_2O milliQ, 12.5 mL of dichloromethane were used to perform three extractions. The combined organic layers were anhydrified on Na_2SO_4.

^{1}H-NMR spectrum is acquired which reveals the formation of thiolactone (yield = 90%).

The synthesized thiolactone (317 mg, 2.11 mmol, 1 eq.) was solubilized in 12.6 mL of H_2O and in 12.6 mL of THF into a flask. LiOH (303.2 mg, 12.66 mmol, 6 eq.) was put into a flask equipped with a magnetic stirring for 16 h at 60°C. 345 mg of crude product were collected

^{1}H-NMR ($CDCl_3$, 200 MHz) δ (ppm): 10.65 (bs, 1H, Hg); 7.50-7.20 (m, 4H, Ha+Hb+ Hc+Hd); 3.88 (s, 2H, Hf); 3.57 (s, 1H, He).

SYNTHESIS OF (2-((3-oxo-3-((tri-tert-butylsilyl)oxy)propyl)disulfanyl)phenyl)acetic acid **16**

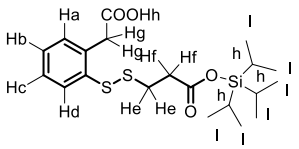

Product **13** (362.3 mg, 0.97 mmol, 1 eq.) was solubilized under nitrogen atmosphere with **15** (244.7 mg, 1.455 mmol, 1.5 eq.) in Et_2O, inside a tube equipped with a magnetic stirrer. The reaction was

carried out at -7°C for 48 h, thanks to the use of a thermostat. The purification process occurred through a flash chromatography by using Et_2O as eluent, obtaining 103 mg of product 14 (yield = 25%).

^{1}H-NMR ($CDCl_3$, 200 MHz) δ (ppm): 7.77 (d, 1H, Hd); 7.30-7.20 (m, 3H, Ha+Hb+Hc); 3.89 (s, 2H, Hg); 2.91 (t, 2H, He); 2.76 (t, 2H, Hf); 1.35-0.9 (m, 21H, Hl + Hh)

COUPLING OF linker **16** with BODIPY **9** to obtain **17**

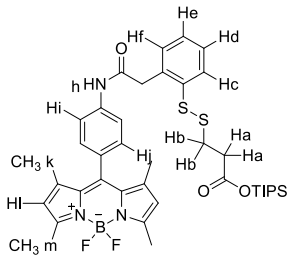

Products **18**(103 mg, 0.240 mmol, 1 eq.) and compound **9** (90 mg, 0.264 mmol, 1.1 eq.) were dissolved in dry DCM, under nitrogen atmosphere. EDC hydrochloride (74.5 mg, 0.36 mmol, 1.5 eq.) was added to the flask for 24 h at room temperature. The crude product was purified by flash chromatography, a mixture of hexane-dichloromethane (1:1) was prepared as eluent. 103 mg were obtained (yield = 57%).

^{1}H-NMR ($CDCl_3$, 200 MHz) δ(ppm): 7.82-7.21 (m, 8H, Hc+Hd+He+Hf+Hi+Hj); 7.40-7.20 (m, 6H, Hc+Hd+He+Hf+Hi); 6.05 (s, 2H, Hl); 3.98 (s, 2H, Hg); 2.91 (t, 2H, Hb); 2.65 (t, 2H, Ha); 2.48 (s, 6H, Hk); 1.45 (s, 6H, Hm).

DEPROTECTION OF TIPS-GROUP FROM COMPOUND **18**

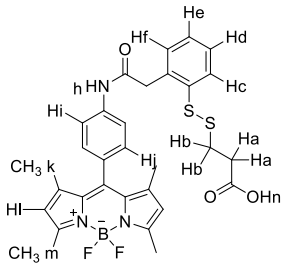

The synthesized amide (product **16**) was dissolved in dry THF into two Eppendorf (103 mg, 0.137 mmol, 1 eq.), and 33.6 µL (0.206 mmol, 1.5 eq.) of TEA fluoride. After 24 h at room temperature, an additional 7 µL of TEA fluoride were introduced in each Eppendorf. After 24h the reaction mixture was washed with BRINE, the same procedure was repeated after the addition of EtOAc and anhydrified on Na_2SO_4.

^{1}H-NMR ($CDCl_3$, 200 MHz) δ(ppm): 7.82-7.21 (m, 8H, Hc+Hd+He+Hf+Hi+Hj); 7.40-7.20 (m, 6H, Hc+Hd+He+Hf+Hi); 6.05 (s, 2H, Hl); 3.98 (s, 2H, Hg); 2.91 (t, 2H, Hb); 2.65 (t, 2H, Ha); 2.48 (s, 6H, Hk); 1.45 (s, 6H, Hm).

SYNTHESIS OF COMPOUND **19**

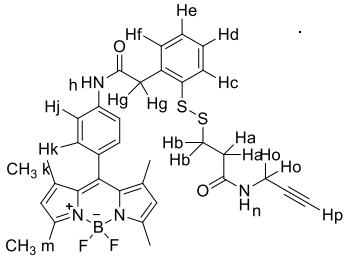

Product **18** (86 mg, 0.145 mmol, 1.6 eq.) was solubilized in 8 mL of dry DCM, under nitrogen atmosphere. Then 15 µL (1.6 eq.) of propargylamine, 45.4 mg (1.6 eq.) of EDC hydrochloride and 32.4 mg (1.6 eq.) of
HOBt. The reaction was carried out for 48 h at r.t. Subsequently the crude product was purified by flash chromatography, using dichloromethane: ethyl acetate (20: 1) as eluent mixture.

^{1}H-NMR (CD_3OD, 200 MHz) _(ppm): 7.81-7.27 (m, 8H, Hc+Hd+He+Hf+Hi+Hj); 6.17 (s, 2H, Hl); 3.94 (s, 2H, Hg); 3.84 (d, 2H, Ho); 3.10 (s, H, Hp); 2.93 (t, 2H, Hb); (t, 2H, Ha); 2.44 (s, 6H, Hk); 1.40 (s, 6H, Hm)

SYNTHESIS OF CNTs-BODIPY-BODIPYLINKER **20**

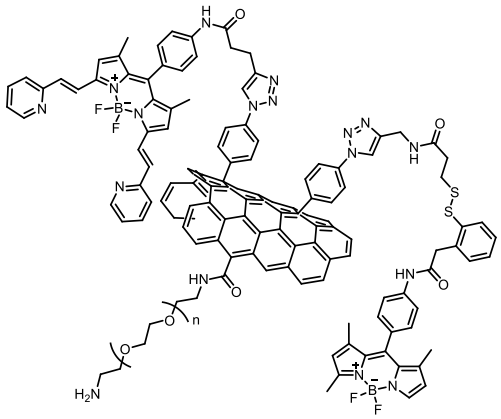

Nitrogen flow was bubbled for 2 hours in dry DMF, where compound **6** was dispersed (5.3 mg, 0.0084 mmol, 0.75 eq.). Substrate 17 (5.3 mg, 0.0084 mmol, 0.75 eq.), DIPEA (5.65 µL, 0.0324 mmol, 2.9 eq.) and $CuIP(OEt)_3$ (1.3 mg, 0.0028 mmol, 0.25 mmol) were added. After 24h the functionalized carbon nanotubes were filtered and washed with fresh DMF and methanol. 4.8 mg of material were collected.

OPENING OF EPOXIDE GO WITH LONG CHAIN OF PEG **22**

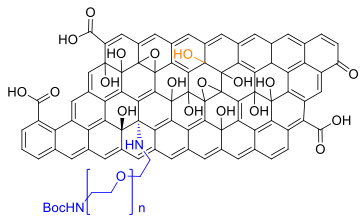

To a suspension of GO **21** (20 mg) in MilliQ water (20 ml) sonicated in a water bath for 20 min, PEG (80 mg, 0.32 mmol) was added. The reaction mixture was stirred for 1 day. To **21**, milliQ water was added and the sample was dialyzed in milliQ water for 5 days. fGO **22** was kept in solution and obtained as a powder after freeze drying only for characterization.

Boc-DEPROTECTION-**23/25**

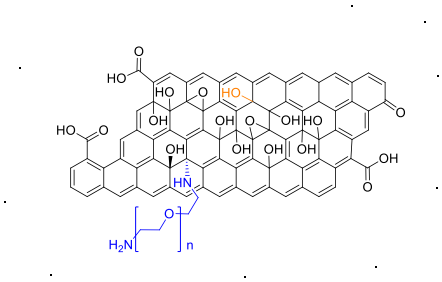

To a solution of Boc protected-f-GO (10 mg) **22/24** in 1,4-dioxane (5 ml), sonicated in a water bath for 10 min, was added a solution of 4M HCl in 1,4-dioxane (5 ml). The reaction mixture was stirred overnight. The reaction mixture was centrifuged at 1400 rcf for 15' at 0°C. The precipitate was dispersed in fresh DMF, sonicated in a water bath for few minutes and centrifuged. This workup sequence was repeated twice with DMF, twice with MeOH and twice with DCM.
The precipitate was dried under vacuum to obtain Boc-deprotected f-GO.

Quantitative Kaiser Test –

Three solutions were prepared separately:
- 10 g of phenol dissolved in 20 ml of ethanol (solution I)
- 2 ml of KCN 1 mM (aqueous solution) dissolved in 98 ml of pyridine (solution II)
- 1.0 g of ninhydrin dissolved in 20 ml of ethanol (solution III)

An amount of approximately 200 µg of GO conjugates was carefully weighted and then the following solutions were carefully added into the test tube: 75 µl of solution I, 100 µl of solution II and 75 µl of solution III. As blank solution, the three solutions were mixed in a test tube without GO. The test tube was sonicated in a water bath for 5 minutes, heated at 110°C for 5 minutes and then cooled rapidly in an ice bath to stop the reaction. 2.75 ml of 60% ethanol were added and the suspension was mixed. A UV-Vis cuvette was filled with the blank solution to collect the baseline. The absorbance of each sample was measured at 570 nm. The calculation of the amine loading was made using the Equation V.1.

The result was expressed as micromole of amino group per gram of material. The test was performed at least three times for each sample.

$$\mu mol/g = \frac{[Abs_{sample} - Abs_{blank}] \cdot dilution\ (mL) \cdot 10^6}{Molar\ extinction\ coefficient \cdot sample\ weight(mg)}$$

Equation: GO loading calculation. Dilution is equal to 5 ml and molar extinction coefficient to 15000 $M^{-1} \cdot cm^{-1}$.[64]

ESTERIFICATION REACTION ON CARBOXYLIC ACID –GO-**24**

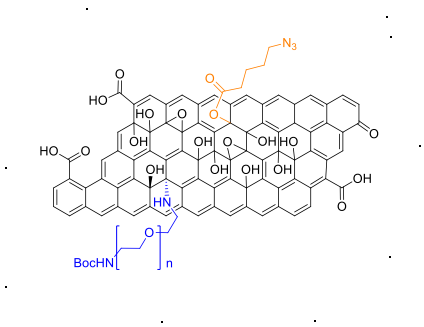

To a suspension of **23** (10 mg) in MilliQ water (10 ml), sonicated in a water bath for 20 min, were added EDC (15 mg, 0.10 mmol), DMAP (20 mg, 0.16 mmol) and 5-azidopentanoic acid (31 mg, 0.16 mmol). The reaction mixture was stirred for 2 days at room temperature. To **24**, milliQ water was added and the sample was dialyzed in milliQ water for 7 days. **24** was kept in solution and obtained as a powder after freeze drying only for characterization.

CONTROL REACTION OF GO_CONT

To a suspension of **22** (10 mg) in MilliQ water (10 ml), sonicated in a water bath for 20 min, 5-azidopentanoic acid (31 mg, 0.16 mmol) was added. The reaction mixture was stirred for 2 days at room temperature. To reaction product, milliQ water was added and the sample was dialyzed in milliQ water for 7 days. The material was kept in solution and obtained as a powder after freeze drying only for characterization.

CLICK REACTION ON fGO TO SYNTHESIZE **26**

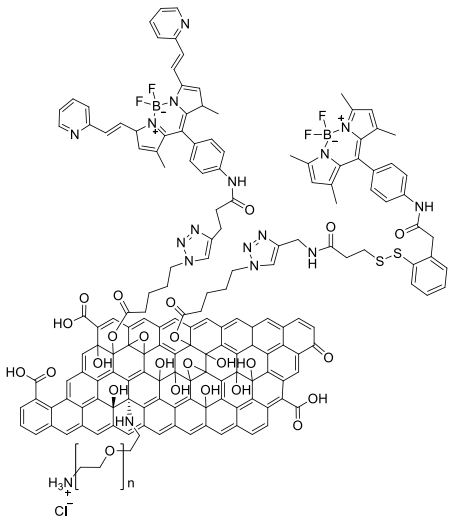

To fGO (2.4 mg) **25** in milliQ H_2O (0.15 ml) under nitrogen a solution of BODIPY amine **11** (3.1 mg, 1.44 µmol) and BODIPY LINKER **19** (3.1 mg, 1.44 µmol) in milliQ H_2O*t*BuOH (2:1, 2.4 ml) was added. Afterwards $CuSO_4$ (92 µg, 0.576 µmol) and sodium ascorbate (0.1 mg, 0.57 µmol) were added. The reaction mixture was stirred for 24h at room temperature. To fGO, milliQ water was added and the sample was dialyzed in milliQ water for 7 days. fGO **26** was kept in solution and obtained as a powder after freeze drying only for characterization.

2.8 REFERENCES

1. Biagiotti, G. *et al.* Multiwalled carbon nanotubes for combination therapy: A biodistribution and efficacy pilot study. *J. Mater. Chem. B* **7**, 2678–2687 (2019).

2. Kostarelos, K. *et al.* Cellular uptake of functionalized carbon nanotubes is independent of functional group and cell type. *Nat. Nanotechnol.* **2**, 108–113 (2007).

3. Liu & Speranza. Functionalization of Carbon Nanomaterials for Biomedical Applications. *C — J. Carbon Res.* **5**, 72 (2019).

4. Curcio, M. *et al.* Functionalized carbon nanostructures versus drug resistance: Promising scenarios in cancer treatment. *Molecules* **25**, 1–31 (2020).

5. Perkins, B. L. & Naderi, N. Carbon Nanostructures in Bone Tissue Engineering. *Open Orthop. J.* **10**, 877–899 (2017).

6. Erol, O. *et al.* Recent advances in bioactive 1D and 2D carbon nanomaterials for biomedical applications. *Nanomedicine Nanotechnology, Biol. Med.* **14**, 2433–2454 (2018).

7. Tasis, D., Tagmatarchis, N., Bianco, A. & Prato, M. Chemistry of carbon nanotubes. *Chem. Rev.* **106**, 1105–1136 (2006).

8. Kumar, S., Rani, R., Dilbaghi, N., Tankeshwar, K. & Kim, K. H. Carbon nanotubes: A novel material for multifaceted applications in human healthcare. *Chem. Soc. Rev.* **46**, 158–196 (2017).

9. Hong, S. Y. *et al.* Filled and glycosylated carbon nanotubes for in vivo radioemitter localization and imaging. *Nat. Mater.* **9**, 485–490 (2010).

10. Wohlstadter, J. N. *et al.* Carbon nanotube-based biosensor. *Adv. Mater.* **15**, 1184–1187 (2003).

11. Fedeli, S. *et al.* Azido-Substituted BODIPY Dyes for the Production of Fluorescent Carbon Nanotubes. *Chem. - A Eur. J.* **21**, 15349–15353 (2015).

12. Mooney, E., Dockery, P., Greiser, U., Murphy, M. & Barron, V. Carbon nanotubes and mesenchymal stem cells: Biocompatibility, proliferation and differentiation. *Nano Lett.* **8**, 2137–2143 (2008).

13. Guo, J., Wang, Y. & Zhao, M. Target-directed functionalized ferrous phosphate-carbon dots fluorescent nanostructures as peroxidase mimetics for cancer cell detection and ROS-mediated therapy. *Sensors Actuators, B Chem.* **297**, 126739 (2019).

14. Janyasupab, M. & Promptmas, C. Development of non-enzymatic N-doped graphene supported cobalt/iron amperometric based sensor for glucose detection in urine. *2018 IEEE EMBS Conf. Biomed. Eng. Sci. IECBES 2018 - Proc.* 577–582 (2019) doi:10.1109/IECBES.2018.8626693.

15. Chiang, Y. C., Lin, W. H. & Chang, Y. C. The influence of treatment duration on multi-walled carbon nanotubes functionalized by H 2 SO 4 /HNO 3 oxidation. *Appl. Surf. Sci.* **257**, 2401–2410 (2011).

16. Chattopadhyay, D., Lastella, S., Kim, S. & Papadimitrakopoulos, F. Length separation of zwitterion-functionalized single wall carbon nanotubes by GPC. *J. Am. Chem. Soc.* **124**, 728–729 (2002).

17. Li, J. & Zhang, Y. Large-scale aligned carbon nanotubes films. *Phys. E Low-Dimensional Syst. Nanostructures* **33**, 235–239 (2006).

18. submitted to Nature on Feb 5, 2004. (2004).

19. Allen, M. J., Tung, V. C. & Kaner, R. B. Honeycomb carbon: A review of graphene. *Chem. Rev.* **110**, 132–145 (2010).

20. Park, S. & Ruoff, R. S. Chemical methods for the production of graphenes. *Nat. Nanotechnol.* **4**, 217–224 (2009).

21. Reina, A. *et al.* Growth of large-area single- and Bi-layer graphene by controlled carbon precipitation on polycrystalline Ni surfaces. *Nano Res.* **2**, 509–516 (2009).

22. Jiao, L., Wang, X., Diankov, G., Wang, H. & Dai, H. Facile synthesis of high-quality graphene nanoribbons. *Nat. Nanotechnol.* **5**, 321–325 (2010).

23. Coliman, J. P. *et al.* "Picket Fence Porphyrins". Synthetic Models for Oxygen Binding Hemoproteins. *J. Am. Chem. Soc.* **97**, 1427–1439 (1975).

24. Brinker, C. J., Lu, Y., Sellinger, A. & Fan, H. ChemInform Abstract: Evaporation-Induced Self-Assembly: Nanostructures Made Easy. *ChemInform* **30**, no-no (2010).

25. Sutter, P., Sadowski, J. T. & Sutter, E. Graphene on Pt(111): Growth and substrate interaction. *Phys. Rev. B - Condens. Matter Mater. Phys.* **80**, 1–10 (2009).

26. Staudenmaier, L. Method for the preparation of the graphite acid. *Eur. J. Inorg. Chem.* **31**, 1481–1487 (1898).

27. Zhang, X. *et al.* Distribution and biocompatibility studies of graphene oxide in mice after intravenous administration. *Carbon N. Y.* **49**, 986–995 (2011).

28. Pan, S. & Aksay, I. A. Factors controlling the size of graphene oxide sheets produced via the graphite oxide route. *ACS Nano* **5**, 4073–4083 (2011).

29. Gonçalves, P. A. D. & Peres, N. M. R. An Introduction to Graphene Plasmonics. *An Introd. to Graphene Plasmon.* 1–431 (2016) doi:10.1142/9948.

30. Pan, Y., Sahoo, N. G. & Li, L. The application of graphene oxide in drug delivery. *Expert Opin. Drug Deliv.* **9**, 1365–1376 (2012).

31. Li, Q.-Y., Zu, Y.-G., Shi, R.-Z. & Yao, L.-P. Review Camptothecin: Current Perspectives. *Curr. Med. Chem.* **13**, 2021–2039 (2006).

32. Liu, Z., Robinson, J. T., Sun, X. & Dai, H. PEGylated nanographene oxide for delivery of water-insoluble cancer drugs. *J. Am. Chem. Soc.* **130**, 10876–10877 (2008).

33. Rana, V. K. *et al.* Synthesis and drug-delivery behavior of chitosan-functionalized graphene oxide hybrid nanosheets. *Macromol. Mater. Eng.* **296**, 131–140 (2011).

34. Eigler, S., Grimm, S., Enzelberger-Heim, M., Müller, P. & Hirscha, A. Graphene oxide: Efficiency of reducing agents. *Chem. Commun.* **49**, 7391–7393 (2013).

35. Hunt, A. *et al.* Epoxide speciation and functional group distribution in graphene oxide paper-like materials. *Adv. Funct. Mater.* **22**, 3950–3957 (2012).

36. Szabó, T. *et al.* Evolution of surface functional groups in a series of progressively oxidized graphite oxides. *Chem. Mater.* **18**, 2740–2749 (2006).

37. Dimiev, A. M., Alemany, L. B. & Tour, J. M. Graphene oxide. Origin of acidity, its instability in water, and a new dynamic structural model. *ACS Nano* **7**, 576–588 (2013).

38. Liu, Y., Yu, D., Zeng, C., Miao, Z. & Dai, L. Biocompatible graphene oxide-based glucose

biosensors. *Langmuir* **26**, 6158–6160 (2010).

39. Paquin, F., Rivnay, J., Salleo, A., Stingelin, N. & Silva, C. Multi-phase semicrystalline microstructures drive exciton dissociation in neat plastic semiconductors. *J. Mater. Chem. C* **3**, 10715–10722 (2015).

40. Yu, R. *et al.* Synthetic possibility of polystyrene functionalization based on hydroxyl groups of graphene oxide as nucleophiles. *New J. Chem.* **39**, 5096–5099 (2015).

41. Chen, H. *et al.* Phosphorylation of graphehe oxide to improve adsorption of U(VI) from aquaeous solutions. *J. Radioanal. Nucl. Chem.* **313**, 175–189 (2017).

42. De Leon, A. C., Alonso, L., Mangadlao, J. D., Advincula, R. C. & Pentzer, E. Simultaneous Reduction and Functionalization of Graphene Oxide via Ritter Reaction. *ACS Appl. Mater. Interfaces* **9**, 14265–14272 (2017).

43. Liao, K. H., Lin, Y. S., MacOsko, C. W. & Haynes, C. L. Cytotoxicity of graphene oxide and graphene in human erythrocytes and skin fibroblasts. *ACS Appl. Mater. Interfaces* **3**, 2607–2615 (2011).

44. Lu, C. H. *et al.* Using graphene to protect DNA from cleavage during cellular delivery. *Chem. Commun.* **46**, 3116–3118 (2010).

45. Wojtoniszak, M. *et al.* Synthesis, dispersion, and cytocompatibility of graphene oxide and reduced graphene oxide. *Colloids Surfaces B Biointerfaces* **89**, 79–85 (2012).

46. Yuan, J. *et al.* Cytotoxicity evaluation of oxidized single-walled carbon nanotubes and graphene oxide on human hepatoma HepG2 cells: An iTRAQ-coupled 2D LC-MS/MS proteome analysis. *Toxicol. Sci.* **126**, 149–161 (2012).

47. Chang, Y. *et al.* In vitro toxicity evaluation of graphene oxide on A549 cells. *Toxicol. Lett.* **200**, 201–210 (2011).

48. Bhattacharya, K. *et al.* Biological interactions of carbon-based nanomaterials: From coronation to degradation. *Nanomedicine Nanotechnology, Biol. Med.* **12**, 333–351 (2016).

49. Kurapati, R. *et al.* Dispersibility-Dependent Biodegradation of Graphene Oxide by Myeloperoxidase. *Small* **11**, 3985–3994 (2015).

50. Chen, S. *et al.* Mechanism-based tumor-targeting drug delivery system. Validation of efficient vitamin receptor-mediated endocytosis and drug release. *Bioconjug. Chem.* **21**, 979–987 (2010).

51. Lee, J. S. *et al.* Synthesis of a BODIPY library and its application to the development of live cell glucagon imaging probe. *J. Am. Chem. Soc.* **131**, 10077–10082 (2009).

52. Kaur, P. & Singh, K. Recent advances in the application of BODIPY in bioimaging and chemosensing. *J. Mater. Chem. C* **7**, 11361–11405 (2019).

53. Moss, G. P. Nomenclature of tetrapyrroles (Recommendations 1986). *Pure Appl. Chem.* **59**, 779–832 (1987).

54. van Koeveringe, J. A. & Lugtenburg, J. Novel pyrromethenes 1-Oxygen and 1-sulfur analogues; evidence for photochemical. *Recueil, J. R. Netherlands Chem. Soc.* **96**, 55–57 (1977).

55. Solomonov, A. V., Marfin, Y. S. & Rumyantsev, E. V. Design and applications of dipyrrin-based fluorescent dyes and related organic luminophores: From individual compounds to supramolecular self-assembled systems. *Dye. Pigment.* **162**, 517–542 (2019).

56. Li, Z., Mintzer, E. & Bittman, R. First synthesis of free cholesterol-BODIPY conjugates. *J. Org.*

Chem. **71**, 1718–1721 (2006).

57. Wagner, R. W. & Lindsey, J. S. Boron-dipyrromethene dyes for incorporation in synthetic multi-pigment light-harvesting arrays. *Pure Appl. Chem.* **68**, 1373–1380 (1996).

58. Thivierge, C., Bandichhor, R. & Burgess, K. Spectral dispersion and water solubilization of BODIPY dyes via palladium-catalyzed C-H functionalization. *Org. Lett.* **9**, 2135–2138 (2007).

59. Shah, M. *et al.* Pyrromethene–BF2 complexes as laser dyes:1. *Heteroat. Chem.* **1**, 389–399 (1990).

60. Yogo, T., Urano, Y., Ishitsuka, Y., Maniwa, F. & Nagano, T. Highly efficient and photostable photosensitizer based on BODIPY chromophore. *J. Am. Chem. Soc.* **127**, 12162–12163 (2005).

61. Scheibe, B., Borowiak-Palen, E. & Kalenczuk, R. J. Oxidation and reduction of multiwalled carbon nanotubes - preparation and characterization. *Mater. Charact.* **61**, 185–191 (2010).

62. Jameson, L. P. & Dzyuba, S. V. Expeditious, mechanochemical synthesis of BODIPY dyes. *Beilstein J. Org. Chem.* **9**, 786–790 (2013).

63. Andersen, J., Madsen, U., Björkling, F. & Liang, X. Rapid synthesis of aryl azides from aryl halides under mild conditions. *Synlett* 2209–2213 (2005) doi:10.1055/s-2005-872248.

64. Ménard-Moyon, C., Fabbro, C., Prato, M. & Bianco, A. One-pot triple functionalization of carbon nanotubes. *Chem. - A Eur. J.* **17**, 3222–3227 (2011).

65. Lin, H. B., Cooper, S. L., Zhao, Z. C., Garcia-Echeverria, C. & Rich, D. H. Synthesis of a novel polyurethane co-polymer containing covalently attached RGD peptide. *J. Biomater. Sci. Polym. Ed.* **3**, 217–227 (1992).

66. Van Agthoven, J. F. *et al.* Structural Basis of the Differential Binding of Engineered Knottins to Integrins αVβ3 and α5β1. *Structure* **27**, 1443-1451.e6 (2019).

67. Sheldrake, H. M. & Patterson, L. H. Strategies to inhibit tumor associated integrin receptors: Rationale for dual and multi-antagonists. *J. Med. Chem.* **57**, 6301–6315 (2014).

68. Maligaspe, E. *et al.* Photosynthetic antenna-reaction center mimicry: Sequential energy- and electron transfer in a self-assembled supramolecular triad composed of boron dipyrrin, zinc porphyrin and fullerene. *J. Phys. Chem. A* **113**, 8478–8489 (2009).

69. Mori, H. *et al.* In silico and pharmacological screenings identify novel serine racemase inhibitors. *Bioorganic Med. Chem. Lett.* **24**, 3732–3735 (2014).

70. Hishikawa, K. *et al.* Photoinduced nitric oxide release from a hindered nitrobenzene derivative by two-photon excitation. *J. Am. Chem. Soc.* **131**, 7488–7489 (2009).

71. Mallesha, N., Prahlada Rao, S., Suhas, R. & Channe Gowda, D. An efficient synthesis of tert-butyl ethers/esters of alcohols/amino acids using methyl tert-butyl ether. *Tetrahedron Lett.* **53**, 641–645 (2012).

72. Mock, J. N. *et al.* Haloenol pyranones and morpholinones as antineoplastic agents of prostate cancer. *Bioorganic Med. Chem. Lett.* **22**, 4854–4858 (2012).

73. König, W. & Geiger, R. Eine neue Methode zur Synthese von Peptiden: Aktivierung der Carboxylgruppe mit Dicyclohexylcarbodiimid unter Zusatz von 1-Hydroxy-benzotriazolen. *Chem. Ber.* **103**, 788–798 (1970).

74. Pérez-Picaso, L., Escalante, J., Olivo, H. F. & Rios, M. Y. Efficient microwave assisted syntheses of 2,5-diketopiperazines in aqueous media. *Molecules* **14**, 2836–2849 (2009).

75. Styers, T. J. *et al.* Synthesis of Sansalvamide A derivatives and their cytotoxicity in the MSS colon cancer cell line HT-29. *Bioorganic Med. Chem.* **14**, 5625–5631 (2006).

76. Lundt, B. F., Johansen, N. L., Vølund, A. & Markussen, J. REMOVAL OF t-BUTYL AND t-BUTOXYCARBONYL PROTECTING GROUPS WITH TRIFLUOROACETIC ACID: Mechanisms, Biproduct Formation and Evaluation of Scavengers. *Int. J. Pept. Protein Res.* **12**, 258–268 (1978).

77. Hughes, A. B. Amino Acids, Peptides and Proteins in Organic Chemistry. *Amin. Acids, Pept. Proteins Org. Chem.* **2**, (2010).

78. Vardhan, D. M. S., Kumara, H. K., Kumar, H. P. & Gowda, D. C. Inhibition of Urease Enzyme Activity By Urea and Thiourea Derivatives of Dipeptides Conjugated 2, 3-Dichlorophenyl Piperazine. *Int. J. Pharm. Pharm. Sci.* **9**, 92 (2017).

79. Kaur, A., Poonam, Patil, M. T., Mehta, S. K. & Salunke, D. B. An efficient and scalable synthesis of potent TLR2 agonistic PAM2CSK4. *RSC Adv.* **8**, 9587–9596 (2018).

80. Brough, P., Klumpp, C., Bianco, A., Campidelli, S. & Prato, M. [60]fullerene-pyrrolidine-N-oxides. *J. Org. Chem.* **71**, 2014–2020 (2006).

81. Saini, N. & Yang, X. Metformin as an anti-cancer agent: Actions and mechanisms targeting cancer stem cells. *Acta Biochim. Biophys. Sin. (Shanghai).* **50**, 133–143 (2018).

82. Pierotti, M. A. *et al.* Targeting metabolism for cancer treatment and prevention: Metformin, an old drug with multi-faceted effects. *Oncogene* **32**, 1475–1487 (2013).

83. Alimova, I. N. *et al.* Metformin inhibits breast cancer cell growth, colony formation and induces cell cycle arrest in vitro. *Cell Cycle* **8**, 909–915 (2009).

84. Morales, D. R. & Morris, A. D. Metformin in cancer treatment and prevention. *Annu. Rev. Med.* **66**, 17–29 (2015).

85. Jaune, E. & Rocchi, S. Metformin: Focus on melanoma. *Front. Endocrinol. (Lausanne).* **9**, 1–9 (2018).

86. Tseng, H. W., Li, S. C. & Tsai, K. W. Metformin treatment suppresses melanoma cell growth and motility through modulation of microRNA expression. *Cancers (Basel).* **11**, (2019).

87. Vancura, A., Bu, P., Bhagwat, M., Zeng, J. & Vancurova, I. Metformin as an Anticancer Agent. *Trends Pharmacol. Sci.* **39**, 867–878 (2018).

88. Mallik, R. & Chowdhury, T. A. Metformin in cancer. *Diabetes Res. Clin. Pract.* **143**, 409–419 (2018).

89. Saraei, P., Asadi, I., Kakar, M. A. & Moradi-Kor, N. The beneficial effects of metformin on cancer prevention and therapy: A comprehensive review of recent advances. *Cancer Manag. Res.* **11**, 3295–3313 (2019).

90. Fedeli, S. *et al.* The 'click-on-tube' approach for the production of efficient drug carriers based on oxidized multi-walled carbon nanotubes. *J. Mater. Chem. B* **4**, 3823–3831 (2016).

91. Baghayeri, M., Tehrani, M. B., Amiri, A., Maleki, B. & Farhadi, S. A novel way for detection of antiparkinsonism drug entacapone via electrodeposition of silver nanoparticles/functionalized multi-walled carbon nanotubes as an amperometric sensor. *Mater. Sci. Eng. C* **66**, 77–83 (2016).

92. Mirazi, N., Shoaei, J., Khazaei, A. & Hosseini, A. A comparative study on effect of metformin and metformin-conjugated nanotubes on blood glucose homeostasis in diabetic rats. *Eur. J.*

Drug Metab. Pharmacokinet. **40**, 343–348 (2015).

93. Yoo, S. *et al.* Enhanced Response of Metformin towards the Cancer Cells due to Synergism with Multi-walled Carbon Nanotubes in Photothermal Therapy. *Sci. Rep.* 1–9 (2017) doi:10.1038/s41598-017-01118-3.

94. Denise, C. *et al.* 5-Fluorouracil resistant colon cancer cells are addicted to OXPHOS to survive and enhance stem-like traits. *Oncotarget* **6**, 41706–41721 (2015).

95. Ota, S. *et al.* Metformin suppresses glucose-6-phosphatase expression by a complex I inhibition and AMPK activation-independent mechanism. *Biochem. Biophys. Res. Commun.* **388**, 311–316 (2009).

96. Chen, Z. *et al.* The Advances of Carbon Nanotubes in Cancer Diagnostics and Therapeutics. *J. Nanomater.* **2017**, (2017).

97. Cui, X., Wan, B., Yang, Y., Ren, X. & Guo, L. H. Length effects on the dynamic process of cellular uptake and exocytosis of single-walled carbon nanotubes in murine macrophage cells /631/80 /704/172 /82/29 /14/19 /14/34 /123 article. *Sci. Rep.* **7**, 1–13 (2017).

98. Yuan, Y. M. & He, C. The glial scar in spinal cord injury and repair. *Neurosci. Bull.* **29**, 421–435 (2013).

99. Su, Z. *et al.* Reactive astrocytes inhibit the survival and differentiation of oligodendrocyte precursor cells by secreted TNF-α. *J. Neurotrauma* **28**, 1089–1100 (2011).

100. Liu, W. *et al.* Folic acid conjugated magnetic iron oxide nanoparticles for nondestructive separation and detection of ovarian cancer cells from whole blood. *Biomater. Sci.* **4**, 159–166 (2016).

101. Stichel, C. C. & Müller, H. W. The CNS lesion scar: New vistas on an old regeneration barrier. *Cell Tissue Res.* **294**, 1–9 (1998).

102. Galtrey, C. M. & Fawcett, J. W. The role of chondroitin sulfate proteoglycans in regeneration and plasticity in the central nervous system. *Brain Res. Rev.* **54**, 1–18 (2007).

103. Bradbury, E. J. & Carter, L. M. Manipulating the glial scar: Chondroitinase ABC as a therapy for spinal cord injury. *Brain Res. Bull.* **84**, 306–316 (2011).

104. Silver, J. & Miller, J. H. Regeneration beyond the glial scar. *Nat. Rev. Neurosci.* **5**, 146–156 (2004).

105. Place, L. W., Sekyi, M. & Kipper, M. J. Aggrecan-mimetic, glycosaminoglycan-containing nanoparticles for growth factor stabilization and delivery. *Biomacromolecules* **15**, 680–689 (2014).

106. Marchesan, S., Kostarelos, K., Bianco, A. & Prato, M. The winding road for carbon nanotubes in nanomedicine. *Mater. Today* **18**, 12–19 (2015).

107. Pinillos-Madrid, J. F. & Gallardo, C. Carbon nanotubes: A viable drug delivery platform for the treatment of cancer. *J. Appl. Pharm. Sci.* **5**, 143–152 (2015).

108. Moradian, H., Fasehee, H., Keshvari, H. & Faghihi, S. Poly(ethyleneimine) functionalized carbon nanotubes as efficient nano-vector for transfecting mesenchymal stem cells. *Colloids Surfaces B Biointerfaces* **122**, 115–125 (2014).

109. Herrero, M. A. *et al.* Synthesis and characterization of a carbon nanotube-dendron series for efficient siRNA delivery. *J. Am. Chem. Soc.* **131**, 9843–9848 (2009).

110. Zhou, M., Peng, Z., Liao, S., Li, P. & Li, S. Design of microencapsulated carbon nanotube-based

microspheres and its application in colon targeted drug delivery. *Drug Deliv.* **21**, 101–109 (2014).

111. Zhang, W., Zuo, X. D. & Wu, C. W. Synthesis and magnetic properties of carbon nanotube-iron oxide nanoparticle composites for hyperthermia: A review. *Rev. Adv. Mater. Sci.* **40**, 165–176 (2015).

112. Jones, L. L., Margolis, R. U. & Tuszynski, M. H. The chondroitin sulfate proteoglycans neurocan, brevican, phosphacan, and versican are differentially regulated following spinal cord injury. *Exp. Neurol.* **182**, 399–411 (2003).

113. Tom, V. J., Steinmetz, M. P., Miller, J. H., Doller, C. M. & Silver, J. Studies on the development and behavior of the dystrophic growth cone, the hallmark of regeneration failure, in an in vitro model of the glial scar and after spinal cord injury. *J. Neurosci.* **24**, 6531–6539 (2004).

114. Matthews, R. T. *et al.* Aggrecan glycoforms contribute to the molecular heterogeneity of perineuronal nets. *J. Neurosci.* **22**, 7536–7547 (2002).

115. Sandvig, A., Berry, M., Barrett, L. B., Butt, A. & Logan, A. Myelin-, reactive glia-, and scar-derived CNS axon growth inhibitors: Expression, receptor signaling, and correlation with axon regeneration. *Glia* **46**, 225–251 (2004).

116. Yiu, G. & He, Z. Glial inhibition of CNS axon regeneration. *Nat. Rev. Neurosci.* **7**, 617–627 (2006).

117. Rhodes, K. E. & Fawcett, J. W. Chondroitin sulphate proteoglycans: Preventing plasticity or protecting the CNS? *J. Anat.* **204**, 33–48 (2004).

118. Gilbert, R. J. *et al.* CS-4,6 is differentially upregulated in glial scar and is a potent inhibitor of neurite extension. *Mol. Cell. Neurosci.* **29**, 545–558 (2005).

119. Zuo, J., Neubauer, D., Dyess, K., Ferguson, T. A. & Muir, D. Degradation of chondroitin sulfate proteoglycan enhances the neurite- promoting potential of spinal cord tissue. *Exp. Neurol.* **154**, 654–662 (1998).

120. McKeon, R. J., Schreiber, R. C., Rudge, J. S. & Silver, J. Reduction of neurite outgrowth in a model of glial scarring following CNS injury is correlated with the expression of inhibitory molecules on reactive astrocytes. *J. Neurosci.* **11**, 3398–3411 (1991).

121. Preston, E., Webster, J. & Small, D. Characteristics of sustained blood-brain barrier opening and tissue injury in a model for focal trauma in the rat. *J. Neurotrauma* **18**, 83–92 (2001).

122. Fitch, M. T., Doller, C., Combs, C. K., Landreth, G. E. & Silver, J. Cellular and molecular mechanisms of glial scarring and progressive cavitation: In vivo and in vitro analysis of inflammation-induced secondary injury after CNS trauma. *J. Neurosci.* **19**, 8182–8198 (1999).

123. Faulkner, J. R. *et al.* Reactive Astrocytes Protect Tissue and Preserve Function after Spinal Cord Injury. *J. Neurosci.* **24**, 2143–2155 (2004).

124. Jones, L. L., Sajed, D. & Tuszynski, M. H. Axonal Regeneration through Regions of Chondroitin Sulfate Proteoglycan Deposition after Spinal Cord Injury: A Balance of Permissiveness and Inhibition. *J. Neurosci.* **23**, 9276–9288 (2003).

125. Levine, J. M., Reynolds, R. & Fawcett, J. W. The oligodendrocyte precursor cell in health and disease. *Trends Neurosci.* **24**, 39–47 (2001).

126. Tan, A. M., Zhang, W. & Levine, J. M. NG2: A component of the glial scar that inhibits axon growth. *J. Anat.* **207**, 717–725 (2005).

127. Yang, L. J. S. *et al.* Sialidase enhances spinal axon outgrowth in vivo. *Proc. Natl. Acad. Sci. U. S. A.* **103**, 11057–11062 (2006).

128. Rhodes, K. E., Raivich, G. & Fawcett, J. W. The injury response of oligodendrocyte precursor cells is induced by platelets, macrophages and inflammation-associated cytokines. *Neuroscience* **140**, 87–100 (2006).

129. Davies, S. J. A., Goucher, D. R., Doller, C. & Silver, J. Robust regeneration of adult sensory axons in degenerating white matter of the adult rat spinal cord. *J. Neurosci.* **19**, 5810–5822 (1999).

130. Dyck, S. M. & Karimi-Abdolrezaee, S. Chondroitin sulfate proteoglycans: Key modulators in the developing and pathologic central nervous system. *Exp. Neurol.* **269**, 169–187 (2015).

131. Muleja, A. A., Mbianda, X. Y., Krause, R. W. & Pillay, K. Synthesis, characterization and thermal decomposition behaviour of triphenylphosphine-linked multiwalled carbon nanotubes. *Carbon N. Y.* **50**, 2741–2751 (2012).

132. Bonini, M., Wiedenmann, A. & Baglioni, P. Small angle polarized neutrons (SANSPOL) investigation of surfactant free magnetic fluid of uncoated and silica-coated cobalt-ferrite nanoparticles. *J. Phys. Chem. B* **108**, 14901–14906 (2004).

133. Chitosan, P. O. F. on the Structure and Properties of Chitosan. **33**, 1899–1904 (1992).

134. Coulson-Thomas, V. & Gesteira, T. Dimethylmethylene Blue Assay (DMMB). *Bio-Protocol* **4**, 1–7 (2014).

135. Shin, H. J. *et al.* Efficient reduction of graphite oxide by sodium borohydride and its effect on electrical conductance. *Adv. Funct. Mater.* **19**, 1987–1992 (2009).

136. Pei, S. & Cheng, H. M. The reduction of graphene oxide. *Carbon N. Y.* **50**, 3210–3228 (2012).

137. Gao, W., Alemany, L. B., Ci, L. & Ajayan, P. M. New insights into the structure and reduction of graphite oxide. *Nat. Chem.* **1**, 403–408 (2009).

138. Pei, S., Zhao, J., Du, J., Ren, W. & Cheng, H. M. Direct reduction of graphene oxide films into highly conductive and flexible graphene films by hydrohalic acids. *Carbon N. Y.* **48**, 4466–4474 (2010).

139. Moon, I. K., Lee, J., Ruoff, R. S. & Lee, H. Reduced graphene oxide by chemical graphitization. *Nat. Commun.* **1**, (2010).

140. Schniepp, H. C. *et al.* Functionalized single graphene sheets derived from splitting graphite oxide. *J. Phys. Chem. B* **110**, 8535–8539 (2006).

141. Fernández-Merino, M. J. *et al.* Vitamin C is an ideal substitute for hydrazine in the reduction of graphene oxide suspensions. *J. Phys. Chem. C* **114**, 6426–6432 (2010).

142. Bosch-Navarro, C., Coronado, E., Martí-Gastaldo, C., Sánchez-Royo, J. F. & Gómez, M. G. Influence of the pH on the synthesis of reduced graphene oxide under hydrothermal conditions. *Nanoscale* **4**, 3977–3982 (2012).

143. Stolle, A., Szuppa, T., Leonhardt, S. E. S. & Ondruschka, B. Ball milling in organic synthesis: Solutions and challenges. *Chem. Soc. Rev.* **40**, 2317–2329 (2011).

144. Szuppa, T., Stolle, A., Ondruschka, B. & Hopfe, W. An alternative solvent-free synthesis of nopinone under ball-milling conditions: Investigation of reaction parameters. *ChemSusChem* **3**, 1181–1191 (2010).

145. Fulmer, D. A., Shearouse, W. C., Medonza, S. T. & Mack, J. Solvent-free Sonogashira coupling

reaction via high speed ball milling. *Green Chem.* **11**, 1821–1825 (2009).

146. Schneider, F., Stolle, A., Ondruschka, B. & Hopf, H. The Suzuki-Miyaura reaction under mechanochemical conditions. *Org. Process Res. Dev.* **13**, 44–48 (2009).

147. Lee, H. C. *et al.* Review of the synthesis, transfer, characterization and growth mechanisms of single and multilayer graphene. *RSC Adv.* **7**, 15644–15693 (2017).

148. Hummers, W. S. & Offeman, R. E. Preparation of Graphitic Oxide. *J. Am. Chem. Soc.* **80**, 1339 (1958).

3. Amino acids/Peptide functionalized BODIPY fluorescent probes

3.1 OBJECTIVES OF THIS CHAPTER (3)

BODIPY Core showed an azido group **27** which could be exploited for Click Chemistry reactions (CuAAC-Copper catalyzed Alkyne-Azide Cycloaddition) to obtain cycloaddition products which presented functionalized BODIPYs as fluorescent probes of CNTs.

One of the goal of this project consisted in the extension of BODIPY's conjugation to connect amino acids or a dipeptides to the fluorescent dye as showed in **Figure 47** . The applied strategies could be two:

. 1. First the *Coupling* of the linker to the selected amino acid, therefore the *Knövenagel Reaction* with the methyl groups connected to pyrroles of BODIPY.

. 2. First the *Knövenagel Reaction* involving the linker and the methyl groups of pyrroles, therefore the *Coupling Reaction* of BODIPY-Linker molecule with the chosen amino acid.

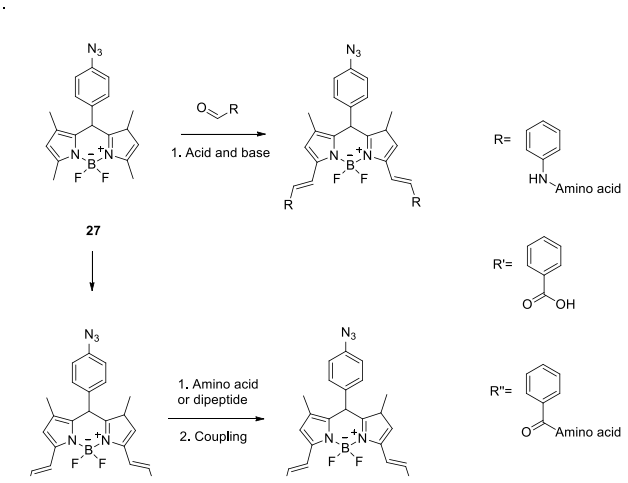

Figure 47.*Pattern of amino acids coupled to BODIPY azido **27** .*

The second part of the project concerned the design of a system based on BODIPY-azido previously synthesized, connected to RGD peptide (Arg-Gly-Asp) thanks to an aldehyde linker, as showed in **Figure 48**. The biological role of the peptide is fundamental both for the properties of pharmacophore, and for the direct interaction with cell adhesion molecules (integrins). The integrins recognize the specific aminoacidic sequence and allow to bind it.

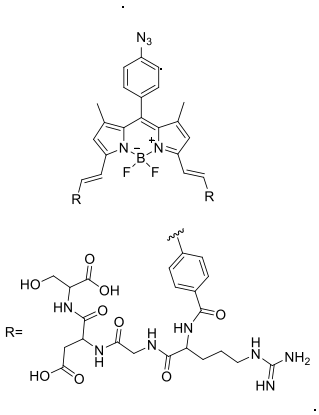

***Figure 48**: Final product due to the coupling of BODIPY dye and RGD sequence.*

3.2 INTRODUCTION

3.2.1 RGD SEQUENCE

Arginylglycylaspartic acid (RGD) is the most common peptide motif responsible for cell adhesion to extracellular matrix (ECM). Many cell adhesion proteins placed in ECM and into blood include *Arginine-Glycine-Aspartic Acid* as cellular recognition site. RGD sequence of cell adhesion proteins are identified from at least one member of transmembrane receptors family, such as integrins, which are heterodynamic proteins with two subunits. The development of new biomaterials was inspired by the recent progresses[65] concerning interactions between peptides containing RGD sequence (Gly-Arg-Asp) and cellular receptors. Understanding the molecular bases of RGD-integrins bond allowed the development of cancer therapy and of new drugs to treat cardiovascular diseases.

THE INTEGRINS

Integrins are heterodimeric membrane proteins, which constitute one family of evolutionary ancient cell adhesion receptors. Integrins play an important role in physiological and pathological processes, such as neo-angiogenesis and tumor dissemination. As shown in **Figure 43** integrins are obligate heterodimers, meaning that they have two subunits: α (alpha) and β (beta). Integrins are made up of an extracellular domain, a transmembrane region and a short cytoplasmatic tail.

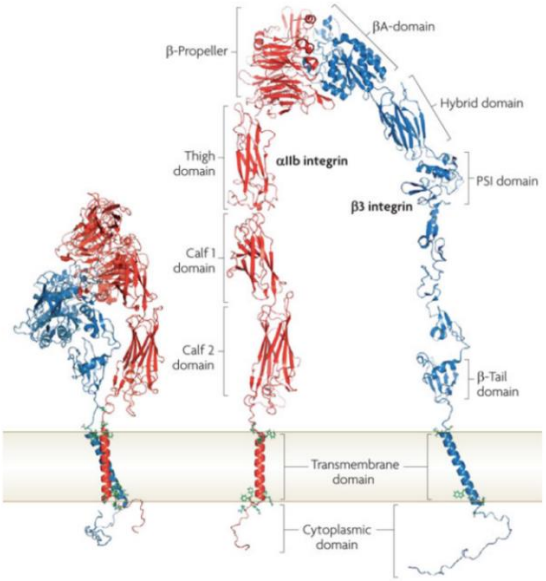

Figure 49. *On the left an inactive integrin; on the right an integrin suitable to interact with a lingand through α and β subunits.* http://www.nature.com/nrm/journal/v11/n4/images/nrm2871-i1.jpg

The cytoplasmatic domain regulates activity and function of integrins, monitoring their affinity state and their activity as bridge with extracellular matrix. In addition to the cytoplasmatic domain promotes the cellular responses demanded by binding with extracellular ligands. The bond with their extracellular ligands (inside-outside signaling pathway) activates integrins and causes different conformations depending on individual responses.

Since integrins lack intrinsic kinase activity, they require the formation of complexes with other signaling and adaptor proteins of cytoplasm. These systems produce macromolecular dynamic structures generally called adhesion complexes, promoting the cell survival and proliferation, thanks to integrins activation. Tumor growth and metastasis process are connected to integrins, generally overexpressed in cancer cells, reason why they are considered important drug targets in the treatment of tumor.

The antagonist of integrins allows to inhibit both cancer cells and their associated cells. Several methods aimed at inhibiting integrins have been carefully studied to treat pathologies actively involving integrins. Synthetic peptides and peptidomimetics, as well as blocking antibodies are antagonist of integrins. The most studied class of synthetic peptides, which mimic the structural of natural ligands of integrins, includes RGD peptides. Several glycoproteins of ECM, such as fibronectin, show this sequence. **Figure 50**

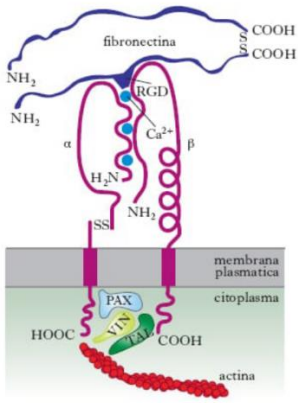

Figure 50. *RGD fibronectina sequence recognized by integrin, which bind it.*http://www.treccani.it/enciclopedia/integrina/

INTERACTIONS

As presented in numerous studies, peptides including RGD sequence, may bind to integrins of membrane of cancer cells, hindering their interactions with natural ligands. When an integrin of a cancer cell interacts with RGD, its functionality was inhibited, as well as the cellular metabolism, proliferation and metastasis. The ability of integrins to connect to extracellular proteins or to cytoskeleton is compromised. An isolation of cancer cell occurred, due to the inhibition of all types of information exchange.

The interaction RGD-integrin, as show in **Figure 51**, consists of:

I. An electrostatic interaction: carboxylate group of the peptide interacts with a metal ion positively charged (usually Mg^{2+}) associated with the subunit β of integrin.[66]

II. Different interactions between acid residues of the α subunit and the basic part of the peptide chain, that is Arginine.

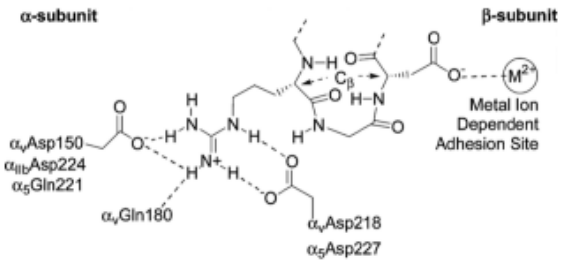

Figure 51. *Principal characteristics of the binding sites of RGD sequence.*[67]

Peptides containing the RGD sequence, consequently, represent a family of potential drugs with anti-thrombotic, anti-angiogenic and antimetastatic activity.[67]

The final product of this work would to exploit a combined effect derived from biological role of the RGD, and the activity of BODIPY probes, for future *imaging* studies.

3.3 RESULTS AND DISCUSSION

The first part of the project was the synthesis of BODIPY Core **Scheme 23** . The final goal consisted in the transformation of -NO_2 in -N_3. This synthetic step allows to exploit the azido group to bond BODIPY molecules to nanostructured materials, thanks to Click chemistry for the decoration of CNTs or GO.

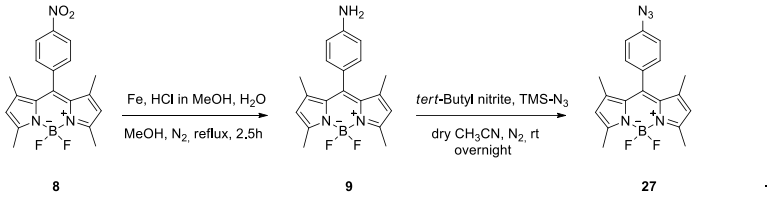

Scheme 23. *Synthesis process to achieve BODIPY Core.*

Starting from 4-Nitrobenzaldehyde and 2,4-dimethylpirrole, compound **27** was obtained in two distinct steps. A first synthetic step was represented by using 2,3,5,6-tetrachlorocyclohexane-1,4-dione as oxidation reagent and then the addition of BF_3 for a complexation procedure.

The first step was a mechanochemistry reaction type, with a catalytic amount of TFA and an oxidation reagent. The workup consisted in hard extractions with DCM-Na_2CO_3. [62],[68]

The second step was the addition of fresh distilled $BF_3{\cdot}Et_2O$ and TEA to the flask containing **Y** to achieve the coordination of -BF_2 to 2N of pyrroles.

These two mentioned steps were limiting in yields. A different synthetic approach allowed to improve the yields and the ease workup.

The reduction of -NO_2 to -NH_2 group occurred by using Fe powder, H_2O and HCl in MeOH for 2.5 h in reflux condition.

^{1}H-NMR spectrum showed:

. Signal at 6.90 ppm: dd of hydrogen atoms of benzene;

. Singlet at 5.97 ppm of pyrrole hydrogens;

. Signal of amino protons at 3.83 ppm;

. Two singlets of methyl hydrogens at 2.54 ppm and 1.29 ppm.

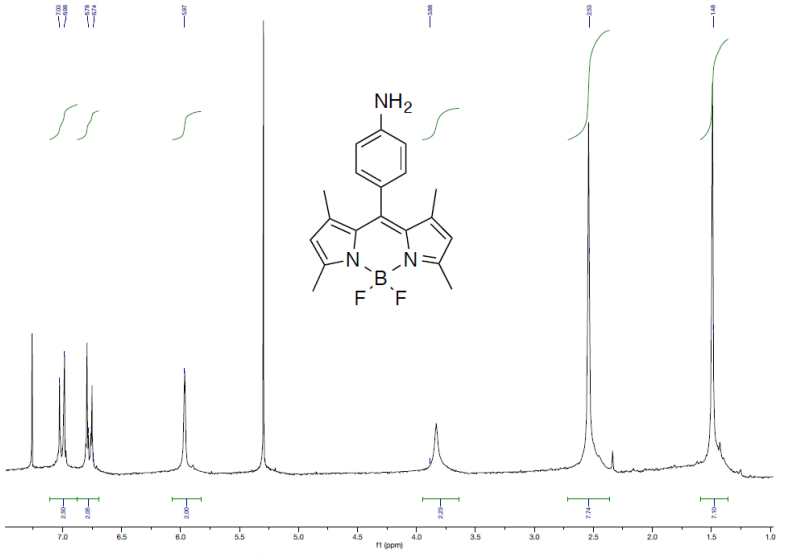

Figure 52. *1H-NMR spectrum of compound* ***9****.*

The second step expected the chemical transformation of -NH_2 in -N_3 by using tert-Butyl nitrite and TMS-N_3 (trimethylsylil azide).

^{1}H-NMR spectrum showed:

. The shift of *chemical shift* of benzene's protons due to the presence of azido group instead of amino group;

. The disappearance of protons of amino signals at 3.90 ppm;

Smaller separation of aromatic signals.

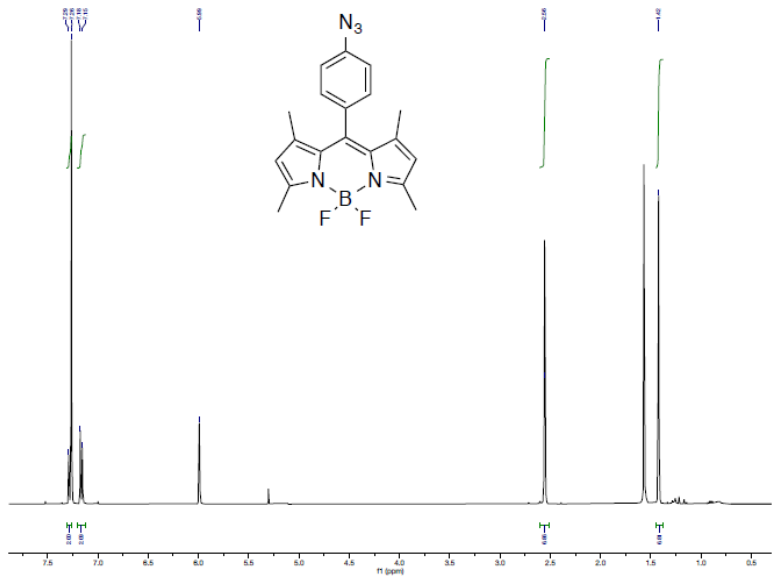

Figure 53*: ^{1}H-NMR spectrum of compound* ***27.***

3.3.1 STRATEGY 1 TO BIND BODIPY AND AMINO ACIDS

As showed in **Scheme 24** the first synthetic strategy to bind an azido-BODIPY to an amino acid consisted of

. synthesize as linker 4-aminobenzaldehyde;

. glycine with BOC protecting group as amino acid.

This synthesized molecule was reacted with methyl groups of BODIPY Core through a Knövenagel reaction.

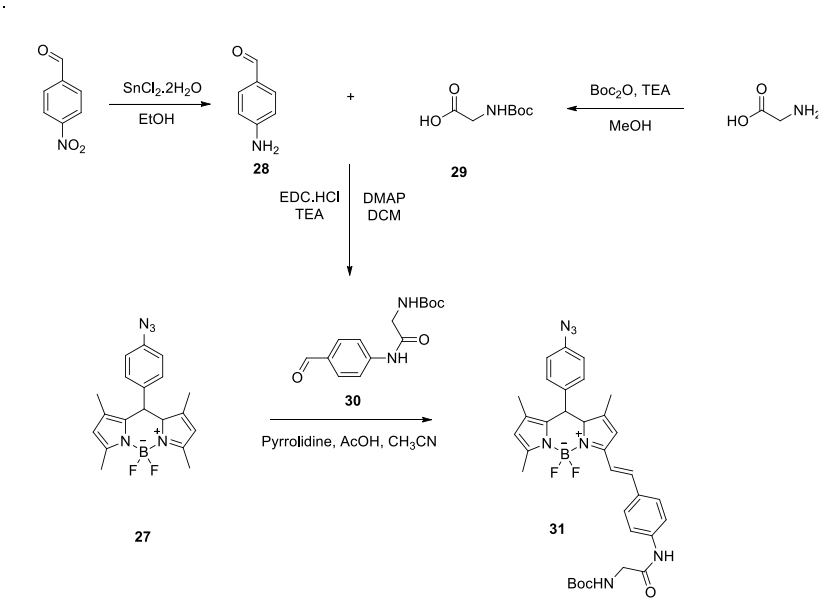

Scheme 24. *Synthetic Pattern to obtain compound* ***31***

The coupling reaction between **28** and **29** expoiting as coupling reagents: EDC·HCl, TEA and DMAP bases in DCM afforded **30**.[69] A problem was the poor solubility of p-aminobenzaldehyde **28** in solvents such as DCM, EtOH, MeOH, Et_2O, H_2O at room temperature. This was the limiting factor in yield (18%). During the reaction, the solution changed from amber to opaque orange. The purification of the product required two columns to remove the starting material.

^{1}HNMR spectrum showed:

. a shift of benzene signals due to the action of the amide group instead of amine group;

. the disappearance of signals due to amine protons and the appearance of a signal due to the amide proton at 5.38ppm;

. the disappearance of mobile acid proton;

. the appearance of the -CH_2 signal (d) from glycine at 3.96ppm.

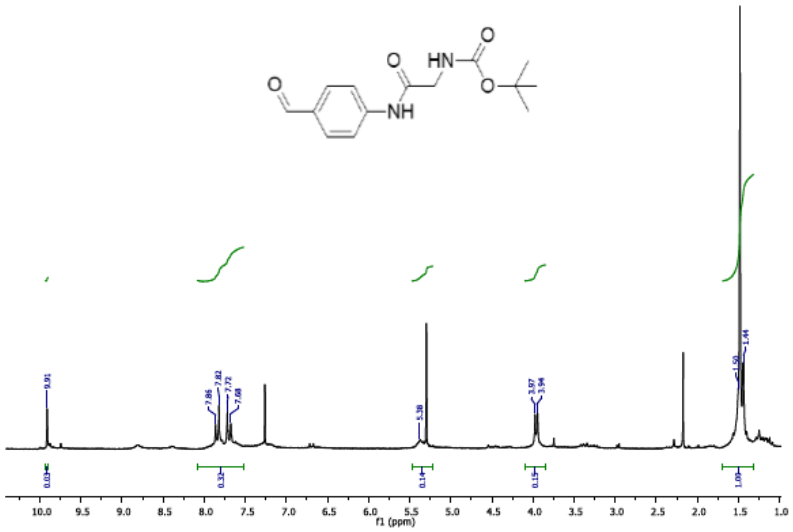

Figure 54. *^{1}H-NMR spectrum of compound **30**.*

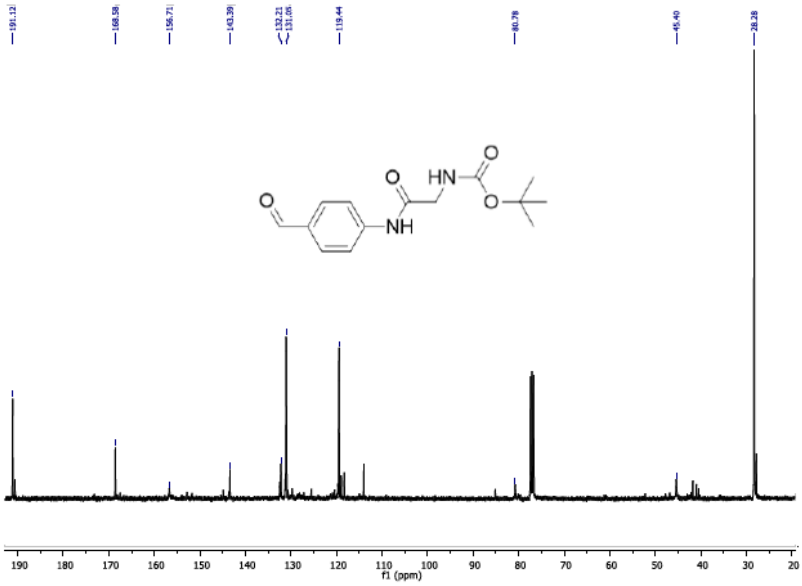

Figure 55*: ^{13}C-NMR spectrum of compound **30***

A small amount of product after the coupling, implicated to perform the Knövenagel Condensation to obtain the monoadduct, using only 2 aldehyde equivalents. The reaction was carried out in inert atmosphere (N_2), in the presence of a secondary amine, pyrrolidine, and AcOH in CH_3CN at reflux (80°C). By lengthening the conjugation of BODIPY Core, the color of the product should change. After 2h the reaction was concluded, but the desired product was not achieved. A possible cause could be due to the poor stability of the -Boc group in these conditions (base + acid at 80°C). This hydrolysis allows to have a free amino group which hinders the reaction.

3.3.2 STRATEGY 2 TO BIND BODIPY AND AMINO ACIDS

.

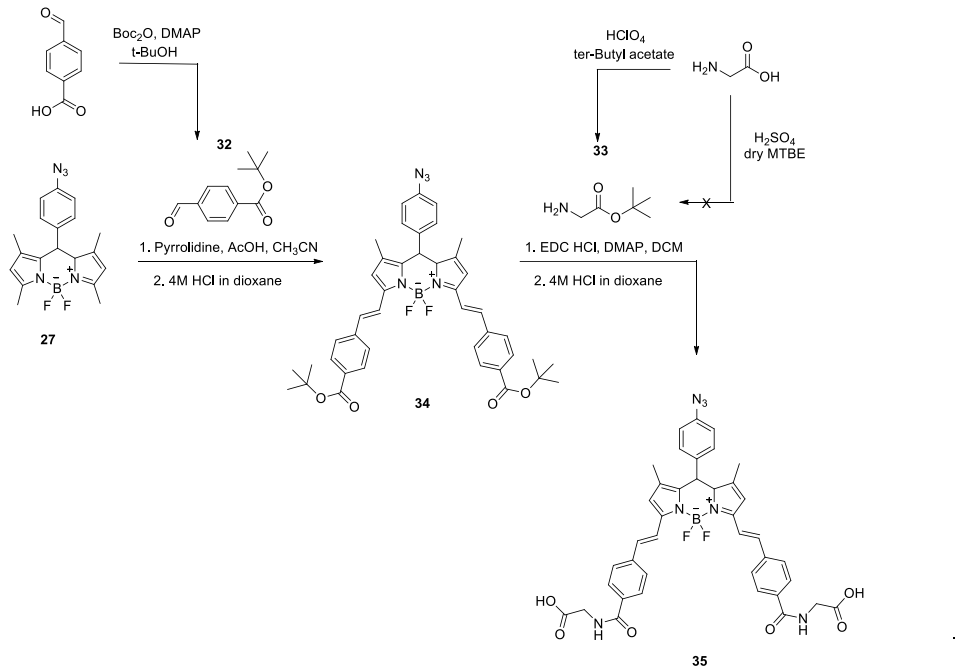

Scheme 25. *Synthetic pattern to obtain fluorescent dye* ***35***

The 2nd strategy consisted in a coupling reaction exploiting a disubstituted BODIPY and 4-formyl benzoic acid as linker (**Scheme 25**). From previously experiments Knövenagel Condensation carried out directly with deprotected aldehyde causes a difficult purification process, reason why the used strategy involved a first protection of carboxyl groups, the coupling with BODIPY, a deprotection of carboxyl groups to proceed with a second coupling with protected amino acid.[70]

Knövenagel Condensation was focus on obtain the substituted adduct by using 5 equivalents of compound **32** . After 10' a strong change in color mixture occurred.

^{1}H-NMR showed:

. the disappearance of aldehydic proton signal;
. the disappearance of the BODIPY methyl proton signal;
. the appearance of the two protons of double bond at 7.80 and 7.26ppm;
. the appearance of the t-butyl signal at 1.61ppm;
. the symmetry of signals.

^{1}H-NMR spectrum of compound **34** was shown in **Figure 56**:

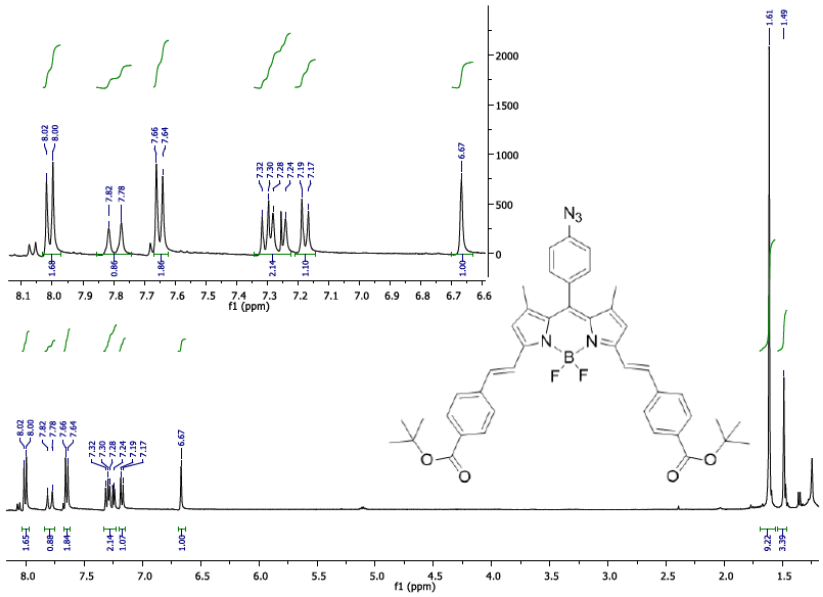

***Figure 56**. [1]H-NMR spectrum of compound **34**.*

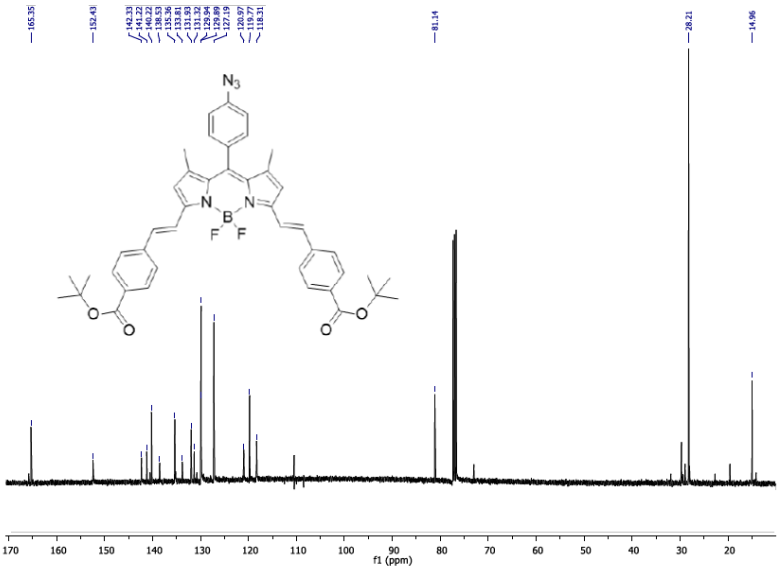

***Figure 57.** [13]C-NMR spectrum of compound **34**.*

The symmetry of the signals confirmed that the product was the bi-adduct.

This reaction was carried out for 3 times varying some parameters such as reaction time, aldehyde equivalents, amount of solvent and the glassware used. The results were presented in **Tab 3** below:

Eq. of aldehydes	BODIPY concentration In CH_3CN	Eq. of Acid and Base	Reaction time	Glassware	Yield
5	0.21	6	1h	Flask	27
10	0.21	6	50’	Flask	/
5	0.41	6	30’	Pyrex vial	82

Tab 3

Deprotection of carboxyl group from t-butyl occurred by using 4M HCl in dioxane. This product showed low solubility in DCM and MeOH, due to their two carboxyl groups.

^{1}H-NMR was presented below:

. the disappearance of t-butyl signal;

. the appearance of acidic protons signal at 13ppm.

. a shift of aromatic signals to higher ppm.

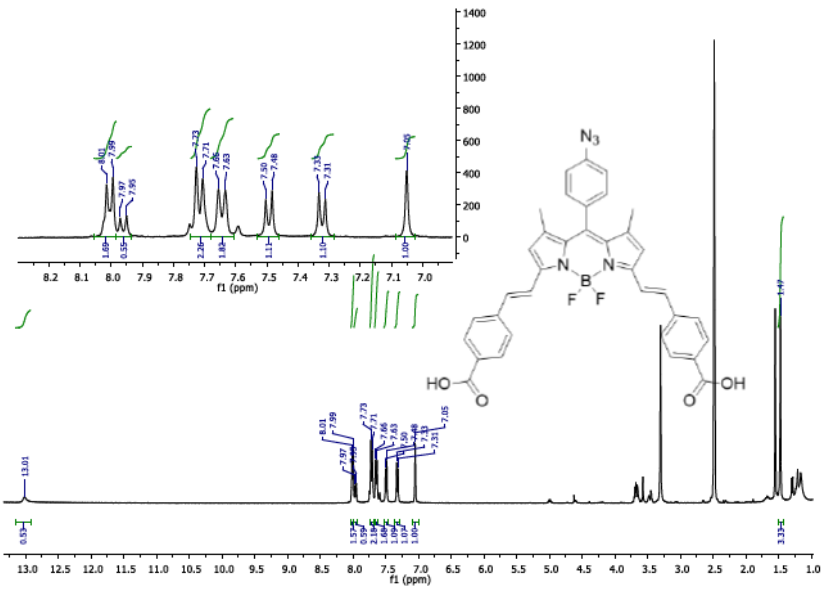

***Figure 58**: ^{1}H-NMR spectrum of compound **39**.*

Before the *coupling,* the carboxyl group of glycine was protected by using t-Butyl group. A first approach to obtain the product consisted in a reaction with H_2SO_4 in MTBE,[71] but the product was not achieved. A second strategy involved the use of HClO4 (70%) in tert-butyl acetate. The yield of reaction was 10%, due to the high number of extractions, the glycine distributed in water phase, numerous extractions with saturated NaCl aqueous solution and organic solvents were required.[72]

Coupling reaction occurred to synthesize two BODIPY adducts:

. the first molecule derived from *mono-deprotection* of compound **34** before the coupling with **33** (lack of symmetry in ^{1}H-NMR spectrum).;

. the second product **35** derived from a complete deprotection of compound **34** and a consequently coupling with **33** (symmetry in ^{1}H-NMR spectrum).

^{1}H-NMR of fraction S showed:

- The disappearance of the signals of acidic proton at 13 ppm;

- The shift of sp^2 no aromatic proton signals;

- The appearance of amide proton signal (t at 6.73 ppm);

- Signal appearance of 2 protons of glycine at 4.16ppm;

- The appearance of the t-butyl signal at 1.51ppm.

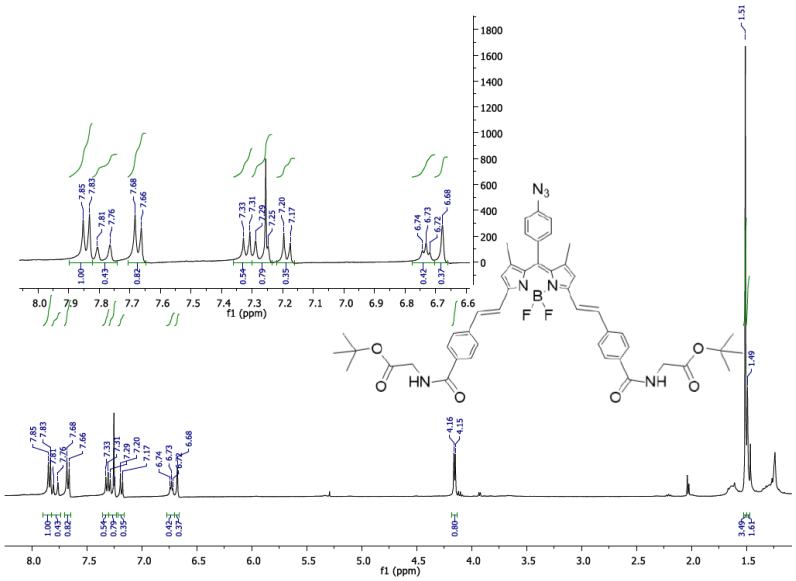

Figure 59. *^{1}H-NMR spectrum of compound* ***protected 35.***

The deprotection of the two t-butyl groups was performed with the same strategy previously mentioned for product **34**.(4M solution of dioxane HCl).

Of this compound UV-Vis absorption and fluorescence measurements were made (by excitation of the sample at 600nm) at different concentrations using MeOH as solvent. Starting from a 10^{-6}M solution and gradually replaced 150µL of starting solution with 150µL of MeOH.

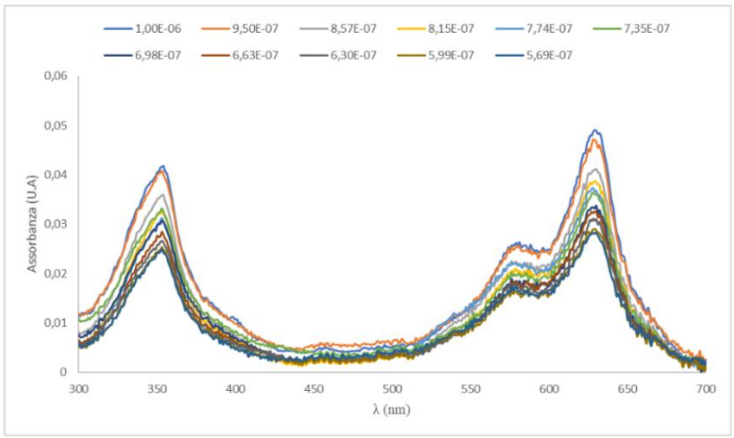

Figure 60. *Uv-Vis Absorbum spectrum of compound 30 at different concentrations (M) in MeOH (λAss.Max= 629nm).*

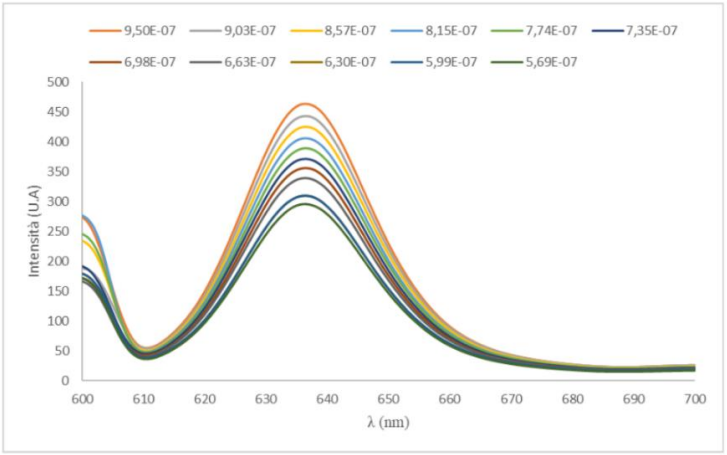

Figure 61. *Fluorescente mission spectrum of compound 31 at different concentrations (M) in MeOH, excited wavelenght 600nm (λEmis.Max= 636nm).*

In addition, from the measurements of UV-Vis, the molar extinction coefficient (ε) was dated back to the wavelength that had maximum absorption, 629nm.

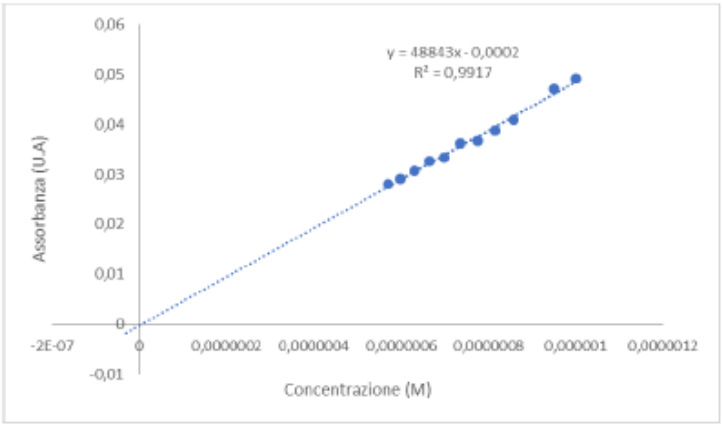

Figure 62*. Absorbance graph (at 629nm)-Product concentration 31 in MeOH for calculation of ε (*ε_{629}*= 48843* $M^{-1}cm^{-1}$*).*

3.3.3 STRATEGY 3 TO BIND BODIPY AND AMINO ACIDS

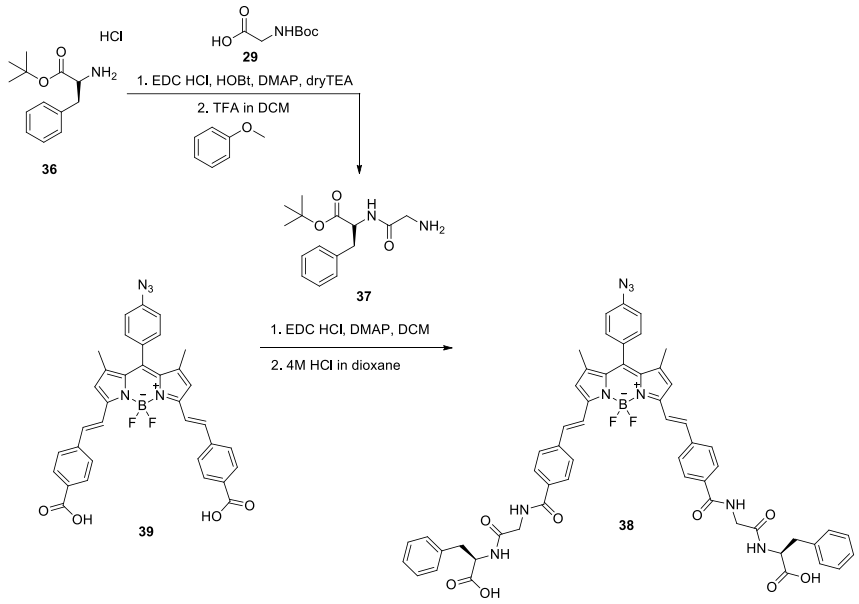

***Scheme 26**: Synthetic pattern for fluorescent probe **38**.*

Following the previously mentioned synthetic path, glycyl-dipeptide L-phenylalanine (Gly-L-Phe) was synthesized. **Scheme 26**. Design and synthesis of the dipeptide with a free amino group on glycine side was the first step of the project, then the coupling with **36**. Glycine-Boc (**36**) was reacted with L-phenylalanine-t-butyl through a coupling reaction using EDC HCl, DMAP, Tea and HOBt (anti-racemizing)[73] in dry DCM.[74]

^{1}H-NMR spectrum showed:

. the disappearance of amide acid proton signals at 6.48 and 5.06ppm;

. the appearance of a d to 6.48ppm due to amide proton of Phe;

. the appearance of a dd at 4.75ppm due to the proton in α of Phe;

. the appearance of 2 dd around 3.70 ppm due to protons in α of Gly.

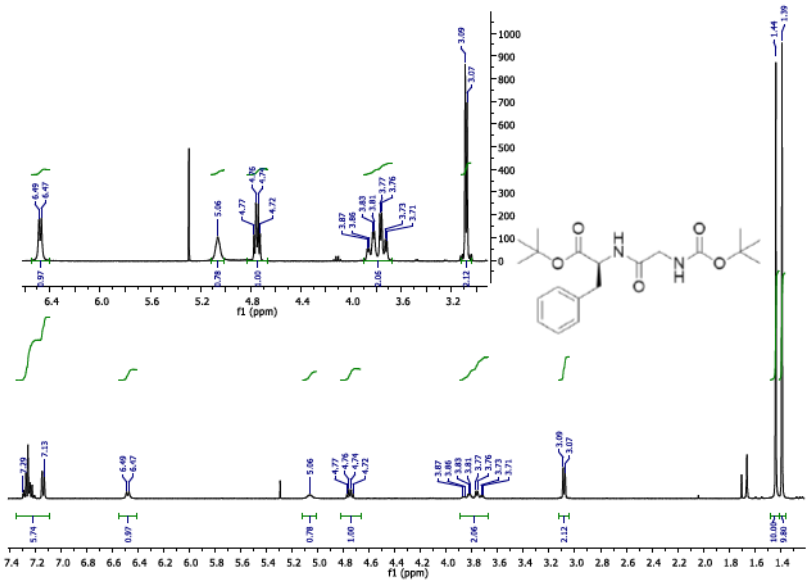

***Figure 63**: [1]H-NMR spectrum of product **37 protected**.*

TFA 20% (w/w) solution was used to remove -Boc from a 0.1M solution of **36** in DCM. 2 eq of anisole[75] as *Scavenger*, were added to reaction mixture, to avoid that *tert*-butyl cation reacted with nucleophiles in the chemical environment. [76],[77]

[1]H-NMR spectrum showed:

. the disappearance of the -Boc signal;

. the disappearance of the amide proton signal from Gly;

. the shift of the amide proton of Phe from 6.48 to 7.56 ppm.

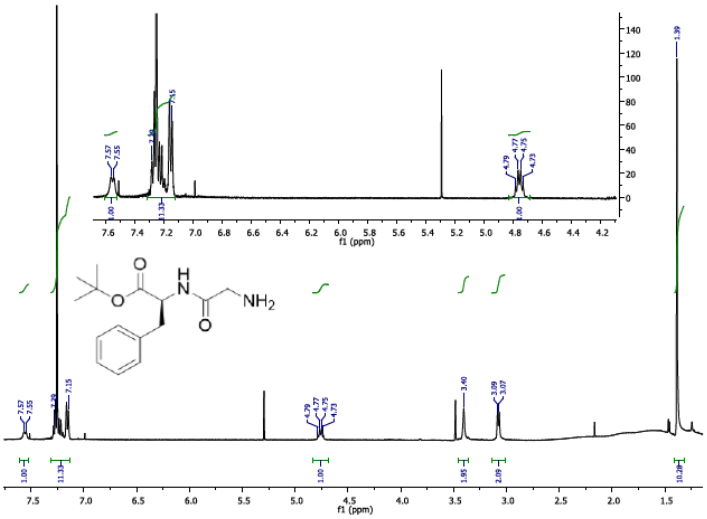

***Figure 64**. H-NMR spectrum of compound **37**.*

Finally, the coupling reaction of compounds **39** and dipeptide **37** were performed adopting the conditions used previously.

. Compound **39** was activated after the addition of EDC HCl and DMAP at room temperature for 1h;

. compound **37** was added in two moments, spaced out 24h from each other; during the second addition 3eq of DMAP and 4eq of EDC HCl were introduced into the flask.

^{1}H-NMR revealed:

- the disappearance of the acid proton signal at 13.0 ppm;

- the change of the *chemical shift* of aromatic signals;

- the change of the positions of the 2 protons in α of the Gly, from 3.40 to ≈ 4.00ppm;

- the shift of the amide proton of Phe from 7.56 to 7.08 ppm.

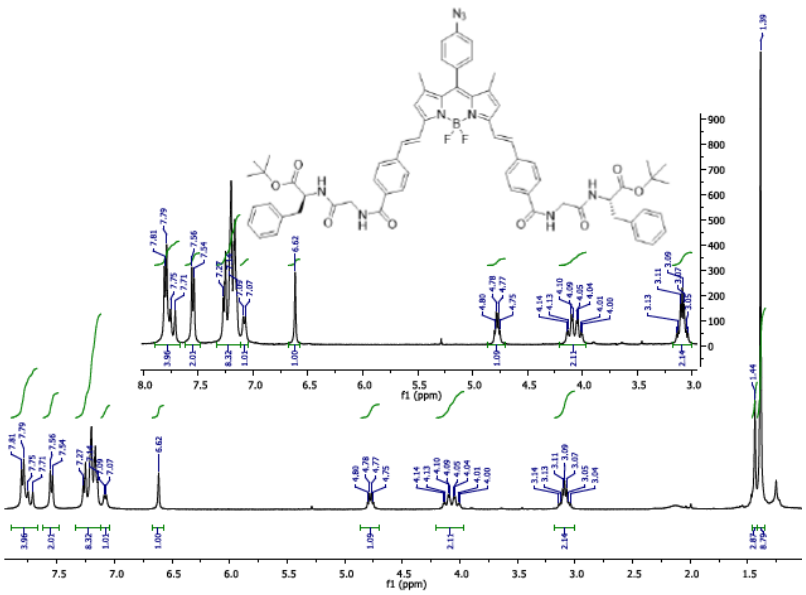

***Figure 65**: ^{1}H-NMR spectrum of compound **38**.*

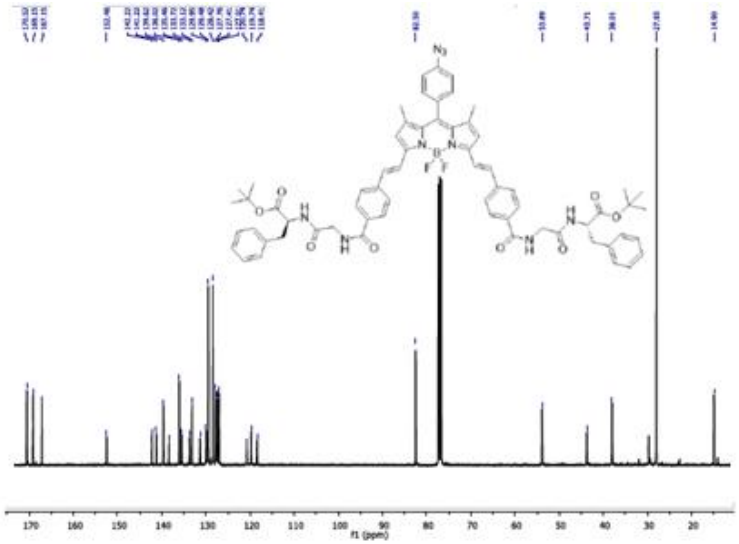

Figure 66. *^{13}C-NMR of product **38**.*

Uv-Vis absorption and fluorescence measurements were carried out for this compound (exciting the sample at 600nm) at different concentration using MeOH as solvent.

The starting 10^{-6}M solution was gradually changed. 100µL of starting solution were gradually replaced with 100µL of MeOH.

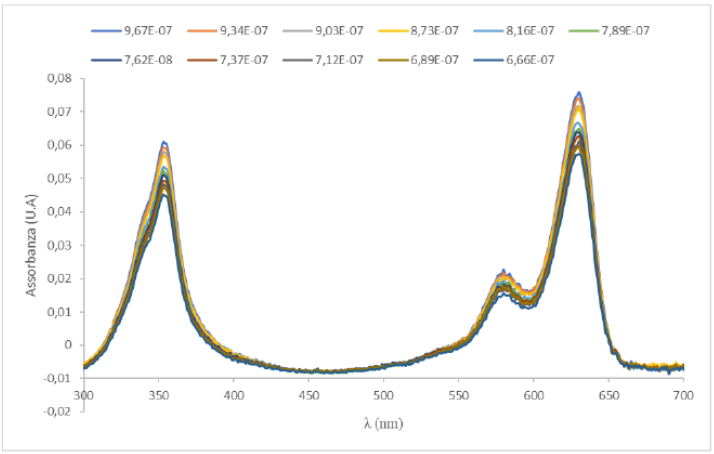

Figure 67. *UV-Vis absorption graph of product **38** at different concentrations (M) in MeOH ($\lambda_{Ass.Max}$ = 630nm)*

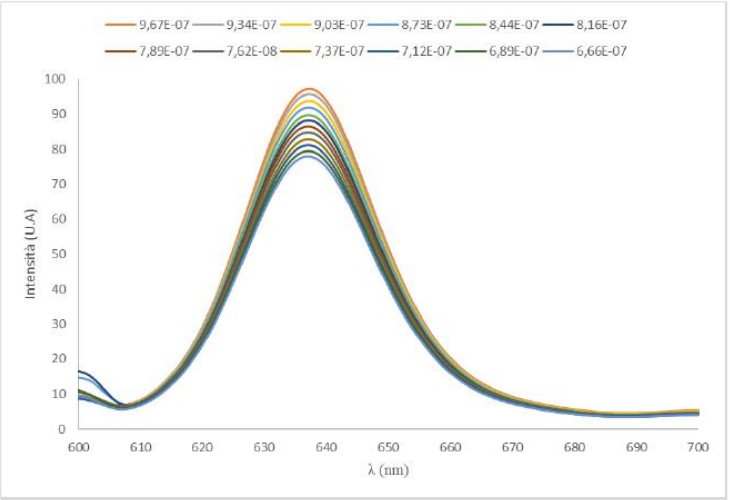

Figure 68. *Fluorescence emission graph of product 38 at different concentrations (M) in MeOH, exciting at 600nm ($\lambda_{Emis.Max}$ = 637nm)*

Furthermore, from the measures of UV-Vis ass, the molar extinction coefficient (ε) was extracted at the maximum absorption wavelength, 630nm.

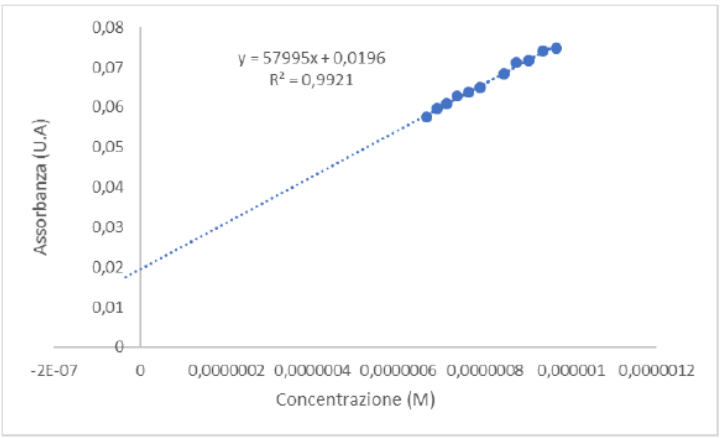

Figure 69. *Absorption graph (at 630nm)-Concentration of product 34 in MeOH to calculate ε (ε_{630}= 57995 $M^{-1}cm^{-1}$)*

Performed a synthesis to obtain a BODIPY-core conjugated with an amino acid or a peptide, was the foundation to the next goal to connect BODIPY dye with a more complex peptide, such as RGD sequence.

3.3.4 SYNTHESIS PLAN OF RGD SEQUENCE

To achieve the final RGD sequence, the synthetic *pattern* involves the realization of two dipeptides, which were reacted in a conclusive coupling.[78]

SYNTHESIS OF DIPEPTIDE ONE

The *first* step, as shown in Chart 11, was the protection of Serine with tert-Butyl acetate and perchloride acid in 6h at room temperature.[79]

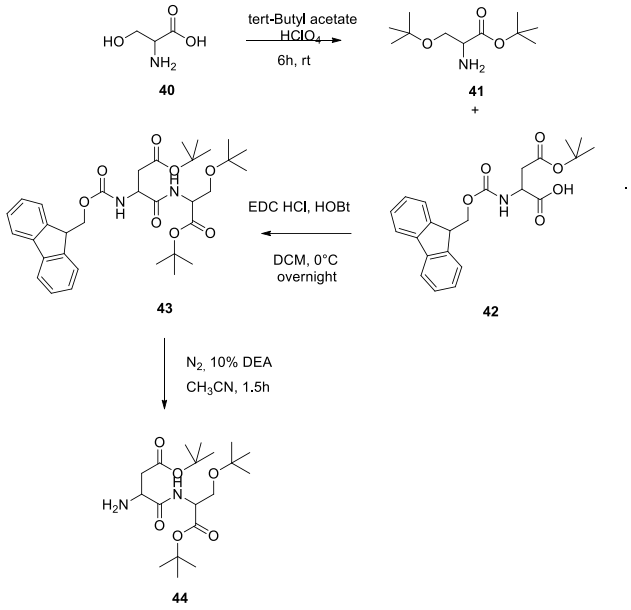

Scheme 27. *Synthetic pattern to synthesize Asp-Ser dipeptide.*

As shown in ^{1}H-NMR spectrum we observed:

. The signals due to protecting group CH_3;

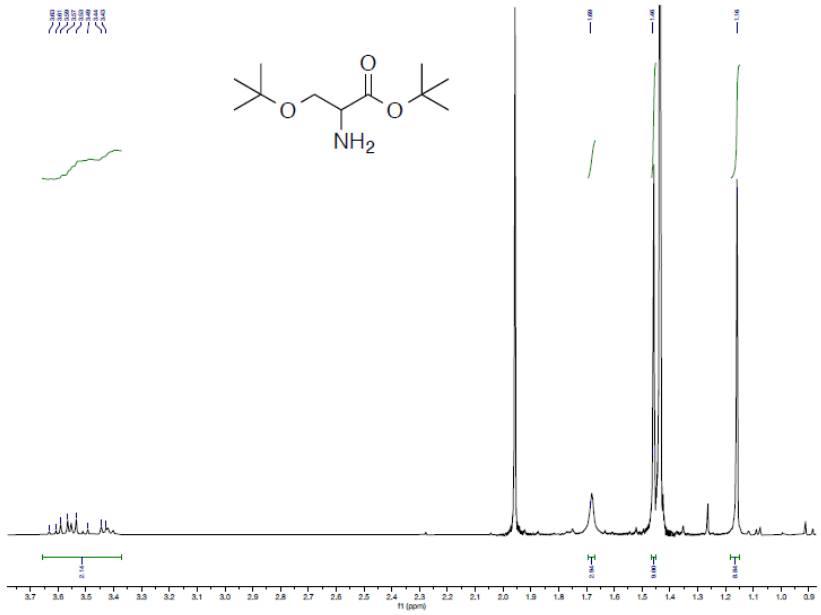

Figure 70. *^{1}H-NMR spectrum of compound **41**.*

In the 2nd step of coupling the protected Serine (compound **41**) was reacted with Fmoc-Asp(OtBu)-OH (compound **42**) in dichloromethane, by adding EDC.HCl and HOBt at 0°C.

^{1}H-NMR spectrum of compound **43** showed:

. a signal connected to aromatic hydrogens of Fmoc;

. an additional signal due to protecting group of aspartic acid;

. the disappearance of signals connected to amino protons of serine.

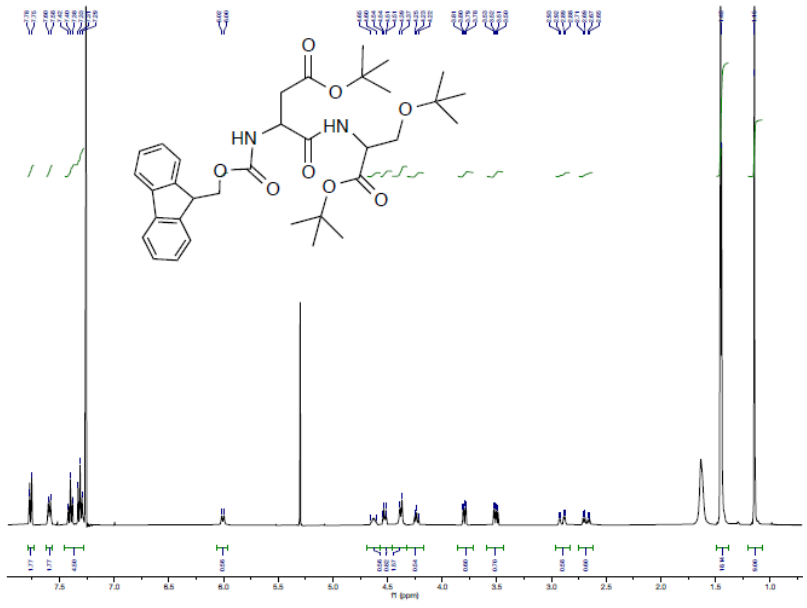

Figure 71. *^{1}H-NMR spectrum of compound **43**.*

The removal of protecting group (Fmoc) of aspartic acid with 10% solution of DEA in CH_3CN (N_2 atmosphere, 1.5 h).

^{1}H -NMR of compound **44** revealed:

. signals of aromatic protons of Fmoc.

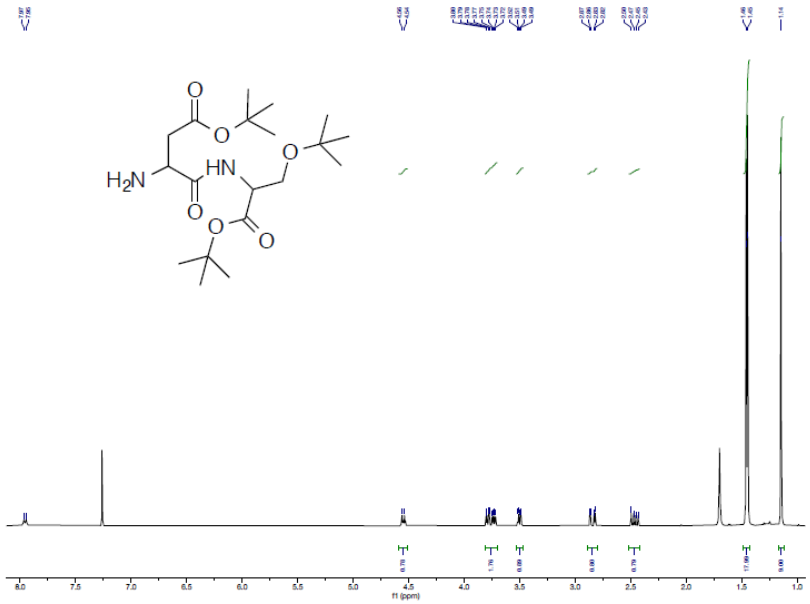

Figure 72. *^{1}H-NMR spectrum of compound **44**.*

SYNTHESIS OF DIPEPTYDE TWO

The protection of Glycine occurred both by using tert-butyloxycarbonyl protecting group to protect amino group and a benzyl group to protect carboxyl group,[80] as shown in **Scheme 28**.

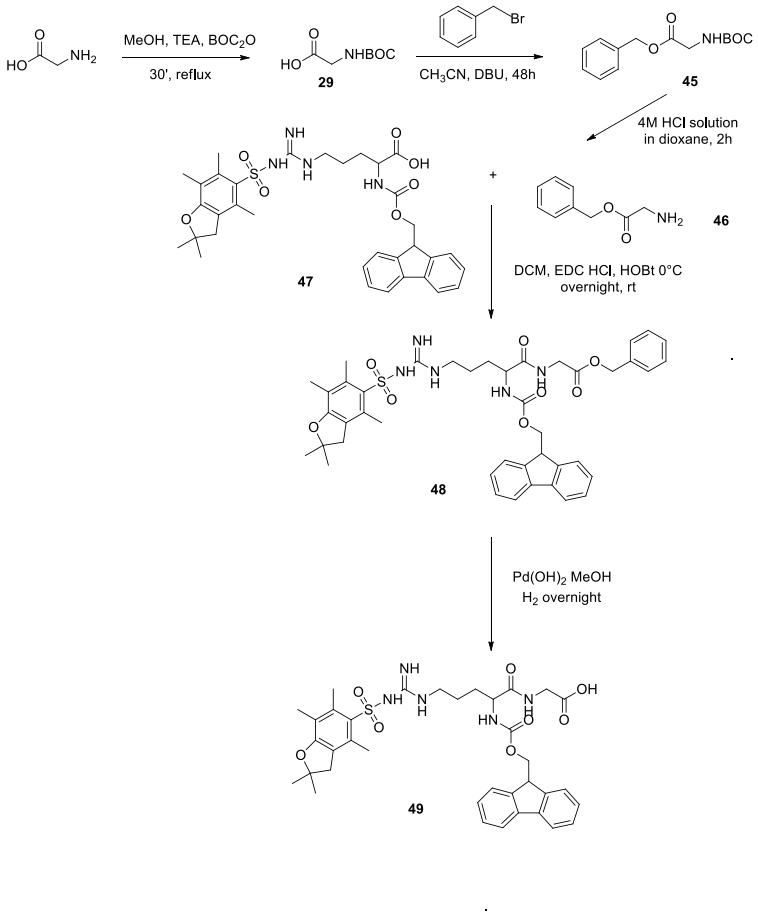

Scheme 28: *Synthetic pattern to synthesize Arg-Gly dipeptide*.

^{1}H-NMR showed:

. CH_3 singlet of tert-butoxycarbonyl in the *first* synthetic step;

. signals due to aromatic hydrogens of benzyl group in the *second* step.

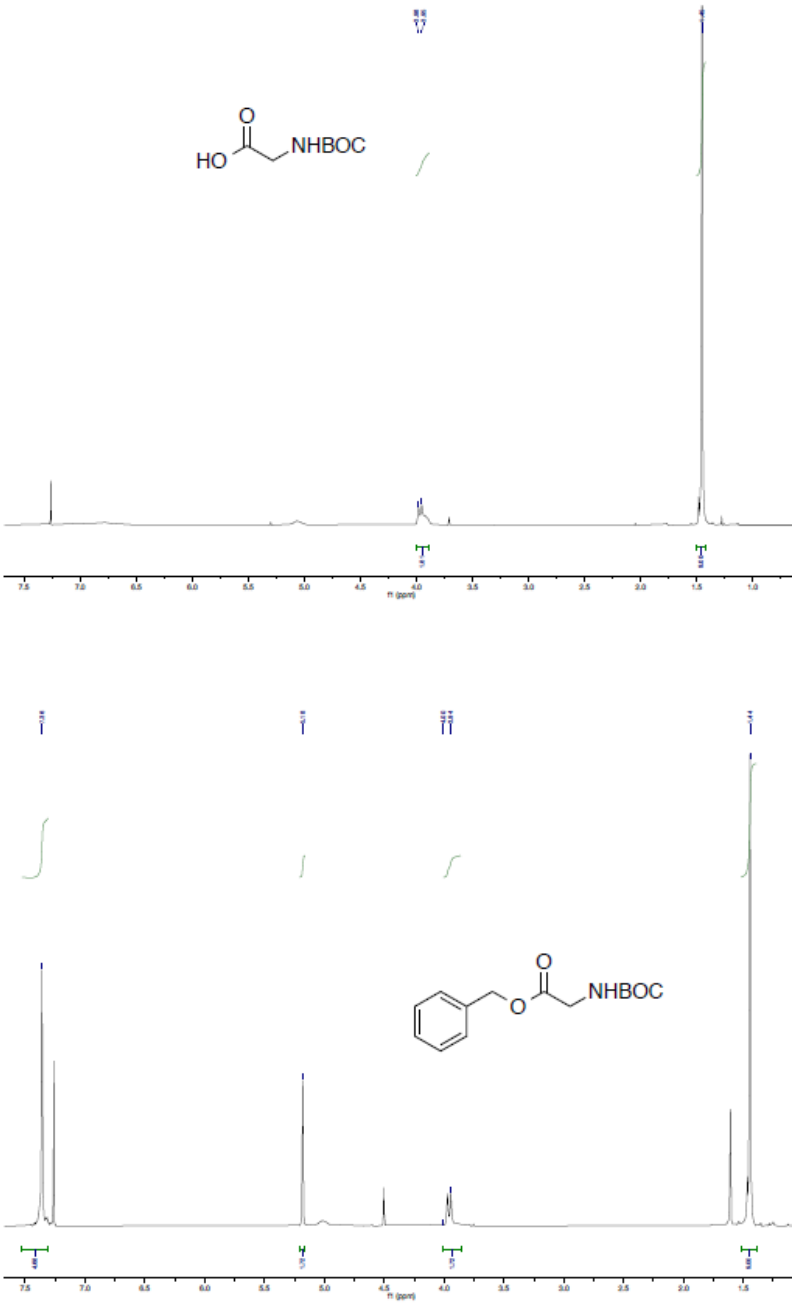

Figure 73. *[1]H-NMR spectrum of compound **29** and **45***

In third step tert-Butyloxycarbonyl protecting group of **45** was removed by using a solution 4M of HCl in dioxane for 2h.

[1]H-NMR of **47** compound revealed:

. the disappearance of -CH_3 signals concerning tert-butyl.

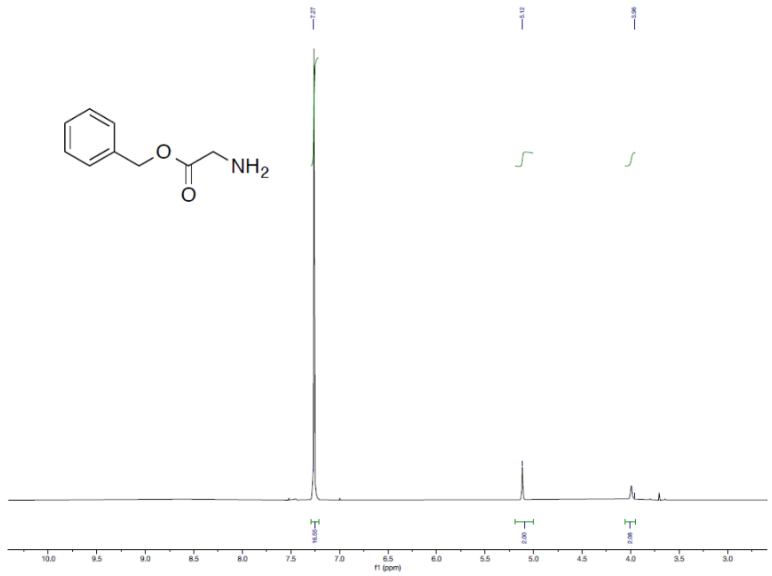

Figure 74. *[1]H-NMR spectrum of compound* ***46***

Compound 46 was reacted with Fmoc-Arg(Pbf)-OH (47) in dichloromethane by adding EDC HCl and HOBt at 0°C.

[1]H-NMR of compound 48 showed:

. signals of aromatic protons regarding Fmoc and benzyl group;

. singlet of -CH2 of benzyl group centered on 5.10 ppm;

. -CH3 singlet of Pbf protecting group;

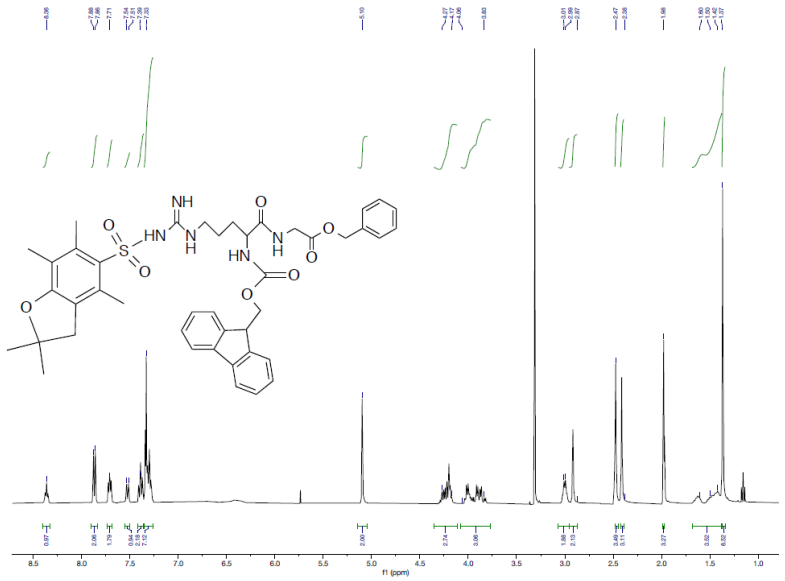

Figure 75. *[1]H-NMR spectrum of compound* ***48***

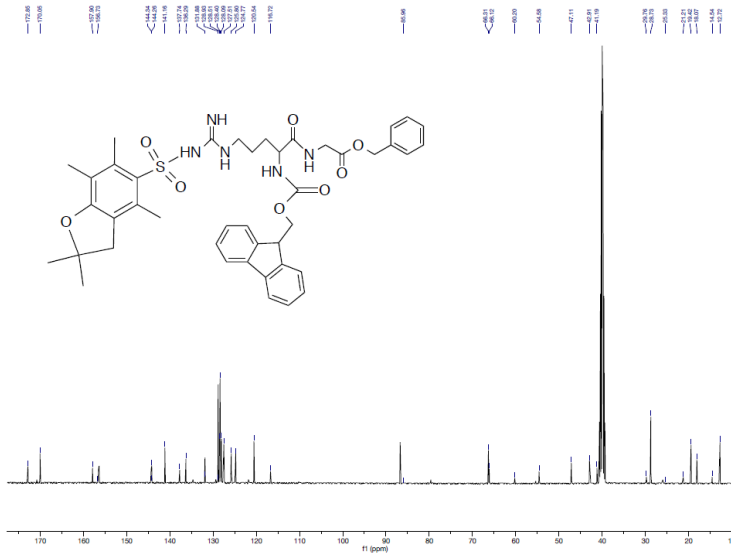

Figure 76. *^{13}C-NMR spectrum of compound* ***48***

$Pd(OH)_2$ and H2 were used in methanol to remove benzyl groups.

^{1}H-NMR of compound **49** was shown below:

. the disappearance of previously mentioned singlet at 5.10 ppm;

. the disappearance of signals concerning aromatic protons.

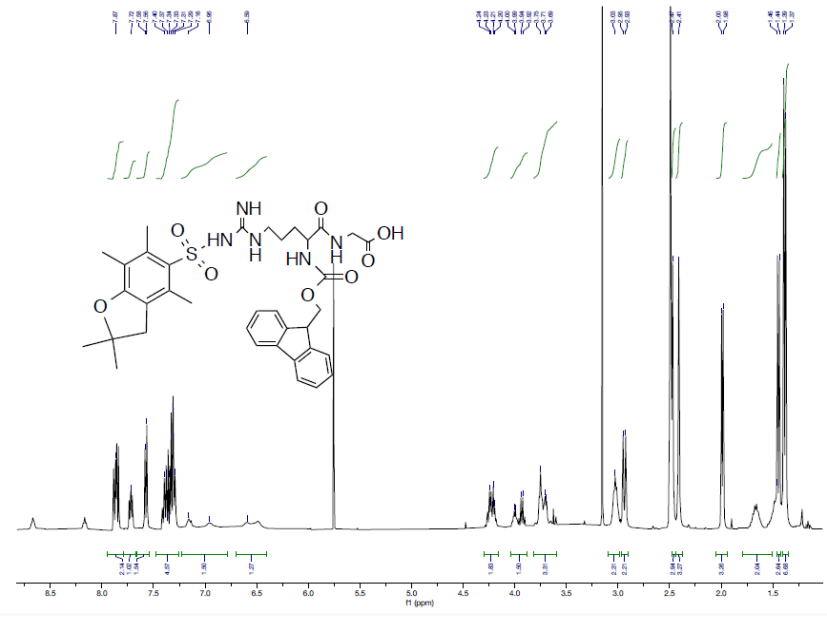

Figure 77. *^{1}H-NMR spectrum of compound* ***49***

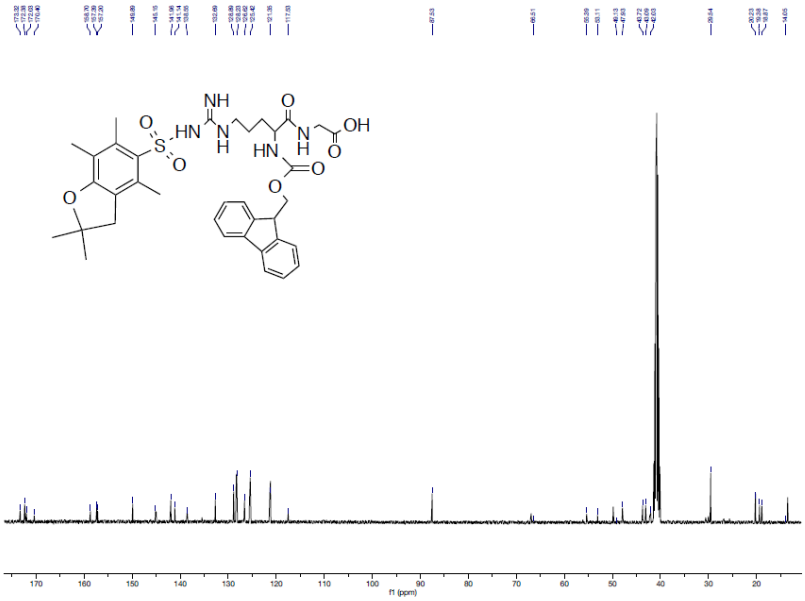

Figure 78. *^{13}C-NMR spectrum of compound* ***49***

SYNTHESIS OF TERAPEPTIDE

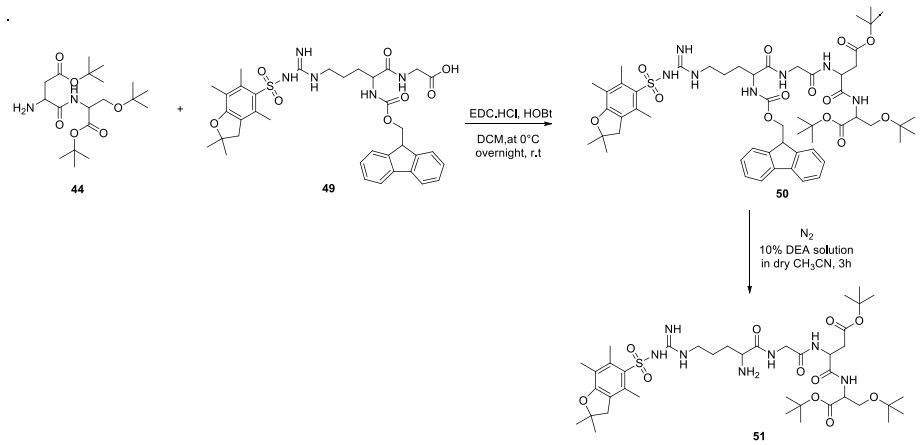

Scheme 29. *Synthetic pattern to obtain RGD tetrapeptide.*

The first step concerned the coupling reaction of dipeptide **44** and dipeptide **45** in dichloromethane, by adding EDC HCl and HOBt at 0°C.

^{1}H-NMR of compound **50** revealed signals connected to all protecting groups:

. tert-butyl around 1.5 ppm;

. methyl groups of Pbf around 2-2.5 ppm;

. aromatic protons of Fmoc around 7-8 ppm.

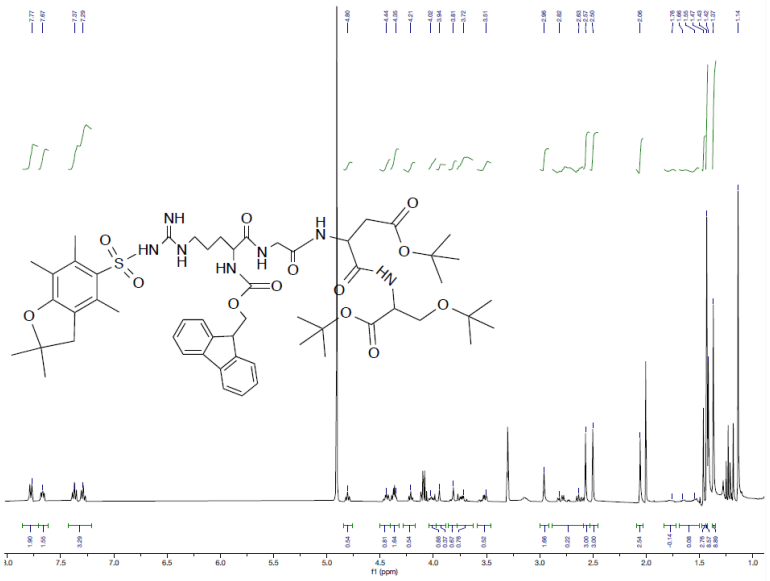

Figure 79. *^{1}H-NMR spectrum of compound* ***50.***

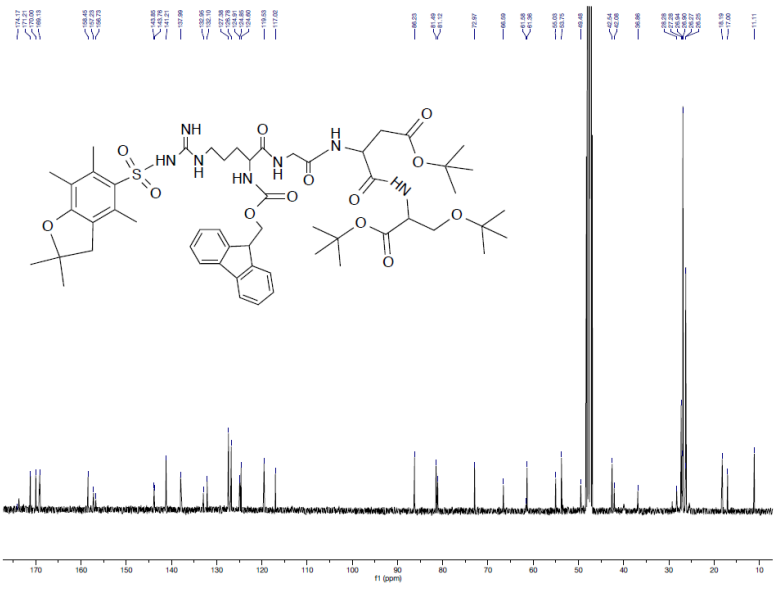

Figure 80. *^{1}H-NMR spectrum of compound* ***50.***

The second step consisted in the removal of amine's Fmoc, protecting group of arginine, achieved by a treatment of a solution 10% DEA in anhydrous CH3CN. This step is fundamental in the consequently coupling to synthesize compound **51**. ^{1}H-NMR revealed that:

. the disappearance of signals concerning aromatic protons of Fmoc group around 8-7 ppm;

. the disappearance of ABX system connected to -CH_2 and -CH of Fmoc group, 4.2 – 4.5 ppm.

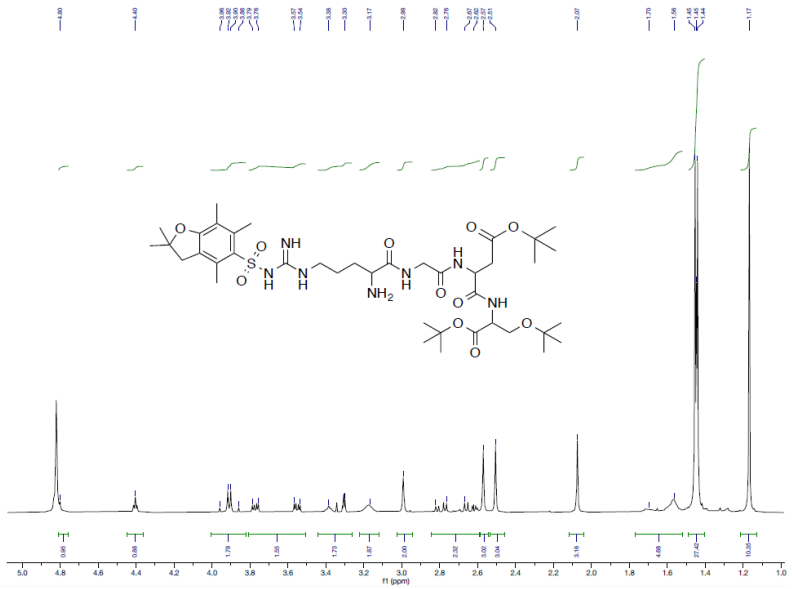

Figure 81. *^{1}H-NMR spectrum of tetrapeptide RGD-Ser **51**.*

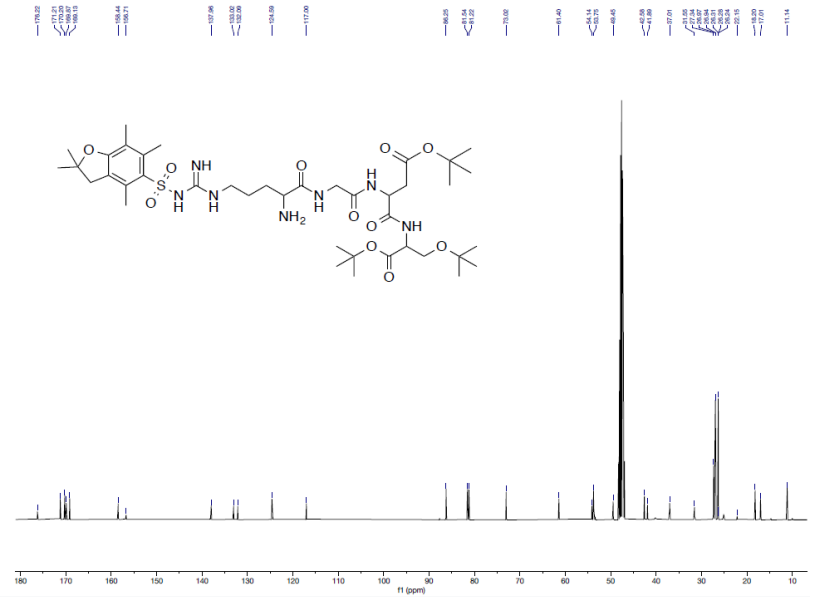

Figure 82. *^{1}H-NMR spectrum of tetrapeptide RGD-Ser **51**.*

FUNCTIONALIZATION OF BODIPY

The first functionalization step was Knövengel Condensation focused on achievement of double adduct, by using 5 eq of 36, pyrrolidine and acetic acid in anhydrous CH3CN. The reaction was carried out at 90°C. After 10' a relevant change of color solution occurred: from red to blue. The reaction was controlled via TLC and stopped after 1h.

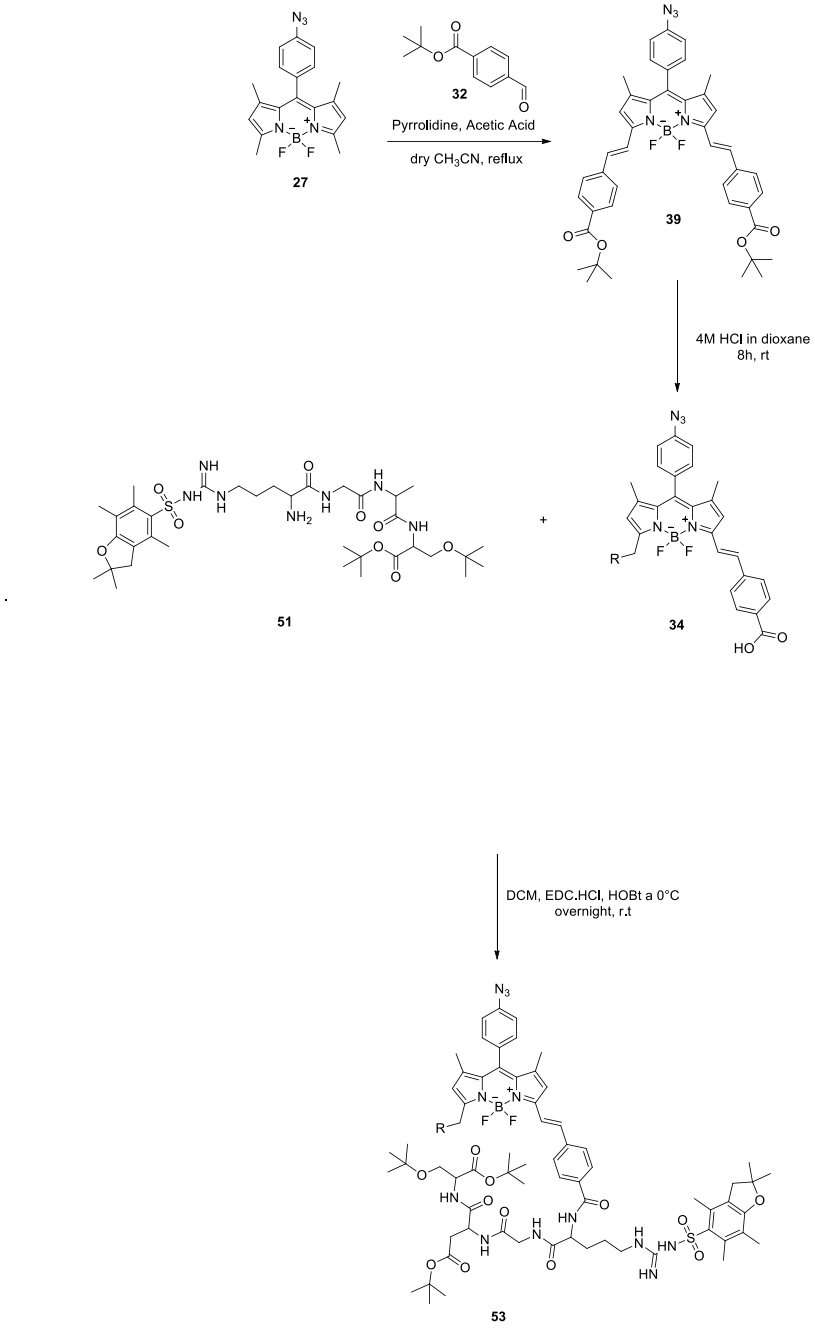

Scheme 30: *Synthetic Pattern for BODIPY functionalization.*

The consecutive step was a coupling reaction concerning tetrapeptide **53** and functionalized Bodipy **34** in dichloromethane with the addition EDC HCl and HOBt at 0°C. ^{1}H-NMR spectrum showed:

. aromatic protons of Bodipy between 7 – 8 ppm;

. the signal of pyrrolic hydrogen at 6.78 ppm;

. the methyl signals of Pbf and tetrabuthyl of Boc.

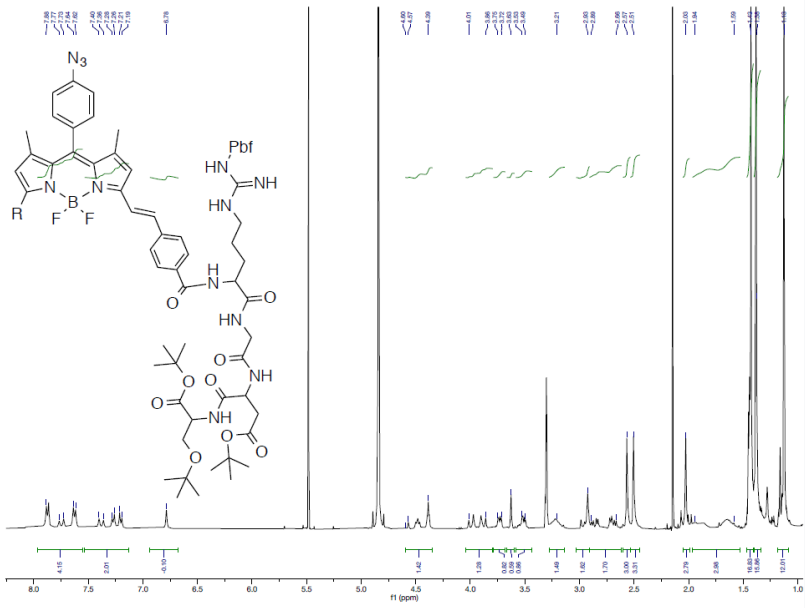

Figure 83. *^{1}H-NMR spectrum of compound **53**.*

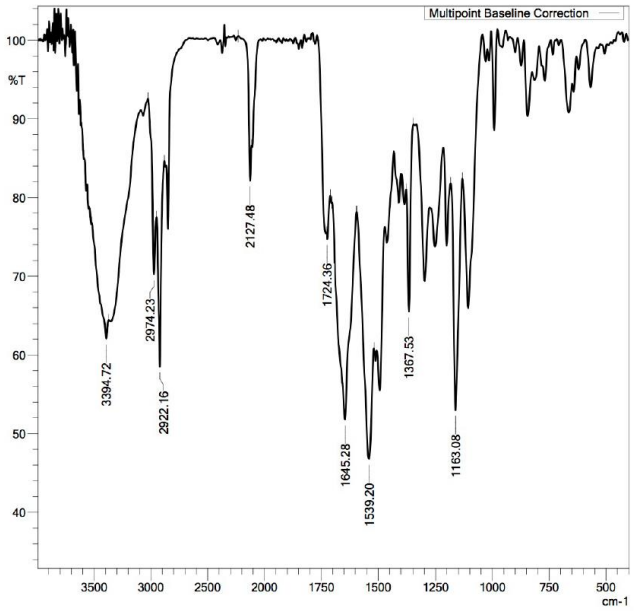

Figure 84. *IR spectrum of compound **53**.*

UV-Vis measures at different concentration in MeOH were presented in the graph below.

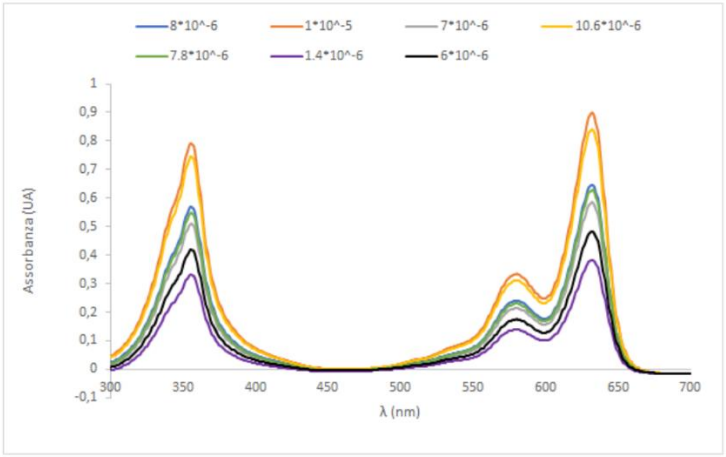

Figure 85. *Uv-Vis absorption graph of compound* ***53*** *at different concentrations (M) in MeOH (λAss.Max= 632nm).*

The removal of all protecting groups, Pbf and Boc, occurred after the reaction of peptide **53** with a solution of TFA/H2O/triisopropylsilane 90/5/5 at a temperature higher of 30°C for 2h, as shown in Chart 15. Compound **54** was purified by C18 reversed-phase chromatography column.

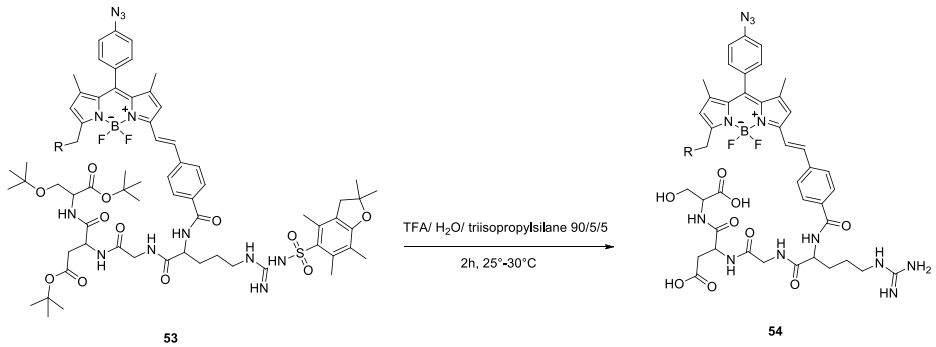

Scheme 31. *Deprotection of compound* ***53*** *to afford compound* ***54***

3.4 CONCLUSION AND PERSPECTIVES

The goal of this project was the design and synthesis of BODIPY dye derivatives for biological applications. Compound 40 was partially characterized thanks to a first purification.

Future outlooks:

. improvement in yields;

. studies of biological and spectrophotometric of BODIPY dyes with different aminoacidic chains;

. exploiting azido groups to include inhibitory or cytotoxic compounds.

3.5 MATERIALS AND METHODS

SYNTHESIS OF BODIPY Azide **27**

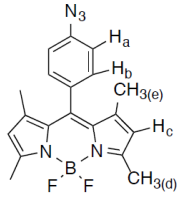

In a 25 mL flask compound **20** (250 mg, 0.73 mmol, 1 eq) was dissolved in dry CH_3CN (10 mL). *t*-buthyl nitrite (113 mg, 0.13 mL, 1.10 mmol, 1.5 eq) and TMS-N_3 (102 mg, 0.12 mL, 0.88 mmol, 1.2 eq) were added to the mixture in an ice-water bath. The reaction was stirred overnight at room temperature. At the end of reaction TLC showed a new spot with R_f: 0.43 (P.Et.:DCM 1:2). The flask was washed with dichloromethane and dried on rotavapor. The crude product was purified on flash chromatography column (2 cm, Pet.E.:DCM 1:4 -> 1:1). Yield: 176mg (66%). Red-pink solid.

^{1}H-NMR ($CDCl_3$, 200Hz) δ (ppm): 7.27 (AA' of a system AA'-BB', 2H, J=7.6Hz, Ha); 7.17 (BB' of a system AA'-BB', 2H, J=8.2Hz, Hb); 5.99 (s, 2H, Hc); 2.56 (s, 6H, Hd); 1.42 (s, 6H, He).

SYNTHESIS OF of p-amino benzaldehyde **28**

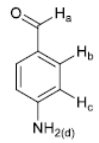

In a 100ml flask p-nitrobenzaldehyde (500mg, 3.3mmol, 1eq) was dissolved in EtOH (45mL). $SnCl_2 \cdot 2H_2O$ (3750mg, 16.6mmol, 5eq) was added and the mixture refluxed for 4h. At the end of the reaction a yellow spot is noted in TLC (2: 1 E.Pet:AcOEt, Rf: 0.52). A saturated solution with $NaHCO_3$ was added up to 7-8 pH of the solution. The organic phase were extracted with EtOAc, washed with water and then with Brine. The organic phase was dried over Na_2SO_4 and the solvent was evaporated. Yield: 325mg (85%). The product is a yellow-orange scaly compound

^{1}H-NMR ($CDCl_3$, 400Hz) δ (ppm): 9.78 (s, 1H, Ha); 7.70 (Part AA 'of an AA system' - BB ', 2H, Hb); 6.70 (Part BB 'of an AA'-BB' system, 2H, Hc); 4.22 (bs, 2H, Hd)

SYNTHESIS OF BOC-Glycine **29**

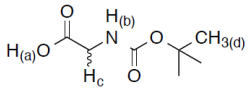

A 50 mL flask equipped with a stirring bar was charged with Glycine (26) (1.5g, 20 mmol), Boc2O (6.5g, 30 mmol, 1.5eq), MeOH (20.6 mL) and TEA (1.65g, 2.28 mL, 16.4 mmol, 0.82eq). The system was heated to reflux for 30'. At the end of reaction, 60 mL of 0.1 M HCl solution were added in an ice-bath, checking pH solution up to 3. The organic layer was extracted with EtOAc, washed with brine and anhydrified on Na2SO4 and dried to achieve a white solid compound. Yield: 1.4g (50%). White solid.

^{1}H-NMR ($CDCl_3$, 200Hz) δ (ppm): 3.95 (dd, 2H, Hc); 1.45 (s, 9H, Hd)

SYNTHESIS OF compound **30**

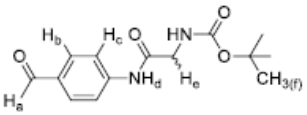

In a 50ml flask p-aminobenzaldehyde (300mg, 2,47mmol, 1eq) and DCM (20mL) were placed. EDC HCl (947mg, 4.94mmol, 2eq), TEA (375mg, 0.515mL, 3.7mmol, 1.5eq), DMAP (30mg, 0.247mmol, 0.1eq) and finally glycine-Boc (435mg, 2.47mmol, 1eq) were added. After 24 hours under stirring the solution gradually became opaque orange. At the end of the reaction. After a TLC check (40: 1 DCM: MeOH, Rf: 0.33) the crude was purified by flash chromatography (column of 5, 50: 1 DCM: MeOH → 5: 1). Yield: 128mg (19%). Pale yellow compound

^{1}H-NMR ($CDCl_3$, 200Hz) δ (ppm): 9.91 (s, 1H, Ha); 7.85 (Part AA 'of an AA system'- BB ', 2H, J = 8.6Hz Hb); 7.70 (Part BB 'of an AA'-BB' system, 2H, J = 8.6Hz, Hc); 5.38 (bs, 1H, Hd); 3.97 (d, 2H, J = 6.0Hz, He); 1.48 (s, 9H, Hf)

^{13}C-NMR (CDCl3, 400Hz) δ (ppm): C10 191.1, C5 168.6, C3 156.7, C6 143.4, C8 132.2, C9 131.0, C7 119.4, C2 80.8, C4 45.4, C1 28.3

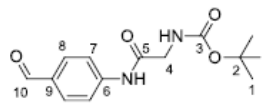

SYNTHESIS OF t-buthyl-4-formylbenzoate **32**

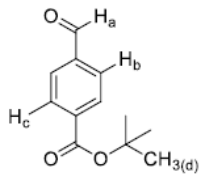

In a 500ml flask, p-formylbenzoic acid (2000mg, 13.3mmol, 1eq) was solubilized in t-BuOH (200mL). Boc_2O (3292mg, 15.06mmol, 1.13eq) and DMAP (1080mg, 8.84mmol, 0.66eq) were added. The reaction was monitored by TLC (1: 1 Pet Et: EtOAc, Rf: 0.88). At the end of reaction, after 16h, the reaction mixture was diluted with DCM (300mL), the organic phase was washed with a saturated solution of Na_2CO_3 (2x100mL) and then with 0.1M of HCl solution (2x120mL). After the addition of Brine (150mL). It was dried on Na_2CO_3 and dried. Yield: 984mg (36%) of a white solid.

^{1}H-NMR ($CDCl_3$, 200Hz) δ (ppm): 10.16 (s, 1H, Ha); 8.20 (Part AA 'of an AA'-BB' system, 2H, J = 7.8Hz, Hb); 7.99 (Part BB 'of an AA'-BB' system, 2H, J = 8.2Hz Hc); 1.68 (s, 9H, Hd)

SYNTHESIS OF compound **34**

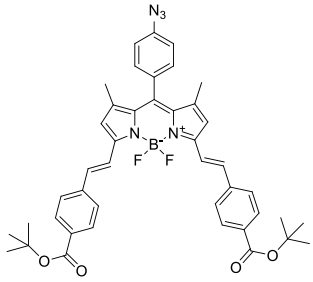

Compound **27** (45mg, 0.12mmol, 1eq) and compound **32** (126mg, 0.61mmol, 5eq) were placed in a pyrex tube. 3 mL of dry CH_3CN were used to solubilize the solid. Pyrrolidine (52mg, 0.060mL, 1.02mmol, 6eq) and the Acetic acid (43mg, 0.041mL, 1.02mmol, 6eq) were added, the mixture refluxed (80-90 ° C). After 10' a change in the color of the solution from red to dark blue was observed. The reaction was monitored by TLC (2: 1 DCM: Pet.Et., Rf: 0.47). After 30 'the reaction was blocked.

The mixture was diluted with 40mL of DCM. The organic phase was washed with H_2O (4x25mL) and Brine (2x30mL), dried on Na_2SO_4 and finally evaporated. The resulting crude is then purified by flash chromatography column (1: 1 DCM: Pet.Et 3: 1) Yield: 75mg (82%). Compound Dark Blue

^{1}H-NMR ($CDCl_3$, 400Hz) δ (ppm): 8.01 (Part AA 'of an AA'-BB' system, 4H, J = 8.0Hz Has); 7.80 (d, 2H, J = 16.4Hz Hb); 7.65 (Part BB 'of an AA'-BB' system, 4H, J = 8.4Hz Hc); 7.31 (Part AA 'of an AA'-BB' system, 2H, J = 8.4Hz, Hd); 7.26 (d, 2H, J = 16.4Hz, He); 7.18 (Part BB 'of an AA'-BB' system, 2H, J = 8.4Hz, Hf); 6.64 (s, 2H, Hg); 1.62 (s, 18H, Hh); 1.50 (s, 6H, Hi)

^{13}C-NMR (CDCl3, 400Hz) δ (ppm): C3 165.4, C10 152.4, C19 142.3, C16 141.2, C7 140.2, C8 138.5, 135.4, 133.81, 131.9, 131.3, 130.0, 129.9, 127.2, C12 121.0, C11 119.8, C9 118.3, C2 81.1, C1 28.2, C13 15.0

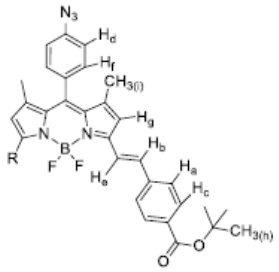

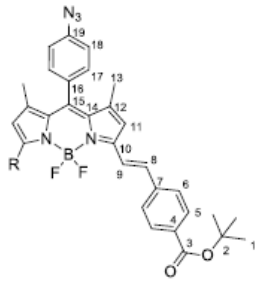

SYNTHESIS OF tert-Butyl-glycine **33**

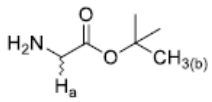

In a 100mL flask, glycine (1000mg, 13.3mmol, 1eq) was suspended in tert-Butyl acetate (50mL). Placed the flask in the ice bath under stirring and drop to drop 70% $HClO_4$ (3034mg, 1.8mL, 20mmol, 1.5eq). At room temperature the reaction proceeded for 40h. The reaction was monitored via TLC (1: 1 MeOH: EtOAc, Rf: 0.45). The reaction mixture was washed with H_2O (125mL) and then with a 1M HCl solution (75mL). The aqueous phase was treated with a 10% (w / w) solution of K_2CO_3, until up to pH 9 (≈250mL)

and then the aqueous phasewere extracted with DCM (300mL). Part of the product remained in the aqueous phase, more extractions were required first with hexane and then with Et_2O. The organic phase was dried over Na_2SO_4. Yield: 180mg (10%) of an oil.

^{1}H-NMR ($CDCl_3$, 200Hz) δ (ppm): 3.31 (s, 2H, Ha); 1.46 (s, 9H, Hb)

SYNTHESIS OF compound **deprotected 34**

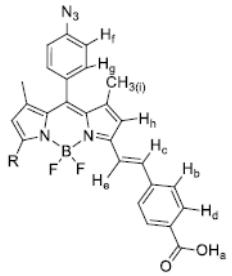

Compound **34** (34mg, 0.046mmol, 1eq) was placed in a Pyrex tube. Then 4M HCl solution in dioxane (0.5mL) was add. The reaction occurred at room temperature for 5.5h and it was monitored via TLC (DCM, Rf: 0). Various aliquots of 4M HCl in Dioxane (for a total of 1.2mL) were added. Once the reaction was finished, the mixture was diluted with DCM (10mL) and dried. Yield: 28mg (Quantitative).

^{1}H-NMR (DMSO, 400Hz) δ (ppm): 13.01 (s, 2H, Ha); 8.00 (Part AA 'of an AA'-BB' system, 4H, J = 8.0Hz, Hb); 7.95 (d, 2H, J = 16.4Hz, Hc); 7.72 (Part BB 'of an AA'-BB' system, 4H, J = 8.0Hz, Hd); 7.64 (d, 2H, J = 16.4Hz, He); 7.49 (Part AA 'of an AA'-BB' system, 2H, J = 8.0Hz, Hf); 7.32 (Part BB 'of system AA'-BB', 2H, J = 8.4Hz, Hg); 7.05 (s, 2H, Hh); 1.48 (s, 6H, Hi).

SYNTHESIS OF protected compound **35**

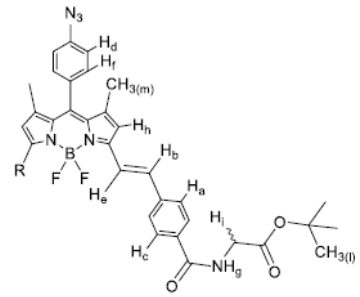

In a 25mL single-neck flask compound **deprotected 34** (24mg, 0.038mmol, 1eq) was dissolve in DCM (6mL). The flask was placed in an ice bath and added DMAP (14mg, 0.114mmol, 3eq) and EDC · HCl (22mg, 0.114mmol, 3eq), then the mixture was stirred at room temperature for 1h. Compound 29 (15mg, 0.114mmol, 3eq) was dissolved in 0.5mL of DCM. After 24h at room temperature additional 6eq of EDC HCl (44mg, 0.228mmol), 3eq of DMAP (14mg, 0.114mmol) and 3eq of compound 29 (15mg, 0.114mmol) were placed in the flask in 0.5mL of DCM. The reaction was monitored via TLC (Rf: 0.21, 2: 1 Pet.Et.:EtOAc). Then the mixture was diluted with DCM (10mL), washed with H_2O (2x10mL) and then with a 5% (w / w) solution of $NaHCO_3$ (20mL).

Re-extractrion of aqueous phase with DCM was required. Then washed with Brine (30mL), dried over Na_2SO_4. The crude was purified by flash chromatography column 15: 1 Pet.Et : EtOAc → EtOAc Yield: 11mg (34%) of a dark blue product

^{1}H-NMR (CDCl3, 400Hz) δ (ppm): 7.84 (Part AA 'of an AA'-BB' system, 4H, J = 8.4Hz, Ha); 7.79 (d, 2H, J = 16.4Hz, Hb); 7.67 (Part BB 'of an AA'-BB' system, 4H, J = 8.4Hz, Hc); 7.32 (Part AA 'of an AA'-BB' system, 2H, J = 8.4Hz, Hd); 7.27 (d, 2H, J = 16.0, He); 7.18 (Part BB 'of an AA'-BB' system, 2H, J = 8.4Hz, Hf); 6.73 (t, 2H, J = 4.8Hz, Hg); 6.68 (s, 2H, Hh); 4.16 (d, 4H, J = 4.8Hz, Hi); 1.51 (s, 18H, H1); 1.49 (s, 6H, Hm)

SYNTHESIS OF compound **35**

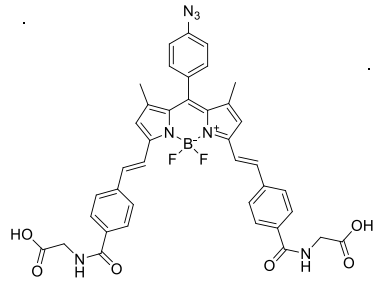

In a 10mL flask compound **protected 35** (11mg, 0.013mmol) was placed. After the addition of 4M HCl solution in dioxane (1.5mL) the mixture was stirred at room temperature for 48h. The reaction was controlled by TLC (Rf: 0, 1: 1 EtOAc:Pet.Et.). At the end of reaction the solvent was evaporated.

SYNTHESIS OF compound **37**

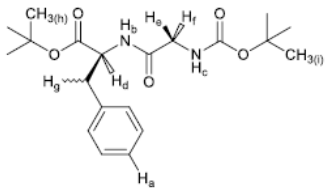

Glycine-Boc (1000mg, 5.71mmol, 1.2eq), Lt-Bu-phenylalanine HCl (1225mg, 4.75mmol, 1eq), EDC HCl (1094mg, 5.71 mmol, 1.2eq), HOBt (772mg, 5.71mmol, 1.2eq) and DMAP (29mg, 0.24mmol, 0.05eq) were placed in a 50 mL flask. With dry DCM (15mL) to solubilize the substrates. At 5 ° C distilled TEA was added. The reaction was monitored via TLC (1.25: 1 EtOAc:Et.Pet, Rf: 0.58. The crude mixture was washed with a saturated solution of NH_4Cl (70mL). The organic phase was extracted, while the aqueous layers were rewashed with DCM (3x50mL). The combined organic phases, were treated with Brine (2x50) and H_2O (70mL). Dried over Na_2SO_4. The product was purified for flash chromatography (500mg of crude, 1.25: 1 EtOAc:Pet.Et, the product was collected. Yield: 493 g

^{1}H-NMR ($CDCl_3$, 400Hz) δ (ppm): 7.29-7.13 (m, 5H, Ha); 6.48 (d, 1H, J = 7.6 Hz, Hb); 5.06 (bs, 1H, Hc); 4.75 (dd, 1H, J = 13.6, 6Hz, Hd); 3.84 (dd, 1H, J = 16.8, 5.6Hz, He); 3.74 (dd, 1H, J = 16.8, 5.6Hz, Hf); 3.08 (d, 2H, J = 6Hz, Hg); 1.44 (s, 9H, Hh); 1.39 (s, 9H, Hi)

SYNTHESIS OF compound **protected 38**

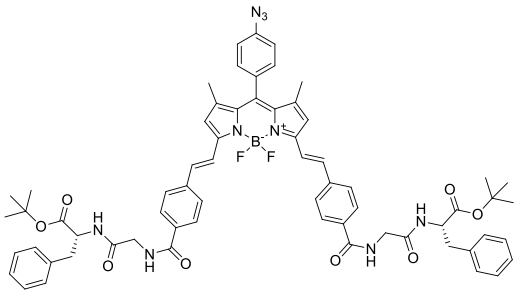

In a 50mL flask, compound **39** (62mg, 0.098mmol, 1eq) was dissolved in DCM (15mL). EDC HCl (75mg, 0.392mmol, 4eq) and DMAP (36mg, 0.294mmol, 3eq) were added. The reaction was stirred at room temperature for 1h. In the meantime, compound **37** (155mg, 0.55mmol, 5.6eq) was dissolved in 6mL of DCM and 3mL of the solution were added to the reaction flask, at room temperature. Other 4eq of EDC HCl, 3eq of DMAP and the remaining solution of compound 33 in DCM, then leave to stir for another 24h. The reaction is monitored by TLC (Rf: 0.29, 2: 1 AcOEt: hexane). The mixture was diluted with DCM (20mL) and washed the organic phase with H_2O (2x25mL), with a 5% (w / w) solution of $NaHCO_3$ (50mL) and with Brine (70mL). The product in solution was dried. The crude was purified by Flash Chromatography (column of 2 cm, 15: 1 hexane: EtOAc → 20: 1 EtOAc: hexane. Yield: 45mg (40%) of a dark blue scaly compound.

^{1}H-NMR (CDCl3, 400Hz) δ (ppm): 7.80 (Part AA 'of an AA'-BB' system, 4H, J = 8.4Hz, Ha); 7.73 (d, 2H, J = 16.4Hz, Hb); 7.55 (Part BB 'of an AA'-BB' system, 4H, J = 8.4Hz, Hc); 7.27-7.14 (m, 14H, Hd); 7.08 (d, 2H, J = 7.6Hz, He); 6.62 (s, 2H, Hf); 4.78 (dd, 2H, J = 13.6, 6.4Hz, Hg); 4.14-4.00 (m, 4H, Hh); 3.14 (m, 4H, Hi); 1.44 (s, 6H, H1); 1.39 (s, 18H, Hm)

^{13}C-NMR (CDCl3, 400Hz) δ (ppm): C3 170.5, C10 169.2, C12 167.2, C19 152.5, C28 142.2, C25 141.2, C16 139.6, C17 138.3, 136.0, C6 135.5, 133.7, 133.1, 131.3, 130.0, 129.5, 128.4, C7 127.8, C8 127.4, C9 127.0, C21 120.7, C20 119.7, C18 118.4, C2 82.5, C4 53.9, C11 43.7, C5 38.0, C1 27.93, C22 14.9

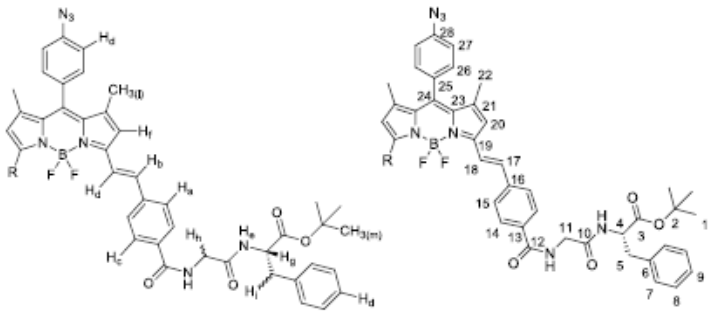

SYNTHESIS OF compound **38**

Compound **protected 38** (40mg, 0.035mmol) was placed in a 25mL flask and 4M HCl solution in Dioxane (5mL) were added. The reaction was monitored via TLC (Rf: 0, 3: 1 AcOEt: E.Pet). The reaction mixture was dried.

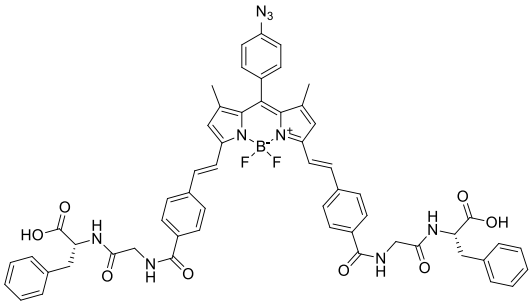

SYNTHESIS OF OtBu-Serine **41**

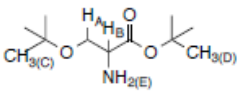

1g (9.5 mmol) of serine and t-buthyl acetate (21 mg, 72 mmol) were placed in a flask equipped with a stirring bar. $HClO_4$ (0.8 mL) were added by using a dropping funnel can. After 6h, 10 mL of HCl (2M) were added and, consequently K_2CO_3 up to pH 9. The reaction mixture was extracted with DCM (60 mL) and the organic layer washed with H_2O (40 mL, 2 times), Brine (40 mL, 2 times). At the end the extracts were combined, dried over anhydrous $MgSO_4$, filtered, and evaporated. Yield: 1.1g (55%). The compound is a colorless oil.

^{1}H-NMR ($CDCl_3$, 200Hz) δ (ppm): 3.57 (m, 2H, HA), 3.43(m, 1H, HB) 1.69 (s, 2H, HE), 1.46 (s, 9H, HD), 1.16 (s, 9H, HC)

SYNTHESIS OF compound **43**

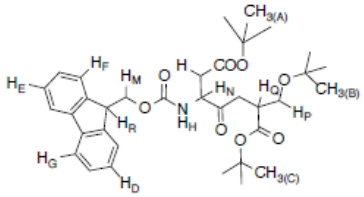

Ser-OtBu (500 mg, 2.3 mmol, 1 eq) and Fmoc-Asp(OtBu)-OH (946 mg, 2.3 mmol, 1 eq) were reacted in a flask with DCM (12 mL) uder stirring at room temperature. At 0°C EDC HCl (490 mg, 2.75 mmol, 1.2eq) was added to the mixture, after 10' HOBt (373 mg, 2.75 mmol, 1.2ew) was placed in the flask. After the

night via TLC a new spot Rf: 0.92 (DCM:EtOAc 3:1) was formed. The mixture was diluted with DCM and washed with H_2O (10 mL x 2), extracted again with fresh DCM. The organic phase was dried over Na2SO4, filtered to obtain an orange-yellow oil. Yield: 840mg (60%)

^{1}H-NMR ($CDCl_3$, 400Hz) δ (ppm): 7.77 (d, 2H, HF); 7.59 (d, 2H, HG); 7.40 (t, 2H, HE); 7.31 (t, 2H, HD); 6.01 (d, 1H, HH); 4.63 (m, part X of a system ABX, 1H, HN); 4.53 (dt, part X of a system ABX, 1H, HR); 4.38 (d, part AB of a system ABX, 2H, HM); 4.23 (t, part X of a system ABX, 1H, HQ); 3.81-3.50 (Part AB of a system ABX, 1H, HP); 2.93-2.65 (part AB of a system ABX, 2H, HL); 1.45 (s, 18H, HA e HC); 1.15 (s, 9H, HB).

SYNTHESIS OF compound **44**

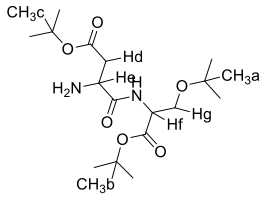

In a 100 mL flask compound **43** (980mg, 1.60mmol, 1eq) was dissolved in 25mL of dry CH_3CN and 2.5mL of DEA. The reaction was carried out under N_2 atmosphere for 1.5h. TLC checking confirmed the end of reaction: a first spot due to fulvene (R_f: 0.92, DCM : EtOAc 50:1) and a second one associated to the product (R_f: 0.71).
After the evaporation of CH_3CN and DEA, a washing with Et_2O occurred. Despite this procedure, ^{1}H-NMR spectrum showed the presence of byproducts. The purification proceeded with a flash chromatography (2 cm column, DCM:EtOAc 100:1 -> EtOAc). Yield: 580mg (93%). The product was an orange-yellow oil.

^{1}H NMR (400 MHz, CDCl3) δ (ppm): 7.96 (d, 1H, HL); 4.55 (dt, part X of a system ABX, 1H, HE); 3.80-3.72 (part AB of a system ABX, 2H, HD); 3.51 (dd, 1H, part X of a system ABX, HF); 2.70 (Part AB of a system ABX, 2H, HG); 1.46 (s, 9H, HC); 1.45 (s, 9H, HB); 1.14 (s, 9H, HA).

SYNTHESIS OF BOC -Gly-OBn **45**

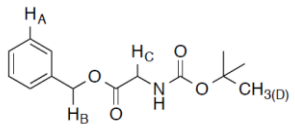

Gly-BOC (1.4g, 8 mmol, 1eq) and CH3CN were placed in a flask, therefore DBU (1.22g, 8 mmol, 1.22 mL, 1.02 g/cm3, 1eq) was added. In an ice-bath benzyl bromide (1.4g, 8 mmol, 1mL, 1.4 g/cm3). After two days at room temperature, CH_3CN was evaporated, the crude product was diluted with DCM (100 mL) e therefore first $KHSO_4$ 1M (2 x 75 mL) and then NaHCO3 were added and the final product extracted and dried over Na_2SO_4. The removal of residual benzyl bromide occurred after the addition of Petroleum Ether to the white crude product and the filtration on Buchner. Yield: 1.19g (50%) The product was a white solid.

^{1}H-NMR (CDCl3, 200Hz) δ (ppm): 7.36 (s, 5H, HA), 5.18 (s, 2H, HB), 3.96 (d, 2H, HC), 1.44 (s, 9H, HD)

SYNTHESIS OF H_2N-Gly-OBn **46**

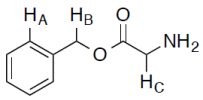

Compound **45** (1.2g, 4.3mmol, 1eq) was dissolved in 8mL of a 4M solution of HCl in dioxane. After 2h under stirring the end of reaction was confirmed by TLC (Rf: 0.91, EtOAc : Pet.E. 1:5). The crude product was dried and after the addition of Et_2O a precipitate was achieved in an ice-bath. Yield: White solid 700mg (Quantitative yield)

^{1}H-NMR ($CDCl_3$, 400Hz) δ (ppm): 7.24 (s, 5H, Ha); 5.16 (bs, 2H, Hb); 4.00 (bs, 2H, Hc)

SYNTHESIS OF compound **48**

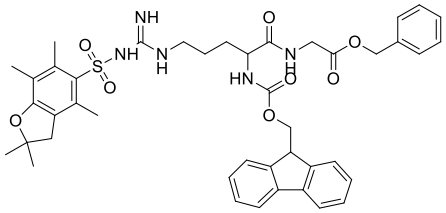

Compound **46** (254mg, 1.54mmol, 1eq) and Fmoc-Arg-(Pbf) (**47**) (1g, 1.54mmol, 1eq) were dissolved in a flask thanks to 5 mL of DCM. Under stirring, at 0°C EDC HCl (328 mg, 1.85mmol, 1.2eq) was added. After 10' HOBt (250 mg, 1.85mmol, 1.2eq) was added in the same reaction conditions. After 16h a TLC checking showed a new spot (R_f: 0.46, DCM: EtOAc 1:1). The crude was washed with H_2O and Brine, dried over Na_2SO_4, filtered and the solvent was evaporated.
The purification occurred through flash chromatography column (4 cm, DCM:EtOAc 12:1 -> 1:1)
Yield: 805mg (66%)

^{1}H NMR (400 MHz, DMSO) δ (ppm): 8.36 (t, 1H, HZ); 7.88-7.33 (m, 13H, HF e HO); 5.10 (s, 2H, HN); 4.27-4.17 (m, 3H, HB e HC) 4.03-3.94 (m, 1H, HD); 3.91-3.82 (m, 2H, HE); (3.00 (m, 2H, HA); 2.87 (s, 2H, HE); 2.47 (s, 3H, HK); 2.38 (s, 3H, HH); 1.98 (s, 3H, HI); 1.60 (m, 2H, HM); 1.46 (m, 2H, HP); 1.37 (s, 6H, HL).

^{13}C-NMR (100 MHz, DMSO) δ (ppm): C19 172.85, C21 170.05, C13 157.90, C14 156.73, C29 144.34, C32 e C43 144.26, C37 e C38 141.16, C8 137.74, C23 136.29, C5 131.88, C25 e C27 128.93, C28 e C24 128.51, C35 128.40, C40 128.09, C36 127.51, C39 125.80, C41 124.77, C34 120.54, C10 116.72, C33 85.96, C42 66.31, C6 66.12, C30 60.20, C22 54.58, C18 47.11, C31 42.91, C4 41.19, C5 29.76, C20 28.73, C17 25.33, C1 e C2 21.21, C16 19.42, C9 18.07, C11 14.54, C7 12.72.

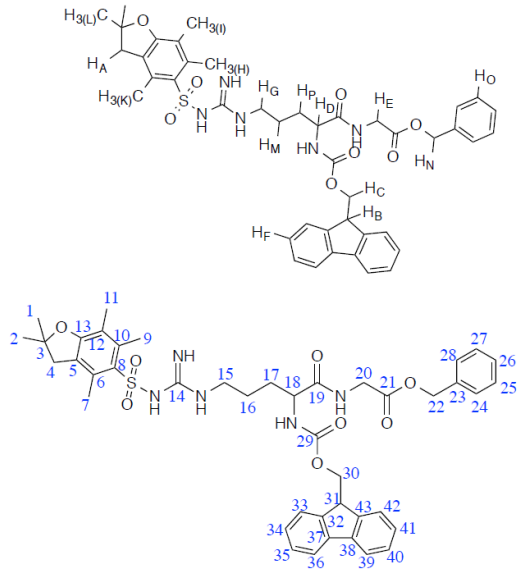

SYNTHESIS OF compound **49**

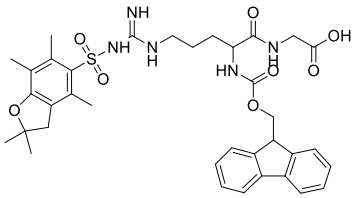

Compound **48** (680mg, 0.96mmol, 1eq) and 10% w/w of $Pd(OH)_2/C$ (68mg, 0.48mmol, 0.5eq) were placed in a 250mL flask under stirring. After the addition of 80mL of MeOH the reaction was kept under N_2 for 10'. The substitution of nitrogen with hydrogen occurred for the night. The end of reaction was checked by TLC (R_f:0). A filtration through celite allows to obtain the final product. Yield: 520mg (77%). The product was a white solid.

^{1}H NMR (400 MHz, DMSO) δ (ppm): 7.87-7.29 (m, 8H, HF); 7.06 (s, 1H, HN); 6.59 (s, 1H, HO); 4.22 (m, part X of a system ABX, 1H, HB); 4.00-3.92 (part AB of a system ABX, 2H, HD); 3.75-3.67 (System ABX, 3H, HD e HE); 3.03 (m, 2H, HG); 2.94 (d, 2H, HG); 2.47 (s, 3H, HH); 2.41 (s, 3H, HZ); 1.99 (d, 3H, HI); 1.45 (m, 2H, HF); 1.39 (s, 3H, HM); 1.37 (s, 6H, HL)

^{13}C NMR (100 MHz, CD3OD) δ (ppm): C21 173.32, C19 172.38, C5 172.03, C14 170.40, C22 158.70, C25 157.39, C32 157.20, C29 149.89, C36 145.00, C9 141.96, C6 141.14, C12 138.55, C28 132.69, C35 128.89, C27 128.33, C11 126.62, C26 125.42, C33 121.35, C8 117.53, C4 87.58, C23 66.51, C18 55.39, C34 53.11, C20 49.13, C1 47.93, C15 43.72, C17 43.09, C2 42.03, C3 29. 54, C16 20.23, C10 19.38, C13 18.87, C7 14.05.

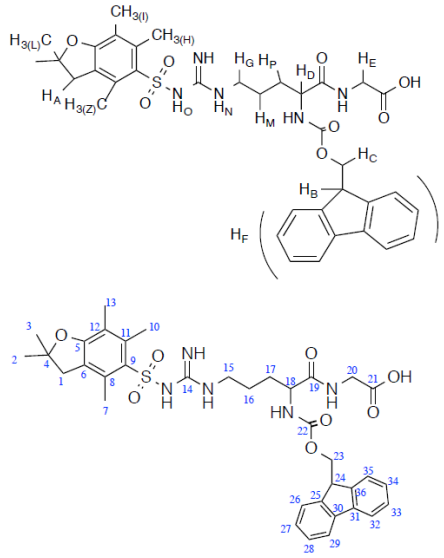

SYNTHESIS OF compound **50**

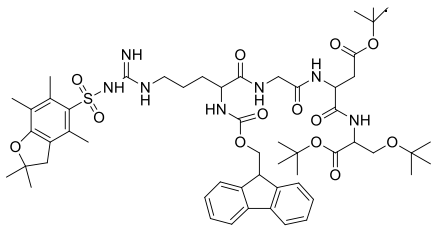

Compound **44** (286mg, 0.74mmol, 1eq) and **49** (520mg, 0.74mmol, 1eq) were placed in a flask with 15 mL of DCM. At 0°C EDC HCl (157mg, 0.89mmol, 1.2eq) was added and after 10' under stirring HOBt (120 mg, 0.89mmol, 1.2eq) was put it into the flask. TLC check displayed the end of reaction (R_f: 0.69, EtOAc : MeOH 10:1). The workup consisted in washing the mixture with H_2O (10 mL x 2) and then Brine (10 mL x 2). The combined organic layers were dried over Na_2SO_4 and the solvent evaporated by rotavapor.

The crude was purified by flash chromatography column (3 cm of diameter, DCM : EtOAc 100:1 -> EtOAc). Yield: 728mg (91%). The product was a white solid.

^{1}H-NMR (400 Hz, CD_3OD) δ (ppm): 7.77-7.29 (8H, HD); 4.80 (t, part X of a system ABX, 1H, HA); 4.44 (m, part AB of a system ABX, 2H, HC); 4.35 (m, part X of a system ABX, 1H, HE); 4.21 (t, part X of a system ABX, 1H, HB); 4.02 (t, part X of a system ABX, 1H, HF); 3.81 (s, 2H, HG); 3.72-3.51 (dd, 2H, part AB of a system ABX, HH); 2.96 (s, 2H, HO); 2.82- 2.63 (dd, parte AB di sistema ABX, 2H, HV); 2.57 (s, 3H, HP); 2.50 (s, 3H, HM); 2.06 (s, 3H, HN); 1.76 (m, 2H, HX); 1.66 (m, 2H, HW); 1.55 (m, 2H, HY); 1.47 (s, 3H, HS); 1.43 (s, 9H, HL); 1.42 (s, 3H, HQ); 1.37 (s, 9H, HT); 1.14 (s, 9H, HU).

^{13}C-NMR (100 MHz, CD3OD) δ (ppm): C21 174. 17, C55 171.21, C19 170.00, C34 169.13, C28 158.45, C10 157.23, C14 156.73, C40 e C39 143.85, C7143.76, C43 e C54 141.21, C2 137.99, C48 e C49 132.95, C3 132.10, C5 127.38, C47 e C50 126.78, C45 e C52 124.91, C44 e C53 124.85, C8 124.60, C51 e C46 119.53, C13 117.02, C24 86.23, C31 81.49, C38 81.12, C41 72.97, C30 66.59, C29 61.58, C42 61.36, C15 55.03,

C17 53.75, C22 49.48, C1 42.54, C20 42.08, C23 36.86, C35 e C36 e C37 28.28, C25 e C26 C27 27.28, C32 e C33 e C34 26.94, C9 26.90, C4 26.27, C6 26.25, C16 18.19, C11 17.00, C12 11.11.

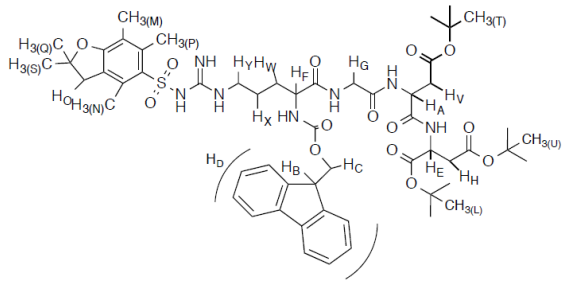

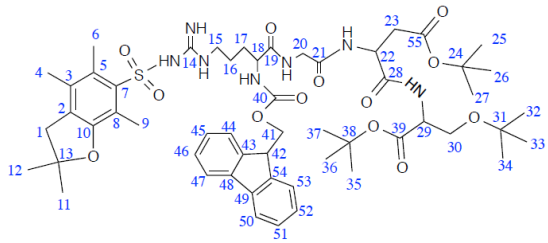

SYNTHESIS OF compound **51**

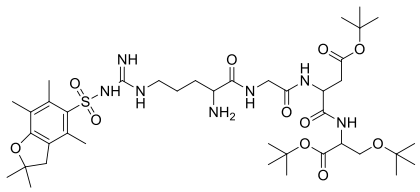

Compound **50** (250mg, 0.23mmol, 1eq) was dissolved in 11mL of dry CH_3CN and 1.1 mL of DEA. The reaction proceeded for 3h, under N_2 atmosphere. At the end of reaction a TLC analysis showed three spots DCM:MeOH 50:1: fulvene R_f: 0.92, *starting material* R_f: 0.5, final product R_f: 0.35.
CH_3CN and DEA were removed by using rotavapor. The workup consisted in a washing with Et_2O. ^{1}H-NMR spectrum presented fulvene's signals; therefore a flash chromatography column allows to achieve the final compound. (1 cm column diameter, DCM -> DCM:MeOH 10:1).
Yield: 166mg (84%). The product was a white solid.

^{1}H-NMR (CD_3OD, 400Hz) δ (ppm): 4.80 (s, part X of a system ABX, 1H, HV); 4.40(t, part X of a system ABX, HT); 3.86-3.91 (m, 2H, HQ); 3.54-3.79 (dd, 2H, HS); 3.34 (m, 2H, HR); 3.17(s, 2H, HP); 2.99 (s, 2H, HN); 2.62-2.82 (part AB of a system ABX, 2H, HM); 2.57 (s, 3H, HL); 2.51 (s, 3H, HI); 2.07 (s, 3H, HH); 1.70 (m, 2H, HG); 1.56 (m, 2H, HF); 1.45 (s, 18H, HB e HC); 1.44 (s, 6H, HE e HD); 1.17 (s, 9H, HA)

^{13}C NMR (100 MHz, CD3OD) δ (ppm): C39 176.22, C38 171.21, C37 170.20, C36 169.87, C35 169.13, C34 158.44, C31156.71, C33 137.96, C29 133.02, C32 132.09, C30 124.59, C28 117.00, C27 86.25, C26 81.54, C25 81.22, C24 73.02, C23 61.40, C22 54.14, C21 53.75, C20 49.45, C18 42.58, C19 41.89, C17 37.01, C40 31.55, C14 27.34, C15 26.97, C12 e C11 e C10 26.94, C9 e C8 and C7 26.31, C6 e C5 e C426.28, C16 26.24, C13 25.12, C3 18.20, C2 17.01, C1 11.14.

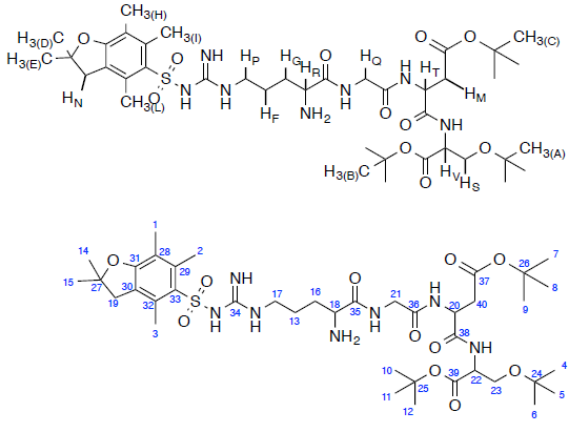

SYNTHESIS OF compound **53**

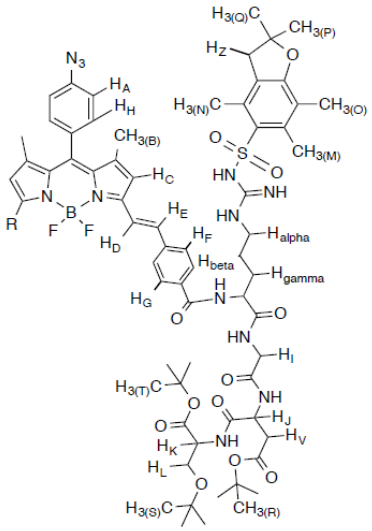

Compounds **34** (166mg, 0.20mmol, 2.5eq) and **51** (49mg, 0.08mmol, 1eq) were put in a flask with 1.5mL of DCM. At 0°C EDC HCl(41.4 mg, 0.23mmol, 2.9eq) was added and after 10' HOBt (31.5mg, 0.23mmol, 2.9eq) was put into the flask. After 16h the mixture was washed with H_2O and Brine. The combined organic layers were dried over Na_2SO_4, filtered and evaporated. Flash chromatography column allows to purify the crude product. R_f: 0.36, DCM:MeOH 50:1 -> 10:1.
Yield: 2, 80mg (45%). Solid blue product.

^{1}H NMR (400 MHz, CD3OD) δ (ppm): 7.88 (Part AA' of a system AA'-BB', 4H, J=8Hz, HF); 7.75 (d, 2H, J=16Hz, HE); 7.63 (Part BB' of a system AA'-BB', 4H, J=8Hz, HG); 7.38 (d, 2H, J=16.0, HD); 7.27(Part AA' of a system AA'-BB', 2H, J=8Hz, HA); 7.20 (Part BB' of a system AA'-BB', 2H, J=8Hz, HH); 6.78(s, 2H, HC); 4.57-4.39 (t, 2H, HK e HJ); 3.89 (dd, 2H, HI); 3.75-3.49 (dd, 2H, HL); 3.63 (t, 1H, HX); 3.21 (m, 2H, Hgamma); 2.93 (s, 2H, HZ); 2.89-2.66 (dd, 2H, HV); 2.57 (s, 3H, HN); 2.51 (s, 3H, HM); 2.03 (s, 3H, HO); 1.94-1.59 (m, 4H, Halfa e Hbeta); 1.43 (s, 15H, HT e HP e HQ); 1.38 (s, 12H, HR e HB); 1.13 (s, 9H, HS).

SYNTHESIS OF compound **54**

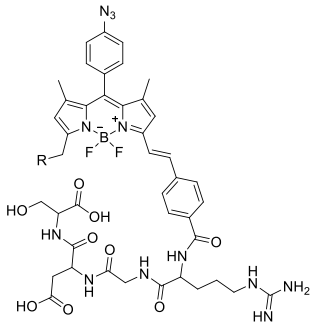

Compound **53** (40mg, 0.02mmol, 1eq) with 80µL of H2O and 80µL of triisopropylsilane were put into a flask. 1.5mL of TFA was added drop by drop. After 2h at room temperature a TLC check showed a new spot with R_f:0. The solvent was evaporated.

Purification occurred by reverse silica gel C18 column. A starting solution 1% of TFA in H_2O was prepared, the purification proceeded by adding CH_3CN. Yield: crude 42mg. Compound dark green.

3.6 REFERENCES

1. Biagiotti, G. *et al.* Multiwalled carbon nanotubes for combination therapy: A biodistribution and efficacy pilot study. *J. Mater. Chem. B* **7**, 2678–2687 (2019).

2. Kostarelos, K. *et al.* Cellular uptake of functionalized carbon nanotubes is independent of functional group and cell type. *Nat. Nanotechnol.* **2**, 108–113 (2007).

3. Liu & Speranza. Functionalization of Carbon Nanomaterials for Biomedical Applications. *C — J. Carbon Res.* **5**, 72 (2019).

4. Curcio, M. *et al.* Functionalized carbon nanostructures versus drug resistance: Promising scenarios in cancer treatment. *Molecules* **25**, 1–31 (2020).

5. Perkins, B. L. & Naderi, N. Carbon Nanostructures in Bone Tissue Engineering. *Open Orthop. J.* **10**, 877–899 (2017).

6. Erol, O. *et al.* Recent advances in bioactive 1D and 2D carbon nanomaterials for biomedical applications. *Nanomedicine Nanotechnology, Biol. Med.* **14**, 2433–2454 (2018).

7. Tasis, D., Tagmatarchis, N., Bianco, A. & Prato, M. Chemistry of carbon nanotubes. *Chem. Rev.* **106**, 1105–1136 (2006).

8. Kumar, S., Rani, R., Dilbaghi, N., Tankeshwar, K. & Kim, K. H. Carbon nanotubes: A novel material for multifaceted applications in human healthcare. *Chem. Soc. Rev.* **46**, 158–196 (2017).

9. Hong, S. Y. *et al.* Filled and glycosylated carbon nanotubes for in vivo radioemitter localization and imaging. *Nat. Mater.* **9**, 485–490 (2010).

10. Wohlstadter, J. N. *et al.* Carbon nanotube-based biosensor. *Adv. Mater.* **15**, 1184–1187 (2003).

11. Fedeli, S. *et al.* Azido-Substituted BODIPY Dyes for the Production of Fluorescent Carbon Nanotubes. *Chem. - A Eur. J.* **21**, 15349–15353 (2015).

12. Mooney, E., Dockery, P., Greiser, U., Murphy, M. & Barron, V. Carbon nanotubes and mesenchymal stem cells: Biocompatibility, proliferation and differentiation. *Nano Lett.* **8**, 2137–2143 (2008).

13. Guo, J., Wang, Y. & Zhao, M. Target-directed functionalized ferrous phosphate-carbon dots fluorescent nanostructures as peroxidase mimetics for cancer cell detection and ROS-mediated therapy. *Sensors Actuators, B Chem.* **297**, 126739 (2019).

14. Janyasupab, M. & Promptmas, C. Development of non-enzymatic N-doped graphene supported cobalt/iron amperometric based sensor for glucose detection in urine. *2018 IEEE EMBS Conf. Biomed. Eng. Sci. IECBES 2018 - Proc.* 577–582 (2019) doi:10.1109/IECBES.2018.8626693.

15. Chiang, Y. C., Lin, W. H. & Chang, Y. C. The influence of treatment duration on multi-walled carbon nanotubes functionalized by H 2 SO 4 /HNO 3 oxidation. *Appl. Surf. Sci.* **257**, 2401–2410 (2011).

16. Chattopadhyay, D., Lastella, S., Kim, S. & Papadimitrakopoulos, F. Length separation of zwitterion-functionalized single wall carbon nanotubes by GPC. *J. Am. Chem. Soc.* **124**, 728–729 (2002).

17. Li, J. & Zhang, Y. Large-scale aligned carbon nanotubes films. *Phys. E Low-Dimensional Syst. Nanostructures* **33**, 235–239 (2006).

18. submitted to Nature on Feb 5, 2004. (2004).

19. Allen, M. J., Tung, V. C. & Kaner, R. B. Honeycomb carbon: A review of graphene. *Chem. Rev.* **110**, 132–145 (2010).

20. Park, S. & Ruoff, R. S. Chemical methods for the production of graphenes. *Nat. Nanotechnol.* **4**, 217–224 (2009).

21. Reina, A. *et al.* Growth of large-area single- and Bi-layer graphene by controlled carbon precipitation on polycrystalline Ni surfaces. *Nano Res.* **2**, 509–516 (2009).

22. Jiao, L., Wang, X., Diankov, G., Wang, H. & Dai, H. Facile synthesis of high-quality graphene nanoribbons. *Nat. Nanotechnol.* **5**, 321–325 (2010).

23. Coliman, J. P. *et al.* "Picket Fence Porphyrins". Synthetic Models for Oxygen Binding Hemoproteins. *J. Am. Chem. Soc.* **97**, 1427–1439 (1975).

24. Brinker, C. J., Lu, Y., Sellinger, A. & Fan, H. ChemInform Abstract: Evaporation-Induced Self-Assembly: Nanostructures Made Easy. *ChemInform* **30**, no-no (2010).

25. Sutter, P., Sadowski, J. T. & Sutter, E. Graphene on Pt(111): Growth and substrate interaction. *Phys. Rev. B - Condens. Matter Mater. Phys.* **80**, 1–10 (2009).

26. Staudenmaier, L. Method for the preparation of the graphite acid. *Eur. J. Inorg. Chem.* **31**, 1481–1487 (1898).

27. Zhang, X. *et al.* Distribution and biocompatibility studies of graphene oxide in mice after intravenous administration. *Carbon N. Y.* **49**, 986–995 (2011).

28. Pan, S. & Aksay, I. A. Factors controlling the size of graphene oxide sheets produced via the graphite oxide route. *ACS Nano* **5**, 4073–4083 (2011).

29. Gonçalves, P. A. D. & Peres, N. M. R. An Introduction to Graphene Plasmonics. *An Introd. to Graphene Plasmon.* 1–431 (2016) doi:10.1142/9948.

30. Pan, Y., Sahoo, N. G. & Li, L. The application of graphene oxide in drug delivery. *Expert Opin. Drug Deliv.* **9**, 1365–1376 (2012).

31. Li, Q.-Y., Zu, Y.-G., Shi, R.-Z. & Yao, L.-P. Review Camptothecin: Current Perspectives. *Curr. Med. Chem.* **13**, 2021–2039 (2006).

32. Liu, Z., Robinson, J. T., Sun, X. & Dai, H. PEGylated nanographene oxide for delivery of water-insoluble cancer drugs. *J. Am. Chem. Soc.* **130**, 10876–10877 (2008).

33. Rana, V. K. *et al.* Synthesis and drug-delivery behavior of chitosan-functionalized graphene oxide hybrid nanosheets. *Macromol. Mater. Eng.* **296**, 131–140 (2011).

34. Eigler, S., Grimm, S., Enzelberger-Heim, M., Müller, P. & Hirscha, A. Graphene oxide: Efficiency of reducing agents. *Chem. Commun.* **49**, 7391–7393 (2013).

35. Hunt, A. *et al.* Epoxide speciation and functional group distribution in graphene oxide paper-like materials. *Adv. Funct. Mater.* **22**, 3950–3957 (2012).

36. Szabó, T. *et al.* Evolution of surface functional groups in a series of progressively oxidized graphite oxides. *Chem. Mater.* **18**, 2740–2749 (2006).

37. Dimiev, A. M., Alemany, L. B. & Tour, J. M. Graphene oxide. Origin of acidity, its instability in water, and a new dynamic structural model. *ACS Nano* **7**, 576–588 (2013).

38. Liu, Y., Yu, D., Zeng, C., Miao, Z. & Dai, L. Biocompatible graphene oxide-based glucose biosensors. *Langmuir* **26**, 6158–6160 (2010).

39. Paquin, F., Rivnay, J., Salleo, A., Stingelin, N. & Silva, C. Multi-phase semicrystalline microstructures drive exciton dissociation in neat plastic semiconductors. *J. Mater. Chem. C* **3**, 10715–10722 (2015).

40. Yu, R. *et al.* Synthetic possibility of polystyrene functionalization based on hydroxyl groups of graphene oxide as nucleophiles. *New J. Chem.* **39**, 5096–5099 (2015).

41. Chen, H. *et al.* Phosphorylation of graphehe oxide to improve adsorption of U(VI) from aquaeous solutions. *J. Radioanal. Nucl. Chem.* **313**, 175–189 (2017).

42. De Leon, A. C., Alonso, L., Mangadlao, J. D., Advincula, R. C. & Pentzer, E. Simultaneous Reduction and Functionalization of Graphene Oxide via Ritter Reaction. *ACS Appl. Mater. Interfaces* **9**, 14265–14272 (2017).

43. Liao, K. H., Lin, Y. S., MacOsko, C. W. & Haynes, C. L. Cytotoxicity of graphene oxide and graphene in human erythrocytes and skin fibroblasts. *ACS Appl. Mater. Interfaces* **3**, 2607–2615 (2011).

44. Lu, C. H. *et al.* Using graphene to protect DNA from cleavage during cellular delivery. *Chem. Commun.* **46**, 3116–3118 (2010).

45. Wojtoniszak, M. *et al.* Synthesis, dispersion, and cytocompatibility of graphene oxide and reduced graphene oxide. *Colloids Surfaces B Biointerfaces* **89**, 79–85 (2012).

46. Yuan, J. *et al.* Cytotoxicity evaluation of oxidized single-walled carbon nanotubes and graphene oxide on human hepatoma HepG2 cells: An iTRAQ-coupled 2D LC-MS/MS proteome analysis. *Toxicol. Sci.* **126**, 149–161 (2012).

47. Chang, Y. *et al.* In vitro toxicity evaluation of graphene oxide on A549 cells. *Toxicol. Lett.* **200**, 201–210 (2011).

48. Bhattacharya, K. *et al.* Biological interactions of carbon-based nanomaterials: From coronation to degradation. *Nanomedicine Nanotechnology, Biol. Med.* **12**, 333–351 (2016).

49. Kurapati, R. *et al.* Dispersibility-Dependent Biodegradation of Graphene Oxide by Myeloperoxidase. *Small* **11**, 3985–3994 (2015).

50. Chen, S. *et al.* Mechanism-based tumor-targeting drug delivery system. Validation of efficient vitamin receptor-mediated endocytosis and drug release. *Bioconjug. Chem.* **21**, 979–987 (2010).

51. Lee, J. S. *et al.* Synthesis of a BODIPY library and its application to the development of live cell glucagon imaging probe. *J. Am. Chem. Soc.* **131**, 10077–10082 (2009).

52. Kaur, P. & Singh, K. Recent advances in the application of BODIPY in bioimaging and chemosensing. *J. Mater. Chem. C* **7**, 11361–11405 (2019).

53. Moss, G. P. Nomenclature of tetrapyrroles (Recommendations 1986). *Pure Appl. Chem.* **59**, 779–832 (1987).

54. van Koeveringe, J. A. & Lugtenburg, J. Novel pyrromethenes 1-Oxygen and 1-sulfur analogues; evidence for photochemical. *Recueil, J. R. Netherlands Chem. Soc.* **96**, 55–57 (1977).

55. Solomonov, A. V., Marfin, Y. S. & Rumyantsev, E. V. Design and applications of dipyrrin-based fluorescent dyes and related organic luminophores: From individual compounds to supramolecular self-assembled systems. *Dye. Pigment.* **162**, 517–542 (2019).

56. Li, Z., Mintzer, E. & Bittman, R. First synthesis of free cholesterol-BODIPY conjugates. *J. Org. Chem.* **71**, 1718–1721 (2006).

57. Wagner, R. W. & Lindsey, J. S. Boron-dipyrromethene dyes for incorporation in synthetic multi-pigment light-harvesting arrays. *Pure Appl. Chem.* **68**, 1373–1380 (1996).

58. Thivierge, C., Bandichhor, R. & Burgess, K. Spectral dispersion and water solubilization of BODIPY dyes via palladium-catalyzed C-H functionalization. *Org. Lett.* **9**, 2135–2138 (2007).

59. Shah, M. *et al.* Pyrromethene–BF2 complexes as laser dyes:1. *Heteroat. Chem.* **1**, 389–399 (1990).

60. Yogo, T., Urano, Y., Ishitsuka, Y., Maniwa, F. & Nagano, T. Highly efficient and photostable photosensitizer based on BODIPY chromophore. *J. Am. Chem. Soc.* **127**, 12162–12163 (2005).

61. Scheibe, B., Borowiak-Palen, E. & Kalenczuk, R. J. Oxidation and reduction of multiwalled carbon nanotubes - preparation and characterization. *Mater. Charact.* **61**, 185–191 (2010).

62. Jameson, L. P. & Dzyuba, S. V. Expeditious, mechanochemical synthesis of BODIPY dyes. *Beilstein J. Org. Chem.* **9**, 786–790 (2013).

63. Andersen, J., Madsen, U., Björkling, F. & Liang, X. Rapid synthesis of aryl azides from aryl halides under mild conditions. *Synlett* 2209–2213 (2005) doi:10.1055/s-2005-872248.

64. Ménard-Moyon, C., Fabbro, C., Prato, M. & Bianco, A. One-pot triple functionalization of carbon nanotubes. *Chem. - A Eur. J.* **17**, 3222–3227 (2011).

65. Lin, H. B., Cooper, S. L., Zhao, Z. C., Garcia-Echeverria, C. & Rich, D. H. Synthesis of a novel polyurethane co-polymer containing covalently attached RGD peptide. *J. Biomater. Sci. Polym. Ed.* **3**, 217–227 (1992).

66. Van Agthoven, J. F. *et al.* Structural Basis of the Differential Binding of Engineered Knottins to Integrins αVβ3 and α5β1. *Structure* **27**, 1443-1451.e6 (2019).

67. Sheldrake, H. M. & Patterson, L. H. Strategies to inhibit tumor associated integrin receptors: Rationale for dual and multi-antagonists. *J. Med. Chem.* **57**, 6301–6315 (2014).

68. Maligaspe, E. *et al.* Photosynthetic antenna-reaction center mimicry: Sequential energy- and electron transfer in a self-assembled supramolecular triad composed of boron dipyrrin, zinc porphyrin and fullerene. *J. Phys. Chem. A* **113**, 8478–8489 (2009).

69. Mori, H. *et al.* In silico and pharmacological screenings identify novel serine racemase inhibitors. *Bioorganic Med. Chem. Lett.* **24**, 3732–3735 (2014).

70. Hishikawa, K. *et al.* Photoinduced nitric oxide release from a hindered nitrobenzene derivative by two-photon excitation. *J. Am. Chem. Soc.* **131**, 7488–7489 (2009).

71. Mallesha, N., Prahlada Rao, S., Suhas, R. & Channe Gowda, D. An efficient synthesis of tert-butyl ethers/esters of alcohols/amino acids using methyl tert-butyl ether. *Tetrahedron Lett.* **53**, 641–645 (2012).

72. Mock, J. N. *et al.* Haloenol pyranones and morpholinones as antineoplastic agents of prostate cancer. *Bioorganic Med. Chem. Lett.* **22**, 4854–4858 (2012).

73. König, W. & Geiger, R. Eine neue Methode zur Synthese von Peptiden: Aktivierung der Carboxylgruppe mit Dicyclohexylcarbodiimid unter Zusatz von 1-Hydroxy-benzotriazolen. *Chem. Ber.* **103**, 788–798 (1970).

74. Pérez-Picaso, L., Escalante, J., Olivo, H. F. & Rios, M. Y. Efficient microwave assisted syntheses of 2,5-diketopiperazines in aqueous media. *Molecules* **14**, 2836–2849 (2009).

75. Styers, T. J. *et al.* Synthesis of Sansalvamide A derivatives and their cytotoxicity in the MSS colon cancer cell line HT-29. *Bioorganic Med. Chem.* **14**, 5625–5631 (2006).

76. Lundt, B. F., Johansen, N. L., Vølund, A. & Markussen, J. REMOVAL OF t-BUTYL AND t-BUTOXYCARBONYL PROTECTING GROUPS WITH TRIFLUOROACETIC ACID: Mechanisms, Biproduct Formation and Evaluation of Scavengers. *Int. J. Pept. Protein Res.* **12**, 258–268 (1978).

77. Hughes, A. B. Amino Acids, Peptides and Proteins in Organic Chemistry. *Amin. Acids, Pept. Proteins Org. Chem.* **2**, (2010).

78. Vardhan, D. M. S., Kumara, H. K., Kumar, H. P. & Gowda, D. C. Inhibition of Urease Enzyme Activity By Urea and Thiourea Derivatives of Dipeptides Conjugated 2, 3-Dichlorophenyl Piperazine. *Int. J. Pharm. Pharm. Sci.* **9**, 92 (2017).

79. Kaur, A., Poonam, Patil, M. T., Mehta, S. K. & Salunke, D. B. An efficient and scalable synthesis of potent TLR2 agonistic PAM2CSK4. *RSC Adv.* **8**, 9587–9596 (2018).

80. Brough, P., Klumpp, C., Bianco, A., Campidelli, S. & Prato, M. [60]fullerene-pyrrolidine-N-oxides. *J. Org. Chem.* **71**, 2014–2020 (2006).

81. Saini, N. & Yang, X. Metformin as an anti-cancer agent: Actions and mechanisms targeting cancer stem cells. *Acta Biochim. Biophys. Sin. (Shanghai).* **50**, 133–143 (2018).

82. Pierotti, M. A. *et al.* Targeting metabolism for cancer treatment and prevention: Metformin, an old drug with multi-faceted effects. *Oncogene* **32**, 1475–1487 (2013).

83. Alimova, I. N. *et al.* Metformin inhibits breast cancer cell growth, colony formation and induces cell cycle arrest in vitro. *Cell Cycle* **8**, 909–915 (2009).

84. Morales, D. R. & Morris, A. D. Metformin in cancer treatment and prevention. *Annu. Rev. Med.* **66**, 17–29 (2015).

85. Jaune, E. & Rocchi, S. Metformin: Focus on melanoma. *Front. Endocrinol. (Lausanne).* **9**, 1–9 (2018).

86. Tseng, H. W., Li, S. C. & Tsai, K. W. Metformin treatment suppresses melanoma cell growth and motility through modulation of microRNA expression. *Cancers (Basel).* **11**, (2019).

87. Vancura, A., Bu, P., Bhagwat, M., Zeng, J. & Vancurova, I. Metformin as an Anticancer Agent. *Trends Pharmacol. Sci.* **39**, 867–878 (2018).

88. Mallik, R. & Chowdhury, T. A. Metformin in cancer. *Diabetes Res. Clin. Pract.* **143**, 409–419 (2018).

89. Saraei, P., Asadi, I., Kakar, M. A. & Moradi-Kor, N. The beneficial effects of metformin on cancer prevention and therapy: A comprehensive review of recent advances. *Cancer Manag. Res.* **11**, 3295–3313 (2019).

90. Fedeli, S. *et al.* The 'click-on-tube' approach for the production of efficient drug carriers based on oxidized multi-walled carbon nanotubes. *J. Mater. Chem. B* **4**, 3823–3831 (2016).

91. Baghayeri, M., Tehrani, M. B., Amiri, A., Maleki, B. & Farhadi, S. A novel way for detection of antiparkinsonism drug entacapone via electrodeposition of silver nanoparticles/functionalized multi-walled carbon nanotubes as an amperometric sensor. *Mater. Sci. Eng. C* **66**, 77–83 (2016).

92. Mirazi, N., Shoaei, J., Khazaei, A. & Hosseini, A. A comparative study on effect of metformin and metformin-conjugated nanotubes on blood glucose homeostasis in diabetic rats. *Eur. J. Drug Metab. Pharmacokinet.* **40**, 343–348 (2015).

93. Yoo, S. *et al.* Enhanced Response of Metformin towards the Cancer Cells due to Synergism

with Multi-walled Carbon Nanotubes in Photothermal Therapy. *Sci. Rep.* 1–9 (2017) doi:10.1038/s41598-017-01118-3.

94. Denise, C. *et al.* 5-Fluorouracil resistant colon cancer cells are addicted to OXPHOS to survive and enhance stem-like traits. *Oncotarget* **6**, 41706–41721 (2015).

95. Ota, S. *et al.* Metformin suppresses glucose-6-phosphatase expression by a complex I inhibition and AMPK activation-independent mechanism. *Biochem. Biophys. Res. Commun.* **388**, 311–316 (2009).

96. Chen, Z. *et al.* The Advances of Carbon Nanotubes in Cancer Diagnostics and Therapeutics. *J. Nanomater.* **2017**, (2017).

97. Cui, X., Wan, B., Yang, Y., Ren, X. & Guo, L. H. Length effects on the dynamic process of cellular uptake and exocytosis of single-walled carbon nanotubes in murine macrophage cells /631/80 /704/172 /82/29 /14/19 /14/34 /123 article. *Sci. Rep.* **7**, 1–13 (2017).

98. Yuan, Y. M. & He, C. The glial scar in spinal cord injury and repair. *Neurosci. Bull.* **29**, 421–435 (2013).

99. Su, Z. *et al.* Reactive astrocytes inhibit the survival and differentiation of oligodendrocyte precursor cells by secreted TNF-α. *J. Neurotrauma* **28**, 1089–1100 (2011).

100. Liu, W. *et al.* Folic acid conjugated magnetic iron oxide nanoparticles for nondestructive separation and detection of ovarian cancer cells from whole blood. *Biomater. Sci.* **4**, 159–166 (2016).

101. Stichel, C. C. & Müller, H. W. The CNS lesion scar: New vistas on an old regeneration barrier. *Cell Tissue Res.* **294**, 1–9 (1998).

102. Galtrey, C. M. & Fawcett, J. W. The role of chondroitin sulfate proteoglycans in regeneration and plasticity in the central nervous system. *Brain Res. Rev.* **54**, 1–18 (2007).

103. Bradbury, E. J. & Carter, L. M. Manipulating the glial scar: Chondroitinase ABC as a therapy for spinal cord injury. *Brain Res. Bull.* **84**, 306–316 (2011).

104. Silver, J. & Miller, J. H. Regeneration beyond the glial scar. *Nat. Rev. Neurosci.* **5**, 146–156 (2004).

105. Place, L. W., Sekyi, M. & Kipper, M. J. Aggrecan-mimetic, glycosaminoglycan-containing nanoparticles for growth factor stabilization and delivery. *Biomacromolecules* **15**, 680–689 (2014).

106. Marchesan, S., Kostarelos, K., Bianco, A. & Prato, M. The winding road for carbon nanotubes in nanomedicine. *Mater. Today* **18**, 12–19 (2015).

107. Pinillos-Madrid, J. F. & Gallardo, C. Carbon nanotubes: A viable drug delivery platform for the treatment of cancer. *J. Appl. Pharm. Sci.* **5**, 143–152 (2015).

108. Moradian, H., Fasehee, H., Keshvari, H. & Faghihi, S. Poly(ethyleneimine) functionalized carbon nanotubes as efficient nano-vector for transfecting mesenchymal stem cells. *Colloids Surfaces B Biointerfaces* **122**, 115–125 (2014).

109. Herrero, M. A. *et al.* Synthesis and characterization of a carbon nanotube-dendron series for efficient siRNA delivery. *J. Am. Chem. Soc.* **131**, 9843–9848 (2009).

110. Zhou, M., Peng, Z., Liao, S., Li, P. & Li, S. Design of microencapsulated carbon nanotube-based microspheres and its application in colon targeted drug delivery. *Drug Deliv.* **21**, 101–109 (2014).

111. Zhang, W., Zuo, X. D. & Wu, C. W. Synthesis and magnetic properties of carbon nanotube-iron oxide nanoparticle composites for hyperthermia: A review. *Rev. Adv. Mater. Sci.* **40**, 165–176 (2015).

112. Jones, L. L., Margolis, R. U. & Tuszynski, M. H. The chondroitin sulfate proteoglycans neurocan, brevican, phosphacan, and versican are differentially regulated following spinal cord injury. *Exp. Neurol.* **182**, 399–411 (2003).

113. Tom, V. J., Steinmetz, M. P., Miller, J. H., Doller, C. M. & Silver, J. Studies on the development and behavior of the dystrophic growth cone, the hallmark of regeneration failure, in an in vitro model of the glial scar and after spinal cord injury. *J. Neurosci.* **24**, 6531–6539 (2004).

114. Matthews, R. T. *et al.* Aggrecan glycoforms contribute to the molecular heterogeneity of perineuronal nets. *J. Neurosci.* **22**, 7536–7547 (2002).

115. Sandvig, A., Berry, M., Barrett, L. B., Butt, A. & Logan, A. Myelin-, reactive glia-, and scar-derived CNS axon growth inhibitors: Expression, receptor signaling, and correlation with axon regeneration. *Glia* **46**, 225–251 (2004).

116. Yiu, G. & He, Z. Glial inhibition of CNS axon regeneration. *Nat. Rev. Neurosci.* **7**, 617–627 (2006).

117. Rhodes, K. E. & Fawcett, J. W. Chondroitin sulphate proteoglycans: Preventing plasticity or protecting the CNS? *J. Anat.* **204**, 33–48 (2004).

118. Gilbert, R. J. *et al.* CS-4,6 is differentially upregulated in glial scar and is a potent inhibitor of neurite extension. *Mol. Cell. Neurosci.* **29**, 545–558 (2005).

119. Zuo, J., Neubauer, D., Dyess, K., Ferguson, T. A. & Muir, D. Degradation of chondroitin sulfate proteoglycan enhances the neurite- promoting potential of spinal cord tissue. *Exp. Neurol.* **154**, 654–662 (1998).

120. McKeon, R. J., Schreiber, R. C., Rudge, J. S. & Silver, J. Reduction of neurite outgrowth in a model of glial scarring following CNS injury is correlated with the expression of inhibitory molecules on reactive astrocytes. *J. Neurosci.* **11**, 3398–3411 (1991).

121. Preston, E., Webster, J. & Small, D. Characteristics of sustained blood-brain barrier opening and tissue injury in a model for focal trauma in the rat. *J. Neurotrauma* **18**, 83–92 (2001).

122. Fitch, M. T., Doller, C., Combs, C. K., Landreth, G. E. & Silver, J. Cellular and molecular mechanisms of glial scarring and progressive cavitation: In vivo and in vitro analysis of inflammation-induced secondary injury after CNS trauma. *J. Neurosci.* **19**, 8182–8198 (1999).

123. Faulkner, J. R. *et al.* Reactive Astrocytes Protect Tissue and Preserve Function after Spinal Cord Injury. *J. Neurosci.* **24**, 2143–2155 (2004).

124. Jones, L. L., Sajed, D. & Tuszynski, M. H. Axonal Regeneration through Regions of Chondroitin Sulfate Proteoglycan Deposition after Spinal Cord Injury: A Balance of Permissiveness and Inhibition. *J. Neurosci.* **23**, 9276–9288 (2003).

125. Levine, J. M., Reynolds, R. & Fawcett, J. W. The oligodendrocyte precursor cell in health and disease. *Trends Neurosci.* **24**, 39–47 (2001).

126. Tan, A. M., Zhang, W. & Levine, J. M. NG2: A component of the glial scar that inhibits axon growth. *J. Anat.* **207**, 717–725 (2005).

127. Yang, L. J. S. *et al.* Sialidase enhances spinal axon outgrowth in vivo. *Proc. Natl. Acad. Sci. U. S. A.* **103**, 11057–11062 (2006).

128. Rhodes, K. E., Raivich, G. & Fawcett, J. W. The injury response of oligodendrocyte precursor cells is induced by platelets, macrophages and inflammation-associated cytokines. *Neuroscience* **140**, 87–100 (2006).

129. Davies, S. J. A., Goucher, D. R., Doller, C. & Silver, J. Robust regeneration of adult sensory axons in degenerating white matter of the adult rat spinal cord. *J. Neurosci.* **19**, 5810–5822 (1999).

130. Dyck, S. M. & Karimi-Abdolrezaee, S. Chondroitin sulfate proteoglycans: Key modulators in the developing and pathologic central nervous system. *Exp. Neurol.* **269**, 169–187 (2015).

131. Muleja, A. A., Mbianda, X. Y., Krause, R. W. & Pillay, K. Synthesis, characterization and thermal decomposition behaviour of triphenylphosphine-linked multiwalled carbon nanotubes. *Carbon N. Y.* **50**, 2741–2751 (2012).

132. Bonini, M., Wiedenmann, A. & Baglioni, P. Small angle polarized neutrons (SANSPOL) investigation of surfactant free magnetic fluid of uncoated and silica-coated cobalt-ferrite nanoparticles. *J. Phys. Chem. B* **108**, 14901–14906 (2004).

133. Chitosan, P. O. F. on the Structure and Properties of Chitosan. **33**, 1899–1904 (1992).

134. Coulson-Thomas, V. & Gesteira, T. Dimethylmethylene Blue Assay (DMMB). *Bio-Protocol* **4**, 1–7 (2014).

135. Shin, H. J. *et al.* Efficient reduction of graphite oxide by sodium borohydride and its effect on electrical conductance. *Adv. Funct. Mater.* **19**, 1987–1992 (2009).

136. Pei, S. & Cheng, H. M. The reduction of graphene oxide. *Carbon N. Y.* **50**, 3210–3228 (2012).

137. Gao, W., Alemany, L. B., Ci, L. & Ajayan, P. M. New insights into the structure and reduction of graphite oxide. *Nat. Chem.* **1**, 403–408 (2009).

138. Pei, S., Zhao, J., Du, J., Ren, W. & Cheng, H. M. Direct reduction of graphene oxide films into highly conductive and flexible graphene films by hydrohalic acids. *Carbon N. Y.* **48**, 4466–4474 (2010).

139. Moon, I. K., Lee, J., Ruoff, R. S. & Lee, H. Reduced graphene oxide by chemical graphitization. *Nat. Commun.* **1**, (2010).

140. Schniepp, H. C. *et al.* Functionalized single graphene sheets derived from splitting graphite oxide. *J. Phys. Chem. B* **110**, 8535–8539 (2006).

141. Fernández-Merino, M. J. *et al.* Vitamin C is an ideal substitute for hydrazine in the reduction of graphene oxide suspensions. *J. Phys. Chem. C* **114**, 6426–6432 (2010).

142. Bosch-Navarro, C., Coronado, E., Martí-Gastaldo, C., Sánchez-Royo, J. F. & Gómez, M. G. Influence of the pH on the synthesis of reduced graphene oxide under hydrothermal conditions. *Nanoscale* **4**, 3977–3982 (2012).

143. Stolle, A., Szuppa, T., Leonhardt, S. E. S. & Ondruschka, B. Ball milling in organic synthesis: Solutions and challenges. *Chem. Soc. Rev.* **40**, 2317–2329 (2011).

144. Szuppa, T., Stolle, A., Ondruschka, B. & Hopfe, W. An alternative solvent-free synthesis of nopinone under ball-milling conditions: Investigation of reaction parameters. *ChemSusChem* **3**, 1181–1191 (2010).

145. Fulmer, D. A., Shearouse, W. C., Medonza, S. T. & Mack, J. Solvent-free Sonogashira coupling reaction via high speed ball milling. *Green Chem.* **11**, 1821–1825 (2009).

146. Schneider, F., Stolle, A., Ondruschka, B. & Hopf, H. The Suzuki-Miyaura reaction under

mechanochemical conditions. *Org. Process Res. Dev.* **13**, 44–48 (2009).

147. Lee, H. C. *et al.* Review of the synthesis, transfer, characterization and growth mechanisms of single and multilayer graphene. *RSC Adv.* **7**, 15644–15693 (2017).

148. Hummers, W. S. & Offeman, R. E. Preparation of Graphitic Oxide. *J. Am. Chem. Soc.* **80**, 1339 (1958).

4. Study of anticancer biological activity of biguanide derivative, compared to metformin activity.

4.1 OBJECTIVES OF THIS CHAPTER (4) I

As presented in our first work,[1] due to the activity of metformin in cancer cells, we decided to conjugate this molecule to carbon nanotubes, but we didn't exploit a covalent bond which failed in the intracellular release, but a system based on Metformin (Met) salts with oxidized multiwalled carbon nanotubes.

4.2 INTRODUCTION: METFORMIN[81]

Metformin (1,1-dimethylbiguanide), a commonly prescribed antitype II diabetes drug, belongs to the biguanide class of compounds, which also includes phenformin and buformin.[82] The glucose and the insulin lowering ability of metformin, along with reduced hepatic glucose output, are shown to lower blood glucose levels and improve several other diseases, including polycystic ovary syndrome and metabolic syndrome. In past decades, several epidemiologic studies have linked metformin use with a decreased risk of several types of cancers, including breast, prostate, pancreatic cancer. There is also a change in fatty acids metabolism in patients treated with metformin, and a their weight loss is experienced.[83] Unlike other antidiabetic drugs, metformin has therapeutic efficacy consolidated, has a good safety profile, is economical, can be used with others antidiabetic drugs without causing problems and is tolerated very well with minimal collateral effects.[84] Lactic acidosis, a potential side effect of other members of the biguanide family, is very rare in patients treated with metformin Together these economical and clinical benefits of metformin support its further development and potential clinical implementation as an anti-cancer therapy

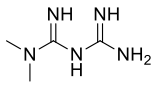

55

***Figure 86**. Metformin chemical structure*

4.2.1 METFORMIN AS ANTICANCER DRUG

Diabetic patients possess a higher risk of developing cancers than healthy patients, which is partly due to increasing levels of circulating growth factors, such as insulin or insulin growth factor 1 and 2 (IGF-1 and 2). In this context, many retrospective analyses in type 2 diabetes patients have shown that metformin possesses antitumoral proprieties. Due to these studies the interest in metformin arose as antitumor agent.[85]

The association between metformin use and reduced cancer risk in patients with diabetes was suggested in a pioneering observational study published in 2005 which reported a 23% decrease in cancer risk with metformin use. Since then, several epidemiologic studies have provided additional evidence linking lower cancer risk in diabetic patients treated with metformin than in non-metformin users.[81]

Direct and indirect effects of metformin may work to inhibit cancer. Indirectly, metformin inhibits glucose production in the liver and stimulates glucose uptake in the muscle, thereby enhancing insulin sensitivity and reducing blood glucose and insulin levels. Directly, metformin activates AMPK by inhibiting the complex I of the mitochondrial respiratory chain, which leads to impaired mitochondrial function and conditions that effectively mimic cellular energy stress, such as glucose deprivation, hypoxia, oxidative stress, ischemia, and muscle contraction or exercise, all of which lead to the activation of the AMPK axis and inhibit the mammalian target of rapamycin complex 1 (mTORC1).[86]

However, the principal effects of metformin on cancer cells are direct effects, which predominantly induce mammalian target of rapamycin complex 1 (mTORC1) inhibition (**Figure 89**). mTORC1 is a protein complex composed of five different proteins. This complex is implicated in many cellular processes but principally in protein synthesis regulation, which is essential for cellular growth. This complex is often activated in cancer cells and can be associated with cancer therapy resistance.

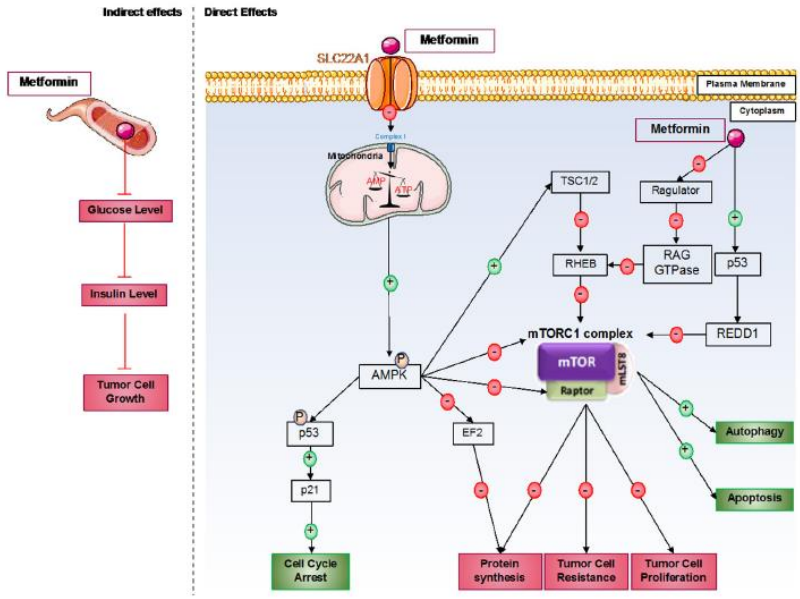

***Figure 89**. | Direct and indirect mechanisms of action of metformin in cancer cells. Metformin induces antitumorigenic effects by both indirect and direct mechanisms. In the blood circulation, metformin decreases glucose levels and therefore insulin levels; insulin can act as a growth factor in tumor cells. For direct effects, metformin acts by AMPK-dependent and independent effects. Generally, metformin induces inhibition of the mTORC1 pathway, which involves an essential protein complex in cellular processes, including protein synthesis and cell proliferation; this complex also promotes tumor cell resistance to therapies. Furthermore, metformin induces cell cycle arrest by p53 activation.*[85]

Moreover, the reduced incidence of liver, pancreatic, colorectal (CRC), and breast cancers in metformin users was reported to be 78%, 46%, 23%, and 6%, respectively, in a meta-analysis of 37 studies comprising 1,535,636 patients. Metformin causes a reduction in dimension of tumor, targets angiogenesis and metastasis in various tumor models, and inhibits tumor cell growth by targeting numerous metabolic pathways involved in cell proliferation in vitro. Finally, it inhibits cell proliferation by inducing a cell cycle arrest in G0 / G1 phase in various tumor cell line models for breast, kidney, pancreas and prostate cancer, while, in endometrial cancer cells, a stop in phases G0 / G1 and G2 / M was induced.[81]

Different results, demonstrate that metformin can suppress cancer cell growth by impairing cell cycle progression and inducing apoptosis in human cancer cells; however, the effects of metformin on cell cycle progression might vary depending on the cancer type and microenvironments.[86] we observed that metformin significantly suppressed melanoma cell motility by modulating the miR-192-5p/EFEMP1 axis. Furthermore, metformin inhibits several genes involved in cell division.[85]

Additionally, studies have demonstrated that the efficacy of metformin is affected by the change in the expression levels of membrane transporters (OCT1-4, PMAT, and MATE1-2) involved in the uptake and secretion of metformin. [81]

Due to its hydrophilicity, metformin cannot simply diffuse through cell membranes and is trans- ported inside the cell via uptake transporters. Metformin is a substrate for OCT1 (organic cation transporter 1), an uptake transporter primarily expressed in the hepatocytes. Once inside the cells, metformin accumulates in the mitochondrial matrix, presumably because of its positive charge and the polarization of the mitochondrial inner membrane [87] Metformin is a positively charged molecule and interacts with the mitochondrial membrane by virtue of its negative charge.[88]

Metformin specifically inhibits the mitochondrial respiratory chain complex 1 in a range of tissues including
hepatocytes, skeletal muscle, endothelial cells, pancreatic beta cells, and neurons. Inhibition of mitochondrial respiratory chain complex 1 induces a transient reduction in cellular energy status, which alters the balance between adenosine triphosphate (ATP) production and consumption, leading to an increase in the intracellular ratio of adenosine monophosphate (AMP) to ATP. Increased levels of AMP activate AMP-activated protein kinase (AMPK) by binding to regulatory sites, causing a conformational change in the enzyme, a process dependent on the upstream actions of the serine–threonine liver kinase B1 (LKB1). AMPK is a phylogenetically conserved protein kinase that monitors cellular energy status and protects cellular functions under energy-restricted conditions. Activation of AMPK causes the cell to switch from an anabolic to a catabolic state in an attempt to restore energy balance through phosphorylation of key metabolic enzymes and activation of transcription factors that modulate gene expression. In turn, activated AMPK leads to inhibition of gluconeogenesis, lipogenesis, and protein synthesis while stimulating fatty acid oxidation and glucose uptake in the liver.[84]

Under stimulation with metformin, the DNA damage response pathway was reactivated, decreasing in cancer cell development. In conclusion, metformin acts as a major disruptor of metabolism in cancer cells, induces an irregularity in energy metabolism and protein synthesis and activates the processes of autophagy and apoptosis.[85]

4.2.2 METFORMIN AND MELANOMA

As previously discussed, metformin can inhibit cancer cell proliferation and induce cancer cell death by many different mechanisms. In melanoma cells, it has been shown that metformin induces cell cycle arrest in melanoma cells in the G0-G1 phase after 24 h of treatment at 10mM. However, the molecular mechanism of this cell cycle arrest has not been identified in melanoma cells. Furthermore, our laboratory has also shown that this cell cycle arrest is responsible for autophagy (at 72 h) and apoptosis (at 96 h) induction by metformin in melanoma cells.[85]

Metformin significantly suppresses the motility and growth of cancer cells melanoma by inducing a cell cycle arrest at the G2 / M phase and promoting cell apoptosis. The migration ability of A375 melanoma

cells comes significantly suppressed after treatment with a metformin concentration equal to 5 mM. When A375 cells are incubated with 5 mM metformin, the number of cells in the S phase and in the G2 / M phase increases relative to the number of cells of the control group, while the number of cells in the G0 / G1 phase decreases. Finally, the number of the apoptotic cell population also increases. These results indicate that the growth of melanoma cells can be suppressed by treatments with the metformin, compromising cell cycle progression and the induction of cellular apoptosis. The suppressive effect of metformin is dose-dependent.[86]

AMPK induces a partial restoration of melanoma cell viability under metformin treatment, suggesting that AMPK plays a partial role in metformin-induced melanoma cell death. This finding also suggests that another AMPK independent mechanism is implicated in metformin-induced melanoma cell death. Metformin decreases the tumoral volume of melanoma cells. In addition, no cellular death has been observed in normal human cells, such as melanocytes, even if endogenous AMPK is expressed.
Interestingly, a recent study showed that metformin can directly act not only on melanoma cells to induce cell death but also on the tumor microenvironment, particularly in the context of an immune response. The results showed that metformin activity on melanoma cells was partly due to the immune system and that the antitumor activity of metformin was lost on immunodeficient (NSG) mice. This group also showed that metformin interaction with the immune system was principally associated with T cells. Interestingly, metformin blocks the inflammatory pathway responsible for stem cell transformation and growth due to cellular metabolism disruption.[85]

4.2.3 METFORMIN AND COMBINED THERAPY

Drugs operate differently in cell cultures and human physiology, which raises some concerns regarding the applicability of the findings of drug effects in cell cultures to humans. The first concern is that the standard range of the therapeutic plasma level of metformin in humans is 0.465–2.5 mg/L, which results when an average patient with a body weight of 60 kg receives a recommended human therapeutic daily dose (1000–2550 mg). The dose of metformin used in this study was 1–10 mM (165–1650 mg/L), leading to 30- to 400-fold excess concentrations that were far in excess of the recommended therapeutic doses.[86]

Thus, concerns regarding the usage of superphysiological concentrations of metformin in preclinical studies could be somewhat resolved by altering the expression of membrane transport proteins through the use of drugs, such as antibiotics and proton pump inhibitors, in combination with metformin to increase cellular uptake and accumulation in tumor cells. Future studies to better understand the role of membrane transport proteins in enhancing metformin's potency as an anti-cancer agent are imperative. Experimental therapeutic strategies include use of metformin in combination with other chemotherapy drugs and / or radiotherapy..[81]

The use of metformin with or without radiotherapy reduces the tumor growth in different types of cancer such as ovarian, prostate, breast cancer and melanoma.[89]

Similarly, metformin in combination with chemotherapeutic drugs have shown significant reductions in tumor and a prolonged tumor remission. In trastuzumab-resistant breast cancer cell and xenograft models.[81]

Finally, several laboratory studies have shown a higher sensitivity to chemotherapy in various cancer cell lines treated with metformin.[84]

4.3 RESULTS AND DISCUSSION-METFORMIN SALTS WITH CNTs

In our ongoing study for the production of new drug delivery systems and with the final goal to produce nano-devices[90] for the combined therapy of cancer, we have started a research activity aimed to verify the efficacy of metformin loaded CNT towards cancer cell lines. There are a few examples of Met decorated CNT in the recent literature.[91,92] In all these examples, Met is covalently linked to CNT profiting of the nucleophilic nature of the bis-guanidine group. In particular the work of Yoo and co-workers[93] is the first one to address directly the synergetic action of Met, linked to CNT, with another therapeutic effect, namely the photothermal effect. Since most of the formulations of Met are composed by its salts with different carboxylic acids, this preliminary study is dedicated to the analysis of the effect of salts of Met with oxidized MWCNTs (**2**) (**Scheme 32**) onto selected cancer cell lines. Our aim is to verify if the action of CNT can improve Met internalization by cells and reduce the amount of Met necessary to induce appreciable biological effects.

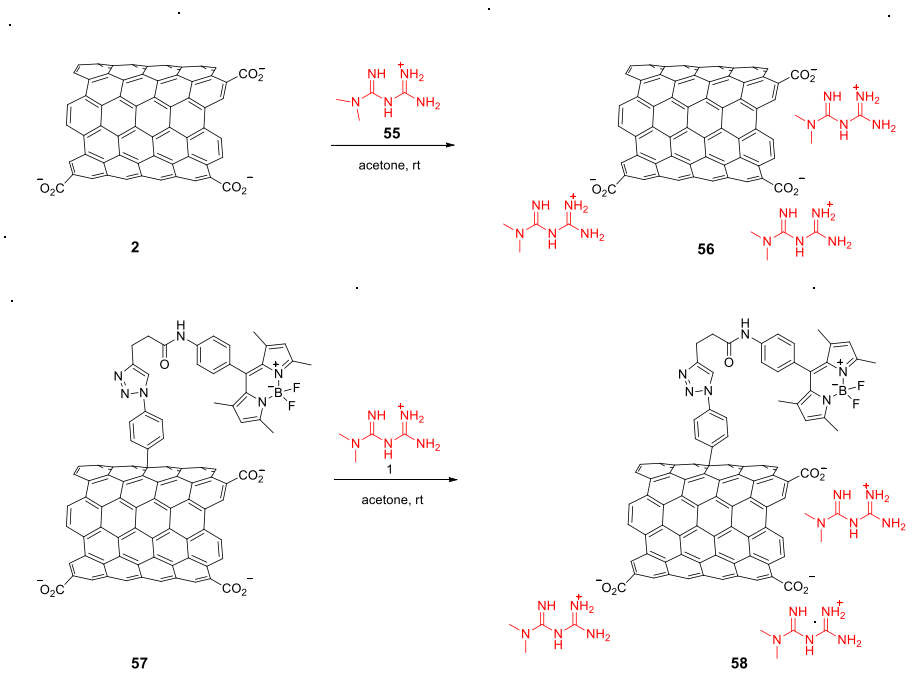

***Scheme 32**. Synthesis of Met-CNTs*

To evaluate the toxicity of the starting substrates and adducts, three different cancer cell lines, selected for their sensitivity to Met (**55**), were chosen. HT29-R [94] (colon carcinoma cell resistant to 5-fluorouracil (5-FU)), MCF7 [83] (breast cancer cell line) and PC3 [92] (human prostate cancer cell line) cells were incubated in the presence of growing doses of compounds and analyzed through MTT assay to assess the cell viability. The results are reported in **Figure 90**.

Figure 90 A shows the effect on Met (**55**) on the selected cell lines. As expected, the toxic effect of Met becomes evident at millimolar concentrations: the LD50 is between 1 and 2.5mM concentration both for HT29R and PC3 cells. **Figure 90 B** shows the effect of CNT-Met **56** on the same cell lines: the toxicity of ox-MWCNT, although more evident for HT29R, is limited in the range of concentrations used in our tests and absent for PC3 cell lines. **Figure 90 C** shows the effect of compound CNT 3. The values reported on the bottom abscissa line refer to the amount of **58** used while the values on the top abscissa line refer to the correspondent content of Met in the material.

The comparison between the values reported in **Figure 90 A** and **C** reveals that the quantity of Met used in the experiments with **58** is around 500 times lower than that used in the experiments of **Figure 90 A**. Nevertheless, the viability MCF7 cells showed a remarkable decrease when added with 10 μg/mL of **58** corresponding to 2.4 μg/mL of free Met. PC3 cell line showed an analogous behavior while HT29R cell line revealed less sensitive to **58** taking in account the intrinsic toxicity of **56** on these cells. It is well described that metformin inhibits mitochondrial respiration by blocking complex I of the electron transport chain, thus inhibiting the oxygen consumption of treated cells [95]. In order to verify the inhibitory activity of internalized metformin, we evaluated the oxygen consumption rate of treated cells. While simple ox-CNT **2** (20 μg/mL) did not alter the oxygen consumption, **58** (20 μg/mL) decreased the oxygen consumption of about 17% (p=0.07, n=2).

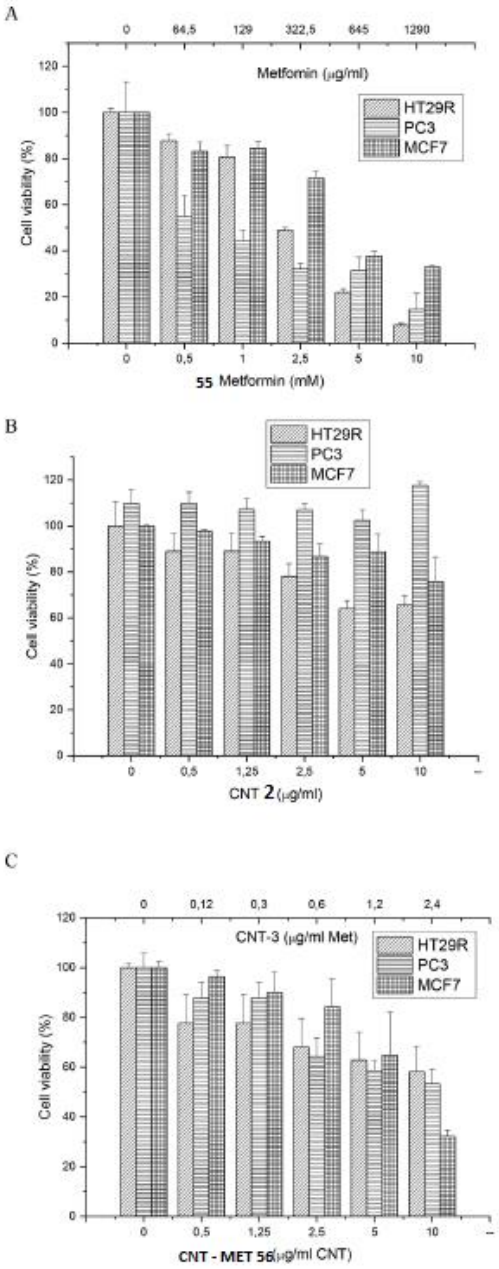

***Figure 90**. MTT vitality assays of HT29R, MCF7 and PC3 cell lines incubated with different concentration of Met (A), CNT **2** (B), CNT-MET **56** (C). Compound **56** revealed an intrinsic toxicity.*

entry	Cell type	time (h)	Control	4	5
1	**HT29R**	2	0.3	47.6	4.2
2	**HT29R**	20	2.4	83.4	5.2
2	**HT29**	2	1.5	75.4	2.7
4	**HT29**	20	2.1	90.5	4.0
5	**PC3**	2	1.8	49	5.2
6	**MCF-7**	2	2.2	81.5	2.5
7	**PANC-1**	2	5.2	12.1	5.5
8	**MDA-MB-231**	2	3.1	79.8	2.7

Tab 4. Percentage of positive cells. For each experiment, 10000 events were analyzed.

The same quantity of free Met (4.8 μg/ml) decreased the oxygen consumption of about 25% (p=0.02, n=2). In order to rationalize the toxicity effect showed by MTT tests, and to highlight any possible influence of Met in the internalization degree of CNT, we evaluated the uploading of both **57** and **58** (fluorescent analogues of 2 and 3) by using flow cytometry. After incubation with CNTs, cells were extensively washed with PBS, detached from the plastic support by trypsin treatment, and analyzed by using a FACSscan apparatus (BD Biosciences). The same gating was used for the cell incubated with the two different CNT; ten thousand cells of each sample were analyzed. The results are reported in **Table 4**.

Unexpectedly, when HT29R cells were analyzed, after 2 h of incubation with **58** (10 μg/ml), the variation of the fluorescent was negligible respect to the control experiment (**Table 4**, entry 1) suggesting that no internalization of **58** occurred. On the contrary, when the experiment was repeated with **57** (still entry 1) the increase of fluorescence was evident, confirming that **57** material is efficiently internalized (as already demonstrated in a previous work).[90]

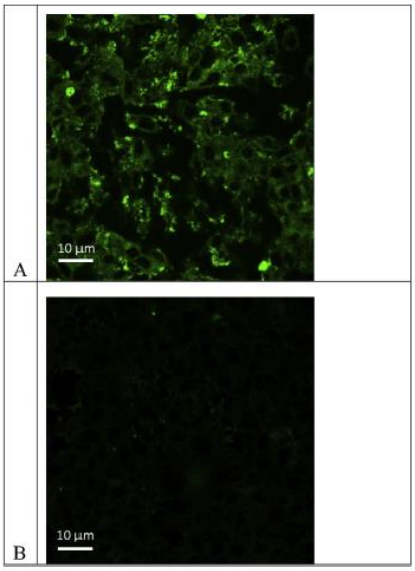

***Fig. 91**. Confocal microscopy analysis of MCF-7 cells incubated in the presence of A) **57** and B) **58**.*

Even prolonging the incubation time did not improve the internalization degree of **58** (entry 2- **Table 4**). To verify that such behavior is not related to HT29R cell type, the same analysis was extended to the other cell lines already studied in the viability tests: MCF7 (entry 6-**Table 4**), and PC3 (entry 5- **Table 4**). Again, the fluorescence values registered after 2 h of incubation with **58** are negligible with respect to the control experiment. Finally, trying to generalize the results, cytofluorimetry analyses were performed also with HT29 (entries 3 and 4- **Table 4**), PANC-1 (entry 7) and MDA-MB-231 (entry 8) cell lines. All these further experiments confirmed the previous results. The viability tests have shown that the Met salts of CNTs have a biological activity with the cell lines tested.

Although modest, such activity is obtained with low quantities of Met. Despite these results, the cytofluorimetry analyses showed that no appreciable internalization is observed, even using a larger pool of cell lines.

Finally, a confocal microscopy analysis was performed on MCF- 7 cells incubated in the presence of **57** and **58**. MCF-7 cells were incubated for 20 h with **57** (**Figure 90A**) and **58** (**Figure 90B**) at the final concentration of 10 µg/ml. The uptake of fluorescent CNTs was evaluated through confocal microscopy. The image in **Figure 90** shows that **57** undergoes a significant uptake from MCF-7 cells and that the fluorescent material is limited to the cytoplasmic region and do not enter in the nucleus, confirming previous results. Image 3B shows that no appreciable incorporation of **58** occurred, confirming the cytofluorimetric analyses results.

Finally, the inhibition of the uptake was not evidenced when MET and **57** were added separately: a cytofluorimetric analysis (MCF- 7 cell culture) shown no difference with the control experiment. The absence of internalization of **58**, appears to be an exception in the literature. Since the work by Bianco et al. [2] many other examples of diversely decorated CNT have been used as efficient DDS, confirming their general ability to cross the cellular membrane.[96] The presence of cationic species on the CNT surface does not hamper the internalization as demonstrated by the various works present in the literature in which CNT functionalized with cationic polymers are efficient DDS for transfection. However, it has been reported that internalization of CNT can be inhibited through the use of known inhibitors of specific internalization mechanisms.[97]

4.4 CONCLUSION METFORMIN SALTS WITH CNTs

The salt formed by Met and ox-MWCNT shown a dose-dependent inhibitory activity towards PC3 and MCF7 cell cultures. Although modest, this activity is significant when considering the low amount of drug administered. However, quite surprising, flow cytofluorimetry and confocal microscopy analyses demonstrated a strong inhibition of the CNT uptake induced by the presence of Met. Although the mechanism of such inhibition is still not disclosed, this observation is a striking exception in the literature data and can help in the work for shedding light on the still debated mechanism of CNT cellular uptake.

4.5 OBJECTIVES AND PRESPECTIVES OF THIS CHAPTER

Due to no profitable application of salt formed by Met and ox-MWCNT, we decided to extend our proposal modifying the chemical structure of metformin. The final goal was to achieve a metformin derivative able to interact with surface of CNT. The extension of aliphatic chain may increase the interaction with nanostructured material through chemical-physical adsorption.

DERIVATIVES OF METFORMIN

Metformin belongs to biguanidine family. Biguanides are molecules derived from guanidine and are useful in diabetes treatment. Guanidine is extracted from Galega officinalis, a plant used in medicine for many years. Indeed, this plant was used for its antidiabetic properties before its effects on glycaemia were discovered in the 1920s. Since this time, many guanidine-derived compounds have been used in type 2 diabetes, such as buformin, phenformin, and metformin. At first, metformin was not truly compared with other guanidine-derived compounds because of its less important effects on insulin sensitivity. Other biguanides, phenformin, and buformin **(Figure 92)**were widely used in diabetic treatments starting in 1920 until their high toxicity in patients was discovered in 1930. Afterwards, biguanides were no longer used in type 2 diabetes treatment until a study by French chemist Jean Sterne in 1957, where he showed metformin's effects on type 2 diabetes without apparent toxicity.[85]

4.6 RESULTS AND DISCUSSION-BIGUANIDE DERIVATIVE

4.6.1 SYNTHESIS OF BIGUANIDINE DERIVATIVE

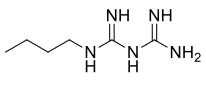

59

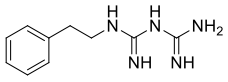

60

***Figure 92**. Buformin and Phenformin chemical structures.*

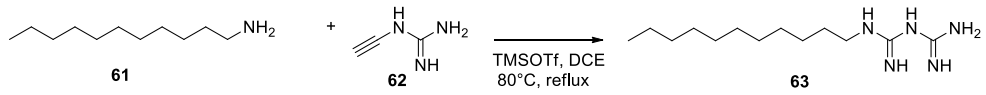

***Scheme 33**. Biguanide derivative synthesis*

Dodecylamine **61** was reacted with cyanoguanidine **62** to provide the commonly known biguanide structure **63**.

The reaction was carried out in DCE. The dodecylamine was added to TMSOTf. TMSOTf works like Lewis acid, exploiting the silylation process, it removes labile protons and decreases the basicity of the atom on which it acts. Cyanoguanidine increments its electrophilicity, nucleophilic attack by nitrogen atom of dodecylamine on the carbon involved in the triple bond is promoted.

At the end of reaction the excess of cyanoguanidine was removed through dichloromethane-water extractions. After the addition of dodecylamine, the reaction proceeded overnight. Washes were then carried out by extracting the organic phase, dissolved in DCM, with milliQ H_2O. This had the purpose of separating the cyanoguanidine present in excess from the created derivative. In fact, the cyanoguanidine remained in the aqueous phase and it was removed with a correct separation of the phases.

The obtained compound is then characterized with ^{1}H NMR, ^{13}C NMR, ESI mass and elemental analysis spectra.

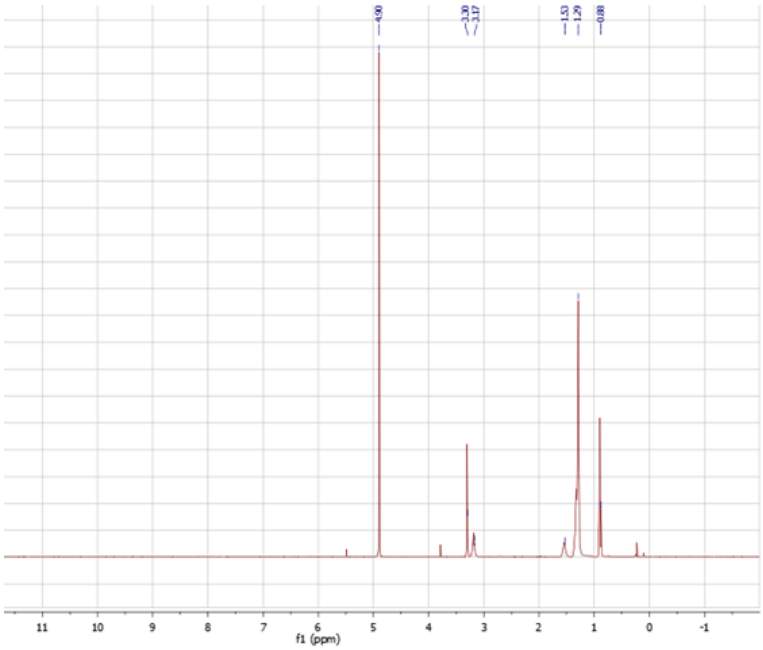

Figure 93**. ^{1}HNMR of **63

No difference compared to the spectrum of dodecylamine were showed.

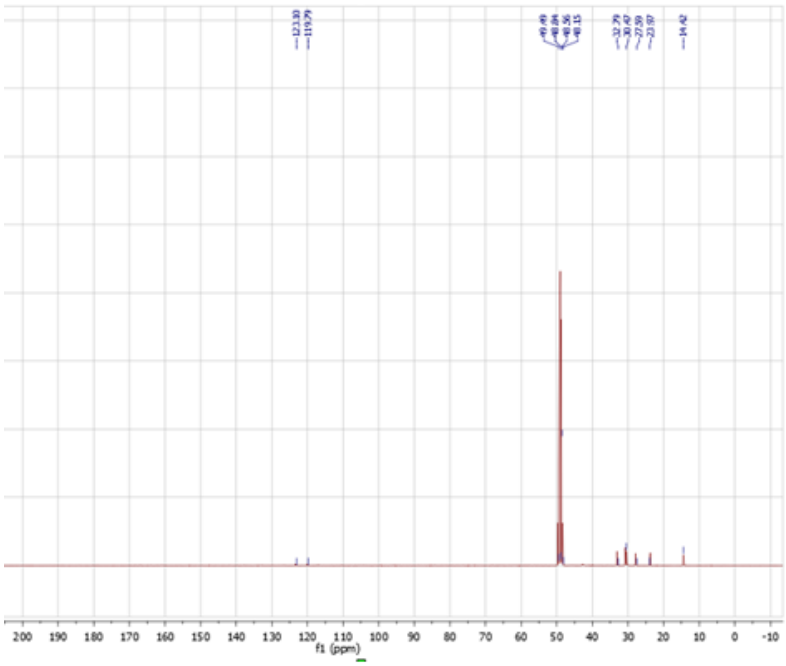

Figure 94**. [13]CNMR of **63

Comparing ^{13}C NMR of biguanidine derivative with the recorded spectrum of dodecylamine two new carbon signals around 120 ppm were revealed, suggesting the occurred reaction.
ESI-MS analysis confirmed the peck attributable to desired compound.
Elemental analysis evaluated an amount of nitrogen, carbon and hydrogen equal to: N:15.02%, C: 47.78%, H:8.06%. These percentages were probably associated to the presence of crystallized water.

4.6.2 IN VITRO TESTS OF BIGUANIDE DERIVATIVE AND METFORMIN

H2524 cell line was treated with metformin (5,00 mM) and with biguanide derivative (25,00 µM). After 20h measures at cytometry flow were performed:

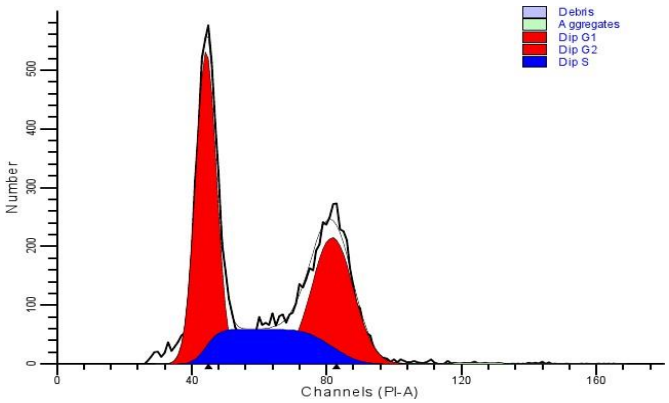

***Figure 95**.-H2524 Flow cytometry analysis*

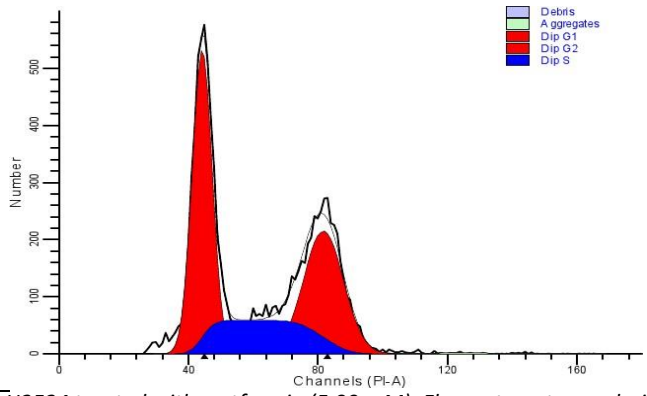

***Figure 96**. H2524 treated with metformin (5,00 mM). Flow cytometry analysis*

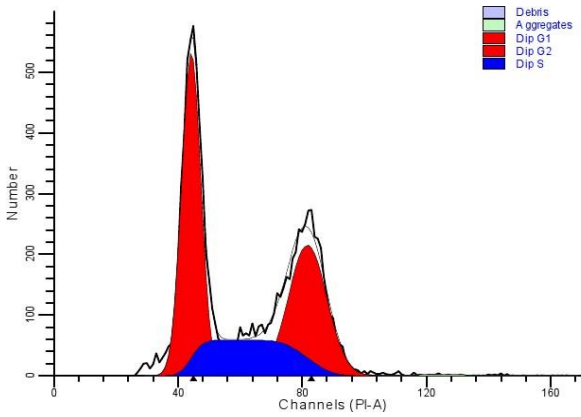

***Figure 97**.- H2524 treated with biguanide derivative (25,00 µM). Flow cytometry analysis.*

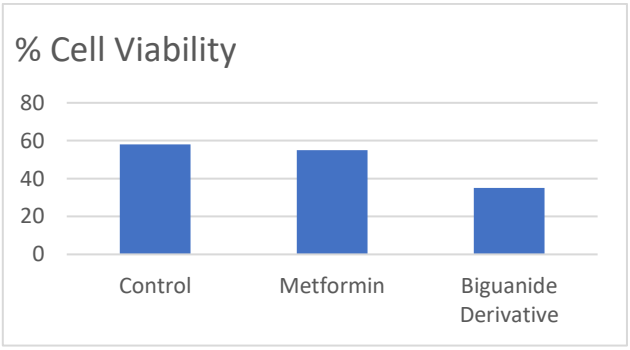

***Figure 98**. Cell cycle analysis: percentage of H2524 cells in G1 phase*

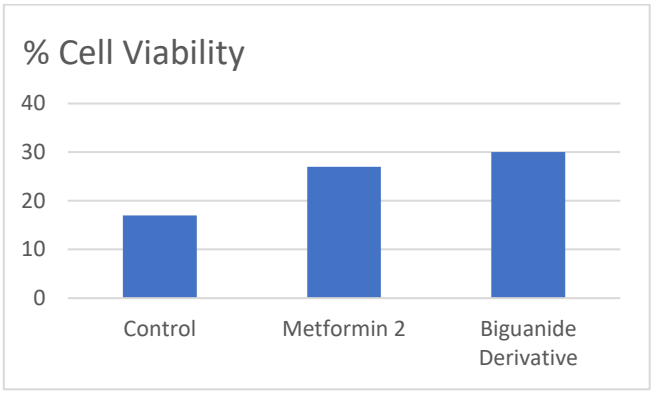

***Figure 99**. Cell cycle analysis: percentage of H2524 cells in G2/M phase*

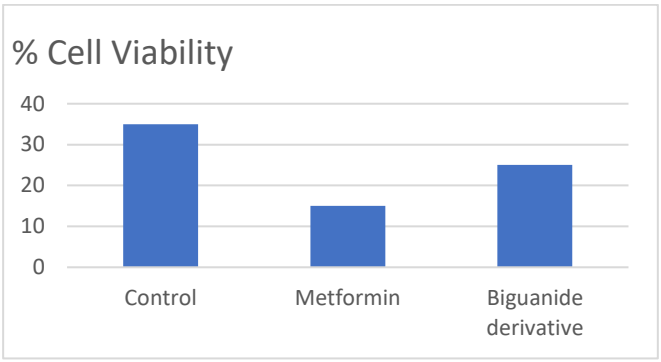

***Figure 100**. Cell cycle analysis: percentage of H2524 cells in S phase*

Metformin suggested to cause accumulation in G2 / M phase (phasse concerning cell division) and a decrease in the S phase (synthesis phase, DNA replication occurs). Biguanide derivative caused an accumulation both in S phase and in the G2 / M phase.

Based on these results the synthesized biguanidine derivative showed an action mechanism different from the mechanism possessed by metformin.

In **Figure 98, 99, 100** a comparison between the activity of metformin and biguanide derivative (dodecyl metformin) on different cell lines was showed..

Biguanide derivative (dodecyl metformin) posses an activity higher both for A375 Cell line, both for HOS Cell line and HepG2 Cell line.

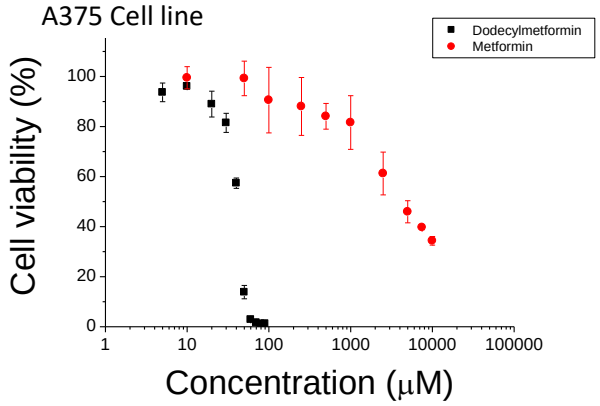

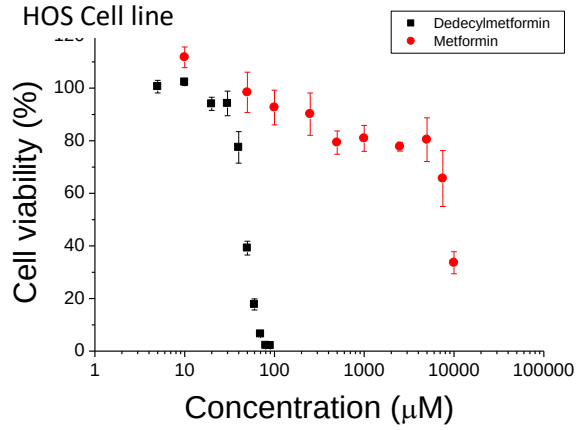

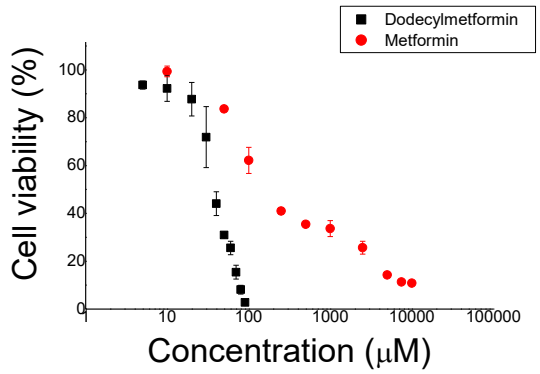

***Figure 101**. Cell viability after metformin or biguanide derivative treatment*

To study the cytotoxic effect of biguanide derivative (dodecyl metformin) on A375 cells we determined the value of LD50 (Lethal Dose 50). Cell line was treated with increasing solutions of dodecyl metformin between 5 and 100 μM; after 48 hours of incubation we evaluated cell viability with the MTT assay. In the graph in **Figure 101** were showed these results and compared to the activity of metformin. The dose

curves dependence of the two molecules established LD50 value, (an indication of the lethal toxicity of half of the population due to a given substance).

The calculated LD was 41.2 ± 0.7 µM for dodecyl metformin and 4558 ± 373 µM for metformin. These values proved that dodecyl metformin has higher cytotoxic effect, indeed, same results in cell viability were obtained by using a concentration 100 times lower of our synthesized derivative, instead of metformin.

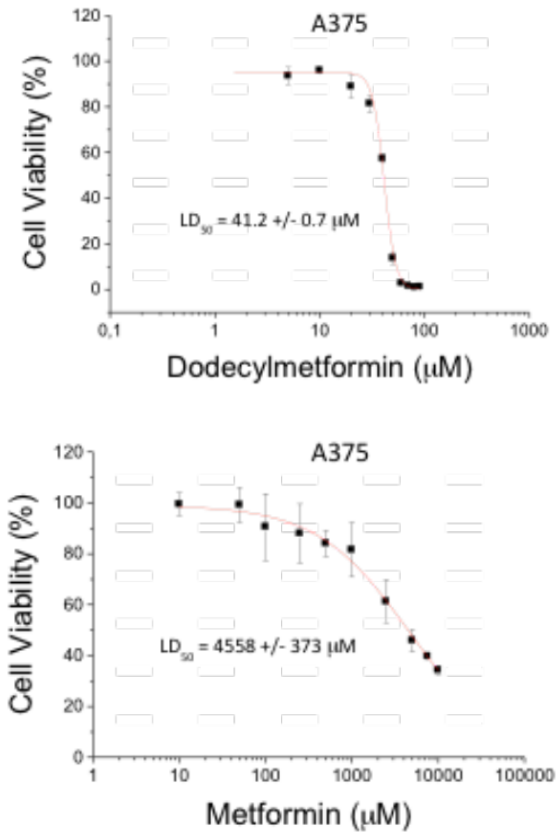

***Figure 102**. A) Determination of the LD50 value for A375 cells. After 48 hours of incubation with increasing doses of dodecyl metformin, cell viability was determined by the MTT assay. B): Determination of the LD50 value for A375 cells. After 48 hours of incubation with increasing doses of metformin, cell viability was determined by the MTT assay.*

A concerned a solution of dodecyl metformin with a concentration of 10 µM causing the death of less than 10% of cells; a 20 µM concentration caused approximately 10% of cells and a 30 µM concentration about 20% of cells death. Solutions at 10 and 20 µM concentration were sublethal doses, not causing the death of a significant number of cells.

A single dose at a concentration of 41.2 µM of dodecyl metformin caused the death of 50% of the treated melanoma cell population. We decided to perform an experiment by administering multiple times a solution of dodecyl metformin at sublethal concentrations. To study the mechanism of action of dodecyl metformin, the growth cell assay was performed by treating melanoma cells every 24 hours with sublethal doses, especially 10 and 20 µM. The results obtained are reported in **Figure 103**.

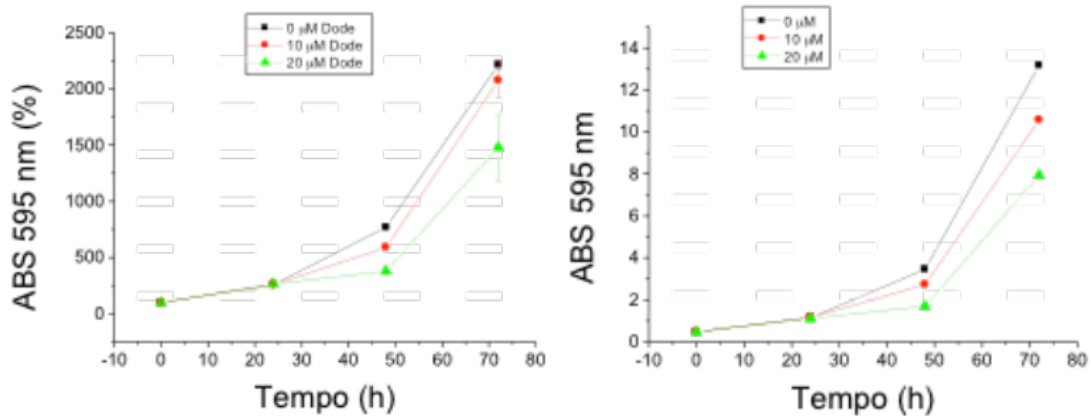

***Figure 103**. A) Graph relating to the results of the cell growth test carried out by treating cells at 0, 24, 48 and 72 hours. The black, red and green curves indicate the absorbance trend of the cells treated respectively with a solution of dodecyl metformin in concentration at 0, 10 and 20 µM and subsequently stained with crystal violet. The data obtained were normalized compared to the control. B) Graph relating to the results of the growth test carried out by treating cells at 0, 24, 48 and 72 hours. The black, red and green curves indicate the absorbance trend of the cells treated respectively with a solution of dodecyl metformin in complete medium at 0, 10 and 20 µM and subsequently stained with crystal violet. The data obtained were normalized compared to the control.*

In **Figures 103 A** dodecyl metformin derivative **63** suggested to have no effect on cells after 24 hours of treatment, while a partial activity was observed at 48 hours inhibition of proliferation by cells incubated with 20 µM solution of biguanide derivative. A minor effect, but nevertheless still evident, was observed, for cell line treated with a 10 µM solution. At 72 hours of treatment, cells proliferated independently by the presence of dodecyl metformin.

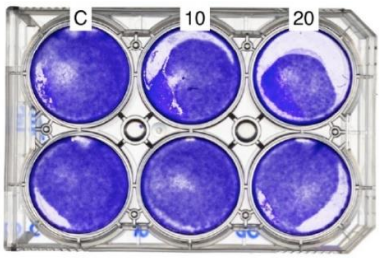

***Figure 104**. Scan of the plate containing the cells treated daily for a total of 72 hours e subsequently colored with crystal violet. The C wells marked belong to the control. Wells numbered 10 and 20 indicate cells treated with a 10 and 20 µM solution of dodecyl metformin in culture medium.*

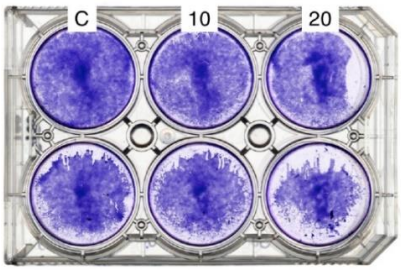

Figure 105. *Scan of the plate containing the cells treated daily for a total of 72 hours e subsequently colored with crystal violet. The C wells marked belong to the control. Wells numbered 10 and 20 indicate cells treated with a 10 and 20 µM solution of dodecyl metformin in culture medium.*

In **Figures 104** and **105** the untreated melanoma cells tend to reach the confluence and the proliferation was partially inhibited in the cells treated with daily doses of a 10 µM solution of dodecyl metformin. The inhibitory effect was higher in cells treated with daily doses of a 20 µM solution. The effect of dodecyl metformin on melanoma cells is dose dependent.

The results of the proliferation test were confirmed by the results collected through cell counting method, showed in **Figure 106**. From the graph appeared the number of cells treated with a 20 µM solution of dodecyl metformin at 24 hours was almost equivalent to untreated cells and to a cell culture treated with a 10 µM solution. At 48 hours, the proliferation was still significantly lower, and then, at 72 hours, a new increment was recorded, with an index growth close to the behavior of the other two cell cultures.

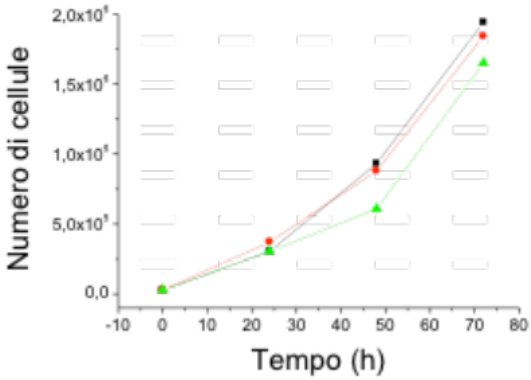

Figure 106*. Results of the cell counting method performed by treating cells at 0, 24, 48 and 72 hours. The black, red and green curves indicate the trend of the number of cells treated respectively with a dodecyl metformin solution in culture medium at 0, 10 and 20 µM. The data obtained were normalized compared to the control.*

Thanks to viability assay (**Figure 106**) the lethality of 50% of cell population after 48 hours of a single dose administration of 41,2 µM solution of dodecyl metformin was established. From cell growth assay (**figures 104** and **105**) and cell counting method confirmed that dodecyl metformin administered in sublethal daily doses has a partial antitumor effect, the cytotoxic effect is evident after 48 hours from the treatment. A dodecyl metformin solution, administered a single time with a concentration equal to 41.2 µM or daily with a concentration equal to 20 µM, posses a partial inhibitory effect on the proliferation of melanoma cells that occurs after 48 hours after the treatment. After this time, the cells no longer respond to the treatment, proliferating undisturbed.

Melanoma cells treated with 20 μM solution of biguanide derivative showed a spherical shape, causing the phenomenon of blebbing, that is the formation and resorption of bubbles on the cell plasma membrane. Although the phenomenon appeared to be critical, suggesting the death of treated cells, quite the opposite 24h after the treatment, the cells emerged to be healthy, active in proliferation and quickly insensitive to additional treatment.

For an accurate description of the phenomenon, we analyzed the A375 cells treated with dodecyl metformin using a confocal microscope. Cells treated with 20 μM solution of dodecyl metformin in culture medium were observed for 25 minutes, acquiring images every 2 seconds. A visual datum of blebbing phenomenon was obtained. Unfortunately, we haven't found yet an exhaustive explication about the phenomenon, but we hypnotize a modification and a rearrangement of the cytoskeleton, which could cause a temporary resistance to biguanide derivative.

To exclude a physical damage to the membrane, A375 cells were treated with dodecyl metformin for 1 hour. Successively the cells were incubated with a propidium iodide (PI) solution and then analyzed using a flow cytometer. The PI is not membrane-permeable, this fluorescent intercalating agent may penetrate only inside the cells showing damages.

The data reported in **Tab 5** confirmed the impossibility of cells treated for short time with dodecyl metformin solutions, to incorporate significantly a higher PI amounts compared to the dose assimilated by the control cells.
The same assay was repeated for cells chronically treated with dodecyl metformin. As showed in **Tab 6** also cells treated for 24h, 48h and 72h with the synthesized molecule didn't incorporate an excess of PI. Therefore this type of treatment induces an evident modification of cell membrane, but any permanent damages occurred.

Concentration of biguanide derivative solution (μM) required for the cellstreatment	Percentage of fluorescent cells (%)	Intensity of fluorescence
0	2	488
10	1.7	477
20	2.7	646
30	2	555
40	2.3	535
50	5.8	520

Tab 5. Results of the assay carried out by treating cells with dodecyl metformin, incubated with PI for 1h and analyzed with a flow cytometer.

Time of treatment (h)	Solution concentration of dodecyl metformin used to treat cells (µM)	Percentage of fluorescent cells (%)	Intensity of average fluorescence (nm)
24	0	1.3	382
24	10	1.8	470
24	20	1.5	367
48	0	1.9	275
48	10	0.8	415
48	20	0.8	436
72	0	1.0	429
72	10	1.2	410
72	20	1.6	360

Table 6: Results of assay carried out by chronically treating the cells with dodecyl metformin, incubated with PI for 24, 48 and 72 hours and analyzed with a flow cytometer.

Treated A375 cells tend to assume a spherical shape giving rise to blebbing. To determine if this phenomenon can promote a metastasis of tumor by causing the detachment of cells from the tissue or surface on which they are located, new assays were performed. A375 cells were incubated with increasing concentrations of dodecyl metformin for 24 hours; after this period, the cells t in the medium of culture, no longer adhered, were recovered and plated again, to evaluate their ability to adhere and proliferate. The plates containing the treated cells were stained with violet crystal to evaluate the quantity of detached cells (**figures 107** and **108**).

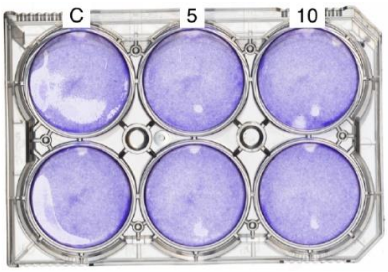

Figure 107*. Scan of the plate containing the treated cells. The cells are been colored with crystal violet. The wells marked C are the control wells, those numbered 5 and 10 indicate the cells treated with a 5 and 10 µM solution of dodecyl metformin in medium, respectively full.*

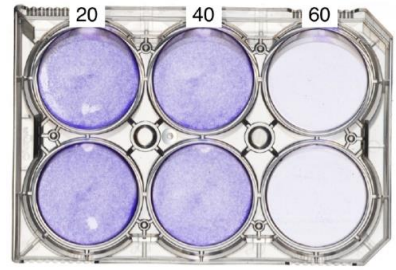

***Figure 108**. Scan of the plate containing the treated cells. The cells were colored with crystal violet. Wells numbered 20, 40 and 60 indicate the treated cells with a 20, 40 and 60 µM solution of dodecyl metformin respectively in medium culture*.

In accordance with the results obtained from the growth and proliferation assays, in the graph in **Figure 109** is shown as 24 hours of dodecyl metformin treatment didn't cause inhibition on cells treated with concentrations of solution equal to 5, 10 and 20 µM. Instead, an inhibition was observed for cells treated with a concentration of 40 and 60 µM respectively.

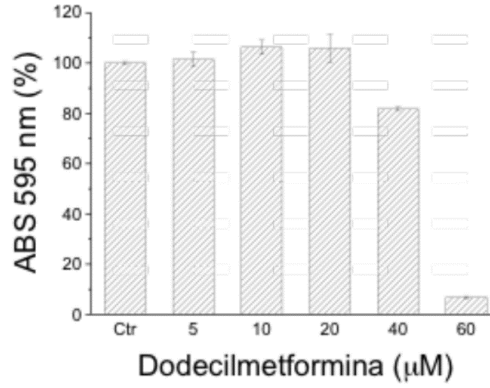

***Figure 109.** Quantification of crystal violet release by the treated cells. After staining, the cells incorporating the crystal violet were treated with 1 mL of DMSO for 10 minutes. Subsequently, the DMSO is recovered, and the absorbance measured by a spectrophotometer. The data obtained were normalized compared to the control.*

After 6 days, the plates containing the detached cells were stained with crystal violet (**Figures 110** and **111**).

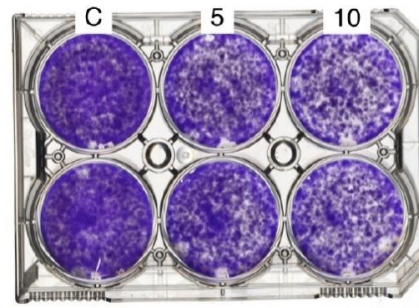

***Figure 110**. Scan of the plate containing the detached cells and were plated again. The cells were stained with crystal violet. The wells marked C were the control, wells numbered 5 and 10 indicate the cells treated with a 5 and 10 µM solution, respectively of dodecyl metformin in culture medium.*

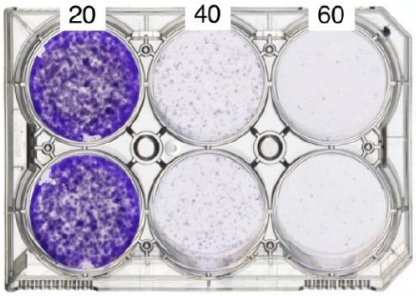

Figure 111. Scan of the plate containing the cells that had detached and were plated again. The cells were stained with crystal violet. Wells numbered 20, 40 and 60 indicate cells treated with a 20, 40 and 60 µM solution of dodecyl metformin in medium culture.

We added 1 mL of DMSO to each well and the plates were rocked for 10 minutes. After this time the absorbance of the various solutions were analyzed to spectrophotometer (**Figure 112**).

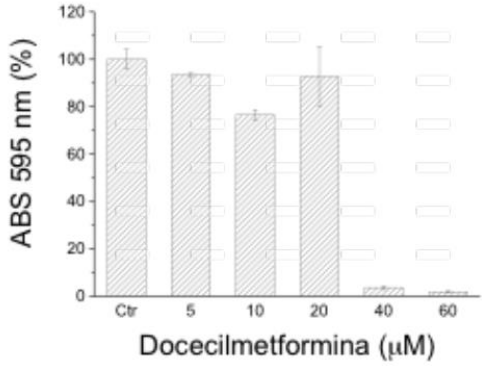

Figure 112*. Quantification of crystal violet release by the treated cells. After staining, the cells incorporating the crystal violet were treated with 1 mL of DMSO for 10 minutes. Subsequently, the DMSO is recovered, and the absorbance measured by a spectrophotometer. The data obtained were normalized compared to the control.*

The obtained results showed a progressive cell detachment of treated cells, a phenomenon dose-dependent. At the same time, the detached cells recovered from the controls (cells untreated) tend to adhere and proliferate rapidly.

However the treated cells showed a lower tendency to adhesion and proliferation. This behavior appeared strictly dose-dependent. The collected data suggested that the biguanidine derivative could act as antimetastatic agent, preventing the adhesion and proliferation of cells detached from a tumor mass, thus blocking metastatic dissemination.
Since melanoma cells show a tendency to detach from the primary tumor mass, entering in the bloodstream or lymphatic stream, we tested the possibility of treated cells to adhere to a tissue or their tendency to die when suspended in the blood/lymphatic stream. The adherent cells were detached and plated again in presence of increasing concentrations of dodecyl metformin. To evaluate the amount of cells adhered and proliferated, after 5 days the cells were colored with crystal violet. (**Figure 113 and 114).**

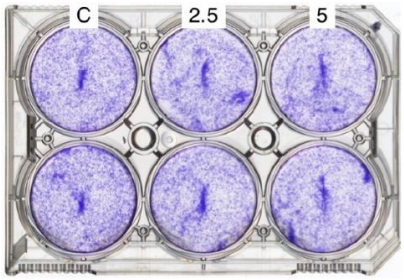

Figure 113*. Scan the plate containing the cells that have been treated in suspension and then plated. The cells were stained with violet crystals. The wells marked C are the control. Wells numbered with 2.5 and 5 indicate the cells treated with a solution 2.5 and 5 respectively µM of dodecyl metformin in medium culture.*

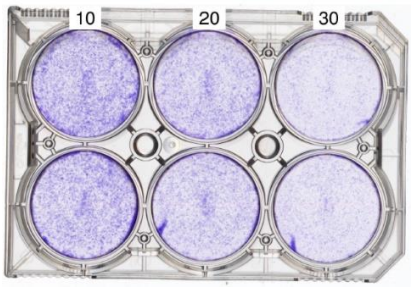

Figure 114. *Scan the plate containing the cells that have been treated in suspension and then plated. The cells were stained with crystal violet. Wells numbered 10, 20 and 30 indicate the cells treated with a 10, 20 and 30 µM solution of dodecyl metformin, respectively, in medium culture.*

The graph in (**Figure 115**) showed that dodecyl metformin caused the decrease of the adhesion of A375 cells of about 20% at 20 µM concentrations and about 50% with a concentration of 30 µM. Quite the opposite, dodecyl metformin appeared to cause an increase in the cited phenomenon of about 10% at 10 µM concentration and less than 10% at 2.5 and 5 µM concentrations.
These assays confirmed that dodecyl metformin promoted the adhesion of melanoma cells in concentrations below 10 µM, instead concentration above 20 µM caused a disadvantage adhesion.

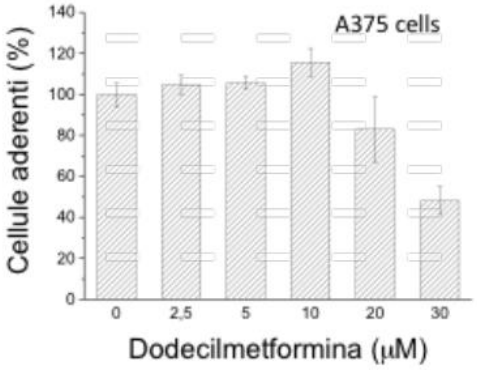

Figure115*. Quantification of the crystal violet released by the cells. After staining, the cells incorporating the crystal violet were treated with 1 mL of DMSO for 10 minutes. Subsequently, the DMSO was recovered, and the absorbance measured by a spectrophotometer. The data obtained were normalized compared to the control.*

4.6.3 SYNTHESIS OF CNT-BIGUANIDE DERIVATIVE

The collected assays demonstrated the good activity of the synthesized biguanide derivative. Our studies were focused on the synthesis of a nanohybrid consisting in biguanide derivative adsorbed on carbon nanotubes.

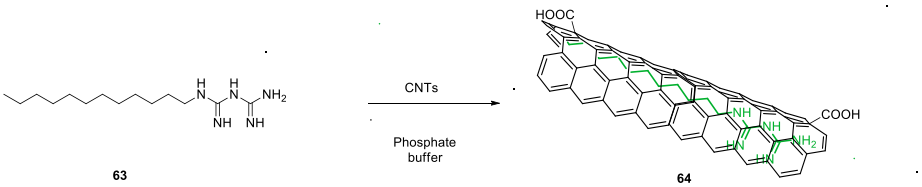

Figure 116. *Synthesis of compound* ***64****.*

This type of functionalization exploited the chemical-physical characteristics of the carbon nanotubes. This type of adsorption did not significantly disturb the structure of the CNTs, but allowed to modify its electronic and transport properties.

Previously the functionalization was already used with another type of drug, doxorubicin, also studied as anticancer drug, biologically active in cells thanks to this functionalization.

The decoration of CNTs with this technique allowed to verify their effective interaction with the long aliphatic chain present on the synthesized biguanide derivative. A phosphate buffer solution at pH 7.4 was used to solubilize the biguanide derivative. The buffer was required to protonate the free amine of the biguanide derivative. By adding CNTs, the protonated amines could bind the nanostructured material through adsorption, preventing the interaction with the carboxylic group to form salts. Compound **64** was obtained after a treatment in an ultrasonic bath for 1 hour, after which the dispersion was filtered with buffer and H2O milliQ. This product was characterized with elemental analysis:

Elemental analysis: N: 5.85%, C: 74.79%, H: 2.92%

The loading degree of biguanide derivative was equal to 0.8 mmol/ g of material.

4.6.4 IN VITRO ASSAYS

Biological assays were carried out on functionalized CNTs. A population of HT29R, which is a type of colon cancer cells resistant to 5-FU and HT29 were used to test compound **64**. The cells were incubated for approximately 72 hours at a temperature of 37 °C.

The culture medium was initially HT29R, subsequently treated with 5-FU. To these cells were administered increasing doses (0.5, 2.5, 5, 10, 20 µg / mL) of functionalized CNTs with biguanide derivative.

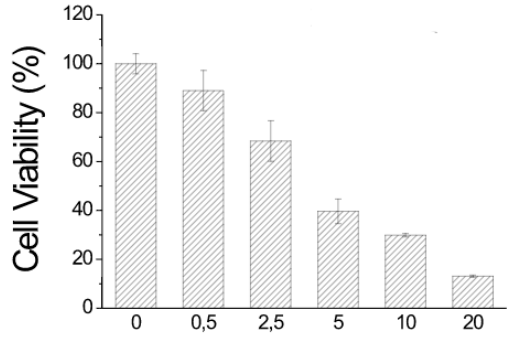

Figure 117. *HT29R con fCNTs*

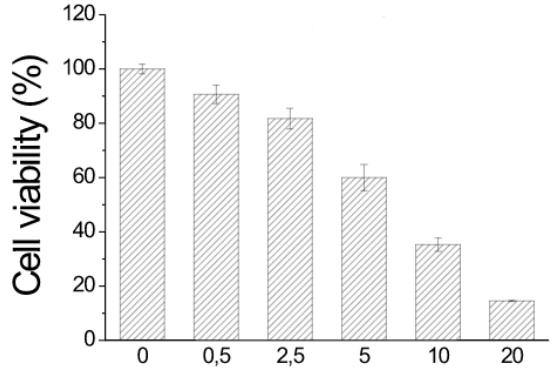

Figure 118. *HT29R con 5-FU e fCNTs*

No differences were noticed between HT29R cells treated with 5-FU or not. A high biological activity even at low concentrations (such as 0.5 µg / mL) up to a mortality rate of up to 80%.
On a population of HT29 cells, not resistant to 5-FU, functionalized CNTs were administered by adsorption both in a complete medium and in a starvation medium.

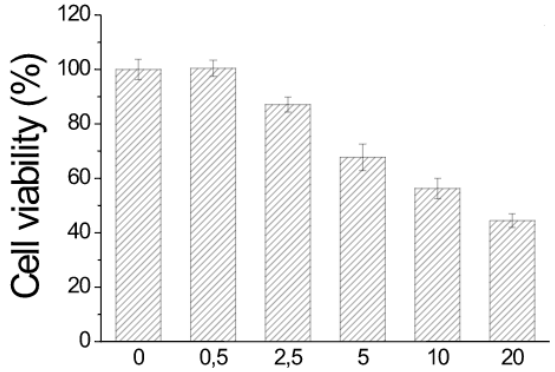

Figure 119. *HT29 with fCNTs in complete medium*

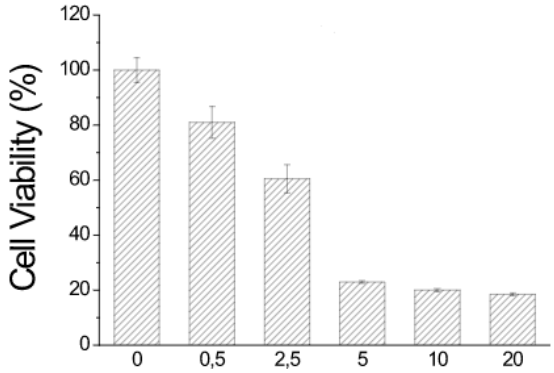

Figure 120. *HT29 with fCNTs in starvation medium*

In this biological assay, a reduction in cell viability of 80% was reported, more marked than the crystal violet described below. These more marked reductions could be due to MTT which was metabolized by mitochondrial dehydrogenases. In the presence of complete medium, a reduction in mitochondrial activity was observed, rather than in vitality.
A hypothesis could be that to compensate the reduction in mitochondrial activity, the cells may be able to increase the speed of glycolysis.
Crystal Violet represented another cell viability assay. The incubation lasted 48 hours and to the cells were administrated the crystal violet dye which enters only in alive or not damaged cells.

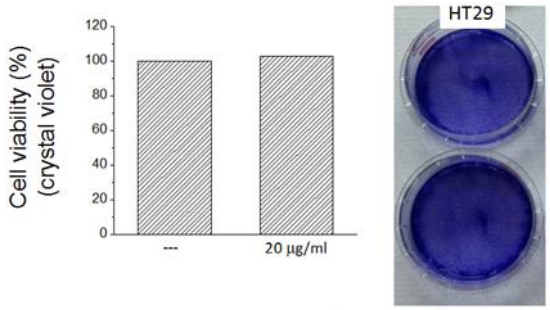

Figure 121. *HT29 with fCNTs in complete medium*

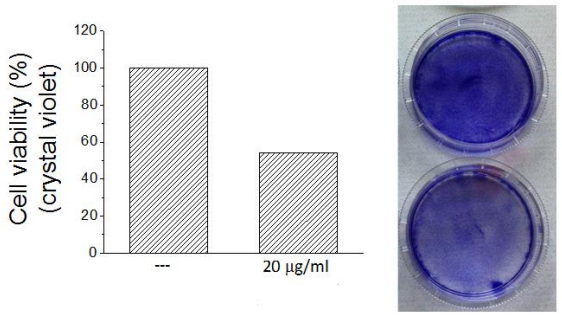

Figure 122. *HT29 with fCNTs in starvation medium*

Crystal violet assay showed a reduced cell viability, equal to 50% (**Figure 121**), MTT assay had provided 80% of reduction. The synthesized molecule exhibited biological activity, but if administered to cells grown in complete medium, no decrease in viability was observed. In starvation medium, quite the opposite, a reduction in viability due to the use of a medium devoid of factors that stimulate growth and glycolysis, was observed in both assays. Since these cells were forced to use more respiration to survive, the biguanide derivative appeared to have a greater effect with a consequent reduction in proliferation or viability.

Other assays were instead performed on a population of HT29R with and without 5-FU with the crystal violet assay. These data have not been verified with the MTT assay.

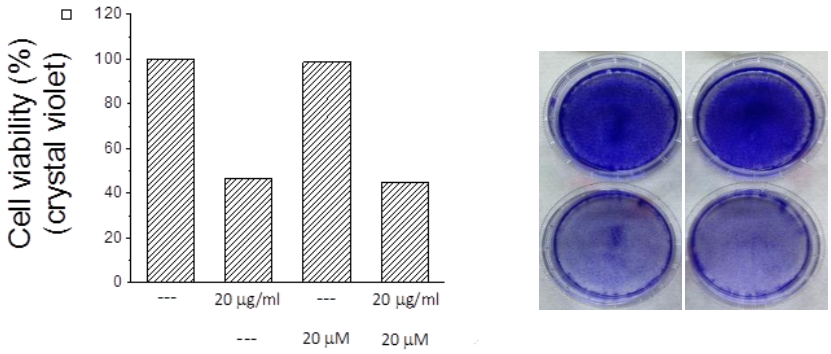

Figure 123. *HT29R with fCNTs in complete medium, with or without 5-FU*

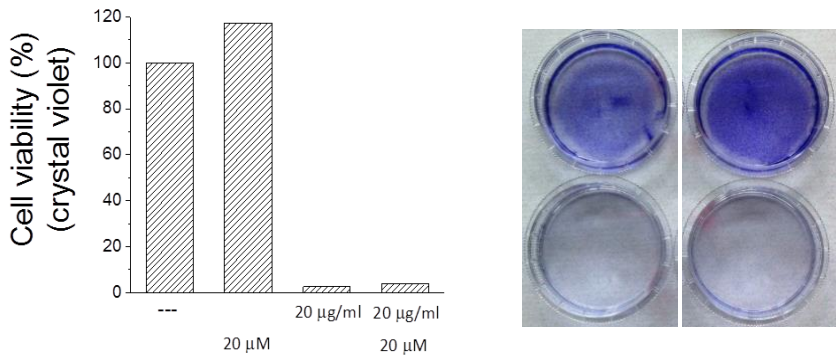

Figure 124. *HT29R with fCNTs in starvation medium, with or without 5-FU*

The viability of resistant cells is not affected by the presence of 5-FU, as expected. These cells were more dependent on respiration to survive. In starvation medium, cells were very sensitive to the biguanide derivative, their cell viability was reduced by almost 100%, as showed in (**Figure 124**).

4.7 CONCLUSION

Several studies proved as patients treated with metformin for diabetes disease showed a reduced incidence of cancer, longer survival to tumors, less metastasis and smaller dimension of mass tumor; compared to patients treated with another antidiabetic drug.

Metformin posses direct and indirect mechanisms which allows to block the cellular cycle and to induce apoptosis in cancer cells with consequent reduction of cell proliferation.
Metformin, in addition, causes metabolic alterations and changes in protein synthesis, metformin activates the processes of autophagy and apoptosis.
The antidiabetic drug metformin also has anticancer properties.
This drug allows only appreciable effect at concentrations so high as to cause serious side effects to the body. Consecutive studies focused on synthesize a derivative of metformin, with a higher activity, which allows to lower administration.

The viability test showed how biguanide derivative showed same toxicity of biguanide derivative, but at concentrations 100 times lower. No data on the possible side effect of biguanide derivative *in vivo* were collected, but the results obtained through *in vitro* assays suggested that the risk of a possible cytotoxic effect should be lower compared to metformin administration.

The proliferation assays showed a partial inhibitory effect of dodecyl metformin on melanoma cell proliferation that occurred after 48 hours of treatment. After 48 hours, the treated cells appeared insensitive to treatment, the cells proliferated independently from the presence of biguanide derivative. A single critical dose or repeated administrations of sublethal doses possessed a partial anticancer effect which is evident after 48 hours of
treatment.
The presented data promote a possible in vivo application of the molecule; many anticancer drugs are administered in cycles consisting of several doses every day. The partial inhibitory effect of dodecyl metformin on the proliferation of cancer cells could lead to a reduction in tumor volume. Future experiments will be performed to establish the reason why after 48h of treatment, the cells develop a certain resistance.

Immediately after a treatment with dodecyl metformin, A375 cells were studied at confocal microscopy. An interesting and curious aspect was the phenomenon of blebbing which occurred immediately after the administration of biguanide derivative, suggesting a possible death of cells. Instead, after 24 hours, cells proliferated, acquiring their original form. Furthermore after about thirty minutes, the blebbing phenomenon blocked and A375 cells resulted insensitive to further treatment. All cells didn't show the same behavior, a part of them were not characterized by this particular phenomenon.

All these data confirmed that dodecyl metformin causes a physical alteration of the cell, probably inducing a rearrangement of the cytoskeleton that concerns the creation and reabsorption of bubbles by the cell membrane. The occurred phenomenon, is not permanent and irreversible. No physical damage is observed, as demonstrated by the assays carried out with the PI.
Future studies will be focused on the temporary developped resistance of melanoma cells subsequent to the treatments, as well as the mechanism by which dodecyl metformin induces these particular phenomena in the cell.

A375 cells were treated with biguanide derivative, therefore the detached cells were plate again. The tendency of treated cells to proliferate again was dose-dependent.
Dodecyl metformin could promote melanoma cell detachment from the adhesion surface, but these detached cells could be not able to adhere to a new surface, or they could undergo cell death.

By treating melanoma cells in suspension and plating them, important effects of biguanide derivative were showed: dodecyl metformin has an inhibitory effect on the adhesion of cells that are in suspension.

We can conclude that dodecyl metformin could constitute a promising antimetastatic drug.

The sublethal and critical concentrations of dodecyl metformin suggest an accessible administration to patients, a weak inhibitory effect of cell proliferation which could lead to a tumor volume reduction and to an important dose-dependent inhibitory effect on metastasis.

The synthesized derivative CNTs-biguanide derivative (fCNTs) showed a lower activity compared to the molecule of biguanide derivative.

MTT and crystal violet assays were performed on fCNTs. The cell viability was significantly affected: on a population of HT29R, with a mortality up to 80% for higher concentrations, which we can also observe with HT29 cells in starvation medium. For the crystal violet assay, populations of HT29R were analyzed in complete and starvation medium. In starvation medium, cell mortality was observed up to 100% of the entire population.

4.8 MATERIALS AND METHODS

Synthesis of compound **56/58**

The salts **56** and **58** were produced mixing **2** or **57** (20 mg) with the same amount of free 1 in 10 ml of acetone under prolonged sonication (10 min). The resulting suspensions were filtered on 200 nm pore Teflon filters, washed repeatedly with fresh acetone and dried under vacuum for 24 h.
The loading of Met was evaluated through elemental analysis: **56** contained 1,86 mmol/g (elemental analysis N, 13,02%) while **58** contained 0.56 mmol/g of material (elemental analysis N, 8.32% starting form compound **57**
Elemental analysis N, 4.37%). TEM analysis of **56** did not show any significant variation respect to **2**.

In vitro Biological Assay

HT29, HT29R, PC3, PANC1, MCF/, MDA-MB-231 cell lines were routinely growth in DMEM medium supplemented with 10% fetal bovine serum, 100 µg/ml penicillin, 100 µg/ml streptomycin and 100 µg/ml L-glutamine (Sigma-Aldrich, St. Louis, USA) in a humidified atmosphere with 5% CO2 at 37 °C. Cell viability was evaluated by using MTT assay (Sigma-Aldrich). Cells were incubated with 0.5 µg/ml MTT solution for 1 h at 37 °C. After removing cell culture medium, DMSO was added to dissolve the insoluble MTT-formazan salt. Results were detected at 595 nm on a microplate reader (BioRad). CNTs internalization was analyzed by using Flow Cytometry. Briefly, cancer cells were grown in 35mm dishes until 60% of confluence and treated with 10 µg/ml of fluorescent carbon nanotubes for different interval times at 37 °C. Then, cells were extensively washed with PBS, trypsinized and collected in DMEM medium. Cells were pelleted by centrifugation, and washed with PBS before flow cytometric analysis using a FACSCanto flow cytometer (Becton-Dickinson). The carbon nanotubes incorporation in MCF7 cells was evaluated by using confocal microscopy. Briefly, 0.5×106 cells were plated on a glass cover slips and then incubated in the presence of 10 µg/ml, of BODIPY decorated carbon nanotubes containing

or not metformin. After 20 h, glass cover slips were extensively washed with PBS, and fixed in 3% paraformaldehyde for 30 min at room temperature before the analysis with the confocal fluorescence microscope. The analysis was made using a Leica TCS SP5 confocal scanning microscope (Leica Microsystems, Mannheim, Germany), equipped with an argon laser source and a Leica Plan Apo 639 oil immersion objective. MCF7 cells treated with Met (1), CNT 2, CNT 3 for 24 h, were trypsinized, washed with PBS and resuspended in complete DMEM medium at the concentration of 106 cells/ml. One ml of cell suspension was transferred to an airtight chamber maintained at 37 °C and oxygen consumption was measured using a Clark-type O2 electrode (Hansatech) Oxygen content was monitored for at least 10 min. The rate of decrease in oxygen content, related to protein amount was taken as index of the respiratory capability.

SYNTHESIS OF compound **63**

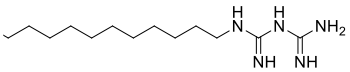

The reaction was carried out in dry DCE (40 mL). Cyanoguandine **62** (400 mg, 4.7 mmol, 2.9 eq) was dissolved in the solvent, under nitrogen atmosphere, then TMSOTf (0.75mL, 2.8 mmol, 1.8 eq) was added. After 30 'at room temperature dodecylamine **61** (367 mg, 1.6 mmol, 1eq) was put in the flask and then the solution was refluxed in an oil bath, under nitrogen flow at 80 ° C overnight.
The crude product was dissolved in EtOAc (70 mL) and then extracted by washing with H2O milliQ (40 mL x 3). The organic phase was dried on Na2SO4 and then filtered. The crude obtained (695 mg) was purified by chromatography column (EtOAc, hexane). Yield 86%.

^{1}H NMR(400 mHz, CD_3OD): δ 0.88 (CH_3), 1.40-1.29 (m, 10H, CH_2), 3.17 (1H, CH_2) ppm.

^{13}C NMR(400 MHz, CD_3OD): δ 14.42 (s, 1C, I), 23.97 (s, 1C, H), 27.39 (s, 1C, C), 30.47 (s, 1C, F), 32.79 (s, 1C, D), 48.15 (s, 4C, E), 48.56 (s, 1C, G), 48.84 (s, 1C, B), 49.49 (s, 1C, A), 119.79 (s, 1C, L), 123.10 (s, 1C, M) ppm.

H2524

H2524 mesothelioma cells were placed in an incubator at 37 ° C, in a humidified atmosphere with 5% CO2, in a culture medium, containing glucose, amino acids, fatty acids, various metals, and antibiotics.

Flow Cytometry

The H2524 cells, plated in P60, were treated with both solutions (3 mL) of metformin (5.00 mM), and with solutions (3 mL) of dodecyl metformin (25.00 µM), making a technical duplicate for each solution. After 20 h the cells were observed to verify that they were alive. Subsequently, the medium was aspirated in each well, washed with PBS (2 mL), aspirated again and then placed 600 µL of a hypotonic solution (propidium iodide (50.00 mg / mL), sodium citrate (0.1%) and NP40 Cell Lysis Buffer (0.1%)). Finally, the measurement was carried out with the flow cytometer.

Proliferation Assay

We performed the proliferation assays to assess the cell proliferation capacity of melanoma treated with 10 and 20 µM dodecyl metformin solutions in complete medium. Melanoma cells were cultured in 2 mL of complete medium in wells of three MultiWell 6 and two P35. The two 35mm plates were needed to acquire the zero time, the three MultiWells to acquire the times at 24, 48 and 72 hours. The first day we carried out the count on the two P35s and treated the cells present in the Multiwell, the following days we performed the protocol on a Multiwell and treated the remaining ones. Cells plated in the MultiWell wells were treated following the diagram below:

C	10	20
C	10	20

The wells marked C are the control wells, those numbered 10 and 20 indicate the cells treated with a 10 and 20 µM solution of dodecyl metformin in respectively complete culture.

We sucked the soil from the wells with the vacuum pump, we made two wash with 1 mL of PBS and we added 1 mL of 0.5% crystal violet solution in 20% MeOH. After placing the plates in the incubator for 5 minutes, we aspirated the violet crystal solution with a pipette and recovered it in a 50 mL falcon; we did a wash with 1 mL of PBS and put the plate on an oscillator for 5 minutes. We carried out two more washes, in the last of which we used 2 mL of PBS, and after each wash we put the plate ad swing for 5 minutes. We added 1 mL of DMSO to the wells and put the plates on the oscillator for 10 minutes. At the spectrophotometer we measured the absorbance of the solutions present in the various wells, the blank was set with 1 mL of DMSO. We collected the measurements at a wavelength of 595 nm and an optical path of 1 cm.

The crystal violet was a cellular dye that works in vivo, internalized into all cells but unable to get out of living cells. The function of MeOH, inside of the dye solution, was its ability to dehydrate the cells and to crystallize them in the temporary situation.

DMSO (dimethyl sulfoxide) is an organic solvent capable of breaking the membrane plasma cell. The crystal violet inside the living cells comes into solution. The obtained values of absorbance were directly proportional to the quantity of dye in the solution and, therefore, to the number of live cells in the well. For this reason is very important that, ideally, the only dye present inside of the plate is the probes

found in living cells. After the application of dye repeated and careful washing were carried out to eliminate the dye which did not enter the cells, but which remained present inside the plate.

Proliferation Assay: Cell Count Assay with BÜCKER ROOM

The cell count assay was used to determine if dodecyl metformin has an inhibitory activity on cell proliferation at 10 and 20 µM concentrations. The cells were plated in two P35 and in two MultiWell 6, the diagram below was followed:

C	10	20
C	10	20

The wells marked with C were the control wells, while those numbered 10 and 20 indicate cells treated with a 10 and 20 µM solution of biguanide derivative in complete medium.
After 24 hours from the plating, the protocol was carried out on the two P35 and the cells present in the Multiwells were treated. The following days the protocol was performed on a Multiwell and the remaining ones were treated.

After the cells washing with 1 mL of PB, for two times; 3 drops of trypsin were added in each plate and putting them back in the incubator for 3 minutes. When the cells detached,1 mL of complete medium to each plate was added.
The cells were picked up and transferred by capillarity to Bücker's chamber. Under the optical microscope the cells were counted in eight quadrants belonging to the two grids, we averaged the counts and multiplied it by 10 000 to get the number of cells present in one milliliter of suspension. We then multiplied the number for the actual volume of suspension present inside the well, obtaining the total number of cells inside the well.
After treating the cells with trypsin and incubating them for 3 minutes, 1 mL of complete medium was added to block the action of trypsin which, otherwise, it would damage cellular proteins.

Short time (1h) PI Assay

To verify if dodecyl metformin created immediate damage to membrane, PI assay in a short time (1 h) was performed.
We plated the cells in 6 P35; after 24 hours, we vacuumed the ground and we have treated the cells in such a way as to have six plates containing a solution respectively 0, 10, 20, 30, 40 50 µM dodecyl metformin in complete medium. After 1 hour, we have washed the discs twice with 2 mL of PBS, we detach the cells with trypsin and we added 1 mL of complete medium. We have transferred the contents of each P35 into six 15 mL falcons and centrifuged for 5 minutes, then aspirated the medium on top of the pellet and resuspended the cells in 500 µL of an isotonic solution at concentrations below 10 mg / mL of propidium iodide (PI) in PBS. After about twenty minutes, we analyzed the samples on a flow cytometer measuring the percentage and, therefore, the number of fluorescent cells and the average fluorescence intensity.

Long time (24h, 48h, 72h) PI Assay

To determine if dodecyl metformin causes cell membrane damage after 24, 48 and 72 hours of processing PI assays were performed after these periods of time.
The cells were plated in three 6 x MultiWells following the diagram below:

C	10	20
C	10	20

The wells marked C are the control wells, those numbered 10 and 20 indicate the cells treated with a 10 and 20 µM solution of dodecyl metformin in respectively complete culture.
Every day we repeated PI assay protocol in a short time on a MultiWell, and the cells in the remaining MultiWells were treated at the same rate.

Cell detachment Assay

We performed the cell detachment assay to determine if dodecyl metformin caused the detachment of A375 cells from the surface to which cells were attached and if, consequently, the metastasis of melanoma was promoted.
Melanoma cells were plated in two 6-inch MultiWells, waiting to reach 70% of the confluence. After having aspirated the culture from the wells of the MultiWell, we treated the cells following the scheme below:

C	5	10	20	40	60
C	5	10	20	40	60

The wells marked with C are the control, those marked with 5, 10, 20, 40 and 60 indicate cells treated with a solution of 5, 10, 20, 40 and 60 µM of biguanide derivative in complete medium.

After 24 hours, some cells were detached. After aspirating the cell suspensions consisting of complete medium and the detached cells. We centrifuged the cell suspensions for 5 minutes at 1000 rpm, we aspirated the medium, and the cells were dispersed again in 4 mL of complete medium. The cells were plated again in two 6-inch MultiWells following the pattern described above and placed them in the incubator. We applied the assay protocol of growth to the cells of the two starting MultiWells, or to the cells that remained adhered to the plates.

Cell Adhesion Assay

Inside the human body, suspended melanoma cells were detached from the main tumor entering into the bloodstream or lymphatic stream and generating metastases. We carried out the adhesion assay to test if dodecyl metformin may inhibit the metastasis process, thus preventing the cancer cells suspended in the circulation blood or lymphatic to adhere to new tissue.

We detached A375 cells, then we created a suspension cell in complete medium in a 50 mL falcon. In different falcons we added 4 mL of cell suspension and a quantity of dodecyl metformin such as to obtain solutions with concentrations of 0, 2.5, 5, 10, 20 and 30 µM. We have added 2 mL of cell suspension and dodecyl metformin to the wells of the two MultiWell following the diagram below:

C	2.5	5	10	20	30
C	2.5	5	10	20	30

The wells marked with C are the control, those marked with 2.5, 5, 10, 20 and 30 indicate cells treated with a solution of 2.5, 5, 10, 20 and 30 μM of dodecyl metformin in complete medium. We waited for the check cells reached at least 80% of confluence in order to perform the assay of cell growth.

Since the solutions of DMSO and crystal violet formed inside the wells were concentrated enough to saturate the spectrophotometer, it was necessary to dilute 10 times the solutions with DMSO.

4.9 REFERENCES

1. Biagiotti, G. *et al.* Multiwalled carbon nanotubes for combination therapy: A biodistribution and efficacy pilot study. *J. Mater. Chem. B* **7**, 2678–2687 (2019).

2. Kostarelos, K. *et al.* Cellular uptake of functionalized carbon nanotubes is independent of functional group and cell type. *Nat. Nanotechnol.* **2**, 108–113 (2007).

3. Liu & Speranza. Functionalization of Carbon Nanomaterials for Biomedical Applications. *C — J. Carbon Res.* **5**, 72 (2019).

4. Curcio, M. *et al.* Functionalized carbon nanostructures versus drug resistance: Promising scenarios in cancer treatment. *Molecules* **25**, 1–31 (2020).

5. Perkins, B. L. & Naderi, N. Carbon Nanostructures in Bone Tissue Engineering. *Open Orthop. J.* **10**, 877–899 (2017).

6. Erol, O. *et al.* Recent advances in bioactive 1D and 2D carbon nanomaterials for biomedical applications. *Nanomedicine Nanotechnology, Biol. Med.* **14**, 2433–2454 (2018).

7. Tasis, D., Tagmatarchis, N., Bianco, A. & Prato, M. Chemistry of carbon nanotubes. *Chem. Rev.* **106**, 1105–1136 (2006).

8. Kumar, S., Rani, R., Dilbaghi, N., Tankeshwar, K. & Kim, K. H. Carbon nanotubes: A novel material for multifaceted applications in human healthcare. *Chem. Soc. Rev.* **46**, 158–196 (2017).

9. Hong, S. Y. *et al.* Filled and glycosylated carbon nanotubes for in vivo radioemitter localization and imaging. *Nat. Mater.* **9**, 485–490 (2010).

10. Wohlstadter, J. N. *et al.* Carbon nanotube-based biosensor. *Adv. Mater.* **15**, 1184–1187 (2003).

11. Fedeli, S. *et al.* Azido-Substituted BODIPY Dyes for the Production of Fluorescent Carbon Nanotubes. *Chem. - A Eur. J.* **21**, 15349–15353 (2015).

12. Mooney, E., Dockery, P., Greiser, U., Murphy, M. & Barron, V. Carbon nanotubes and mesenchymal stem cells: Biocompatibility, proliferation and differentiation. *Nano Lett.* **8**, 2137–2143 (2008).

13. Guo, J., Wang, Y. & Zhao, M. Target-directed functionalized ferrous phosphate-carbon dots fluorescent nanostructures as peroxidase mimetics for cancer cell detection and ROS-mediated therapy. *Sensors Actuators, B Chem.* **297**, 126739 (2019).

14. Janyasupab, M. & Promptmas, C. Development of non-enzymatic N-doped graphene supported cobalt/iron amperometric based sensor for glucose detection in urine. *2018 IEEE EMBS Conf. Biomed. Eng. Sci. IECBES 2018 - Proc.* 577–582 (2019) doi:10.1109/IECBES.2018.8626693.

15. Chiang, Y. C., Lin, W. H. & Chang, Y. C. The influence of treatment duration on multi-walled carbon nanotubes functionalized by H 2 SO 4 /HNO 3 oxidation. *Appl. Surf. Sci.* **257**, 2401–2410 (2011).

16. Chattopadhyay, D., Lastella, S., Kim, S. & Papadimitrakopoulos, F. Length separation of zwitterion-functionalized single wall carbon nanotubes by GPC. *J. Am. Chem. Soc.* **124**, 728–729 (2002).

17. Li, J. & Zhang, Y. Large-scale aligned carbon nanotubes films. *Phys. E Low-Dimensional Syst. Nanostructures* **33**, 235–239 (2006).

18. submitted to Nature on Feb 5, 2004. (2004).

19. Allen, M. J., Tung, V. C. & Kaner, R. B. Honeycomb carbon: A review of graphene. *Chem. Rev.* **110**, 132–145 (2010).

20. Park, S. & Ruoff, R. S. Chemical methods for the production of graphenes. *Nat. Nanotechnol.* **4**, 217–224 (2009).

21. Reina, A. *et al.* Growth of large-area single- and Bi-layer graphene by controlled carbon precipitation on polycrystalline Ni surfaces. *Nano Res.* **2**, 509–516 (2009).

22. Jiao, L., Wang, X., Diankov, G., Wang, H. & Dai, H. Facile synthesis of high-quality graphene nanoribbons. *Nat. Nanotechnol.* **5**, 321–325 (2010).

23. Coliman, J. P. *et al.* "Picket Fence Porphyrins". Synthetic Models for Oxygen Binding Hemoproteins. *J. Am. Chem. Soc.* **97**, 1427–1439 (1975).

24. Brinker, C. J., Lu, Y., Sellinger, A. & Fan, H. ChemInform Abstract: Evaporation-Induced Self-Assembly: Nanostructures Made Easy. *ChemInform* **30**, no-no (2010).

25. Sutter, P., Sadowski, J. T. & Sutter, E. Graphene on Pt(111): Growth and substrate interaction. *Phys. Rev. B - Condens. Matter Mater. Phys.* **80**, 1–10 (2009).

26. Staudenmaier, L. Method for the preparation of the graphite acid. *Eur. J. Inorg. Chem.* **31**, 1481–1487 (1898).

27. Zhang, X. *et al.* Distribution and biocompatibility studies of graphene oxide in mice after intravenous administration. *Carbon N. Y.* **49**, 986–995 (2011).

28. Pan, S. & Aksay, I. A. Factors controlling the size of graphene oxide sheets produced via the graphite oxide route. *ACS Nano* **5**, 4073–4083 (2011).

29. Gonçalves, P. A. D. & Peres, N. M. R. An Introduction to Graphene Plasmonics. *An Introd. to Graphene Plasmon.* 1–431 (2016) doi:10.1142/9948.

30. Pan, Y., Sahoo, N. G. & Li, L. The application of graphene oxide in drug delivery. *Expert Opin. Drug Deliv.* **9**, 1365–1376 (2012).

31. Li, Q.-Y., Zu, Y.-G., Shi, R.-Z. & Yao, L.-P. Review Camptothecin: Current Perspectives. *Curr. Med. Chem.* **13**, 2021–2039 (2006).

32. Liu, Z., Robinson, J. T., Sun, X. & Dai, H. PEGylated nanographene oxide for delivery of water-insoluble cancer drugs. *J. Am. Chem. Soc.* **130**, 10876–10877 (2008).

33. Rana, V. K. *et al.* Synthesis and drug-delivery behavior of chitosan-functionalized graphene oxide hybrid nanosheets. *Macromol. Mater. Eng.* **296**, 131–140 (2011).

34. Eigler, S., Grimm, S., Enzelberger-Heim, M., Müller, P. & Hirscha, A. Graphene oxide: Efficiency of reducing agents. *Chem. Commun.* **49**, 7391–7393 (2013).

35. Hunt, A. *et al.* Epoxide speciation and functional group distribution in graphene oxide paper-like materials. *Adv. Funct. Mater.* **22**, 3950–3957 (2012).

36. Szabó, T. *et al.* Evolution of surface functional groups in a series of progressively oxidized graphite oxides. *Chem. Mater.* **18**, 2740–2749 (2006).

37. Dimiev, A. M., Alemany, L. B. & Tour, J. M. Graphene oxide. Origin of acidity, its instability in water, and a new dynamic structural model. *ACS Nano* **7**, 576–588 (2013).

38. Liu, Y., Yu, D., Zeng, C., Miao, Z. & Dai, L. Biocompatible graphene oxide-based glucose biosensors. *Langmuir* **26**, 6158–6160 (2010).

39. Paquin, F., Rivnay, J., Salleo, A., Stingelin, N. & Silva, C. Multi-phase semicrystalline microstructures drive exciton dissociation in neat plastic semiconductors. *J. Mater. Chem. C* **3**, 10715–10722 (2015).

40. Yu, R. *et al.* Synthetic possibility of polystyrene functionalization based on hydroxyl groups of graphene oxide as nucleophiles. *New J. Chem.* **39**, 5096–5099 (2015).

41. Chen, H. *et al.* Phosphorylation of graphehe oxide to improve adsorption of U(VI) from aquaeous solutions. *J. Radioanal. Nucl. Chem.* **313**, 175–189 (2017).

42. De Leon, A. C., Alonso, L., Mangadlao, J. D., Advincula, R. C. & Pentzer, E. Simultaneous Reduction and Functionalization of Graphene Oxide via Ritter Reaction. *ACS Appl. Mater. Interfaces* **9**, 14265–14272 (2017).

43. Liao, K. H., Lin, Y. S., MacOsko, C. W. & Haynes, C. L. Cytotoxicity of graphene oxide and graphene in human erythrocytes and skin fibroblasts. *ACS Appl. Mater. Interfaces* **3**, 2607–2615 (2011).

44. Lu, C. H. *et al.* Using graphene to protect DNA from cleavage during cellular delivery. *Chem. Commun.* **46**, 3116–3118 (2010).

45. Wojtoniszak, M. *et al.* Synthesis, dispersion, and cytocompatibility of graphene oxide and reduced graphene oxide. *Colloids Surfaces B Biointerfaces* **89**, 79–85 (2012).

46. Yuan, J. *et al.* Cytotoxicity evaluation of oxidized single-walled carbon nanotubes and graphene oxide on human hepatoma HepG2 cells: An iTRAQ-coupled 2D LC-MS/MS proteome analysis. *Toxicol. Sci.* **126**, 149–161 (2012).

47. Chang, Y. *et al.* In vitro toxicity evaluation of graphene oxide on A549 cells. *Toxicol. Lett.* **200**, 201–210 (2011).

48. Bhattacharya, K. *et al.* Biological interactions of carbon-based nanomaterials: From coronation to degradation. *Nanomedicine Nanotechnology, Biol. Med.* **12**, 333–351 (2016).

49. Kurapati, R. *et al.* Dispersibility-Dependent Biodegradation of Graphene Oxide by Myeloperoxidase. *Small* **11**, 3985–3994 (2015).

50. Chen, S. *et al.* Mechanism-based tumor-targeting drug delivery system. Validation of efficient vitamin receptor-mediated endocytosis and drug release. *Bioconjug. Chem.* **21**, 979–987 (2010).

51. Lee, J. S. *et al.* Synthesis of a BODIPY library and its application to the development of live cell glucagon imaging probe. *J. Am. Chem. Soc.* **131**, 10077–10082 (2009).

52. Kaur, P. & Singh, K. Recent advances in the application of BODIPY in bioimaging and chemosensing. *J. Mater. Chem. C* **7**, 11361–11405 (2019).

53. Moss, G. P. Nomenclature of tetrapyrroles (Recommendations 1986). *Pure Appl. Chem.* **59**, 779–832 (1987).

54. van Koeveringe, J. A. & Lugtenburg, J. Novel pyrromethenes 1-Oxygen and 1-sulfur analogues; evidence for photochemical. *Recueil, J. R. Netherlands Chem. Soc.* **96**, 55–57 (1977).

55. Solomonov, A. V., Marfin, Y. S. & Rumyantsev, E. V. Design and applications of dipyrrin-based fluorescent dyes and related organic luminophores: From individual compounds to supramolecular self-assembled systems. *Dye. Pigment.* **162**, 517–542 (2019).

56. Li, Z., Mintzer, E. & Bittman, R. First synthesis of free cholesterol-BODIPY conjugates. *J. Org. Chem.* **71**, 1718–1721 (2006).

57. Wagner, R. W. & Lindsey, J. S. Boron-dipyrromethene dyes for incorporation in synthetic multi-pigment light-harvesting arrays. *Pure Appl. Chem.* **68**, 1373–1380 (1996).

58. Thivierge, C., Bandichhor, R. & Burgess, K. Spectral dispersion and water solubilization of BODIPY dyes via palladium-catalyzed C-H functionalization. *Org. Lett.* **9**, 2135–2138 (2007).

59. Shah, M. *et al.* Pyrromethene–BF2 complexes as laser dyes:1. *Heteroat. Chem.* **1**, 389–399 (1990).

60. Yogo, T., Urano, Y., Ishitsuka, Y., Maniwa, F. & Nagano, T. Highly efficient and photostable photosensitizer based on BODIPY chromophore. *J. Am. Chem. Soc.* **127**, 12162–12163 (2005).

61. Scheibe, B., Borowiak-Palen, E. & Kalenczuk, R. J. Oxidation and reduction of multiwalled carbon nanotubes - preparation and characterization. *Mater. Charact.* **61**, 185–191 (2010).

62. Jameson, L. P. & Dzyuba, S. V. Expeditious, mechanochemical synthesis of BODIPY dyes. *Beilstein J. Org. Chem.* **9**, 786–790 (2013).

63. Andersen, J., Madsen, U., Björkling, F. & Liang, X. Rapid synthesis of aryl azides from aryl halides under mild conditions. *Synlett* 2209–2213 (2005) doi:10.1055/s-2005-872248.

64. Ménard-Moyon, C., Fabbro, C., Prato, M. & Bianco, A. One-pot triple functionalization of carbon nanotubes. *Chem. - A Eur. J.* **17**, 3222–3227 (2011).

65. Lin, H. B., Cooper, S. L., Zhao, Z. C., Garcia-Echeverria, C. & Rich, D. H. Synthesis of a novel polyurethane co-polymer containing covalently attached RGD peptide. *J. Biomater. Sci. Polym. Ed.* **3**, 217–227 (1992).

66. Van Agthoven, J. F. *et al.* Structural Basis of the Differential Binding of Engineered Knottins to Integrins αVβ3 and α5β1. *Structure* **27**, 1443-1451.e6 (2019).

67. Sheldrake, H. M. & Patterson, L. H. Strategies to inhibit tumor associated integrin receptors: Rationale for dual and multi-antagonists. *J. Med. Chem.* **57**, 6301–6315 (2014).

68. Maligaspe, E. *et al.* Photosynthetic antenna-reaction center mimicry: Sequential energy- and electron transfer in a self-assembled supramolecular triad composed of boron dipyrrin, zinc porphyrin and fullerene. *J. Phys. Chem. A* **113**, 8478–8489 (2009).

69. Mori, H. *et al.* In silico and pharmacological screenings identify novel serine racemase inhibitors. *Bioorganic Med. Chem. Lett.* **24**, 3732–3735 (2014).

70. Hishikawa, K. *et al.* Photoinduced nitric oxide release from a hindered nitrobenzene derivative by two-photon excitation. *J. Am. Chem. Soc.* **131**, 7488–7489 (2009).

71. Mallesha, N., Prahlada Rao, S., Suhas, R. & Channe Gowda, D. An efficient synthesis of tert-butyl ethers/esters of alcohols/amino acids using methyl tert-butyl ether. *Tetrahedron Lett.* **53**, 641–645 (2012).

72. Mock, J. N. *et al.* Haloenol pyranones and morpholinones as antineoplastic agents of prostate cancer. *Bioorganic Med. Chem. Lett.* **22**, 4854–4858 (2012).

73. König, W. & Geiger, R. Eine neue Methode zur Synthese von Peptiden: Aktivierung der Carboxylgruppe mit Dicyclohexylcarbodiimid unter Zusatz von 1-Hydroxy-benzotriazolen. *Chem. Ber.* **103**, 788–798 (1970).

74. Pérez-Picaso, L., Escalante, J., Olivo, H. F. & Rios, M. Y. Efficient microwave assisted syntheses of 2,5-diketopiperazines in aqueous media. *Molecules* **14**, 2836–2849 (2009).

75. Styers, T. J. *et al.* Synthesis of Sansalvamide A derivatives and their cytotoxicity in the MSS colon cancer cell line HT-29. *Bioorganic Med. Chem.* **14**, 5625–5631 (2006).

76. Lundt, B. F., Johansen, N. L., Vølund, A. & Markussen, J. REMOVAL OF t-BUTYL AND t-BUTOXYCARBONYL PROTECTING GROUPS WITH TRIFLUOROACETIC ACID: Mechanisms, Biproduct Formation and Evaluation of Scavengers. *Int. J. Pept. Protein Res.* **12**, 258–268 (1978).

77. Hughes, A. B. Amino Acids, Peptides and Proteins in Organic Chemistry. *Amin. Acids, Pept. Proteins Org. Chem.* **2**, (2010).

78. Vardhan, D. M. S., Kumara, H. K., Kumar, H. P. & Gowda, D. C. Inhibition of Urease Enzyme Activity By Urea and Thiourea Derivatives of Dipeptides Conjugated 2, 3-Dichlorophenyl Piperazine. *Int. J. Pharm. Pharm. Sci.* **9**, 92 (2017).

79. Kaur, A., Poonam, Patil, M. T., Mehta, S. K. & Salunke, D. B. An efficient and scalable synthesis of potent TLR2 agonistic PAM2CSK4. *RSC Adv.* **8**, 9587–9596 (2018).

80. Brough, P., Klumpp, C., Bianco, A., Campidelli, S. & Prato, M. [60]fullerene-pyrrolidine-N-oxides. *J. Org. Chem.* **71**, 2014–2020 (2006).

81. Saini, N. & Yang, X. Metformin as an anti-cancer agent: Actions and mechanisms targeting cancer stem cells. *Acta Biochim. Biophys. Sin. (Shanghai).* **50**, 133–143 (2018).

82. Pierotti, M. A. *et al.* Targeting metabolism for cancer treatment and prevention: Metformin, an old drug with multi-faceted effects. *Oncogene* **32**, 1475–1487 (2013).

83. Alimova, I. N. *et al.* Metformin inhibits breast cancer cell growth, colony formation and induces cell cycle arrest in vitro. *Cell Cycle* **8**, 909–915 (2009).

84. Morales, D. R. & Morris, A. D. Metformin in cancer treatment and prevention. *Annu. Rev. Med.* **66**, 17–29 (2015).

85. Jaune, E. & Rocchi, S. Metformin: Focus on melanoma. *Front. Endocrinol. (Lausanne).* **9**, 1–9 (2018).

86. Tseng, H. W., Li, S. C. & Tsai, K. W. Metformin treatment suppresses melanoma cell growth and motility through modulation of microRNA expression. *Cancers (Basel).* **11**, (2019).

87. Vancura, A., Bu, P., Bhagwat, M., Zeng, J. & Vancurova, I. Metformin as an Anticancer Agent. *Trends Pharmacol. Sci.* **39**, 867–878 (2018).

88. Mallik, R. & Chowdhury, T. A. Metformin in cancer. *Diabetes Res. Clin. Pract.* **143**, 409–419 (2018).

89. Saraei, P., Asadi, I., Kakar, M. A. & Moradi-Kor, N. The beneficial effects of metformin on cancer prevention and therapy: A comprehensive review of recent advances. *Cancer Manag. Res.* **11**, 3295–3313 (2019).

90. Fedeli, S. *et al.* The 'click-on-tube' approach for the production of efficient drug carriers based on oxidized multi-walled carbon nanotubes. *J. Mater. Chem. B* **4**, 3823–3831 (2016).

91. Baghayeri, M., Tehrani, M. B., Amiri, A., Maleki, B. & Farhadi, S. A novel way for detection of antiparkinsonism drug entacapone via electrodeposition of silver nanoparticles/functionalized multi-walled carbon nanotubes as an amperometric sensor. *Mater. Sci. Eng. C* **66**, 77–83 (2016).

92. Mirazi, N., Shoaei, J., Khazaei, A. & Hosseini, A. A comparative study on effect of metformin and metformin-conjugated nanotubes on blood glucose homeostasis in diabetic rats. *Eur. J. Drug Metab. Pharmacokinet.* **40**, 343–348 (2015).

93. Yoo, S. *et al.* Enhanced Response of Metformin towards the Cancer Cells due to Synergism

with Multi-walled Carbon Nanotubes in Photothermal Therapy. *Sci. Rep.* 1–9 (2017) doi:10.1038/s41598-017-01118-3.

94. Denise, C. *et al.* 5-Fluorouracil resistant colon cancer cells are addicted to OXPHOS to survive and enhance stem-like traits. *Oncotarget* **6**, 41706–41721 (2015).

95. Ota, S. *et al.* Metformin suppresses glucose-6-phosphatase expression by a complex I inhibition and AMPK activation-independent mechanism. *Biochem. Biophys. Res. Commun.* **388**, 311–316 (2009).

96. Chen, Z. *et al.* The Advances of Carbon Nanotubes in Cancer Diagnostics and Therapeutics. *J. Nanomater.* **2017**, (2017).

97. Cui, X., Wan, B., Yang, Y., Ren, X. & Guo, L. H. Length effects on the dynamic process of cellular uptake and exocytosis of single-walled carbon nanotubes in murine macrophage cells /631/80 /704/172 /82/29 /14/19 /14/34 /123 article. *Sci. Rep.* **7**, 1–13 (2017).

98. Yuan, Y. M. & He, C. The glial scar in spinal cord injury and repair. *Neurosci. Bull.* **29**, 421–435 (2013).

99. Su, Z. *et al.* Reactive astrocytes inhibit the survival and differentiation of oligodendrocyte precursor cells by secreted TNF-α. *J. Neurotrauma* **28**, 1089–1100 (2011).

100. Liu, W. *et al.* Folic acid conjugated magnetic iron oxide nanoparticles for nondestructive separation and detection of ovarian cancer cells from whole blood. *Biomater. Sci.* **4**, 159–166 (2016).

101. Stichel, C. C. & Müller, H. W. The CNS lesion scar: New vistas on an old regeneration barrier. *Cell Tissue Res.* **294**, 1–9 (1998).

102. Galtrey, C. M. & Fawcett, J. W. The role of chondroitin sulfate proteoglycans in regeneration and plasticity in the central nervous system. *Brain Res. Rev.* **54**, 1–18 (2007).

103. Bradbury, E. J. & Carter, L. M. Manipulating the glial scar: Chondroitinase ABC as a therapy for spinal cord injury. *Brain Res. Bull.* **84**, 306–316 (2011).

104. Silver, J. & Miller, J. H. Regeneration beyond the glial scar. *Nat. Rev. Neurosci.* **5**, 146–156 (2004).

105. Place, L. W., Sekyi, M. & Kipper, M. J. Aggrecan-mimetic, glycosaminoglycan-containing nanoparticles for growth factor stabilization and delivery. *Biomacromolecules* **15**, 680–689 (2014).

106. Marchesan, S., Kostarelos, K., Bianco, A. & Prato, M. The winding road for carbon nanotubes in nanomedicine. *Mater. Today* **18**, 12–19 (2015).

107. Pinillos-Madrid, J. F. & Gallardo, C. Carbon nanotubes: A viable drug delivery platform for the treatment of cancer. *J. Appl. Pharm. Sci.* **5**, 143–152 (2015).

108. Moradian, H., Fasehee, H., Keshvari, H. & Faghihi, S. Poly(ethyleneimine) functionalized carbon nanotubes as efficient nano-vector for transfecting mesenchymal stem cells. *Colloids Surfaces B Biointerfaces* **122**, 115–125 (2014).

109. Herrero, M. A. *et al.* Synthesis and characterization of a carbon nanotube-dendron series for efficient siRNA delivery. *J. Am. Chem. Soc.* **131**, 9843–9848 (2009).

110. Zhou, M., Peng, Z., Liao, S., Li, P. & Li, S. Design of microencapsulated carbon nanotube-based microspheres and its application in colon targeted drug delivery. *Drug Deliv.* **21**, 101–109 (2014).

111. Zhang, W., Zuo, X. D. & Wu, C. W. Synthesis and magnetic properties of carbon nanotube-iron oxide nanoparticle composites for hyperthermia: A review. *Rev. Adv. Mater. Sci.* **40**, 165–176 (2015).

112. Jones, L. L., Margolis, R. U. & Tuszynski, M. H. The chondroitin sulfate proteoglycans neurocan, brevican, phosphacan, and versican are differentially regulated following spinal cord injury. *Exp. Neurol.* **182**, 399–411 (2003).

113. Tom, V. J., Steinmetz, M. P., Miller, J. H., Doller, C. M. & Silver, J. Studies on the development and behavior of the dystrophic growth cone, the hallmark of regeneration failure, in an in vitro model of the glial scar and after spinal cord injury. *J. Neurosci.* **24**, 6531–6539 (2004).

114. Matthews, R. T. *et al.* Aggrecan glycoforms contribute to the molecular heterogeneity of perineuronal nets. *J. Neurosci.* **22**, 7536–7547 (2002).

115. Sandvig, A., Berry, M., Barrett, L. B., Butt, A. & Logan, A. Myelin-, reactive glia-, and scar-derived CNS axon growth inhibitors: Expression, receptor signaling, and correlation with axon regeneration. *Glia* **46**, 225–251 (2004).

116. Yiu, G. & He, Z. Glial inhibition of CNS axon regeneration. *Nat. Rev. Neurosci.* **7**, 617–627 (2006).

117. Rhodes, K. E. & Fawcett, J. W. Chondroitin sulphate proteoglycans: Preventing plasticity or protecting the CNS? *J. Anat.* **204**, 33–48 (2004).

118. Gilbert, R. J. *et al.* CS-4,6 is differentially upregulated in glial scar and is a potent inhibitor of neurite extension. *Mol. Cell. Neurosci.* **29**, 545–558 (2005).

119. Zuo, J., Neubauer, D., Dyess, K., Ferguson, T. A. & Muir, D. Degradation of chondroitin sulfate proteoglycan enhances the neurite- promoting potential of spinal cord tissue. *Exp. Neurol.* **154**, 654–662 (1998).

120. McKeon, R. J., Schreiber, R. C., Rudge, J. S. & Silver, J. Reduction of neurite outgrowth in a model of glial scarring following CNS injury is correlated with the expression of inhibitory molecules on reactive astrocytes. *J. Neurosci.* **11**, 3398–3411 (1991).

121. Preston, E., Webster, J. & Small, D. Characteristics of sustained blood-brain barrier opening and tissue injury in a model for focal trauma in the rat. *J. Neurotrauma* **18**, 83–92 (2001).

122. Fitch, M. T., Doller, C., Combs, C. K., Landreth, G. E. & Silver, J. Cellular and molecular mechanisms of glial scarring and progressive cavitation: In vivo and in vitro analysis of inflammation-induced secondary injury after CNS trauma. *J. Neurosci.* **19**, 8182–8198 (1999).

123. Faulkner, J. R. *et al.* Reactive Astrocytes Protect Tissue and Preserve Function after Spinal Cord Injury. *J. Neurosci.* **24**, 2143–2155 (2004).

124. Jones, L. L., Sajed, D. & Tuszynski, M. H. Axonal Regeneration through Regions of Chondroitin Sulfate Proteoglycan Deposition after Spinal Cord Injury: A Balance of Permissiveness and Inhibition. *J. Neurosci.* **23**, 9276–9288 (2003).

125. Levine, J. M., Reynolds, R. & Fawcett, J. W. The oligodendrocyte precursor cell in health and disease. *Trends Neurosci.* **24**, 39–47 (2001).

126. Tan, A. M., Zhang, W. & Levine, J. M. NG2: A component of the glial scar that inhibits axon growth. *J. Anat.* **207**, 717–725 (2005).

127. Yang, L. J. S. *et al.* Sialidase enhances spinal axon outgrowth in vivo. *Proc. Natl. Acad. Sci. U. S. A.* **103**, 11057–11062 (2006).

128. Rhodes, K. E., Raivich, G. & Fawcett, J. W. The injury response of oligodendrocyte precursor cells is induced by platelets, macrophages and inflammation-associated cytokines. *Neuroscience* **140**, 87–100 (2006).

129. Davies, S. J. A., Goucher, D. R., Doller, C. & Silver, J. Robust regeneration of adult sensory axons in degenerating white matter of the adult rat spinal cord. *J. Neurosci.* **19**, 5810–5822 (1999).

130. Dyck, S. M. & Karimi-Abdolrezaee, S. Chondroitin sulfate proteoglycans: Key modulators in the developing and pathologic central nervous system. *Exp. Neurol.* **269**, 169–187 (2015).

131. Muleja, A. A., Mbianda, X. Y., Krause, R. W. & Pillay, K. Synthesis, characterization and thermal decomposition behaviour of triphenylphosphine-linked multiwalled carbon nanotubes. *Carbon N. Y.* **50**, 2741–2751 (2012).

132. Bonini, M., Wiedenmann, A. & Baglioni, P. Small angle polarized neutrons (SANSPOL) investigation of surfactant free magnetic fluid of uncoated and silica-coated cobalt-ferrite nanoparticles. *J. Phys. Chem. B* **108**, 14901–14906 (2004).

133. Chitosan, P. O. F. on the Structure and Properties of Chitosan. **33**, 1899–1904 (1992).

134. Coulson-Thomas, V. & Gesteira, T. Dimethylmethylene Blue Assay (DMMB). *Bio-Protocol* **4**, 1–7 (2014).

135. Shin, H. J. *et al.* Efficient reduction of graphite oxide by sodium borohydride and its effect on electrical conductance. *Adv. Funct. Mater.* **19**, 1987–1992 (2009).

136. Pei, S. & Cheng, H. M. The reduction of graphene oxide. *Carbon N. Y.* **50**, 3210–3228 (2012).

137. Gao, W., Alemany, L. B., Ci, L. & Ajayan, P. M. New insights into the structure and reduction of graphite oxide. *Nat. Chem.* **1**, 403–408 (2009).

138. Pei, S., Zhao, J., Du, J., Ren, W. & Cheng, H. M. Direct reduction of graphene oxide films into highly conductive and flexible graphene films by hydrohalic acids. *Carbon N. Y.* **48**, 4466–4474 (2010).

139. Moon, I. K., Lee, J., Ruoff, R. S. & Lee, H. Reduced graphene oxide by chemical graphitization. *Nat. Commun.* **1**, (2010).

140. Schniepp, H. C. *et al.* Functionalized single graphene sheets derived from splitting graphite oxide. *J. Phys. Chem. B* **110**, 8535–8539 (2006).

141. Fernández-Merino, M. J. *et al.* Vitamin C is an ideal substitute for hydrazine in the reduction of graphene oxide suspensions. *J. Phys. Chem. C* **114**, 6426–6432 (2010).

142. Bosch-Navarro, C., Coronado, E., Martí-Gastaldo, C., Sánchez-Royo, J. F. & Gómez, M. G. Influence of the pH on the synthesis of reduced graphene oxide under hydrothermal conditions. *Nanoscale* **4**, 3977–3982 (2012).

143. Stolle, A., Szuppa, T., Leonhardt, S. E. S. & Ondruschka, B. Ball milling in organic synthesis: Solutions and challenges. *Chem. Soc. Rev.* **40**, 2317–2329 (2011).

144. Szuppa, T., Stolle, A., Ondruschka, B. & Hopfe, W. An alternative solvent-free synthesis of nopinone under ball-milling conditions: Investigation of reaction parameters. *ChemSusChem* **3**, 1181–1191 (2010).

145. Fulmer, D. A., Shearouse, W. C., Medonza, S. T. & Mack, J. Solvent-free Sonogashira coupling reaction via high speed ball milling. *Green Chem.* **11**, 1821–1825 (2009).

146. Schneider, F., Stolle, A., Ondruschka, B. & Hopf, H. The Suzuki-Miyaura reaction under

mechanochemical conditions. *Org. Process Res. Dev.* **13**, 44–48 (2009).

147. Lee, H. C. *et al.* Review of the synthesis, transfer, characterization and growth mechanisms of single and multilayer graphene. *RSC Adv.* **7**, 15644–15693 (2017).

148. Hummers, W. S. & Offeman, R. E. Preparation of Graphitic Oxide. *J. Am. Chem. Soc.* **80**, 1339 (1958).

5. Artificial Sponges to promote spinal cord regeneration

5.1 OBJECTIVES OF THIS CHAPTER (5)

Spiral cord injury is a common and devastating central nervous system (CNS) insult that result in disruption of cord microstructure with a limited neuronal regeneration and insufficient functional recovery in adult mammals. After severe spiral cord injury and in response to changes in the local microenvironment, astrocytes, the most abundant glial cells in the CNS, transform themselves into reactive astrocytes as a consequence of dramatic morphological changes[98] as well as massive variations in gene expression.[99] One of the most reactive changes occurring after a spinal cord injury is the formation of a glial scar, a reactive cellular process whereby glial cells accumulate and surround CNS injury sites to seal in the wound.[98–100] The glial scar plays an important role in stabilizing CNS tissue by re-establishing the physical and chemical integrity of the CNS and closing the blood brain barrier to reduce infiltration of non-CNS tissue. As a consequence, this behavior minimizes the occurrence of infections and the spread of cellular damage.[99] However, the glial scar also creates both a physical and molecular barrier to regenerate injured axons, preventing the re-growth and repair of axonal projections. The physical presence of a dense meshwork of reactive glial cells can block advancement of the growth cone, while proteoglycans (PG) present in the extracellular matrix of the glial scar, can actively inhibit axon outgrowth[101,102,102] (**Figure 125**).

The effect of removal of chondroitin sulfate proteoglicans (CSPG) on regeneration and plasticity of axons. It is widely accepted that removal of these PG and in particular chondroitin sulfates (CS) could provide beneficial effects on axon growth, its sprouting and plasticity and, most importantly, on promoting the recovery its function. Bacterial chondroitinase (ChABC) and aggrecanase-1 combination has proved a successful enzymatic treatment for both acute spinal cord injury and, recently, for chronic spinal cord injury, in experimental animals. However, since prolonged treatments are necessary (thus increasing the risk of further traumas or infections as well as triggering immune responses), their long-term administration require modification. Furthermore, the development of new therapeutic treatments can meet with important obstacles related to the process safety, biodistribution phenomena, thermal stability effects and - last but not least - final costs.[103] It is important to note that a recent work involving enzymatic treatment has revealed that multiple regions of proteoglycans can inhibit neurite outgrowth, so chondroitinase digestion might not remove all aspects of CS that prevent regeneration, and therefore other strategies are urgently required.[104]

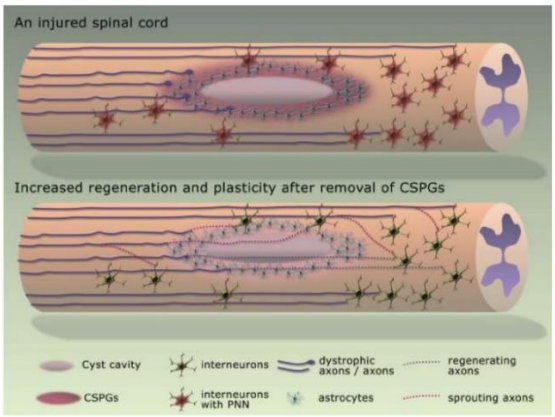

***Figure 125**. The effect of removal of chondroitin sulfate proteoglicans (CSPG) on regeneration and plasticity of axons.*

The key and original hypothesis in our proposal is that it should be possible to develop an innovative chemical strategy for the removal of the inhibitory molecules CS implied as barriers to CNS axons regeneration. For this goal, we have devised "nano-sponges", novel nanoconstructures that selectively soaks CS and, doing so, promotes regeneration of injured axons.

To address this challenge, we have designed nano-devices, with the desired chemical and physical properties, consisting of "polycationic structures" assembled around a central backbone made of nanostructured carbon materials [NCM, graphene oxide (GO) and oxidized carbon nanotube (Ox-CNT)], thus creating what we claim "nano-sponges". We believe that the total removal of inhibitory molecules may be attained if the designed device is able to soak-up them efficiently. To support our idea, it has recently been shown that polycationic molecules, such as chitosan, poly(L-lysine) or poly-(ethyleneimine), are capable to bind CS thus forming polymeric "nanoparticles" that can be removed from glial scars.[105] Since our "artificial sponges" are expected to remove proteoglycans with a similar action path (purely ionic interaction) and even more efficiently compared to other materials/molecules of the state-of the art, this would prevent the presence of "inhibitory" fragments (contrary to what happens with the enzymatic therapeutic strategy). Furthermore, nano-constructs will be able to bind a large variety of sulfated glycosaminoglycans (chondroitin, heparin, dermatan and/or keratan sulfates) thereby offering an all-purpose strategy regardless of their molecular structures.

The use of nanosponges for the removal of CS can be accomplished with the use of properly functionalized NCMs. It has been definitely proved that functionalized NCMs with tailored surface groups are not toxic and can be easily excreted from organisms (in mice through kidneys).[106,107] Furthermore, NCMs are ideal supports to be chemically modified through the formation of ad-hoc C-C bonds or through their supramolecular decoration. The literature presents several examples of decoration of NCMs with policationic residues: for example, Ox-CNT have efficiently been covered with poly(ethyleneimine) residues,[108] with PAMAM dendron,[109] Chitosan[110] and many others.

Herein, we propose the functionalization of NCMs with amino groups as a first step. These functional groups are basic and protonated at physiological pH, affording a simple nanosponge. Another possibility is the use of carboxylic and azido groups which can be conveniently conceived as grafting points for the attachment of more complex polycationic residues [i.e. PAMAM dendrimers, poly(L-lysine), poly-(ethyleneimine) or chitosan] through a brush like or a multidentate approach. The activity of the nano-sponges will assay in a model of glial scar.

Finally, we propose the decoration of our nano-sponges with magnetic iron oxide (IO) nanoparticles.[111] The IO–NCM composites will stick stably to chondroitin sulfates, thereby making the glycosaminoglycans magnetic (**Figure 126**). The latter will be separated from the glial scar without destruction under the action of an external magnetic field.

Recently, a similar concept has been applied in the treatment of cancer by sticking magnetic nanoparticles to freefloating cancer cells. This has allowed them to be captured and carried out from the body.[100]

Finally, the activity of the new magnetic nano-devices as well as their removal from the hosting bodies will be studied at the National Hospital for Paraplejics in Toledo (Spain) as research partner of the SPIDER proposal in Spain.

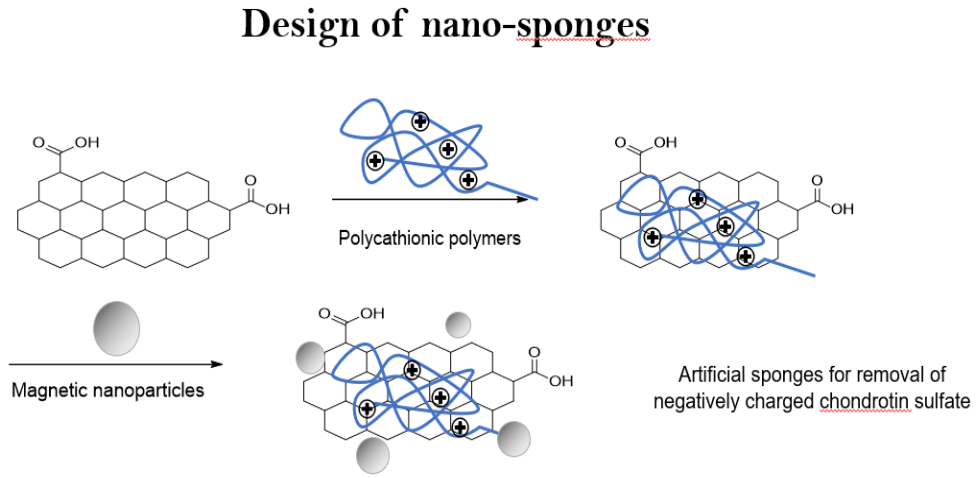

Figure 126. *General structure of magnetic artificial sponges based on nanostructured carbon material.*

5.2 INTRODUCTION

Chondroitin sulfate proteoglycans (CSPGs) are molecules of the extracellular matrix (ECM) that are widely expressed in the developing and adult central nervous system (CNS) and have a potent inhibitory influence on regeneration of the CNS.[112] After injury to the CNS, a glial scar is formed primarily by reactive astrocytes, which increase expression of CSPGs in the vicinity of the disrupted blood–brain barrier (BBB). This increase in CSPGs halts regeneration and induces the formation of dystrophic growth cones.[113] In addition, CSPGs located in perineuronal nets (PNNs) have an important role in preventing unwanted synaptic plasticity in uninjured adult animals.[114] In both cases, CSPG-mediated inhibition of growth seems to be linked to the activation of several signaling pathways.

Much of the inhibitory influence of CSPGs can be alleviated by administration of chondroitinase ABC (ChABC) — an enzyme that selectively cleaves GAG chains from the protein core. ChABC is often used in combination with other repair strategies to facilitate the greatest regeneration possible. In addition to CSPGs, several other axon guidance molecules function to inhibit regenerating axons.[115] Degenerating myelin has been identified as another chief source of inhibition after injury and has been the subject of several recent reviews.[116]

Recent developments in our understanding of the function of the ECM after damage to the adult CNS were examined.

Proteoglycans: general structure and function Proteoglycans are involved in numerous processes such as growth, adhesion, receptor binding, migration, barrier formation and interactions with other components of the ECM.[117] CSPGs include aggrecan, brevican, neurocan, NG2, versican and

phosphacan. During development, CSPGs pattern cell migration, regulate axonal pathfinding and limit plasticity.

Proteoglycans consist of a protein core to which glycosaminoglycan (GAG) side chains are bound. GAG chains attached to the core protein vary markedly in length and number. These variations in GAG chain number and degree of sulfation determine the unique functions of different proteoglycans within and between classes.[118]

Much evidence suggests that most of the inhibitory activity of CSPGs is derived from their GAG side chains, because treatment with ChABC reduces or eliminates inhibition.[119]

SCAR FORMATION

A glial scar forms after injury to the CNS and acts as a barrier to regenerating neurons **(Figure 127)**.

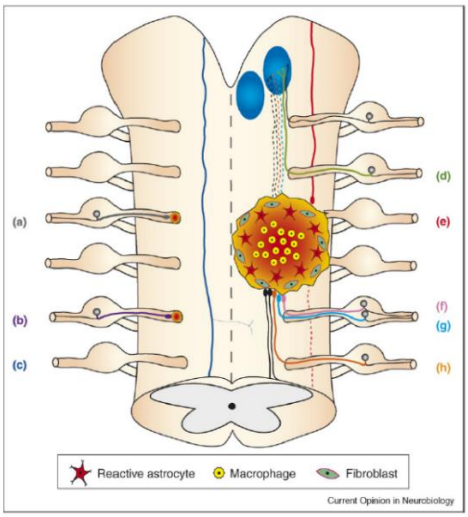

Figure 127. *Elements of typical spinal cord and dorsal root entry zone lesions. After a stab lesion to the spinal cord, the lesion core is devoid of neurons and astrocytes and is populated by phagocytic macrophages. Fibroblasts deposit basal lamina and form a barrier between the lesion core and the penumbra. Reactive astrocytes secrete inhibitory CSPGs, which are deposited in an increased gradient (orange to red) and are highest in the lesion core. (a,b) After injury, CSPGs are upregulated in the dorsal root entry zone; neurons fail to regenerate and form dystrophic, club endings (gray, purple). (c) Descending bulbospinal axons (dark blue) cross the midline and innervate the contralateral phrenic nucleus. (d) Uninjured sensory neurons (green) are capable of limited sprouting to neighboring regions of the denervated cuneate nucleus. (e–h) Descending motor and ascending sensory fibers (green, red, pink, light blue, orange) fail to regenerate after injury and form dystrophic endings.*

Glial scars consist mainly of reactive astrocytes, which become hypertrophic and greatly increase their expression of intermediate filament proteins such as vimentin and glial fibrillary acidic protein. Reactive astrocytes and oligodendrocyte precursor cells (OPCs) have been shown to upregulate their expression of scar-associated inhibitory CSPGs such as neurocan, phosphacan and versican. Interestingly, the expression of both growth-inhibitory and growth-promoting ECM molecules increases in reactive astroglia, but the inhibitory ECM components are more markedly upregulated.[120] In more severe injuries resulting in breakdown of the meninges, connective tissue elements, such as fibroblasts, mix with astrocytes and other invading cells, including macrophages, in the lesion.[121]

Development of the scar begins within hours of injury, and a correlation among the areas of most significant BBB breakdown, highest infiltration of activated macrophages and greatest glial scar

formation has been demonstrated.[122] Reactive microglia and OPCs are recruited to the forming scar, where they proliferate. Immediately after injury, astrocytes undergo a process known as 'reactive gliosis'. Transgenically targeted ablation of the dividing population of reactive astrocytes after spinal cord injury (SCI) prevents reestablishment of the BBB, resulting in an increase in lesion size, cell death, an exacerbated immune response and marked motor deficits.[123] Thus, despite its inhibitory properties, the glial scar is vital to seclusion of the damaged site and to protection of the surrounding regions from secondary injury.

The role of NG2-expressing OPCs after injury remains a matter of debate.[124] It has been widely speculated that the NG2 molecule negatively regulates axonal growth in vivo.[125] It has been reported that neutralizing the NG2 proteoglycan with anti-NG2 antibodies modestly enhances the regeneration of sensory axons after spinal cord transection in the adult rat;[126] however, recent evidence indicates that NG2 cells themselves might not be inhibitory to growing neonatal axons but instead might act as a permissive substrate owing to their enhanced production of growth-promoting molecules.[127] OPCs do not become hypertrophic or increase their expression of NG2 in lesions in which the BBB is not ruptured, suggesting that the mechanisms controlling the responses of OPCs differ from those of astrocytes or microglia.[128]

AXON RESPONSE

The central role of inhibitory ECM molecules in regeneration failure has been revealed by a series of microtransplantation experiments.[129] These studies showed that adult sensory neurons that are microtransplanted atraumatically into injured white matter tracts can grow through the CNS environment, but halt abruptly as they approach the vicinity of the lesion. Upregulation of proteoglycans occurs in the latter region in an increasing gradient, which is highest at the lesion core. In the region where the glial scar forms, the ends of severed axons form 'dystrophic endbulbs', which were first described by Ramo´n y Cajal and have long been thought to be in a permanent state of quiescence.

POSSIBLE TREATMENTS

It is widely accepted that the removal of these chondroitin sulfate could provide beneficial effects on axon growth and, most importantly, on promoting functional recovery. The use of ABC bacterial chondroitinase has proven to be an effective treatment in animal experiments, both for acute and conical spinal cord injuries.[130] However, treatment requires repeated injections, thus increasing the risk of further trauma and infection, and also of causing a severe immune response. Furthermore, important obstacles in the development of this as a therapeutic agent are in particular safety, biodistribution, thermal instability and above all its high cost.[103] These limitations demonstrated the need to develop new strategies for the removal of CSPGs inhibitor molecules.

5.3 RESULTS AND DISCUSSION

The first part of this project was focus on carbon nanotubes oxidation. The chemical process started from pristine carbon nanotubes, allowed to shorten their length, making a variety of CNTs from few nanometers to 2 µm.

5.3.1 SYNTHESIS OF CNTs-PDA

Oxidized carbon nanotubes (CNTs) were functionalized through no-covalent bonds with Dopamine (DOA). Dopamine, generally auto-polymerizes in basic conditions to obtain poli-dopamine (PDA) which

stick to CNTs. CNTs-PDA showed a higher water dispersibility compared to CNTs. The chemical procedure was carried out at 25°C for 24h in Tris Buffer solution. The workup consisted in centrifugations and filtrations.

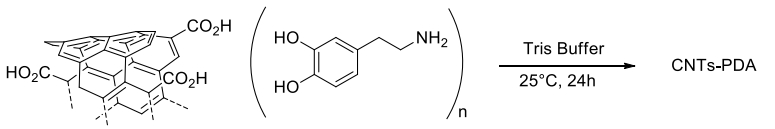

2 64

***Scheme 34**. Functionalization CNTs-PDA.*

FT-IR, UV-Vis, Raman spectroscopy and Transmission Electron Microscope characterized the product. TEM images in **Figure 128** showed nanostructured materials with a good dispersibility. No significant difference could be found in the morphology of the materials. CNTs-PDA diameter was calculated around10 nm, and lengths ranging from 100 nm to 1 µm.

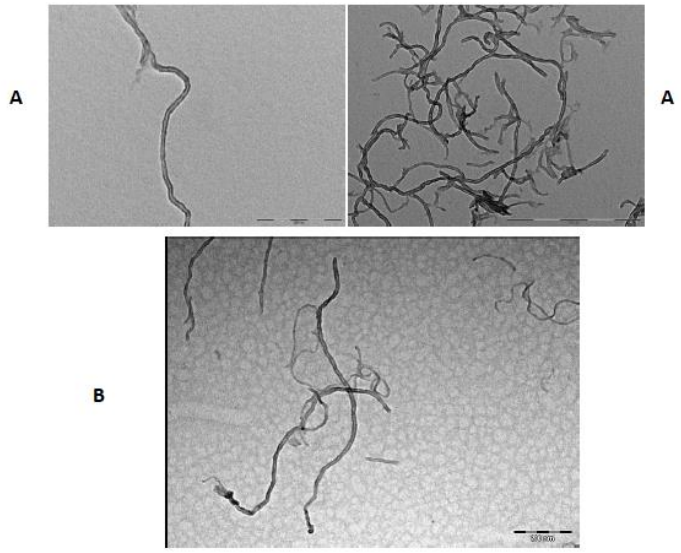

***Figure 128.**TEM images of CNTs-PDA (A); CNTs (B).*

The functionalization of material can be confirmed by two intense bands at 3431 cm^{-1} and 1631 cm^{-1} revealed in FT-IR spectrum (**Figure 129**). An attribution to two specific functional groups of these bands was not possible due to the complexity of the system.

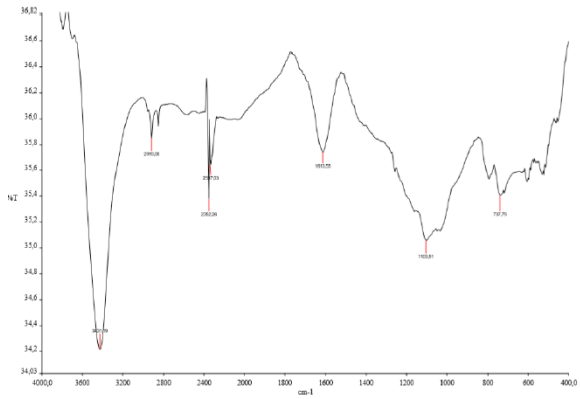

Figure 129. *IR Spectrum (KBr) of CNTs-PDA* ***64***

A comparison in UV-Vis Absorption spectrum of CNTs-PDA and CNTs was reported in **Figure 130**. At 280 nm a characteristic dopamine pick attested the formation of the product.

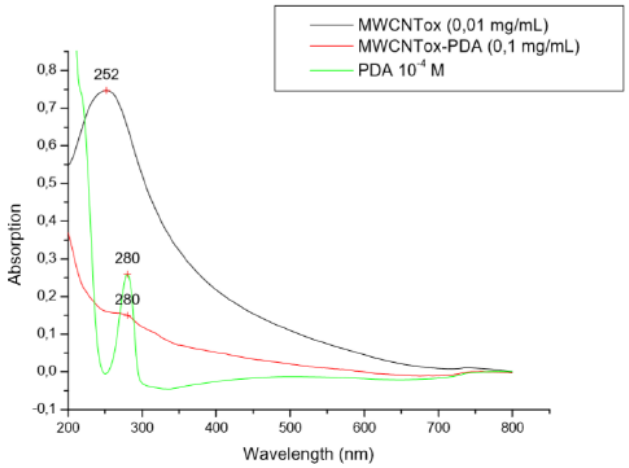

Figure 130. *UV-Vis Spectrum of CNTs (black), CNTs-PDA (red) and PDA (green).*

Raman spectroscopy analyses were performed on the sample **(Figure 131).** Generally, carbon nanomaterials showed two main bands in their Raman spectra: one at ≈1580 cm−1 (G band) related to sp^2 graphitic domain and the second at ≈1360 cm−1 (D band) attributed to the amorphous carbon or deformation vibrations of a hexagonal ring.[131] Raman spectra of CNTs (**Figure 132**) showed the D and G bands centered at 1302 and 1590 cm^{-1}, respectively. The functionalization with Dopamine further decreased the D band intensity, but the *I*D/*I*G for the product was not significant different from *I*D/*I*G of CNTs.

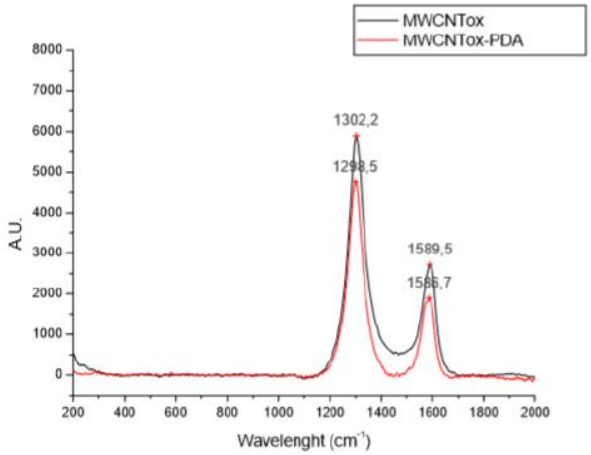

Figure 132. *Raman Spectrum of CNTs (black); CNTs-PDA (red);*

Quantitative analyses concerning the functionalization loading degree of CNTs-PDA were collected through elemental analyses and XPS spectroscopy. The amount of C, N and H were showed in **Tab 7.**

	%C	%N	%H
Elemental Analyses	79.88	1.23	0.65
XPS	97.2	2.8	-

Tab 7

These measures established a loading degree of PDA in the range 134 – 306 mg/g CNTs-PDA.

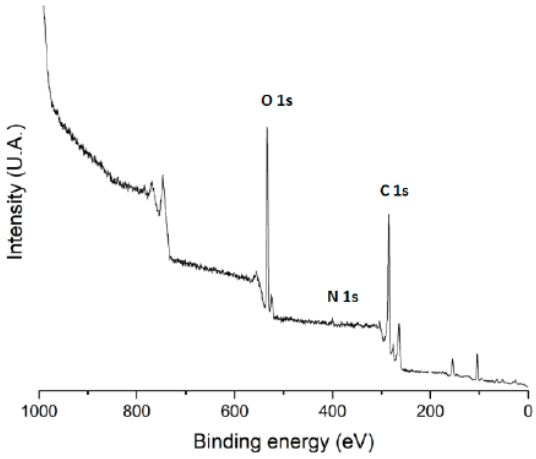

Figure 133 *XPS spectrum CNTs-PDA* ***64****.*

5.3.2 SYNTHESIS OF CNTs-PAAH

CNTs were modified with a no-covalent strategy to decorate the nanostructured carbon material with Poly(allylamine) (PAH). PAH is a linear polymer prepared by the polymerization of allylamine. Many -NH_2 groups provide a higher water solubility. The reaction was carried out in water at 70°C for 24h, with a KOH solution. At the end of reaction the mixture was centrifuged and filtered.

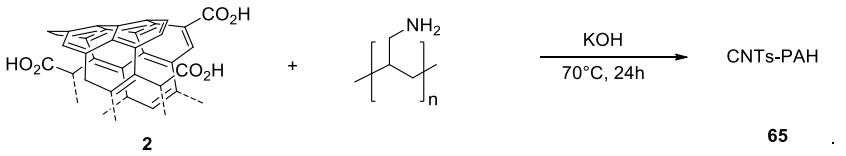

Scheme 35. *CNTs functionalization with PAH.*

Compound **65** was characterized through UV-Vis spectroscopy and electron transmission microscope (TEM). The images showed in **Figure 134** are analogue to the previously presented (**Figure 128**), since obviously, any morphological changes were involved. Nanotubes appear as non-aggregated and well dispersed structures.

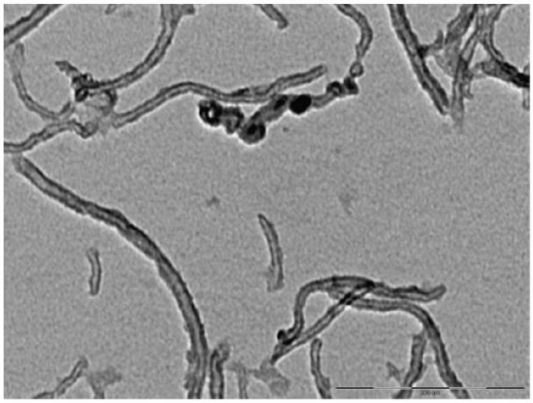

Figure 134: *TEM images of CNTs-PAH **65**.*

The comparison of UV-Vis spectrum of samples **2** and **65** showed a 5 nm shift of λmax adsorption, due to the functionalization.

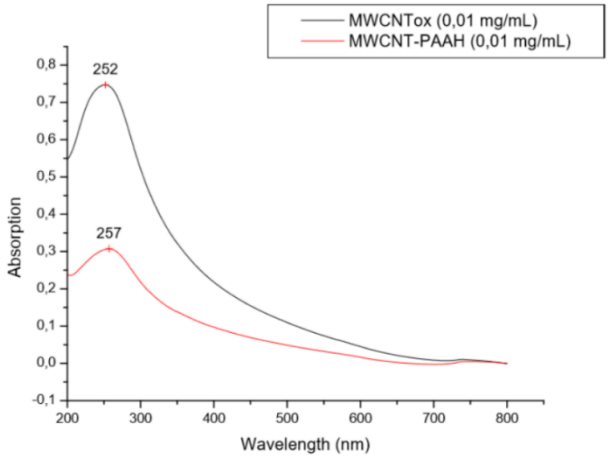

Figure 135. *UV-Vis Spectrum of compound **2** (black), **65** (red).*

Additional values were achieved thanks to TGA and XPS measures. In **Figure 136** the TGA profiles showed a weight loss by 800°C, of 24.8% for compound **65** compared to 22.0 % for compound **2**.

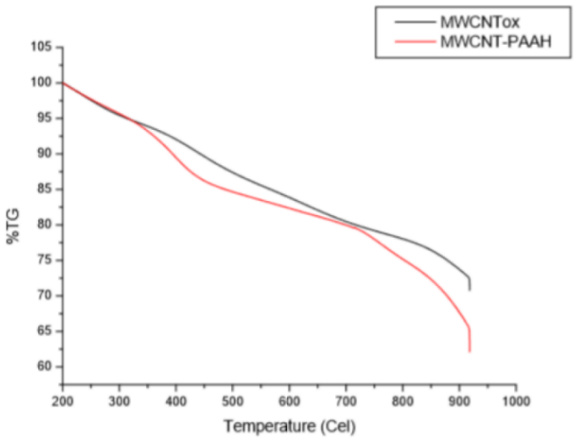

Figure 136. *TGA profile of compound* ***2*** *(black) and compound* ***65*** *(red).*

XPS measures evaluated an amount of carbon and nitrogen as presented in **Tab.8**, the estimated loading of PAH was 245 mg/g.

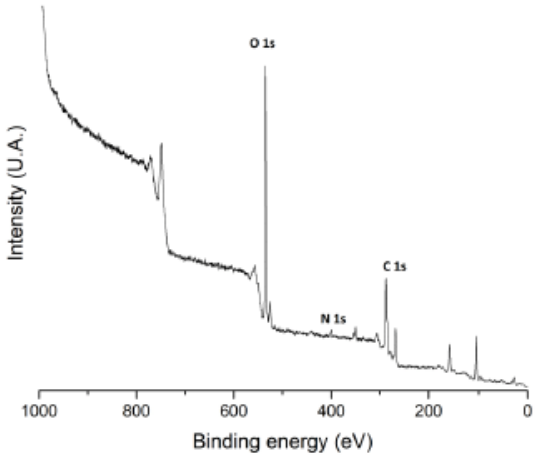

Figure 139 *XPS Spectrum of CNTs-PAH* ***65****.*

	%C	%N
XPS of **65**	94.0	6.0

Tab 8

5.3.3 SYNTHESIS CNTs-PEI

A different strategy consisted in the covalent functionalization of CNTs with branched PEI (Polyethylenimine). The decoration occurred through amide bonds and the formations of C-N bonds, derived from epoxide ring opening on CNTs surface. The reaction was carried out in water at 25°C for 24h, EDC and NHS were exploited as activating agent for carboxyl groups. The CNTs derivative **65** was isolated through filtration over a 0.2 µm polycarbonate membranes followed by repeated washings with different solvents to remove excess reagents, while compound **66** was recovered after several cycles of centrifugation and dispersion.

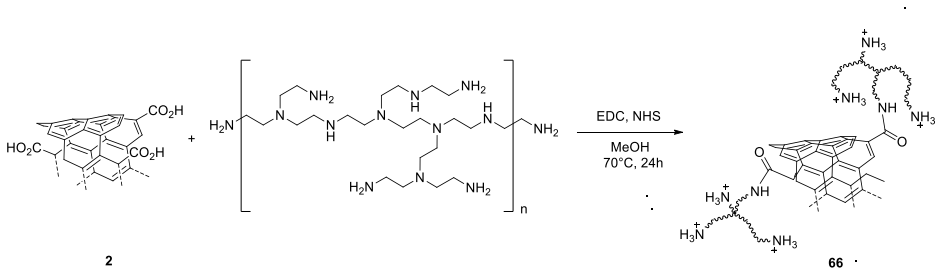

Scheme 36. *Functionalization of CNTs with PEI* ***66***

The confirmation of the occurred reaction was obtained by UV-Vis, Raman spectroscopy and Electron Transmission Microscope (TEM). As with CNTs-PAH, TEM images of **66** showed similar chemical behavior: any morphological changes occurred. CNTs-PAH were dispersed and coupled structures of length in the order of hundreds of nm and diameters about 16 nm.

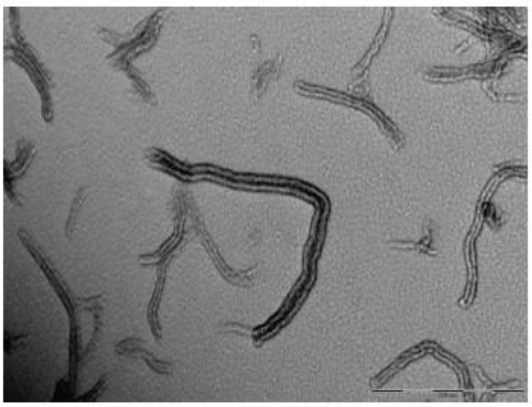

Figure 140. *TEM images of CNTs-PEI* ***66****..*

The comparison of UV-Vis spectrum of compound **2** and **6** (**Figure 141**) reported a shift of λ_{max} adsorption from 252 nm to 257 nm, due to the functionalization of carbon material.

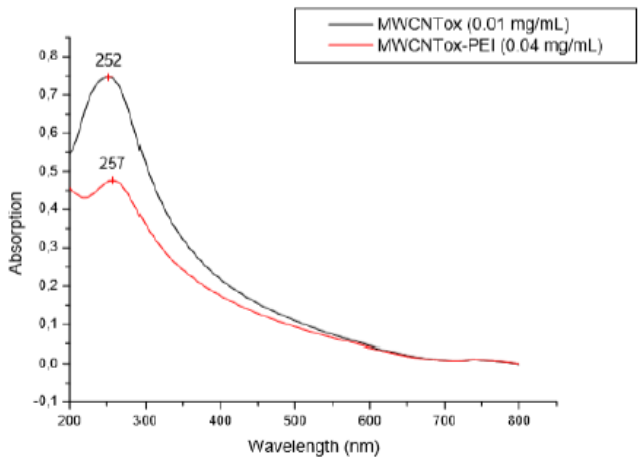

Figure 141.*UV-Vis Spectrum of compound* ***2*** *(black),* ***66*** *(red).*

Raman spectroscopy's measures revealed an increased intensity of D band of CNTs-PEI compared to CNTs. An increment of sp^3 sites due to the new C-N bonds, therefore a new hybridisation could represent a possible explanation.

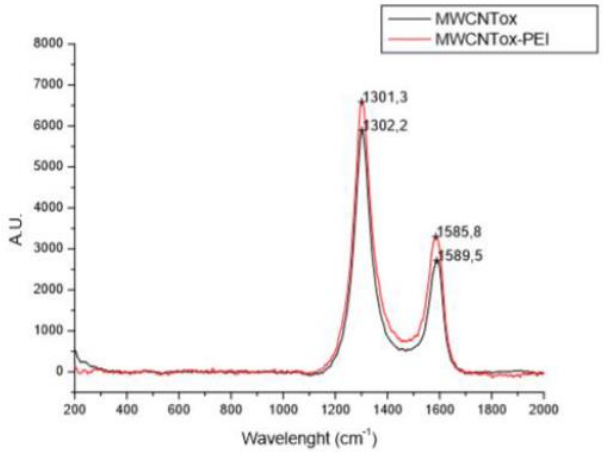

Figure 142 *Raman Spectrum of CNTs* ***2*** *(black); CNTs-PEI (red)* ***66****;*

Elemental analyses and XPS measures **(Figure 143)** evaluated a loading degree of branched PEI on CNTs as presented in **Tab 9**.

	%C	**%N**	**%H**
Elemental analyses	70.91	5.16	2.46
XPS	96.1	3.9	-

Tab 9

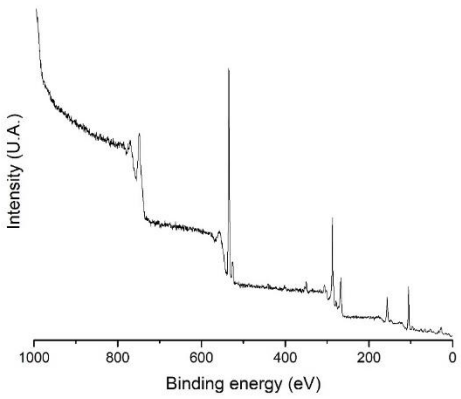

Figure 143*. XPS spectrum of CNTs-PEI.*

Based on these results, the value of PEI grafted on CNTs was evaluated in the range 114-150 mg/g.

Zeta potential analyses were exploited to evaluate the charge values for the previously synthesized nano-adducts (**Tab 10**). The desired hybrid should show a positive charge to form "polycationic structures" able to bind a large variety of chondroitin sulphate and chitosan sulphate.

	CNTs	CNTs-PDA	CNTs-PAH	CNTs-PEI
Zeta potential	-19.4 mV	-5.8 mV	+4.2 mV	+4.8 mV
0.1 mg/mL MilliQ water dispersion	σ= 4.9	σ= 5.1	σ= 3.8	σ= 4.8

Tab.10 Zeta-potential values.

CNTs-PEI appeared to be the best choice due to their positive *charge* value and the better dispersibility in water compared to the features of the other synthesized nano-hybrids. Covalent bonds, moreover, allowed to have steady structures.

An additional possibility to functionalize carbon material through covalent bonds, could occur by using metformin, as showed in **Scheme 37**.

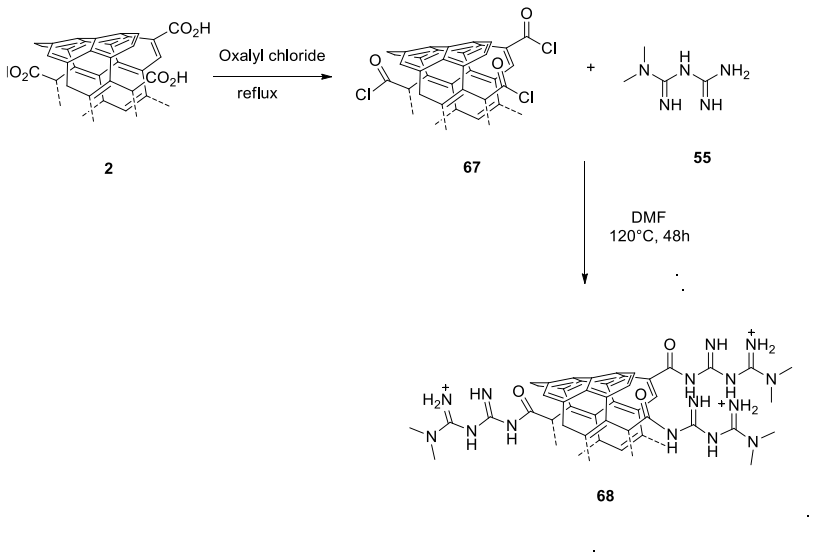

***Scheme 37**. Synthetic Pattern for the synthesis Met-CNTs.*

The activation of carboxyl groups on CNTs was performed by adding oxalyl chloride. Metformin was added to the mixture to synthesize compound **68**. An evaluation of loading degree occurred thanks to elemental analyses: 2 mmol/g was the estimated value of metformin on CNTs-MET.

The two described systems CNTs-PEI and CNTs-MET were selected to propose the decoration of future nano-sponges with magnetic iron oxide (IO) nanoparticles, making magnetic systems. This strategy will allow to achieve composites which stick stably to chondroitin sulfates or chitosan sulfate.
The chemical procedure planned the formation of magnetic iron oxide nanoparticles by adding two iron salts ($FeCl_2 \cdot 5H_2O$, $FeCl_3 \cdot 6H_2O$) to the mixture.[132] CNTs-MET were directly reacted as described to synthesize nano-sponges as CNTs-MET-IO. **Scheme 38**

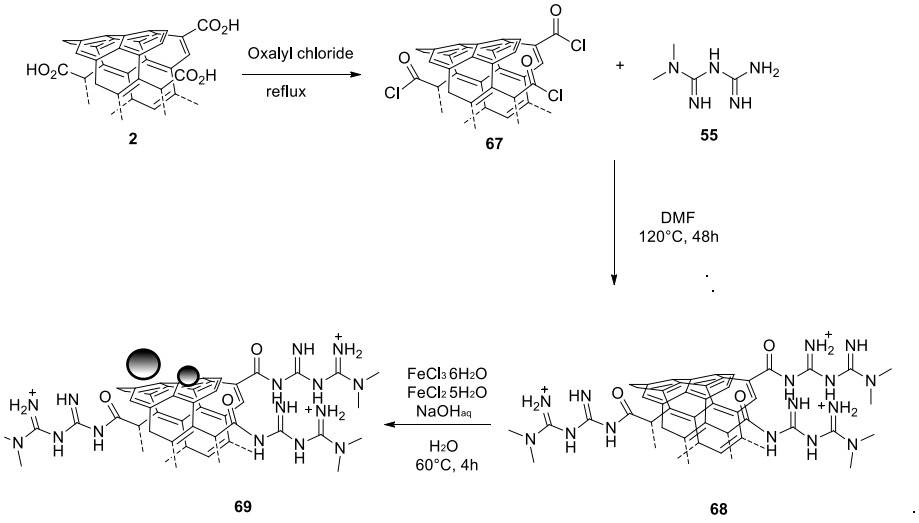

Scheme 38. *Total Synthetic pattern for CNTs-MET-IO* ***69***

A first qualitative analyses of compound **69** occurred by FT-IR technique. The spectrum reported in **Figure 144** showed a peck at 580nm suggesting the formation of iron oxide nanoparticles.

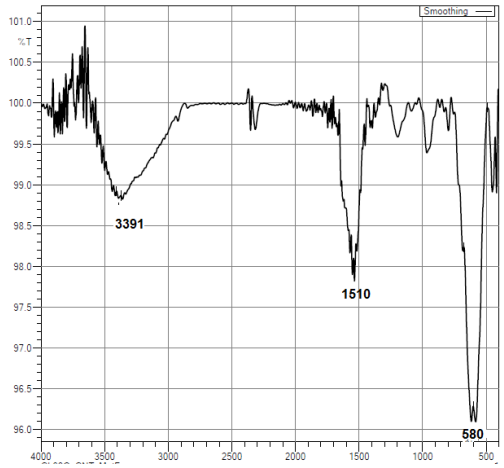

***Figure 144**. IR spectrum of compound **69**.*

This hypothesis was confirmed by ICP-AES analysis: 28.1% was the amount of iron established on CNTs-MET-IO by quantitative evaluation. Iron oxide nanoparticles were distinctly exhibited in TEM images (**Figure 145**). Iron oxide nanoparticles were not uniformly spread on nanostructured surface, but assembled in local agglomerates.

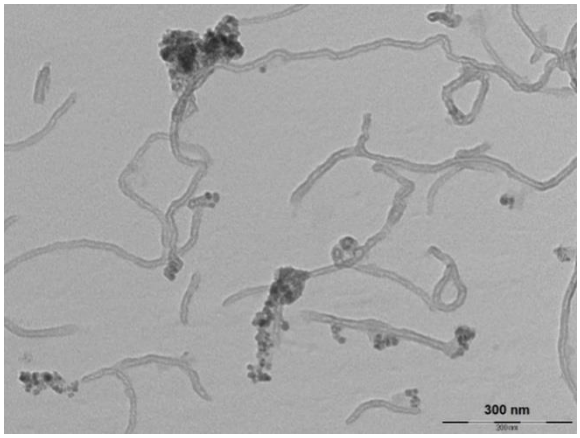

***Figure 145**. TEM images of compound **69**.*

Zeta potential measures were performed to verify the charge value of nano-sponges CNTs-MET-IO in MilliQ water dispersion at 0.1 mg/mL at room temperature. The results were reported in **Tab 11**

	CNTs	CNts-IO	**CNTs-MET-IO**
Zeta potential analyses	-19.4 mV	-19.8 mV	-6.3 mV
0.1 mg/mL (MilliQ water dispersion)	σ= 4.9	σ= 5.1	σ= 5.0

Tab 11

The synthesized complexes showed a negative charge value (in red **in Tab 11**). Unfortunately these nano-hybrids were not suitable for the conclusive goal of our proposal.

The natural evolution of this project consisted in the design and synthesis of CNTs-IO-PEI. The first step to realize this system was iron oxide nanoparticles synthesis, achieved by following the previously mentioned chemical procedure.[132] **(Scheme 39)**

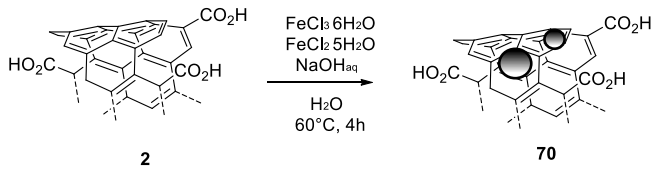

2 **70**

Scheme39*. Synthesis of CNTs-IO* ***70***

Consequently the addition of branched PEI was performed by following the reaction conditions adopted to obtain product **66**. **(Scheme 36)** The decision to switch the order of the two synthetic steps was due to the reaction temperatures. We preferred to postpone the decoration of nanostructured material with PEI, which occurs at room temperature, to the formation of magnetic nanoparticles which requires 60°C. (**Scheme 40**)

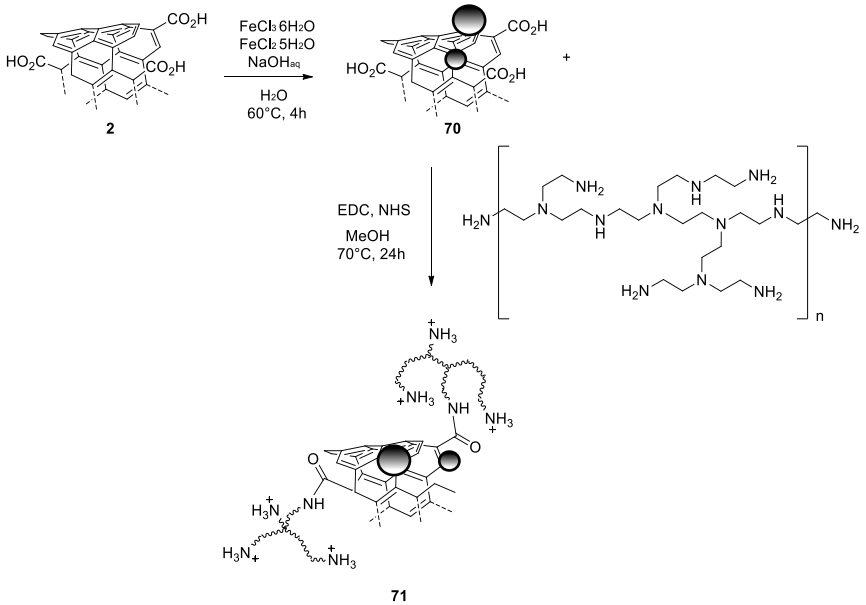

71

Scheme 40*. Synthetic pattern to achieve CNTs-IO-PEI* ***71****.*

After the first step, FT-IR spectroscopy was used to confirm the presence of iron oxide nanoparticles on CNTs. In **Figure 146** a comparison between IR spectrum of compound **2** and **70** was reported. At 581 nm a new peck in spectrum **B** suggested iron oxide nanoparticles.

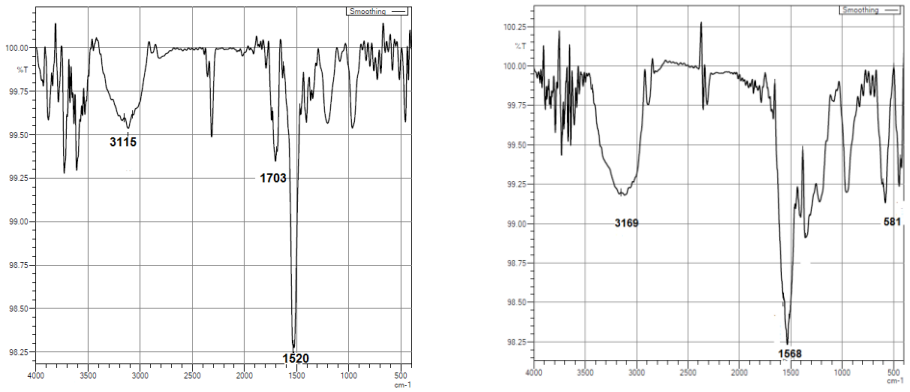

A B

Figure 146*. Spectrum of compound **2** (A), Spectrum of compound **71** (B).*

ICP-AES analyses evaluated a loading degree of metal equal to 50%, therefore an improvement in result compared to the iron quantitative amount collected for compound **71**.

After the second reaction step, elemental analyses of CNTs-IO-PEI **71** occurred to establish the quantitative amount of grafted PEI equal to 10.8%.

To prove an effectively application of compound Z as nano-sponges, the complexes were tested in Zeta potential analyses. The results were showed in **Tab 12**.

	CNTs	CNts-IO	CNTs-PEI	**CNTs-IO-PEI**
Zeta potential analyses	-19.4 mV	-19.8 mV	+4.8 mV	**+5.2 mV**
0.1 mg/mL (MilliQ water dispersion)	σ= 4.9	σ= 5.1	σ= 4.8	**σ= 3.7**

Tab 12

To test the real potential of the synthesized nano-sponges, the ability of polycationic nano-hybrids to complex chondroitin sulfate proteoglycans and chitosan sulfate molecules was evaluated. Chitosan sulfate groups are similar in structures to chondroitin sulfate, but with a higher number of sulfate groups.[133] Due to the negative charges of these groups they showed an improved possibility to bind positively charged amino groups of PEI. The decorated carbon material was dispersed in MilliQ water at room temperature for 24h. **(Scheme 41)**

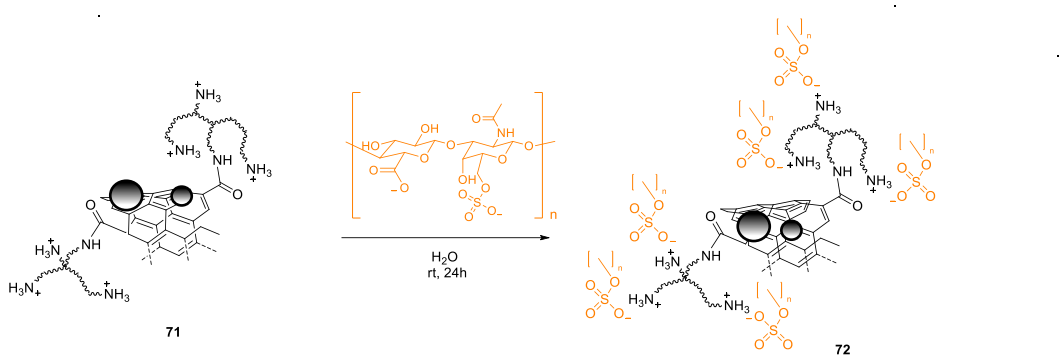

***Scheme 41**. Synthesis of compound **72**.*

After numerous centrifugations to remove an excess of reagents, the compounds were characterized by Zeta potential measures. In **Tab 13** charge values of compounds CNTs-IO-PEI complexed with chitosan (Ch58SA3) or chondroitin sulfates (CS-A,C or CS-E) were reported and compared to the potential collected for CNTs-IO-PEI.

	CNTs-IO-PEI-Ch58SA3	CNTs-IO-PEI-CS-A, C	CNTs-IO-PEI-CS-E
Zeta potential analyses	-12.4 mV	-8.8 mV	-9.8 mV
0.1 mg/mL (MilliQ water dispersion of compound **72**)	σ= 4.6	σ= 5.7	σ= 6.6

CNTs-IO-PEI
+5.2 mV
σ= 3.7

Tab 13

CS: Chondroitin sulfate ChS: Chitosan sulfate

According to our hypothesis, Zeta potential value of CNTs-PEI-CS decreased. The new calculated potentials (-8.8 mV, -9.8 mV) for the whole system suggested the occurred reaction. CNTs-PEI-Ch also allowed to have a negative charge value.

A first procedure to quantify the amount of Chondroitin sulfate able to form complexes with CNTs-PEI was carried out according to a useful bioprotocol.[134]

Spectrophotometric assays to measure the Glycosaminoglycans, such as chondroitin sulfate, content in biological fluids and tissue/cell extracts are valuable tools. The dye 1,9- dimethylmethylene is a thiazine chromotrope agent that presents a change in the absorption spectrum due to the induction of metachromasia when bound to sulfated GAGs enabling rapid detection of GAGs in solution. Moreover,

there is a window in which a linear curve may be drawn (approximately between 0.5-5 µg of GAGs) enabling the quantification of GAGs in solution.

After several cycles of centrifugation and dispersion compound **72** was recovered. At the end of every cycle the washing water was analyzed by adopting the mentioned bio-protocol, previously explained, to evaluate the removed chondroitin sulfate. Comparing the total amount of chondroitin sulfate at the beginning of the reaction to the residue of glycosaminoglycans contained in the washing water, the Chondroitin sulfate grafted on CNTs was calculated. Thanks to spectrophotometric analyses **Figure 147**, **Figure 148** 74 mg (CS-A, C)/ g (CNTs-IO-PEI-CS A, C) were quantified. In **Figure 147** the absorbances of four water dispersions of compound **72** at different concentrations were reported. In **Figure 148** the absorbance measures at 535 nm of the four mentioned dispersions were correlated to different concentrations of chondroitin sulfate. This graph allowed to establish the amount of CS-A, C solubilized in washing reaction water.

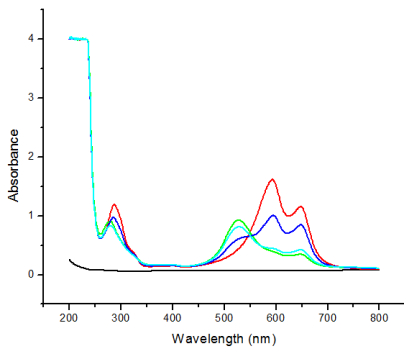

Figure 147

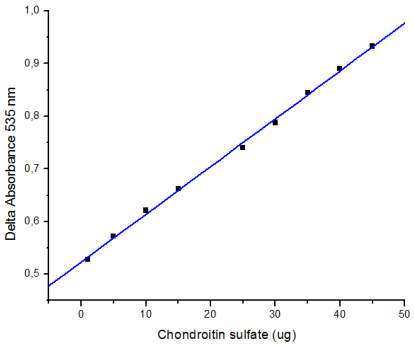

Figure 148

This amount of compound was confirmed by ICP-AES analyses, which provided a result equal to 101 mg (CS-A, C)/ g (CNTs-IO-PEI-CS A, C).

5.4 CONCLUSION AND PERSPECTIVES

In conclusion synthesis of nano-sponges consisting in central backbone made of oxidized carbon nanotubes (CNTs) assembled with “polycationic structures” (polyethylenimine branched or metformin) and decorated with magnetic nanoparticles were performed.

The ability of our nano-devices (**CNTs-IO-PEI**) to bind chondroitin sulfate or chitosan sulfate was checked.

Next step will be in vitro test to confirm the potential of nano-sponges to remove molecules of the extracelluar matrix that have a potent inhibitory influence on tissue regeneration of the Central Nervous System.

5.5 MATERIAL AND METHODS

SYNTHESIS OF CNTs-PDA **64**

Oxidized carbon nanotubes (2) (50 mg) were dispersed in 50 mL of Tris Buffer solution (10mM, pH 8.5) Dopamine (25 mg) was added. The mixture was sonicated for 10 'in an ice bath and stirred at 25 °C for 24 h. At the end, the reaction was centrifuged at 1400 rcf for 10’. The supernatant was removed and the precipitate was dispersed in water and centrifuged a second time. The obtained nanotubes were

dried under vacuum, dispersed in 0.01 M HCl and filtered on 0.2 µm membrane, washed with MilliQ water up to pH 7. The solid was collected and dried, under vacuum and in an oven at 80 ° for 2 hours, obtaining compound **64** as black powder (37 mg).

Elemental analysis: C 79.88%; N 1.23%; H 0.65%

SYNTHESIS OF CNTs-PAAH **65**

Oxidized carbon nanotubes (2) (20 mg) were dispersed in 100 mL of MilliQ water and sonicated for 5. PAAH (82 mg) was added and the dispersion sonicated again for 15 '. KOH (100 mg) was added and the reaction was carried out at 70 °C for 24 h under nitrogen atmosphere. At the end the reaction was to cool at room temperature and centrifuged at 1400 rcf for 60 '. The supernatant was removed and the precipitate was filtered on polycarbonate membrane (Whatman, pore size 0.2 µm, Ø 47mm), washing several times with milliQ water until the pH of the filtrate resulted neutral. The solid was dried under vacuum and subsequently was put in an oven at 120 °C for 2 h, obtaining functionalized carbon nanotubes (**65**) as black powder (9.4 mg).

SYNTHESIS OF CNTs-PEI **66**

CNTs or CNTs-IO (2) (50 mg) were dispersed in 250 mL of methanol, the dispersion was sonicated for 5 '. EDC (300 mg) and NHS (300 mg) were added to activate the carboxyl groups on CNTs (2). The mixture was stirred at room temperature for 3 h. PEI is then added (300 mg) and the reaction is again stirred at room temperature for 24 h. At the end the mixture was centrifuged at 1400 rcf for 10 '. The supernatant was removed, the precipitate was dispersed in fresh methanol. The centrifugation operations and dispersion were repeated 2 more times to remove the excess of polymer. The solid was dried under vacuum and subsequently put in an oven at 120 °C for 2 h, obtaining the modified nanotubes (**66**) as black powder (37 mg).

Elemental analysis (8): C 70.91%; N 5.16%; H 2.46%

SYNTHESIS OF CNTs-MET **68**

Oxidized carbon nanotubes (**2**) (35 mg) were dispersed in freshly distilled oxalyl chloride (10 mL) under nitrogen. Then the dispersion was stirred at reflux for 24 h, after that the oxalyl chloride was accurately removed under vacuum. The acyl chloride CNT directly dispersed in dry DMF (9.5 mL), using an ultrasound bath, metformin (170 mg) was added to the dispersion and the mixture stirred at 120 °C under nitrogen for 40 h. CNT-MET were recovered by filtration over a 0.2 µm nylon membrane washing several times with DMF and methanol to remove the unreacted metformin.

Metformin loading ranged from 1.8 to 2 mmol/g as evaluated from elemental analysis on three different samples.

SYNTHESIS OF Magnetic Nanoparticles **70**

CNTs or CNTs-MET (20 mg) were dispersed in MilliQ water (5 mL). 2.5 mL of a 0.04 M aqueous solution of $FeCl_2$ 4(H_2O) (0.103 mmol in 2.5 mL of water) and 2.5 mL of a 0.09 M aqueous solution of $FeCl_3$ 6(H_2O) (0.218 mmol in 2.5 mL of water) were added to the flask, under stirring. A 2M aqueous solution of NaOH was used to obtain a dispersion with pH 11. The mixture was heated at 60°C for 4h. At the end of reaction the dispersion was centrifuged for 20' at 1500 rcf. The mixture was filtered on nylon membrane 0.2 µm pores. The recovered material was 40 mg.

ICP: CNTs-MET-IO : Fe 28.1%

ICP: CNTs-IO-PEI: Fe 55.2%

SYNTHESIS OF CHONDROITIN SULFATE/CHITOSAN SULFATE WITH CNTs-IO-PEI **72**

4.2 mg of CNTs-IO-PEI or CNTs-MET-IO were dispersed in 3 mL of MilliQ water at room temperature. 3.4 mg of Chondroitin Sulfate or Chitosan Sulfate were added to the mixture. After 24h at room temperature the mixture was dialyzed for 3 days and freeze dried.

ICP (S): 78 mg of Chondroitin sulfate/g of material

5.6 REFERENCES

1. Biagiotti, G. *et al.* Multiwalled carbon nanotubes for combination therapy: A biodistribution and efficacy pilot study. *J. Mater. Chem. B* **7**, 2678–2687 (2019).

2. Kostarelos, K. *et al.* Cellular uptake of functionalized carbon nanotubes is independent of functional group and cell type. *Nat. Nanotechnol.* **2**, 108–113 (2007).

3. Liu & Speranza. Functionalization of Carbon Nanomaterials for Biomedical Applications. *C — J. Carbon Res.* **5**, 72 (2019).

4. Curcio, M. *et al.* Functionalized carbon nanostructures versus drug resistance: Promising scenarios in cancer treatment. *Molecules* **25**, 1–31 (2020).

5. Perkins, B. L. & Naderi, N. Carbon Nanostructures in Bone Tissue Engineering. *Open Orthop. J.* **10**, 877–899 (2017).

6. Erol, O. *et al.* Recent advances in bioactive 1D and 2D carbon nanomaterials for biomedical applications. *Nanomedicine Nanotechnology, Biol. Med.* **14**, 2433–2454 (2018).

7. Tasis, D., Tagmatarchis, N., Bianco, A. & Prato, M. Chemistry of carbon nanotubes. *Chem. Rev.* **106**, 1105–1136 (2006).

8. Kumar, S., Rani, R., Dilbaghi, N., Tankeshwar, K. & Kim, K. H. Carbon nanotubes: A novel material for multifaceted applications in human healthcare. *Chem. Soc. Rev.* **46**, 158–196 (2017).

9. Hong, S. Y. *et al.* Filled and glycosylated carbon nanotubes for in vivo radioemitter localization and imaging. *Nat. Mater.* **9**, 485–490 (2010).

10. Wohlstadter, J. N. *et al.* Carbon nanotube-based biosensor. *Adv. Mater.* **15**, 1184–1187 (2003).

11. Fedeli, S. *et al.* Azido-Substituted BODIPY Dyes for the Production of Fluorescent Carbon Nanotubes. *Chem. - A Eur. J.* **21**, 15349–15353 (2015).

12. Mooney, E., Dockery, P., Greiser, U., Murphy, M. & Barron, V. Carbon nanotubes and mesenchymal stem cells: Biocompatibility, proliferation and differentiation. *Nano Lett.* **8**, 2137–2143 (2008).

13. Guo, J., Wang, Y. & Zhao, M. Target-directed functionalized ferrous phosphate-carbon dots fluorescent nanostructures as peroxidase mimetics for cancer cell detection and ROS-mediated therapy. *Sensors Actuators, B Chem.* **297**, 126739 (2019).

14. Janyasupab, M. & Promptmas, C. Development of non-enzymatic N-doped graphene supported cobalt/iron amperometric based sensor for glucose detection in urine. *2018 IEEE EMBS Conf. Biomed. Eng. Sci. IECBES 2018 - Proc.* 577–582 (2019) doi:10.1109/IECBES.2018.8626693.

15. Chiang, Y. C., Lin, W. H. & Chang, Y. C. The influence of treatment duration on multi-walled carbon nanotubes functionalized by H 2 SO 4 /HNO 3 oxidation. *Appl. Surf. Sci.* **257**, 2401–2410 (2011).

16. Chattopadhyay, D., Lastella, S., Kim, S. & Papadimitrakopoulos, F. Length separation of zwitterion-functionalized single wall carbon nanotubes by GPC. *J. Am. Chem. Soc.* **124**, 728–729 (2002).

17. Li, J. & Zhang, Y. Large-scale aligned carbon nanotubes films. *Phys. E Low-Dimensional Syst. Nanostructures* **33**, 235–239 (2006).

18. submitted to Nature on Feb 5, 2004. (2004).

19. Allen, M. J., Tung, V. C. & Kaner, R. B. Honeycomb carbon: A review of graphene. *Chem. Rev.* **110**, 132–145 (2010).

20. Park, S. & Ruoff, R. S. Chemical methods for the production of graphenes. *Nat. Nanotechnol.* **4**, 217–224 (2009).

21. Reina, A. *et al.* Growth of large-area single- and Bi-layer graphene by controlled carbon precipitation on polycrystalline Ni surfaces. *Nano Res.* **2**, 509–516 (2009).

22. Jiao, L., Wang, X., Diankov, G., Wang, H. & Dai, H. Facile synthesis of high-quality graphene nanoribbons. *Nat. Nanotechnol.* **5**, 321–325 (2010).

23. Coliman, J. P. *et al.* "Picket Fence Porphyrins". Synthetic Models for Oxygen Binding Hemoproteins. *J. Am. Chem. Soc.* **97**, 1427–1439 (1975).

24. Brinker, C. J., Lu, Y., Sellinger, A. & Fan, H. ChemInform Abstract: Evaporation-Induced Self-Assembly: Nanostructures Made Easy. *ChemInform* **30**, no-no (2010).

25. Sutter, P., Sadowski, J. T. & Sutter, E. Graphene on Pt(111): Growth and substrate interaction. *Phys. Rev. B - Condens. Matter Mater. Phys.* **80**, 1–10 (2009).

26. Staudenmaier, L. Method for the preparation of the graphite acid. *Eur. J. Inorg. Chem.* **31**, 1481–1487 (1898).

27. Zhang, X. *et al.* Distribution and biocompatibility studies of graphene oxide in mice after intravenous administration. *Carbon N. Y.* **49**, 986–995 (2011).

28. Pan, S. & Aksay, I. A. Factors controlling the size of graphene oxide sheets produced via the graphite oxide route. *ACS Nano* **5**, 4073–4083 (2011).

29. Gonçalves, P. A. D. & Peres, N. M. R. An Introduction to Graphene Plasmonics. *An Introd. to Graphene Plasmon.* 1–431 (2016) doi:10.1142/9948.

30. Pan, Y., Sahoo, N. G. & Li, L. The application of graphene oxide in drug delivery. *Expert Opin. Drug Deliv.* **9**, 1365–1376 (2012).

31. Li, Q.-Y., Zu, Y.-G., Shi, R.-Z. & Yao, L.-P. Review Camptothecin: Current Perspectives. *Curr. Med. Chem.* **13**, 2021–2039 (2006).

32. Liu, Z., Robinson, J. T., Sun, X. & Dai, H. PEGylated nanographene oxide for delivery of water-insoluble cancer drugs. *J. Am. Chem. Soc.* **130**, 10876–10877 (2008).

33. Rana, V. K. *et al.* Synthesis and drug-delivery behavior of chitosan-functionalized graphene oxide hybrid nanosheets. *Macromol. Mater. Eng.* **296**, 131–140 (2011).

34. Eigler, S., Grimm, S., Enzelberger-Heim, M., Müller, P. & Hirscha, A. Graphene oxide: Efficiency of reducing agents. *Chem. Commun.* **49**, 7391–7393 (2013).

35. Hunt, A. *et al.* Epoxide speciation and functional group distribution in graphene oxide paper-like materials. *Adv. Funct. Mater.* **22**, 3950–3957 (2012).

36. Szabó, T. *et al.* Evolution of surface functional groups in a series of progressively oxidized graphite oxides. *Chem. Mater.* **18**, 2740–2749 (2006).

37. Dimiev, A. M., Alemany, L. B. & Tour, J. M. Graphene oxide. Origin of acidity, its instability in water, and a new dynamic structural model. *ACS Nano* **7**, 576–588 (2013).

38. Liu, Y., Yu, D., Zeng, C., Miao, Z. & Dai, L. Biocompatible graphene oxide-based glucose

biosensors. *Langmuir* **26**, 6158–6160 (2010).

39. Paquin, F., Rivnay, J., Salleo, A., Stingelin, N. & Silva, C. Multi-phase semicrystalline microstructures drive exciton dissociation in neat plastic semiconductors. *J. Mater. Chem. C* **3**, 10715–10722 (2015).

40. Yu, R. *et al.* Synthetic possibility of polystyrene functionalization based on hydroxyl groups of graphene oxide as nucleophiles. *New J. Chem.* **39**, 5096–5099 (2015).

41. Chen, H. *et al.* Phosphorylation of graphehe oxide to improve adsorption of U(VI) from aquaeous solutions. *J. Radioanal. Nucl. Chem.* **313**, 175–189 (2017).

42. De Leon, A. C., Alonso, L., Mangadlao, J. D., Advincula, R. C. & Pentzer, E. Simultaneous Reduction and Functionalization of Graphene Oxide via Ritter Reaction. *ACS Appl. Mater. Interfaces* **9**, 14265–14272 (2017).

43. Liao, K. H., Lin, Y. S., MacOsko, C. W. & Haynes, C. L. Cytotoxicity of graphene oxide and graphene in human erythrocytes and skin fibroblasts. *ACS Appl. Mater. Interfaces* **3**, 2607–2615 (2011).

44. Lu, C. H. *et al.* Using graphene to protect DNA from cleavage during cellular delivery. *Chem. Commun.* **46**, 3116–3118 (2010).

45. Wojtoniszak, M. *et al.* Synthesis, dispersion, and cytocompatibility of graphene oxide and reduced graphene oxide. *Colloids Surfaces B Biointerfaces* **89**, 79–85 (2012).

46. Yuan, J. *et al.* Cytotoxicity evaluation of oxidized single-walled carbon nanotubes and graphene oxide on human hepatoma HepG2 cells: An iTRAQ-coupled 2D LC-MS/MS proteome analysis. *Toxicol. Sci.* **126**, 149–161 (2012).

47. Chang, Y. *et al.* In vitro toxicity evaluation of graphene oxide on A549 cells. *Toxicol. Lett.* **200**, 201–210 (2011).

48. Bhattacharya, K. *et al.* Biological interactions of carbon-based nanomaterials: From coronation to degradation. *Nanomedicine Nanotechnology, Biol. Med.* **12**, 333–351 (2016).

49. Kurapati, R. *et al.* Dispersibility-Dependent Biodegradation of Graphene Oxide by Myeloperoxidase. *Small* **11**, 3985–3994 (2015).

50. Chen, S. *et al.* Mechanism-based tumor-targeting drug delivery system. Validation of efficient vitamin receptor-mediated endocytosis and drug release. *Bioconjug. Chem.* **21**, 979–987 (2010).

51. Lee, J. S. *et al.* Synthesis of a BODIPY library and its application to the development of live cell glucagon imaging probe. *J. Am. Chem. Soc.* **131**, 10077–10082 (2009).

52. Kaur, P. & Singh, K. Recent advances in the application of BODIPY in bioimaging and chemosensing. *J. Mater. Chem. C* **7**, 11361–11405 (2019).

53. Moss, G. P. Nomenclature of tetrapyrroles (Recommendations 1986). *Pure Appl. Chem.* **59**, 779–832 (1987).

54. van Koeveringe, J. A. & Lugtenburg, J. Novel pyrromethenes 1-Oxygen and 1-sulfur analogues; evidence for photochemical. *Recueil, J. R. Netherlands Chem. Soc.* **96**, 55–57 (1977).

55. Solomonov, A. V., Marfin, Y. S. & Rumyantsev, E. V. Design and applications of dipyrrin-based fluorescent dyes and related organic luminophores: From individual compounds to supramolecular self-assembled systems. *Dye. Pigment.* **162**, 517–542 (2019).

56. Li, Z., Mintzer, E. & Bittman, R. First synthesis of free cholesterol-BODIPY conjugates. *J. Org.*

Chem. **71**, 1718–1721 (2006).

57. Wagner, R. W. & Lindsey, J. S. Boron-dipyrromethene dyes for incorporation in synthetic multi-pigment light-harvesting arrays. *Pure Appl. Chem.* **68**, 1373–1380 (1996).

58. Thivierge, C., Bandichhor, R. & Burgess, K. Spectral dispersion and water solubilization of BODIPY dyes via palladium-catalyzed C-H functionalization. *Org. Lett.* **9**, 2135–2138 (2007).

59. Shah, M. *et al.* Pyrromethene–BF2 complexes as laser dyes:1. *Heteroat. Chem.* **1**, 389–399 (1990).

60. Yogo, T., Urano, Y., Ishitsuka, Y., Maniwa, F. & Nagano, T. Highly efficient and photostable photosensitizer based on BODIPY chromophore. *J. Am. Chem. Soc.* **127**, 12162–12163 (2005).

61. Scheibe, B., Borowiak-Palen, E. & Kalenczuk, R. J. Oxidation and reduction of multiwalled carbon nanotubes - preparation and characterization. *Mater. Charact.* **61**, 185–191 (2010).

62. Jameson, L. P. & Dzyuba, S. V. Expeditious, mechanochemical synthesis of BODIPY dyes. *Beilstein J. Org. Chem.* **9**, 786–790 (2013).

63. Andersen, J., Madsen, U., Björkling, F. & Liang, X. Rapid synthesis of aryl azides from aryl halides under mild conditions. *Synlett* 2209–2213 (2005) doi:10.1055/s-2005-872248.

64. Ménard-Moyon, C., Fabbro, C., Prato, M. & Bianco, A. One-pot triple functionalization of carbon nanotubes. *Chem. - A Eur. J.* **17**, 3222–3227 (2011).

65. Lin, H. B., Cooper, S. L., Zhao, Z. C., Garcia-Echeverria, C. & Rich, D. H. Synthesis of a novel polyurethane co-polymer containing covalently attached RGD peptide. *J. Biomater. Sci. Polym. Ed.* **3**, 217–227 (1992).

66. Van Agthoven, J. F. *et al.* Structural Basis of the Differential Binding of Engineered Knottins to Integrins αVβ3 and α5β1. *Structure* **27**, 1443-1451.e6 (2019).

67. Sheldrake, H. M. & Patterson, L. H. Strategies to inhibit tumor associated integrin receptors: Rationale for dual and multi-antagonists. *J. Med. Chem.* **57**, 6301–6315 (2014).

68. Maligaspe, E. *et al.* Photosynthetic antenna-reaction center mimicry: Sequential energy- and electron transfer in a self-assembled supramolecular triad composed of boron dipyrrin, zinc porphyrin and fullerene. *J. Phys. Chem. A* **113**, 8478–8489 (2009).

69. Mori, H. *et al.* In silico and pharmacological screenings identify novel serine racemase inhibitors. *Bioorganic Med. Chem. Lett.* **24**, 3732–3735 (2014).

70. Hishikawa, K. *et al.* Photoinduced nitric oxide release from a hindered nitrobenzene derivative by two-photon excitation. *J. Am. Chem. Soc.* **131**, 7488–7489 (2009).

71. Mallesha, N., Prahlada Rao, S., Suhas, R. & Channe Gowda, D. An efficient synthesis of tert-butyl ethers/esters of alcohols/amino acids using methyl tert-butyl ether. *Tetrahedron Lett.* **53**, 641–645 (2012).

72. Mock, J. N. *et al.* Haloenol pyranones and morpholinones as antineoplastic agents of prostate cancer. *Bioorganic Med. Chem. Lett.* **22**, 4854–4858 (2012).

73. König, W. & Geiger, R. Eine neue Methode zur Synthese von Peptiden: Aktivierung der Carboxylgruppe mit Dicyclohexylcarbodiimid unter Zusatz von 1-Hydroxy-benzotriazolen. *Chem. Ber.* **103**, 788–798 (1970).

74. Pérez-Picaso, L., Escalante, J., Olivo, H. F. & Rios, M. Y. Efficient microwave assisted syntheses of 2,5-diketopiperazines in aqueous media. *Molecules* **14**, 2836–2849 (2009).

75. Styers, T. J. *et al.* Synthesis of Sansalvamide A derivatives and their cytotoxicity in the MSS colon cancer cell line HT-29. *Bioorganic Med. Chem.* **14**, 5625–5631 (2006).

76. Lundt, B. F., Johansen, N. L., Vølund, A. & Markussen, J. REMOVAL OF t-BUTYL AND t-BUTOXYCARBONYL PROTECTING GROUPS WITH TRIFLUOROACETIC ACID: Mechanisms, Biproduct Formation and Evaluation of Scavengers. *Int. J. Pept. Protein Res.* **12**, 258–268 (1978).

77. Hughes, A. B. Amino Acids, Peptides and Proteins in Organic Chemistry. *Amin. Acids, Pept. Proteins Org. Chem.* **2**, (2010).

78. Vardhan, D. M. S., Kumara, H. K., Kumar, H. P. & Gowda, D. C. Inhibition of Urease Enzyme Activity By Urea and Thiourea Derivatives of Dipeptides Conjugated 2, 3-Dichlorophenyl Piperazine. *Int. J. Pharm. Pharm. Sci.* **9**, 92 (2017).

79. Kaur, A., Poonam, Patil, M. T., Mehta, S. K. & Salunke, D. B. An efficient and scalable synthesis of potent TLR2 agonistic PAM2CSK4. *RSC Adv.* **8**, 9587–9596 (2018).

80. Brough, P., Klumpp, C., Bianco, A., Campidelli, S. & Prato, M. [60]fullerene-pyrrolidine-N-oxides. *J. Org. Chem.* **71**, 2014–2020 (2006).

81. Saini, N. & Yang, X. Metformin as an anti-cancer agent: Actions and mechanisms targeting cancer stem cells. *Acta Biochim. Biophys. Sin. (Shanghai).* **50**, 133–143 (2018).

82. Pierotti, M. A. *et al.* Targeting metabolism for cancer treatment and prevention: Metformin, an old drug with multi-faceted effects. *Oncogene* **32**, 1475–1487 (2013).

83. Alimova, I. N. *et al.* Metformin inhibits breast cancer cell growth, colony formation and induces cell cycle arrest in vitro. *Cell Cycle* **8**, 909–915 (2009).

84. Morales, D. R. & Morris, A. D. Metformin in cancer treatment and prevention. *Annu. Rev. Med.* **66**, 17–29 (2015).

85. Jaune, E. & Rocchi, S. Metformin: Focus on melanoma. *Front. Endocrinol. (Lausanne).* **9**, 1–9 (2018).

86. Tseng, H. W., Li, S. C. & Tsai, K. W. Metformin treatment suppresses melanoma cell growth and motility through modulation of microRNA expression. *Cancers (Basel).* **11**, (2019).

87. Vancura, A., Bu, P., Bhagwat, M., Zeng, J. & Vancurova, I. Metformin as an Anticancer Agent. *Trends Pharmacol. Sci.* **39**, 867–878 (2018).

88. Mallik, R. & Chowdhury, T. A. Metformin in cancer. *Diabetes Res. Clin. Pract.* **143**, 409–419 (2018).

89. Saraei, P., Asadi, I., Kakar, M. A. & Moradi-Kor, N. The beneficial effects of metformin on cancer prevention and therapy: A comprehensive review of recent advances. *Cancer Manag. Res.* **11**, 3295–3313 (2019).

90. Fedeli, S. *et al.* The 'click-on-tube' approach for the production of efficient drug carriers based on oxidized multi-walled carbon nanotubes. *J. Mater. Chem. B* **4**, 3823–3831 (2016).

91. Baghayeri, M., Tehrani, M. B., Amiri, A., Maleki, B. & Farhadi, S. A novel way for detection of antiparkinsonism drug entacapone via electrodeposition of silver nanoparticles/functionalized multi-walled carbon nanotubes as an amperometric sensor. *Mater. Sci. Eng. C* **66**, 77–83 (2016).

92. Mirazi, N., Shoaei, J., Khazaei, A. & Hosseini, A. A comparative study on effect of metformin and metformin-conjugated nanotubes on blood glucose homeostasis in diabetic rats. *Eur. J.*

Drug Metab. Pharmacokinet. **40**, 343–348 (2015).

93. Yoo, S. *et al.* Enhanced Response of Metformin towards the Cancer Cells due to Synergism with Multi-walled Carbon Nanotubes in Photothermal Therapy. *Sci. Rep.* 1–9 (2017) doi:10.1038/s41598-017-01118-3.

94. Denise, C. *et al.* 5-Fluorouracil resistant colon cancer cells are addicted to OXPHOS to survive and enhance stem-like traits. *Oncotarget* **6**, 41706–41721 (2015).

95. Ota, S. *et al.* Metformin suppresses glucose-6-phosphatase expression by a complex I inhibition and AMPK activation-independent mechanism. *Biochem. Biophys. Res. Commun.* **388**, 311–316 (2009).

96. Chen, Z. *et al.* The Advances of Carbon Nanotubes in Cancer Diagnostics and Therapeutics. *J. Nanomater.* **2017**, (2017).

97. Cui, X., Wan, B., Yang, Y., Ren, X. & Guo, L. H. Length effects on the dynamic process of cellular uptake and exocytosis of single-walled carbon nanotubes in murine macrophage cells /631/80 /704/172 /82/29 /14/19 /14/34 /123 article. *Sci. Rep.* **7**, 1–13 (2017).

98. Yuan, Y. M. & He, C. The glial scar in spinal cord injury and repair. *Neurosci. Bull.* **29**, 421–435 (2013).

99. Su, Z. *et al.* Reactive astrocytes inhibit the survival and differentiation of oligodendrocyte precursor cells by secreted TNF-α. *J. Neurotrauma* **28**, 1089–1100 (2011).

100. Liu, W. *et al.* Folic acid conjugated magnetic iron oxide nanoparticles for nondestructive separation and detection of ovarian cancer cells from whole blood. *Biomater. Sci.* **4**, 159–166 (2016).

101. Stichel, C. C. & Müller, H. W. The CNS lesion scar: New vistas on an old regeneration barrier. *Cell Tissue Res.* **294**, 1–9 (1998).

102. Galtrey, C. M. & Fawcett, J. W. The role of chondroitin sulfate proteoglycans in regeneration and plasticity in the central nervous system. *Brain Res. Rev.* **54**, 1–18 (2007).

103. Bradbury, E. J. & Carter, L. M. Manipulating the glial scar: Chondroitinase ABC as a therapy for spinal cord injury. *Brain Res. Bull.* **84**, 306–316 (2011).

104. Silver, J. & Miller, J. H. Regeneration beyond the glial scar. *Nat. Rev. Neurosci.* **5**, 146–156 (2004).

105. Place, L. W., Sekyi, M. & Kipper, M. J. Aggrecan-mimetic, glycosaminoglycan-containing nanoparticles for growth factor stabilization and delivery. *Biomacromolecules* **15**, 680–689 (2014).

106. Marchesan, S., Kostarelos, K., Bianco, A. & Prato, M. The winding road for carbon nanotubes in nanomedicine. *Mater. Today* **18**, 12–19 (2015).

107. Pinillos-Madrid, J. F. & Gallardo, C. Carbon nanotubes: A viable drug delivery platform for the treatment of cancer. *J. Appl. Pharm. Sci.* **5**, 143–152 (2015).

108. Moradian, H., Fasehee, H., Keshvari, H. & Faghihi, S. Poly(ethyleneimine) functionalized carbon nanotubes as efficient nano-vector for transfecting mesenchymal stem cells. *Colloids Surfaces B Biointerfaces* **122**, 115–125 (2014).

109. Herrero, M. A. *et al.* Synthesis and characterization of a carbon nanotube-dendron series for efficient siRNA delivery. *J. Am. Chem. Soc.* **131**, 9843–9848 (2009).

110. Zhou, M., Peng, Z., Liao, S., Li, P. & Li, S. Design of microencapsulated carbon nanotube-based

microspheres and its application in colon targeted drug delivery. *Drug Deliv.* **21**, 101–109 (2014).

111. Zhang, W., Zuo, X. D. & Wu, C. W. Synthesis and magnetic properties of carbon nanotube-iron oxide nanoparticle composites for hyperthermia: A review. *Rev. Adv. Mater. Sci.* **40**, 165–176 (2015).

112. Jones, L. L., Margolis, R. U. & Tuszynski, M. H. The chondroitin sulfate proteoglycans neurocan, brevican, phosphacan, and versican are differentially regulated following spinal cord injury. *Exp. Neurol.* **182**, 399–411 (2003).

113. Tom, V. J., Steinmetz, M. P., Miller, J. H., Doller, C. M. & Silver, J. Studies on the development and behavior of the dystrophic growth cone, the hallmark of regeneration failure, in an in vitro model of the glial scar and after spinal cord injury. *J. Neurosci.* **24**, 6531–6539 (2004).

114. Matthews, R. T. *et al.* Aggrecan glycoforms contribute to the molecular heterogeneity of perineuronal nets. *J. Neurosci.* **22**, 7536–7547 (2002).

115. Sandvig, A., Berry, M., Barrett, L. B., Butt, A. & Logan, A. Myelin-, reactive glia-, and scar-derived CNS axon growth inhibitors: Expression, receptor signaling, and correlation with axon regeneration. *Glia* **46**, 225–251 (2004).

116. Yiu, G. & He, Z. Glial inhibition of CNS axon regeneration. *Nat. Rev. Neurosci.* **7**, 617–627 (2006).

117. Rhodes, K. E. & Fawcett, J. W. Chondroitin sulphate proteoglycans: Preventing plasticity or protecting the CNS? *J. Anat.* **204**, 33–48 (2004).

118. Gilbert, R. J. *et al.* CS-4,6 is differentially upregulated in glial scar and is a potent inhibitor of neurite extension. *Mol. Cell. Neurosci.* **29**, 545–558 (2005).

119. Zuo, J., Neubauer, D., Dyess, K., Ferguson, T. A. & Muir, D. Degradation of chondroitin sulfate proteoglycan enhances the neurite- promoting potential of spinal cord tissue. *Exp. Neurol.* **154**, 654–662 (1998).

120. McKeon, R. J., Schreiber, R. C., Rudge, J. S. & Silver, J. Reduction of neurite outgrowth in a model of glial scarring following CNS injury is correlated with the expression of inhibitory molecules on reactive astrocytes. *J. Neurosci.* **11**, 3398–3411 (1991).

121. Preston, E., Webster, J. & Small, D. Characteristics of sustained blood-brain barrier opening and tissue injury in a model for focal trauma in the rat. *J. Neurotrauma* **18**, 83–92 (2001).

122. Fitch, M. T., Doller, C., Combs, C. K., Landreth, G. E. & Silver, J. Cellular and molecular mechanisms of glial scarring and progressive cavitation: In vivo and in vitro analysis of inflammation-induced secondary injury after CNS trauma. *J. Neurosci.* **19**, 8182–8198 (1999).

123. Faulkner, J. R. *et al.* Reactive Astrocytes Protect Tissue and Preserve Function after Spinal Cord Injury. *J. Neurosci.* **24**, 2143–2155 (2004).

124. Jones, L. L., Sajed, D. & Tuszynski, M. H. Axonal Regeneration through Regions of Chondroitin Sulfate Proteoglycan Deposition after Spinal Cord Injury: A Balance of Permissiveness and Inhibition. *J. Neurosci.* **23**, 9276–9288 (2003).

125. Levine, J. M., Reynolds, R. & Fawcett, J. W. The oligodendrocyte precursor cell in health and disease. *Trends Neurosci.* **24**, 39–47 (2001).

126. Tan, A. M., Zhang, W. & Levine, J. M. NG2: A component of the glial scar that inhibits axon growth. *J. Anat.* **207**, 717–725 (2005).

127. Yang, L. J. S. *et al.* Sialidase enhances spinal axon outgrowth in vivo. *Proc. Natl. Acad. Sci. U. S. A.* **103**, 11057–11062 (2006).

128. Rhodes, K. E., Raivich, G. & Fawcett, J. W. The injury response of oligodendrocyte precursor cells is induced by platelets, macrophages and inflammation-associated cytokines. *Neuroscience* **140**, 87–100 (2006).

129. Davies, S. J. A., Goucher, D. R., Doller, C. & Silver, J. Robust regeneration of adult sensory axons in degenerating white matter of the adult rat spinal cord. *J. Neurosci.* **19**, 5810–5822 (1999).

130. Dyck, S. M. & Karimi-Abdolrezaee, S. Chondroitin sulfate proteoglycans: Key modulators in the developing and pathologic central nervous system. *Exp. Neurol.* **269**, 169–187 (2015).

131. Muleja, A. A., Mbianda, X. Y., Krause, R. W. & Pillay, K. Synthesis, characterization and thermal decomposition behaviour of triphenylphosphine-linked multiwalled carbon nanotubes. *Carbon N. Y.* **50**, 2741–2751 (2012).

132. Bonini, M., Wiedenmann, A. & Baglioni, P. Small angle polarized neutrons (SANSPOL) investigation of surfactant free magnetic fluid of uncoated and silica-coated cobalt-ferrite nanoparticles. *J. Phys. Chem. B* **108**, 14901–14906 (2004).

133. Chitosan, P. O. F. on the Structure and Properties of Chitosan. **33**, 1899–1904 (1992).

134. Coulson-Thomas, V. & Gesteira, T. Dimethylmethylene Blue Assay (DMMB). *Bio-Protocol* **4**, 1–7 (2014).

135. Shin, H. J. *et al.* Efficient reduction of graphite oxide by sodium borohydride and its effect on electrical conductance. *Adv. Funct. Mater.* **19**, 1987–1992 (2009).

136. Pei, S. & Cheng, H. M. The reduction of graphene oxide. *Carbon N. Y.* **50**, 3210–3228 (2012).

137. Gao, W., Alemany, L. B., Ci, L. & Ajayan, P. M. New insights into the structure and reduction of graphite oxide. *Nat. Chem.* **1**, 403–408 (2009).

138. Pei, S., Zhao, J., Du, J., Ren, W. & Cheng, H. M. Direct reduction of graphene oxide films into highly conductive and flexible graphene films by hydrohalic acids. *Carbon N. Y.* **48**, 4466–4474 (2010).

139. Moon, I. K., Lee, J., Ruoff, R. S. & Lee, H. Reduced graphene oxide by chemical graphitization. *Nat. Commun.* **1**, (2010).

140. Schniepp, H. C. *et al.* Functionalized single graphene sheets derived from splitting graphite oxide. *J. Phys. Chem. B* **110**, 8535–8539 (2006).

141. Fernández-Merino, M. J. *et al.* Vitamin C is an ideal substitute for hydrazine in the reduction of graphene oxide suspensions. *J. Phys. Chem. C* **114**, 6426–6432 (2010).

142. Bosch-Navarro, C., Coronado, E., Martí-Gastaldo, C., Sánchez-Royo, J. F. & Gómez, M. G. Influence of the pH on the synthesis of reduced graphene oxide under hydrothermal conditions. *Nanoscale* **4**, 3977–3982 (2012).

143. Stolle, A., Szuppa, T., Leonhardt, S. E. S. & Ondruschka, B. Ball milling in organic synthesis: Solutions and challenges. *Chem. Soc. Rev.* **40**, 2317–2329 (2011).

144. Szuppa, T., Stolle, A., Ondruschka, B. & Hopfe, W. An alternative solvent-free synthesis of nopinone under ball-milling conditions: Investigation of reaction parameters. *ChemSusChem* **3**, 1181–1191 (2010).

145. Fulmer, D. A., Shearouse, W. C., Medonza, S. T. & Mack, J. Solvent-free Sonogashira coupling

reaction via high speed ball milling. *Green Chem.* **11**, 1821–1825 (2009).

146. Schneider, F., Stolle, A., Ondruschka, B. & Hopf, H. The Suzuki-Miyaura reaction under mechanochemical conditions. *Org. Process Res. Dev.* **13**, 44–48 (2009).

147. Lee, H. C. *et al.* Review of the synthesis, transfer, characterization and growth mechanisms of single and multilayer graphene. *RSC Adv.* **7**, 15644–15693 (2017).

148. Hummers, W. S. & Offeman, R. E. Preparation of Graphitic Oxide. *J. Am. Chem. Soc.* **80**, 1339 (1958).

6. Heterogenous organo- and metal catalysis using phosphine oxide derivatives anchored on multiwalled carbon nanotubes.

6.1 INTRODUCTION AND OBJECTIVES OF CHAPTER (6)

A significant attention in the development of catalytic organophosphorus-based reactions featured last decade.[1] Thanks to numerous studies that have been published, important progress in the use of phosphines-mediated reactions for organic synthesis occurred. Substituted phosphines can catalyze many different kind of reactions recovering theirs starting oxidation state as the end of the process, such as when they act as nucleophiles in wide range of transformations ranging from Michael to Rauhut−Currier reaction.[2] However, there are several examples in which their oxidation state change from P(III) to P(V). This is the case of Staudinger ligation,[3] Mitsunobu,[4] Wittig[5] and Appel[6] reactions in which the byproduct is a phosphine oxide, which is often not easy to remove form the reaction mixture. In these cases, to obtain a catalytic process it is necessary to add a reduction step in which the former phosphine is recovered. The work of many researchers developed catalytic version of these reactions. First O'Brien et al presented the opportunity to evolve into a catalytic protocol the Wittig reaction.[7,8] By using a phosphine oxide as pre-catalyst and phenyl silanes as reducing agents, they achieve different alkenes in presence of either aldehyde or ketone as starting materials. Ashfeld et al showed a preeminent strategy for amide C-N bond construction exploiting a direct traceless Staudinger ligation of carboxylic acids and azides based on phosphine redox catalysis.[9] Inspired by the development of the previously mentioned Staudinger Ligation and Wittig reaction, also Mitsunobu reaction catalytic in phosphine was disclosed by O'Brien and coworkers[7] in the patent literature, and later optimized by Aldrich *et al.*[10] The same occurred with the Appel reaction.[11]

All this literature production, that has largely improved the efficiency of the procedures, is focused on the use of phosphine as homogeneous catalysts.[12] Quite the opposite, no catalyst in heterogeneous phase has been exploited. On the other hand, carbon nanotubes (CNTs) have already demonstrated an efficient support for heterogeneous catalysis both profiting of their high surface area, able to host a large number of catalytic species,[13,14] and their inner space.[15] Their easy functionalization and the large amount of literature produced on their applications.[16,17,18,19,20] made them ideal candidate for combining the use of phosphorus derivatives, as active component, and CNTs as heterogeneous support, in a catalytic process. Through this work we present examples of heterogeneous phosphorus-organocatalysis to synthesize small organic molecules. This goal was obtained decorating carbon nanotubes with phosphine oxide derivatives. Our catalytic system consists of a physical support, made of multi walled carbon nanotubes (MWCNT), for triphenyl phosphine oxide or phospholane oxide moieties. The high surface area of carbon nanotubes, permits to incorporate a significant phosphine moiety, achieved thanks to easy functionalization. The phosphorus-based molecules work to promote the organic reactions; the nanostructured carbon material allows an easy separation of products from the reaction mixture and consequently a straightforward purification: at the end of the process the reformed phosphine oxide is not discarded but recycled. The opportunity to reuse the catalyst after the first cycle of reaction is one of the major advantage of heterogeneous organocatalysis, making it a "greener process" if compared to chemical reactions carried out in homogeneous phase, seeing as the amount of needed phosphine is minor. To the best of our knowledge this is one of the few heterogeneous organocatalytic process described[21,22] in the literature and the firs using phosphine oxides.

In a previous work,[23] we have shown how it is possible to covalently functionalize carbon based nanostructured materials using amino substituted and azido substituted phosphine derivatives to prepare new materials that has been preliminarily tested in a Staudinger ligation experiment. Here we extend the use of the catalysts to Wittig and Mitsunobu reactions and demonstrate the possibility of a different use of the same material in which the phosphine moieties act as ligand for Pd nanoparticles to afford a nanocomposite that can catalyze the Heck reaction.[24] Heck reaction is a useful method for forming C-C bond on the double bond carbon atoms, with a wide application in organic synthesis.[25]

6.2 RESULTS AND DISCUSSION

The synthesis of the heterogeneous catalysts started from pristine MWCNT (**1**) that were oxidized using a HNO_3/H_2SO_4 mixture at 100 °C for 30 min. The oxidation removed any metal impurity, shortened the nanotubes and improved their dispersibility in most solvent due to the insertion of oxygenated functional groups as shown by IR spectra. The oxidized multiwalled carbon nanotubes (Ox-MWCNTs) **2** were used as substrate for the reaction with three different phosphine oxide derivatives: (4-aminophenyl)diphenyl phosphine oxide (**73**)[26]; (4-azidophenyl)diphenyl phosphine oxide (**74**)[23] and 3-azido-1-phenylphospholane 1-oxide (**75**) (**Figure 149**). Compound **75** was synthetized for this study since it is an analogue of the phospholane derivatives used by O'Brien[8] and Aldrich[10] in their works: the presence of an azido allowed an easy functionalization of the CNT. The synthesis started from phosphol-2-ene 1-oxide modifying a previous procedure.[27,28,29,30]

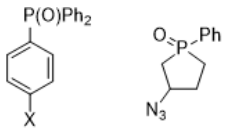

Figure 149. *Structure of starting phosphine oxides 7**3**, 7**4** and of phospholane 7**5**.*

The three compounds were used to covalently decorate the nanotubes **2** using the Tour protocol[31,32] for the amino derivative **73** (**Scheme 43**) to afford compound **76**, while profiting of the reactivity of the azido group, in compound **74** and **75**, towards carbon nanotube walls at high temperature[33] to afford compounds **77** and **78**, respectively **(Scheme 42)**.

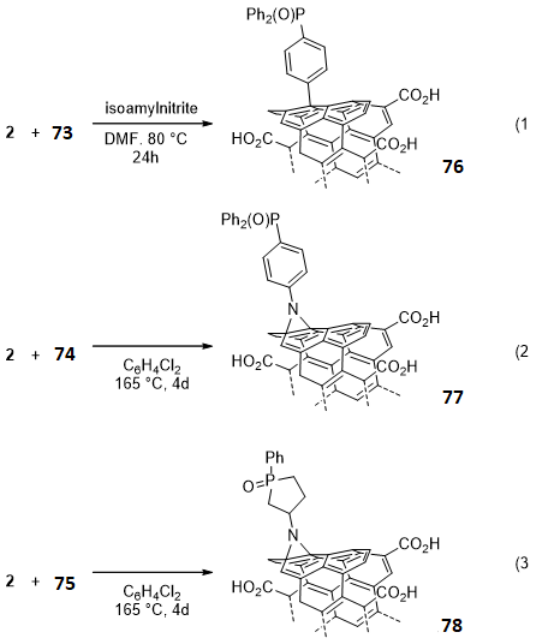

Scheme 42. *Synthesis of **76, 77** and **78**.*

The loading of the resulting materials can be evaluated using different techniques. A simple IR spectrum, for examples, can afford qualitative evaluation of the successful reaction based on the appearance of an intense band at 1140 cm^{-1} due to the P=O stretching.[34] All the IR spectra of materials **76**, **77** and **78** showed this diagnostic band (**Figure 150**)

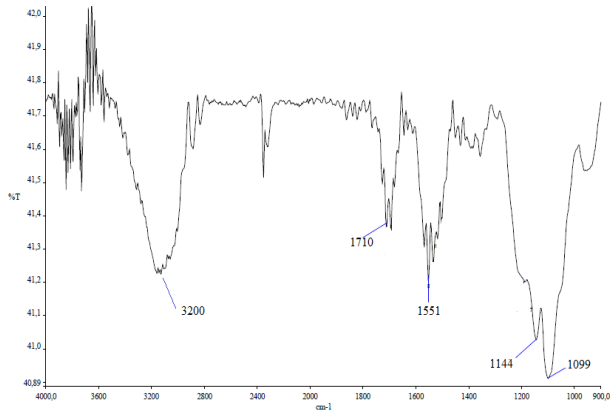

Figure 150*. IR spectra of **76***

A quantitative evaluation can also be offered by inductively coupled ion plasma atomic emission spectroscopy (ICP-AES) analyses evaluating the amount of phosphorus present on material **76**-**78** (**Table 14**).

Compound	ICP/AES P%	mmol/g P
76	1,84	0,59
77	2,25	0,73
78	2,09	0,67

Tab 14. Content of phosphorus calculated using ACP-AES.

The % content of nitrogen, estimated by elemental analyses, for compound **7** (1.12%), was in accordance with the loading degree suggested by ICP-AES. (Table 1). The synthetic approach consisting of nitrene cycloaddition provided a slightly higher loading both for compound **77** and **78** if compared to compound **76**.

The following chemical transformation was the reduction of phosphine oxides **76** and **77** to the corresponding phosphines (catalysts **79** and **80**, **Figure 151**), using trichloro silane.

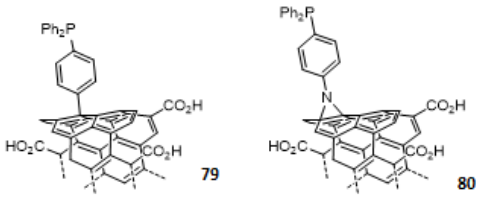

***Figure 151**. Structure of compounds **79** and **80**.*

We demonstrated the successful reduction using an XPS analysis (**Figure 142),** but the same qualitative information can be obtained from a simple IR spectrum showing the disappearance of the P=O stretching band at 1100 cm^{-1}. (**Figure 153**).

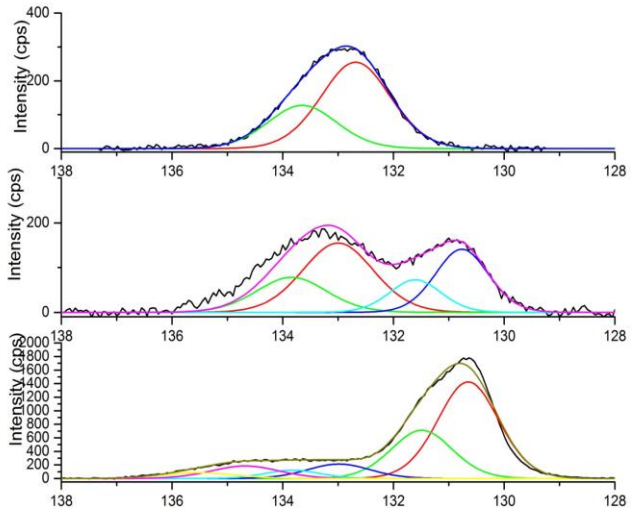

***Figure 152**. XPS analysis of samples form the reduction reaction of compound: starting material (top), after 24 h (middle), after 48 h (bottom).*

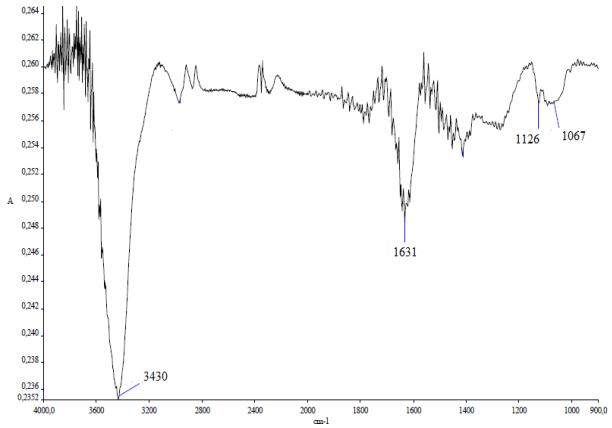

Figure 153. *IR spectrum of compound* ***80.***

Inspired by O'Brien and coworkers,[8] who demonstrated the application of the catalytic Wittig methodology by using 3-methyl-1-phenylphospholane 1-oxide as catalyst, the material **78**, carrying a similar substituent on the nanotube surface, was tested as heterogeneous organocatalyst in a Wittig reaction. Methyl bromoacetate (**82**) and benzaldehyde (**81**) were reacted to afford methyl cinnamate (**83**) in three repeated reaction cycles (**Scheme 43**) (**Table 14**). As base, DIPEA was preferred to Na_2CO_3 since it made easier to recycle the solid catalyst controlling the amount of base present in the reaction vessel.

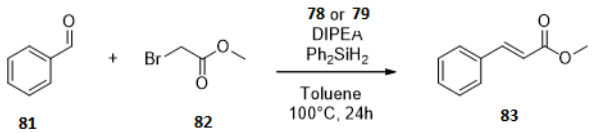

Scheme 43. The Witting reaction of **81** and **82** to afford cinnamate **83**

The catalytic process was guaranteed by the presence of Ph_2SiH_2 that reduced the phospholane oxide to the reacting phospholane at the beginning of every reaction cycle. Comparing our system with the results collected by O'Brien and coworkers (methyl cinnamate was obtained up to 80% yield using 0.1 equivalent of of phosphole), the performances of catalyst **78** is comparable for the first cycle (**Table 15**, entry 1) to the results obtained in solution considering that the reaction was conducted with an amount of catalysts corresponding to 0.057 equivalent of phospholane. Unluckily the catalyst efficiency degraded quickly in the second and third cycles. (**Table 15**, entry 1). The same reaction was performed using catalyst **79** (0.05 equivalents of phosphine substituent) with lower yields (**Table 16** entry2). Increasing the amount of catalysts, up to 0.1 equivalent did not increase the yields, while any reduction did not afford any product. This adopted heterogeneous organocatalysis allows a recycle of catalyst for both compounds (**78**, **79**): after an easy filtration, the decorated CNTs were suitable for the successive synthetic cycle.

Entry	catalyst	Amount of phosphole (mmol %)	Cycle 1	Cycle 2	Cycle 3
1	**78**	5.7	70%	52%	25%
2	**79**	5	55%	24%	-

*Tab 15. Catalytic Wittig reaction: yields of methyl cinnamate (**13**) over the different cycles*

The same redox driven approach, involving phosphorus compound with different valence, could be applied for Mitsunobu catalytic reaction. Again, inspired by the work of Aldrich and coworkers,[10] who used 1-phenylphospholane 1-oxide as catalyst (5%), we used catalyst **78** for the synthesis of the benzyl 4-nitrobenzoate (**86)** (**Scheme 44**) following Aldrich's procedure: refluxing THF in the presence of diisopropyl azodicarboxylate and phenyl silane as reducing agent.

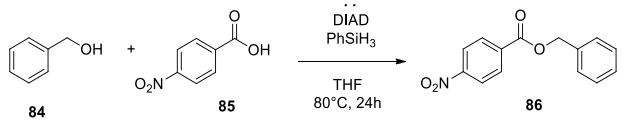

84 85 86

Scheme 44. *The Mitsunobu reaction of **84** and **85** to afford benzoate **86**.*

catalyst	Amount of phosphole (mmol %)	Cycle 1	Cycle 2	Cycle 3
78	2	54%	40%	22%

*Tab 16. Catalytic Mitsunobu reaction: yields of benzoate **86** over the different cycles.*

The reaction was conducted using an amount of **78** corresponding to 2% mol of phospholane derivative obtaining for the first cycle a conversion of 54%, Again the efficiency of the catalyst decrease rapidly in the second and third cycles and the amount of catalyst was critical to obtain acceptable yields.
Catalysts **79** and **80** were, then, used in a Staudinger Ligation reaction. Compound **80** was already used in our previous work. [83] Here we report a comparison of the activity of catalyst **79** and catalyst **80** in the Staudinger ligation reaction between benzoic acid (**87**) and benzyl azide (**88**) to obtain N-Benzylbenzamide (**89**). (**Scheme 45**) using the same reaction conditions as reported by Ashfeld and coworkers:[9] refluxing toluene in the presence of phenyl silane and the catalyst (triphenyl phosphine (10% mol) in the case of the work of Ashfeld and catalysts **79** or **80** (1% mol of phosphorus moiety) in this work)

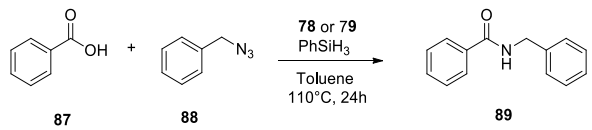

87 88 89

Scheme 45*. The Staudinger ligation reaction of **87** and **88** to afford benzamide **89***

Entry	catalyst	Amount of phosphine (mmol %)	Cycle 1	Cycle 2	Cycle 3
1	**79**	1	75%	30%	20%
2	**80**	1	69%	34%	21%

*Tab 17. Catalytic Staudinger Ligation: yields of benzamide **19** over the different cycles*

The results reported in **Table 17** show that catalysts **79** and **80** perform very similarly and regardless of the different way in which the triphenylphosphine group is linked to the nanotube surface. Again, the catalysts efficiency decreases rapidly upon recycling in the following reaction cycles.
Finally, adduct **80** was tested as support for Pd nanoparticles to produce a new nanocomposite (adduct **90**) in which the phosphine groups might play the role to coordinate and stabilize catalytically active Pd(0) nanoparticles. The nanoparticles were produced, in the presence of adduct **80**, upon reduction of Pd acetate in hydrogen atmosphere.

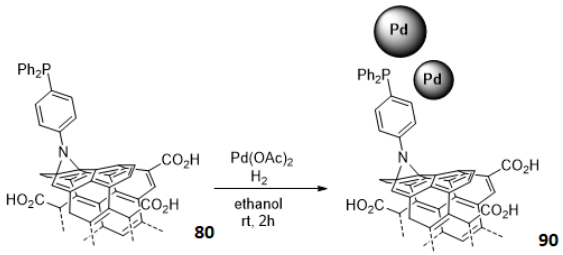

Scheme 46**. Synthesis of nanocomposite **20

The nanostructured material represented the carbon support for the effective catalyst: the nanoparticles synthesized from a palladium salt. TEM images confirmed the formation of nanoparticles (**Figure 154**). The evaluation of their diameter distribution is showed in **Figure 154**. ICP-plasma analysis estimated a loading degree of palladium 1.03 mmol/g for catalyst **20**.

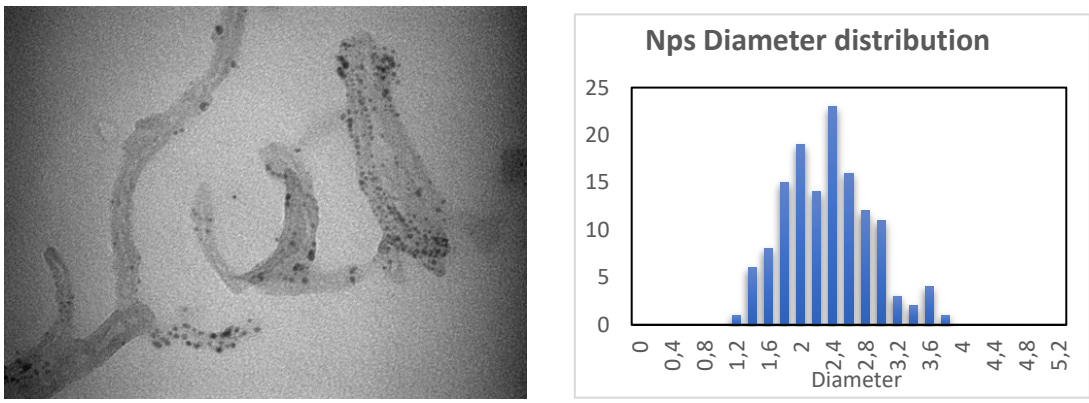

***Figure 154.** TEM image of nanocomposite 20 (up); Size distribution of Pd(0) nanoparticles (down).*

In a previous experiment Fareghi et al[24] synthetized trans-stilbene (**24**) (among many other substrates), via Heck reaction, in one cycle with 95% of yield, exploiting a catalytic system consisting of immobilized Pd nanoparticles on phosphine-functionalized graphene. We tested catalyst **20** to synthesize the same product in four different cycles starting from iodobenzene (**21**)

and styrene (**22**). (**Scheme 47**) The results are reported in table 5 (entry 1). Comparing the amount of Pd used by Fareghi and coworkers[24] (1.7 mol%) with our system **20** (0.92 mol%) the results are good. The decrease in performance recorded for the last reaction cycle can be explained with a significant leaching of palladium. An ICP-AES analysis showed a metal loading of 0.18 mmol/g after the fourth reaction cycle, suggesting a loss of 80% of the catalytic species.

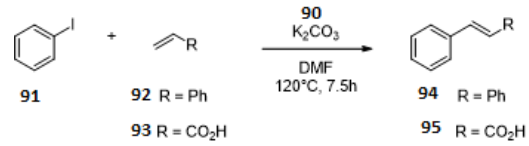

***Scheme 47**. Heck reactions between iodobenzene (**91**) and olefins catalyzed by **90**.*

Entry	olefin	Amount of Pd (mmol %)	Cycle 1	Cycle 2	Cycle 3	Cycle 4
1	**92**	0,97	66%	89%	90%	37
2	**93**	0,12	58%	61%	61	51

Tab 18 Catalytic Heck reaction: yields over the different cycles

Better results were obtained in the synthesis of trans-cinnamic acid in which the catalyst loading could be lowered down to 0.12 % of active Pd species preserving acceptable yields up to the forth cycle (table 5, entry 2).

6.3 CONCLUSIONS

The decoration of MWCNT with phosphine oxide derivatives has demonstrated a straightforward method to produce new nanostructured material with promising properties as catalysts. Although the limited efficiency of the processes study, this is, to the best of our knowledge, the first example of an organocatalytic processes based on phosphine oxides that has been transferred to heterogeneous materials.

6.4 MATERIALS AND METHODS

Materials and Methods should be described with sufficient details to allow others to replicate Materials MWCNTs were purchased from Sigma-Aldrich reagent, O.D. × L.= 6–9 nm × 5 µm, carbon >95%, CoMoCat©. All the other reagents, whose synthesis is not described, were commercially available and have been used without any further purification, if not specified otherwise. R_f values are referred to TLC on silica gel plate (0.25 mm, Merck silica gel 60 F254). NMR spectra were recorded on Varian Gemini 200 MHz or Varian Mercury 400 MHz at room temperature. Chemical shifts were reported in parts per million (ppm) relative to the residual solvent peak rounded to the nearest 0.01 for proton and 0.1 for carbon (reference: $CHCl_3$ [^{1}H:7.26, ^{13}C:77.2]. Coupling constants J were reported in Hz to the nearest 0.01 Hz. Peak multiplicity was indicated by s (singlet), d (doublet), t (triplet), q (quartet), m (multiplet) and br (broad signal). IR spectra were recorded on a Perkin-Elmer FT-IR 881 or Shimadzu FT-IR 8400s spectrometer. IR data are reported as frequencies in wavenumbers (cm^{-1}). Elemental analyses were performed with a Thermofinnigan CHN-S Flash E1112 analyzer. ICP analysis were made using an Optima 2000 Perkin Elmer Inductively Coupled Plasma (ICP) Dual Vision instrument after acidic mineralization.

TEM images were acquired at the electronic microscopic center CNR Florence (CE.M.E.) with a Philips CM12 with CRYO-GATAN UHRST 3500 technology, digital camera and EDAX microanalysis.

Compounds **3,**[26] **4, 6** and **7**, **9** and **10**[23] were synthesized following published procedures.

SYNTHESIS OF 3-azido-1-phenylphospholane 1-oxide **75**

Synthesis of this compound was accomplished by adaptation of the previously developed procedures.[27,28]

SYNTHESIS OF 1-phenyl-3-benzylaminophospholane 1-oxide **A**

In a Schlenk flask equipped with a magnetic stirrer was placed 1.78 g of phosphol-2-ene 1-oxide, 10.71 g (100 mmol) of benzylamine, and 10 mL of water. The resulting mixture was heated at 110 °C for 72 h. After cooling to room temperature, the reaction mixture was extracted with chloroform (3x30 mL), the extracts were combined, dried over anhydrous MgSO4, filtered, and evaporated. The excess of benzylamine was distilled off in vacuo to give crude product in the form of two diasteroisomers in ca. 1:2.5 ratio (^{31}P NMR: δ 58.63 and 56.38 ppm, respectively). Final purification of this mixture on a silica gel column using chloroform/metanol mixture (15:1) as eluent afforded 1.36 g (48%)of pure major adduct as an oil.

^{1}H NMR (CDCl3) δ 1.58 (bs, 1H), 1.95-2,07 (bm, 2H), 2.07-2.36 (bm, 3H), 2.37-2.46 (m,2H),3.35-3.46 (m, 1H), 3.89 (q, J = 13.1 Hz, 2H), 7.26-7.32 (m, 1H), 7.33-7.39 (m, 4H), 7.48-7.59 (m, 3H), 7.68-7.76 (m, 2H).

^{13}C NMR (CDCl3) δ 27.9 (d, J_{P-C} = 65.9 Hz), 31.3 (d, J_{P-C} = 5.5 Hz), 36.8 (d, J_{P-C} = 67.0 Hz), 51.7, 57.2 (d, J_{P-C} = 12.2 Hz), 127.1, 128.0, 128.5, 128.7 (d, J_{P-C} = 12.5 Hz), 129.8 (d, J_{P-C} = 11.,4 Hz),131.6 (d, J_{P-C} = 2.7 Hz), 134.4 (d, J_{P-C} = 91.6 Hz), 139.8.

^{31}P NMR(CDCl3) δ 56.38 ppm.
Elemental Anal. Calcd. for $C_{17}H^{20}NOP$: C, 71.61; H, 7.06; found C, 71.45; H, 6.99.
The minor adduct was washed from the column in the first fraction together with unreacted phosphol-2-ene 1-oxide and was not be separated. Considering that the double bond in phosphol-2-ene oxides is known to undergo attacks by the incoming reagents exclusively, or at least preferentially, from the side opposite to the bigger P-substituent,[29,30] the stereochemical array of the 3-amino and P-Ph substituents in the major adduct is tentatively assigned as *anti*.

SYNTHESIS OF 3-azido-1-phenylphospholane 1-oxide **75**

A solution of sodium azide (333 mg, 5.12 mmol) in H_2O (1.7 mL) and CH_2Cl_2 (0.5 mL) was added with a solution of trifluoromethanesulfonic anhydride (233 mg, 1.02 mmol) in CH_2Cl_2 (1 mL) at 0°C. The resulting suspension was stirred for 10’ at 0 °C and at room temperature for 3 h. After the addition of 5 mL of H_2O the mixture was extracted three times with CH_2Cl_2 (10 mL*3). The combined organic extracts were first washed with a saturated solution of Na_2CO_3, therefore stored.

$CuSO_4$ (0.9 mg, 0,005 mmol) and K_2CO_3 (106 mg, 0.77 mmol) were added to a solution of **A** (100 mg, 0.512 mmol) in H_2O/MeOH (7mL/18mL). The stirring solution was mixed to the previously achieved solution. After 19 h the reaction was completed. R_f of product 0.9 (EtOAc/MeOH 5:1). The mixture was

extracted five times with CH_2Cl_2 (15 mL). The combined organic extracts were washed with brine (35 mL), dried over anhydrous MgSO4, filtered, and evaporated in vacuo to afford **5** as a white solid. (80 mg, 71% yield).

IR spectrum *v* cm^{-1} 2100 s, 1710 s. (see SI: Figure S3);

^{1}HNMR (400 MHz, 298K, CDCl3) δH 7.69-7.63 (m, 2H), 7.53-7.44 (m, 3H), 4.20–4.11 (m, 2H), 2.37-2.02 (m, 7H).

MS-ESI 244.0, (M+Na) 464.8 (2M+Na)

SYNTHESIS OF CNTs-(PO-phospholane)-Nitrene (**78**)

A 100 mL flask was added with CNTs (20 mg) and 40 mL of 1,2- dichlorobenzene. The mixture was kept in an ultrasound bath for 20 min. 3-azido-1-phenylpfospholane 1-oxide (**5**) (60 mg 0.27 mmol) was added. The dispersion was kept at 165 °C under vigorous stirring for 4.5 days. The dispersion was diluted with isopropanol and centrifuged for 15 min at 1500 rcf. The supernatant was removed. The precipitate was washed, dispersed and centrifugated (5 min in ultrasound bath and centrifugation for 15 min at 1500 rcf) with a solution of diisopropyl ether and isopropanol 1:1. After the removal of supernatant, the solid was washed by cycle of dispersion in fresh methanol and centrifugation (two times). The product was recovered and dried to afford 66.8 mg of a black powder.
ICP-AES: phosphorus 0.67 mmol/g.
FTIR (KBr): 3380, 1713, 1586, 1159 and 1123 cm−1 P=O stretching. (see SI: Figure: S12).

SYNTHESIS OF Pd nanocomposite **(90**)

In a 5 mL flask, 5.2 mg (0.023 mmol) of $Pd(OAc)_2$ were added to a dispersion of 12.9 mg of **80** in 3 mL of ethanol. The mixture was kept under hydrogen atmosphere for 24 h. The reaction mixture was filtered through a polycarbonate membrane filter (pore diameter: 0.2 μm) and the solid washed (30 mL of ethanol) and dried. The product was recovered as 15.9 mg as a black powder.

ICP-AES of Pd: 1.04 mmol/g.
Procedure for the Wittig Reaction

A pyrex tube equipped with a stirring bar was charged with **78** or **79** (6 mg) and 0.2 mL of dry toluene. After 5 minutes in an ultrasonic bath, DIPEA (10 mg, 1.2 eq), benzaldehyde (7.5 mg, 1 eq), methyl bromoacetate (13 mg, 1.2 eq), diphenyl silane (26 mg, 2 eq) and 0.1 mL of dry toluene were added to the mixture. The reaction was heated at 100°C for 24 h. The catalyst was recovered first by centrifugation (2 x 15 min at 1500 rcf) and dispersion with toluene 20 mL, then same procedure by using methanol 20 mL. The solution was evaporated under vacuum giving the crude product. After flash chromatography (silica) using a mixture of hexane / ethyl acetate 10 : 1 the product was achieved as white solid.

GC-MS Spectrum (EI) retention time: 12.4'. m/z 163 (M+1)
^{1}H-NMR (400 MHz, 298 K, $CDCl_3$) δ H 7.70 (d, J= 16.0 Hz, 1H), 7.53-7.51 (m, 2H), 7.38-7.36 (m, 3H) 6.44 (d, J= 16.0 Hz, 2H). (see SI: Figure S18)

Procedure for the Mitsunobu Reaction

A pyrex tube equipped with a stirring bar was charged with **78** (5 mg) and 0.3 mL of tetrahydrofuran. After 5 minutes in an ultrasonic bath, 4-nitro benzoic acid (42 mg, 1.5 eq), benzyl alcohol (18 mg, 1 eq), diisopropyl azodicarboxylate (38 mg, 1.1 eq), phenyl silane (27 mg, 1.5 eq) were added to the mixture. The reaction was heated at 80°C for 24 h. The reaction mixture was filtered through a PTFE membrane filter (pore diameter: 0.2 µm). The catalyst was washed with fresh tetrahydrofuran and recovered. The solution was evaporated under vacuum giving the crude product. After flash chromatography (silica) using a mixture of hexane / ethyl acetate 20 : 1 the product (benzyl 4-nitrobenzoate) was achieved as a yellow solid.

GC-MS Spectrum (EI) retention time: 21.5'. 257 (M+1) m/z. (see SI: Figure S19)

^{1}H-NMR (400 MHz, 298 K, $CDCl_3$) δ H 8.30-8.23 (q, J= 9.2 Hz, 4H), 7.48-7.37 (m, 5H), 5.42 (s, 2H).

Procedure for the Staudinger Ligation

A pyrex tube was added with **80** (5 mg) degassed dry toluene (1 mL), carboxyl acid (0.19 mmol, 1 eq), a solution of benzyl azide (0.19 mmol) in 0.5 mL of degassed toluene and phenylsilane (21 mg, 0.19 mmol, 1 eq) and the reaction was stirred at 110 °C under nitrogen atmosphere for 24 h. The catalyst was recovered by dispersion with 20 mL of toluene and centrifugation 2 times for 15 minutes at 1500 rcf. The solution was evaporated under vacuum giving the crude product. The amide was recovered after flash chromatography (silica) using a mixture of hexane/ ethyl acetate 1:1. N-Benzylbenzamide: R_f = 0.48.

GC-MS spectrum (CI) retention time: 23.0'. m/z 212 (M+1). (see SI: Figure: S15) ^{1}H-NMR (200 MHz, 298 K, $CDCl_3$) δ H 7.79 (d, J= 9.6 Hz, 2H), 7.51-7.29 (m, 8H), 6.44 (bs, 1H), 4.65 (d, J= 5.6 Hz, 2H).

Procedure for Heck reaction

A pyrex tube was added with catalyst **90** (3.5 mg), potassium carbonate (138 mg, 2 eq), N,N-dimethyl formamide (1.5 mL), alkene (1.2 eq) and iodobenzene (79 mg, 1 eq) and the reaction was stirred at 120°C for 6 hours. The reaction mixture was diluted with 20 mL of isopropyl alcohol and centrifuged at 1500 rcf for 15'. The catalyst was recovered.
After flash chromatography the product was recovered.

trans-stilbene (hexane: ethyl acetate 2:1), was obtained as a white solid.
GC-MS Spectrum (CI) retention time: 29.1'. m/z 181 (M+1).
^{1}H-NMR (200 MHz, 278K, $CDCl_3$) δ H 7.53 (d, J= 6.8 Hz, 4H), 7.41-7.30 (m, 6H), 7.12 (s, 2H).

trans-cinnamic acid (hexane: dichloromethane 20:1), was obtained as a white solid.
GC-MS Spectrum (CI) retention time 15.3'. m/z 149 (M+1).

^{1}H-NMR (200 MHz, 298K, $CDCl_3$) δ H 7.81 (d, J=16 Hz 1H), 7.59-7.52 (m, 2H), 7.46–7.40 (m, 3H), 6.47 (d, J=16 Hz, 1H).

6.5 REFERENCES

1. Guo, H.; Fan, Y.C.; Sun, Z.; Wu, Y.; Kwon, O. Phosphine Organocatalysis. *Chemical Reviews* **2018**, *118*, 10049–10293, doi:10.1021/acs.chemrev.8b00081.

2. Aroyan, C.E.; Dermenci, A.; Miller, S.J. The Rauhut–Currier reaction: a history and its synthetic application. *Tetrahedron* **2009**, *65*, 4069–4084, doi:10.1016/j.tet.2009.02.066.

3. Bednarek, C.; Wehl, I.; Jung, N.; Schepers, U.; Bräse, S. The Staudinger Ligation. *Chem. Rev.* **2020**, *120*, 4301–4354, doi:10.1021/acs.chemrev.9b00665.

4. Fletcher, S. The Mitsunobu reaction in the 21 st century. *Organic Chemistry Frontiers* **2015**, *2*, 739–752, doi:10.1039/C5QO00016E.

5. Maercker, A. The Wittig Reaction. In *Organic Reactions*; American Cancer Society, 2011; pp. 270–490 ISBN 978-0-471-26418-7.

6. Appel, R.; Knoll, F.; Miche, W.; Morbach, W.; Wihler, H.-D.; Veltmann, H. Reaktionen im Zweikomponentensystem Triphenylphosphin/Tetrachlormethan1). *Chemische Berichte* **1976**, *109*, 58–70, doi:10.1002/cber.19761090103.

7. O'Brien, C.J.; Nixon, Z.S.; Holohan, A.J.; Kunkel, S.R.; Tellez, J.L.; Doonan, B.J.; Coyle, E.E.; Lavigne, F.; Kang, L.J.; Przeworski, K.C. Part I: The Development of the Catalytic Wittig Reaction. *Chemistry – A European Journal* **2013**, *19*, 15281–15289, doi:10.1002/chem.201301444.

8. O'brien, C.J. Catalytic wittig and mitsunobu reactions 2010.

9. Kosal, A.D.; Wilson, E.E.; Ashfeld, B.L. Phosphine-Based Redox Catalysis in the Direct Traceless Staudinger Ligation of Carboxylic Acids and Azides. *Angewandte Chemie International Edition* **2012**, *51*, 12036–12040, doi:10.1002/anie.201206533.

10. Buonomo, J.A.; Aldrich, C.C. Mitsunobu Reactions Catalytic in Phosphine and a Fully Catalytic System. *Angewandte Chemie International Edition* **2015**, *54*, 13041–13044, doi:10.1002/anie.201506263.

11. van Kalkeren, H.A.; van Delft, F.L.; Rutjes, F.P.J.T. Organophosphorus Catalysis to Bypass Phosphine Oxide Waste. *ChemSusChem* **2013**, *6*, 1615–1624, doi:10.1002/cssc.201300368.

12. Voituriez, A.; Saleh, N. From phosphine-promoted to phosphine-catalyzed reactions by in situ phosphine oxide reduction. *Tetrahedron Letters* **2016**, *57*, 4443–4451, doi:10.1016/j.tetlet.2016.08.036.

13. Campisciano, V.; Gruttadauria, M.; Giacalone, F. Modified Nanocarbons for Catalysis. *ChemCatChem* **2019**, *11*, 90–133, doi:10.1002/cctc.201801414.

14. Liang, Y.N.; Oh, W.-D.; Li, Y.; Hu, X. Nanocarbons as platforms for developing novel catalytic composites: overview and prospects. *Applied Catalysis A: General* **2018**, *562*, 94–105, doi:10.1016/j.apcata.2018.05.021.

15. Iglesias, D.; Melchionna, M. Enter the Tubes: Carbon Nanotube Endohedral Catalysis. *Catalysts* **2019**, *9*, 128, doi:10.3390/catal9020128.

16. Abousalman-Rezvani, Z.; Eskandari, P.; Roghani-Mamaqani, H.; Salami-Kalajahi, M. Functionalization of carbon nanotubes by combination of controlled radical polymerization and

"grafting to" method. *Advances in Colloid and Interface Science* **2020**, *278*, 102126, doi:10.1016/j.cis.2020.102126.

17. Negri, V.; Pacheco-Torres, J.; Calle, D.; López-Larrubia, P. Carbon Nanotubes in Biomedicine. *Top Curr Chem (Z)* **2020**, *378*, 15, doi:10.1007/s41061-019-0278-8.

18. Vázquez, E.; Giacalone, F.; Prato, M. Non-conventional methods and media for the activation and manipulation of carbon nanoforms. *Chem. Soc. Rev.* **2013**, *43*, 58–69, doi:10.1039/C3CS60164A.

19. Tasis, D.; Tagmatarchis, N.; Bianco, A.; Prato, M. Chemistry of Carbon Nanotubes. *Chem. Rev.* **2006**, *106*, 1105–1136, doi:10.1021/cr050569o.

20. Karousis, N.; Tagmatarchis, N.; Tasis, D. Current Progress on the Chemical Modification of Carbon Nanotubes. *Chem. Rev.* **2010**, *110*, 5366–5397, doi:10.1021/cr100018g.

21. Liu, X.; Tang, B.; Long, J.; Zhang, W.; Liu, X.; Mirza, Z. The development of MOFs-based nanomaterials in heterogeneous organocatalysis. *Science Bulletin* **2018**, *63*, 502–524, doi:10.1016/j.scib.2018.03.009.

22. Savateev, A.; Antonietti, M. Heterogeneous Organocatalysis for Photoredox Chemistry. *ACS Catal.* **2018**, *8*, 9790–9808, doi:10.1021/acscatal.8b02595.

23. Biagiotti, G.; Langè, V.; Ligi, C.; Caporali, S.; Muniz-Miranda, M.; Flis, A.; Pietrusiewicz, K.M.; Ghini, G.; Brandi, A.; Cicchi, S. Nanostructured carbon materials decorated with organophosphorus moieties: Synthesis and application. *Beilstein Journal of Nanotechnology* **2017**, *8*, 485–493, doi:10.3762/bjnano.8.52.

24. Fareghi-Alamdari, R.; Haqiqi, M.G.; Zekri, N. Immobilized Pd(0) nanoparticles on phosphine-functionalized graphene as a highly active catalyst for Heck, Suzuki and N-arylation reactions. *New J. Chem.* **2016**, *40*, 1287–1296, doi:10.1039/C5NJ02227D.

25. Zhang, Y.; Chu, W.; Xie, L.; Sun, W. Preparation and Catalytic Performance of Carbon Nanotube Supported Palladium Catalyst. *Chinese Journal of Chemistry* **2010**, *28*, 879–883, doi:10.1002/cjoc.201090165.

26. Zhang, X.; Liu, H.; Hu, X.; Tang, G.; Zhu, J.; Zhao, Y. Ni(II)/Zn Catalyzed Reductive Coupling of Aryl Halides with Diphenylphosphine Oxide in Water. *Org. Lett.* **2011**, *13*, 3478–3481, doi:10.1021/ol201141m.

27. Pietrusiewicz, K.M.; Zablocka, M. Optically active phosphine oxides. 3. Conjugate Adddition to Vinyl Phosphine Oxides in Aqueous Conditions. *Tetrahedron Lett.* **1988**, *29*, 937–940.

28. Maj, A. M.; Pietrusiewicz, K.M.; Suisse, I.; Agbossou, F.; Mortreux, A. Chiral β-Aminophosphine Oxides as Ligands for Ruthenium Assisted Enantioselective Transfer Hydrogenation of Ketones. *Tetrahedron: Asymmetry* **1999**, *10*, 831–835.

29. Brandi, A.; Cicchi, S.; Goti, A.; Koprowski, M.; Pietrusiewicz, K.M. Kinetic Resolution in 1,3-Dipolar Cycloaddition of Tartaric Acid-Derived Nitrones to 2,3-Dihydro-1-phenyl-1H-phospholes. An Enantioselective Approach to the 2,2'-Coupled Pyrrolidine–Phospholane Ring System. *Journal of Organic Chemistry* **1994**, *59*, 1315–1318, doi:10.1021/jo00085a019.

30. Goti, A.; Cicchi, S.; Brandi, A.; Pietrusiewicz, K.M. Nitrone cycloadditions to 2,3-dihydro-1-phenyl-1H-phosphole 1-oxide. Double asymmetric induction and kinetic resolution by a chiral nitrone. *Tetrahedron: Asymmetry* **1991**, *2*, 1371–1378, doi:10.1016/S0957-4166(00)80033-6.

31. Bahr, J.L.; Tour, J.M. Highly Functionalized Carbon Nanotubes Using in Situ Generated Diazonium Compounds. *Chem. Mater.* **2001**, *13*, 3823–3824, doi:10.1021/cm0109903.

32. Mechanism of the Coupling of Diazonium to Single-Walled Carbon Nanotubes and Its Consequences - Schmidt - 2009 - Chemistry – A European Journal - Wiley Online Library.

33. Holzinger, M.; Vostrowsky, O.; Hirsch, A.; Hennrich, F.; Kappes, M.; Weiss, R.; Jellen, F. Sidewall Functionalization of Carbon Nanotubes. *Angewandte Chemie International Edition* **2001**, *40*, 4002–4005, doi:10.1002/1521-3773(20011105)40:21<4002::AID-ANIE4002>3.0.CO;2-8.

34. Cotton, F.A.; Barnes, R.D.; Bannister, E. 442. The effect of complex-formation by phosphine oxides on their P–O stretching frequencies. *J. Chem. Soc.* **1960**, 2199–2203, doi:10.1039/JR9600002199.

7. Functionalization of GO with amines and phenols *via* Ball Milling

7.1 OBJECTIVES OF THIS CHAPTER (7)

The aim of this chapter was to obtain derivatives of graphene oxide through a covalent decoration with phenols, alcohols and amines.

Graphene oxide was reacted with the following compounds:

8-hydroxyquinoline (**96**), 4-nitrophenol (**97**), 4-hydroxyacetanilide (**98**), 4-chloro-2-nitrophenylmethanol (**99**), N-ferrocenyl-1,2-diaminoethane (**100**).

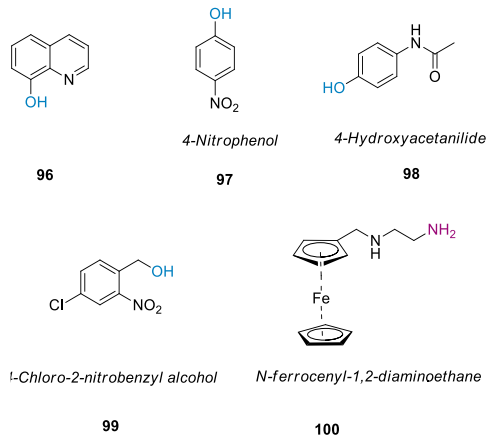

***Figure 155**. Molecules used in reactions with graphene oxide*

The study concerned the possibility of using nitrogenous or oxygenated nucleophiles to open epoxide rings, onto of graphene oxide surface.

These reactions with amines and phenols are well known when carried out in solution. By using non-classical reaction conditions such as, Ball Milling, no example was reported in literature.

This technique, based on the high energy impact of spheres of various materials, allows to perform reactions in the solid state avoiding the use of solvents. Sometimes completely different reactivity results were collected from those obtained by performing the same solution responses.

To favor the nucleophilicity of oxygenated reagents, phenols, the reaction was also carried out in the presence of sodium carbonate as a base.

The interest in this type of reactions is related to the possibility to perform the reduction of graphene oxide derivatives to obtain functionalized reduced graphene oxide.

Two different methods were used for this: hydrothermal reduction and chemical reaction with sodium borohydride reduction.

7.2 INTRODUCTION OF CHAPTER 7

7.2.1 CHEMICAL REDUCTION OF GRAPHENE OXIDE

Different methods to reduce dispersed graphene oxide in solution are known. The most classic procedure involves the use of hydrazine monohydrate, which has the advantage of not reacting with water. This characteristic allows to react graphene oxide in aqueous dispersions, unlike reducing agents such as lithium aluminum hydride which give rise to side reactions with solvents.

The reaction was carried out at 80-100 ° C. Hydrazine was added to a dispersion of graphene oxide in water and the precipitation of a black solid was observed, probably due to the increase in hydrophobicity of the material related to the decrease in polarity on the surface.

A disadvantage of this reduction was the introduction of heteroatoms, since nitrogen tends to remain covalently bonded to the graphene oxide surface.

To overcome this problematic sodium borohydride was added as reducing agent. Although this substrate was hydrolyzed by water, the process was slow enough to take place successfully in freshly prepared solutions with a large excess of $NaBH_4$. Improvements in conductivity were observed in rGO films obtained with $NaBH_4$ compared to products synthesized by using N_2H_4.[135]

A selective effect is shown by the majority of chemical reducing reagents A single reducing agent is not enough to remove all the functional groups containing oxygen.[136] Reductive processes consisting in several consecutive steps have been developed: Gao *et al*,[137] proposed a chemical strategy which involves a reduction with $NaBH_4$ followed by dehydration with sulfuric acid and annealing at high temperatures. The method proved particularly effective in restoring the conjugate structure of graphene.

Reduction techniques concerning the use of hydrogen iodide[138,139], showing high values in the C: O ratio of the products (about 15) and in sample conductivity (about 300 S / cm), and with ascorbic acid,[140] which provides results similar to the collected values connected with the use of hydrazine with the advantage of non-toxicity.

7.2.2 THERMAL REDUCTION

GO can also be reduced by thermal processes[141]: this process occurs by CO_2 extrusion performed by heating the graphite oxide to 1050 ° C. At high-temperature gas creates enormous pressure between the layers (up to 130 MPa at 1000 ° C) causing their separation. However, a considerable damage to the GO structure, was observed, around 30% of its mass was lost, leaving vacancies and topological defects that affect the properties of the material.

7.2.3 IDROTHERMAL REDUCTION

Hydrothermal synthesis allowed the transformation of the material by using aqueous solutions at high temperature and pressure.

The sample was dispersed in water (0.7 mg / mL), the suspension was brought up to pH 11 and transferred to an autoclave. The reaction was carried out under stirring for 6 h at 180 ° C.

Using a sealed tube, the water can be brought to a temperature well above its boiling point thanks to the increase in pressure resulting from heating.

The process was pH sensitive, as confirmed by HR-TEM, XPS and Raman studies. The acidic conditions led to a greater amount of defects in rGO samples, with thin sheet sizes and greater tendency to

aggregate. The increase in negative charge on the sheets was obtained by increasing the pH, which determines the repulsion between the layers.[142]

7.2.4 CHEMISTRY FUNCTIONALIZATION: GO REACTIVITY WITH ALCOHOLS AND AMINES

It is possible to covalently bind molecules to graphene oxide by exploiting the reactions which occur with the functional groups present on its surface (the carboxylic acids found on the sides, the epoxy groups and the hydroxyl groups). The ability to initiate these reactions makes graphene oxide a versatile precursor for a wide range of applications. Several reactions can occur simultaneously: nucleophiles such as amines or alcohols can react with carboxylic groups, after their activation, giving rise to the formation of amides and esters, and opening reactions of the epoxy ring can occur following nucleophilic attack. The groups more reactive are the epoxy rings.

Amines are better nucleophiles than alcohols, reacting more effectively with the electrophilic group. Alcohols and phenols can be activated by carrying out the reaction in a basic environment, to deprotonate the hydroxyl groups making them better nucleophiles. (**Figure 156**)

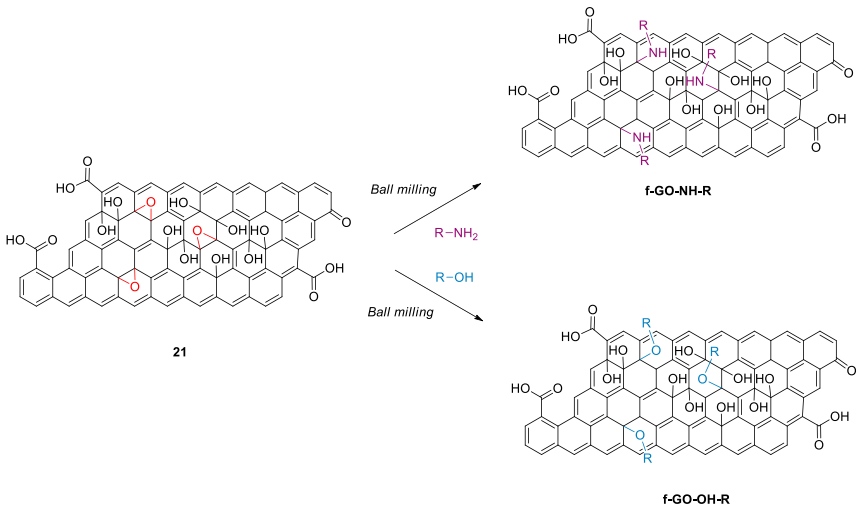

***Figure 156**. Reaction of epoxide rings of GO with amines and alcohols.*

7.2.5 BALL MILLING

A "mechano-chemical reaction" is defined, by IUPAC as "a chemical reaction induced by the direct absorption of mechanical energy". The input can be provided by various types of mechanical action, including grinding. The term "ball milling" describes processes of this type performed with ball mills The reagents are transferred into jars containing spheres that can vary in material and size, and subjected to mechanical agitation. The fine grinding of the material that occurs during the process reduces the size of the particles down to the nanoscale, increasing the surface area of the solid. The amount of highly active regions on the surface of material was increased.

The advantages of using mechanochemical techniques are numerous: the process is "green", delating the problem of wasting solvents, the reactions are carried out at lower temperatures compared to the

analogous reactions in solution, requiring less energy. No problems relating to the solubility of the products occurred.

7.2.6 PARAMETERS INFLUENCING THE REACTIONS

Several parameters influence the success of chemical reactions carried out by ball milling. The type of mill used, the frequency of oscillation / rotation, the reaction time, the material that constitutes jars and spheres, the size and number of spheres should be evaluated.[143]

There are planetary ball mills, the movement gave to the jars is a rotation in the horizontal plane, and vibration mills, the jars are accelerated by oscillations in vertical or horizontal plane. The latter are the most common mills. Since the physical mechanism is different, it is difficult to compare the results obtained with the two different types of mill.

The kinetic energy related to the movement of oscillation or rotation is directly proportional to the value of the frequency, so this parameter is fundamental. The frequency influences the reaction yield and the selectivity. The grade of effect of frequency depends on the type of reaction.[142,143]

The reaction time is an additional parameter that may be modulated: normally the reaction yield increases with the time,[144] unless secondary reactions occur that lead to a conversion of the products.

The choice of material of apparatus represents another influential parameter. Some reactions show an increase in yield when heavier materials are used,[145] others show no particular effects.[146] Tungsten carbide, steel, zirconium, corundum and agate jars can be used. In this work steel or agate jars were used. It is important, of course, to choose materials that are inert towards the reagents.

There may be problems due to abrasion of the material, which can determine the presence of impurities in the desired product.

Finally, the number of spheres significantly affects the reaction. when the density of the material and the diameter of the spheres was constant. There is a proportionality between the yield and the number of spheres given the linear correlation between mass, moment of inertia and kinetic energy of the system. The diameter of the balls is important when the total mass is not constant

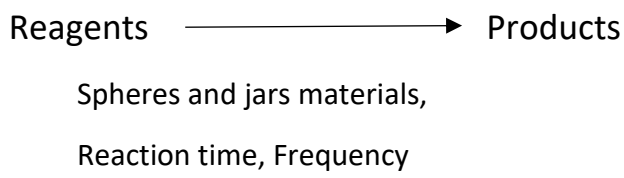

***Figure 157**. Parameters affecting ball milling reactions*

7.2.7 BALL MILLING APLLICATION TO GRAPHENE DERIVATIVE

Ball milling has been successfully used in reactions involving graphene, such as obtaining graphene oxide from flaked graphite and the production of graphene nanolayers: the kinetic energy generated during collisions is sufficient to break the bonds between the graphite layers e, also allowing the introduction of functional groups.

Ball milling can be used to functionalize graphene oxide, such as to obtain functionalized GO with PEG for targeting cancer cells.

In our work, ball milling was used to covalently bind different types of nucleophiles to the graphene oxide substrate. This technique is useful to avoid the consumption of high volumes of solvent that would otherwise be necessary in order not to aggregate the graphene oxide in suspension.

7.3 DISCUSSION AND RESULTS

The goal of this work was the functionalization of graphene oxide with different nucleophiles and consecutive reduction of synthesized products. The opportunity to use the Ball milling technique allows to achieve a greener process compared to the reaction in liquid phase, without solvents. The solid phase, furthermore avoids the reaction workout, saving time and resources.

7.3.1 FUNCTIONALIZATION OF GRAPHENE OXIDE

The reactions were carried out through ball milling technique, the powdered samples were placed into steel or agate jars containing a sphere and subjecting them to mechanical stirring. The material of the jars and the spheres was specified for each reaction in the experimental part. Reactions ratio ratio by weight between the reactants was 1: 1.

The oxygenated nucleophiles were pre-mixed with sodium carbonate for 10 minutes at 25 Hz (1500 rpm) and then mixed with the GO at 25 Hz for 40 minutes, time required to quantitatively perform the reaction, without overheating the jars. The premixing with Na_2CO_3 promoted the deprotonation of phenols making them better nucleophiles, profitable to open epoxy ring.

The amine was reacted directly with GO.

In all reactions, about 100 mg of inert NaCl was added to the jars in order to increase the volume occupied.

The samples were then subjected to several washes with suitable solvents, in order to remove both NaCl and the excess reagent not reacted with GO. The washes were carried out by dispersing the sample in the solvent, later repeated centrifuges were performed. Washing waters were checked by using UV-vis spectroscopy to verify the absence of the unreacted starting material. The product was then filtered under vacuum, dispersed in MilliQ water and freeze-dried. The samples functionalized with phenols showed some difficulties, when washed with water quite stable dispersions were formed. A large part of the sample remained dispersed in the solvent. The following centrifuges, leading to a difficult recovery of it.

All lyophilized samples were characterized by UV-vis, IR spectroscopy and elemental analysis. The results of the elemental analyses were shown below. Brackets (1) indicate the product obtained without premixing and (2) the product obtained by premixing with Na_2CO_3.

Sample	N%	C%	H%	mmol N / 100 mg
GO – Hydroxyquinoline (**1**)	0,826	52,920	2,580	0,059
GO – Hydroxyquinoline (**2**)	1,921	51,805	1,981	0,137
GO – 4-Nitrophenol (**1**)	0,000	39,322	1,535	0,000
GO – 4-Nitrophenol (**2**)	0,000	33,599	1,151	0,000
GO – 4-Hydroxyanalide (**1**)	0,237	48,267	2,402	0,017
GO – 4-Hydroxycetanalide (**2**)	0,438	45,455	2,065	0,031
GO – 4-Chloro-2-nitrobenzyl methanol (**1**)	0,000	43,550	2,146	0,000
GO – 4-Chloro-2-nitrobenzyl methanol (**1**)	0,000	37,872	1,974	0,000
GO – N-ferrocenyl-1,2-diaminoethane	1,202	43,497	2,385	0,043

Tab 19. Elemental analyses to evaluate the loading degree on GO.

That functionalization did not occur successfully with 4-chloro-2-nitrophenylmethanol and 4-nitrophenol, which are obviously too weak nucleophiles.

The GO functionalization with phenols occurred by activating the molecule in a basic environment, the final product exhibits greater functionalization (the nitrogen loading degree was approximately double in both cases).

For GO -N-ferrocenyl-1,2-diaminoethane, the functionalization of the sample was also confirmed by the ICP analysis, which indicates an amount of iron equal to 33.82 µg / mg.

The provided results can be compared with the information obtainable from the UV-vis spectra of the products **(Figure 158**)

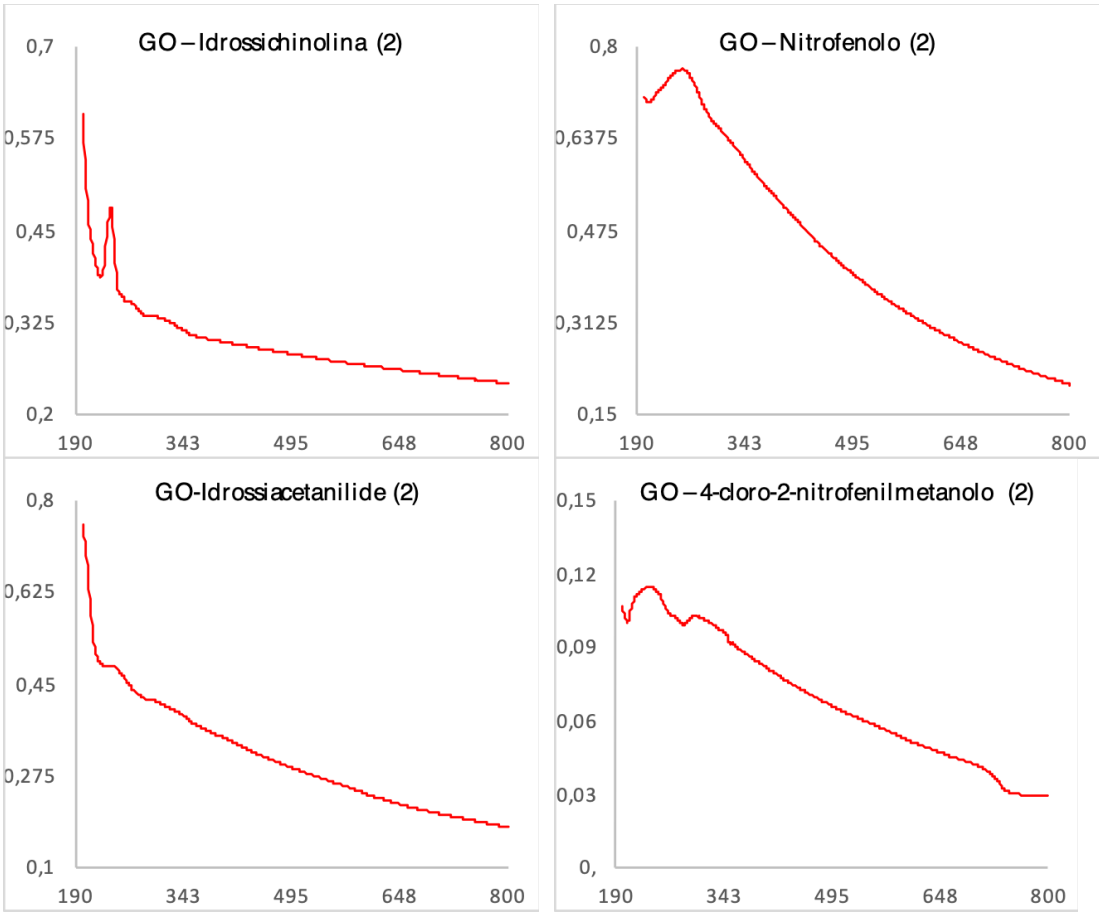

***Figure 158**. UV-vis spectrum of functionalized GO.*

The spectra of the samples pre-mixed with sodium carbonate have been reported.

The spectrum of GO - N-ferrocenyl-1,2-diaminoethane was not carried out, since the amine does not show absorption peaks in the UV.

In general, the absorption peak of GO and that of the molecules bund onto GO should be observed, possibly overlapping.

Typically, GO has an absorption peak spectrum around 230 nm, which is attributed to the $\pi - \pi^*$ transition caused by the aromatic ring, while rGO shows a peak, shifted at 270 nm.[147]

In all spectra, the peak of the GO was shifted to longer wavelengths, this could be an indication of a partial reduction of the GO which occurred during the functionalization process.

The functionalization was confirmed in spectrum 1, a peak at 240 nm characteristic of hydroxyquinoline was clearly visible.

In spectrum 3, a peak at 243 nm relating to hydroxyacetanilide should be observed, but it was not very intense and superimposed on GO curve.

The peak relative to nitrophenol (317 nm) in spectrum 2 was not observed, elemental analysis confirmed that the reaction did not occur.

4-chloro-2-nitrophenylmethanol showed a peak at 253 nm, it was not clearly identifiable in spectrum 4. Elemental analysis, indicated the lack of functionalization.

IR spectra of oxidized products (reported in methods and synthesis) showed OH, C = C and C-O stretching and the characteristic of graphene oxide material. Peaks relative to other molecular vibrations were less intense and superimposed on these. The spectra were therefore not useful in confirming the functionalization.

7.3.1 THERMAL REDUCTION

The most functionalized products, GO - hydroxyquinoline and GO - N-ferrocenyl-1,2-diaminoethane, were subjected to hydrothermal reduction. This method had already given good results in previous experiments on the reduction of GO functionalized with amines.

A 0.7 mg / mL suspension of the sample in MilliQ water was brought to pH 11 by the addition of NaOH 0.1 M solution and transferred to a 20 mL capacity sealed autoclave.

The autoclave was heated to 180 ° C and the reaction was carried out for 6 hours under magnetic stirring. The crude product was then filtered under vacuum and washed with MilliQ water.

Advantages of the method were undoubtedly the simplicity of the procedure and the standardization of the method for all samples.

In **Tab 20** the results of elemental analyses of reduced products were reported.

Sample	N%	C%	H%	mmol N / 100 mg
GO – N-ferrocenyl-1,2-diaminoethane	1,026	66,227	1,441	0,037
GO – Hydroxyquinoline (**2**)	2,287	60,202	2,184	0,163

Tab 20. Elemental analyses of reduced products.

Both samples, showed an increased percentage of carbon compared to the amount of carbon of the corresponding oxidized product. The functionalization during the process was preserved, as highlighted by the quantity of nitrogen, which was slightly decreased for GO - N-ferrocenyl-1,2-diaminoethane, while for GO - Hydroxyquinoline increased, suggesting that the percentage of oxygen on reduced sample had actually decreased.

No peaks useful for characterization in UV spectra of the samples were observed, the reduced compounds were difficult to disperse.

7.3.2 GO REDUCTION WITH $NaBH_4$

Sodium borohydride reduction was performed for all samples. To verify the effectiveness of the process, first the reaction was applied to no-functionalized GO. An excess of $NaBH_4$ was added to a 0.5 mg / mL suspension of GO and the reaction mixture was heated at 100 ° C for 3 h.

Characteristic peck of GO in UV measures moves from 228 nm to 273 nm, confirming the occurred reduction (**Figure 159**):

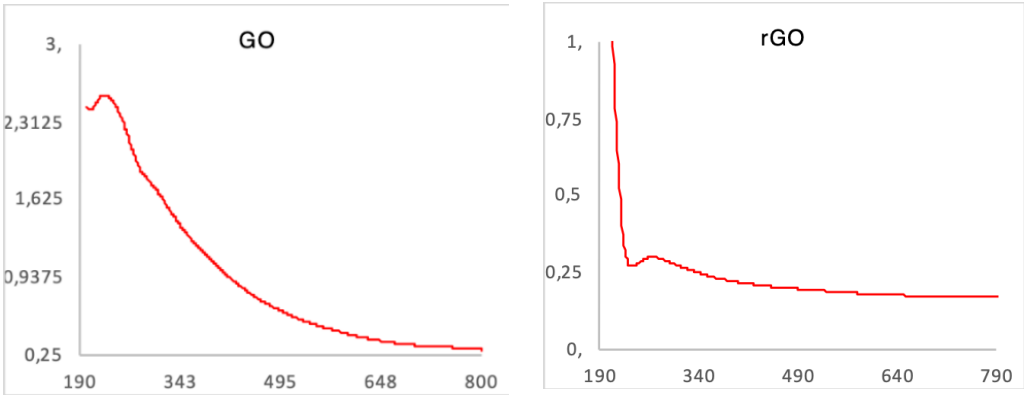

Figure 159. *UV spectra of GO and rGO reduced with sodium borohydride.*

The procedure was then replicated on all functionalized samples.

The method provided good results: elemental analyses revealed that the quantity of nitrogen and carbon has increased compared to the corresponding oxidized samples.

Sample	N%	C%	H%	mmol N / 100 mg
rGO	0,000	55,671	0,615	0,000
rGO – N-ferrocenyl-1,2-diaminoethane	1,409	52,247	2,818	0,050
rGO – Hydroxyquinoline	2,266	60,709	2,649	0,162
rGO – 4-Hydroxycetanalide	0,555	56,904	1,779	0,040

Tab 21

The procedure is therefore efficient for all samples, giving results comparable to the values collected with hydrothermal reduction. The chemical reductions performed with the addition of $NaBH_4$, presented an increase in the percentage of hydrogen, if compared to the samples reduced by hydrothermal method. Additional OH groups were impurities generated during this reductive process.[148]

The reduced products were difficult to disperse in water, improving slightly in basic solutions. It was therefore complicated to obtain information from the UV-vis spectra. Spectrum of rGO - N-ferrocenyl-1,2-diaminoethane was reported, the shifted peak of reduced GO moved around 270 nm.

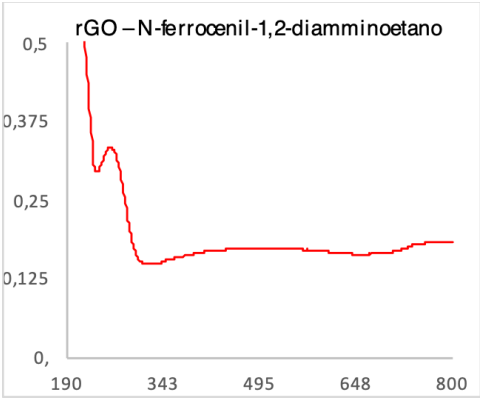

***Figure 160**. UV spectrum of rGO – N-ferrocenyl-1,2-diaminoethane*

In all the IR spectra of the reduction products (shown in the Experimental Part), a widened band was observed relating to the presence of OH groups. These groups were not totally eliminated through the reductive processes. However, many spectra showed a reduction in intensity of this band, in particular in the products obtained through hydrothermal reduction.

XPS measures performed on samples containing N-ferrocenyl-1,2-diaminoethane. **Figure 161** showed the XPS spectra of GO - N-ferrocenyl-1,2-diaminoethane (A), rGO - N-ferrocenyl-1,2-diaminoethane reduced with hydrothermal treatment (B), rGO - N-ferrocenyl-1 , 2-diaminoethane reduced with sodium borohydride (C).

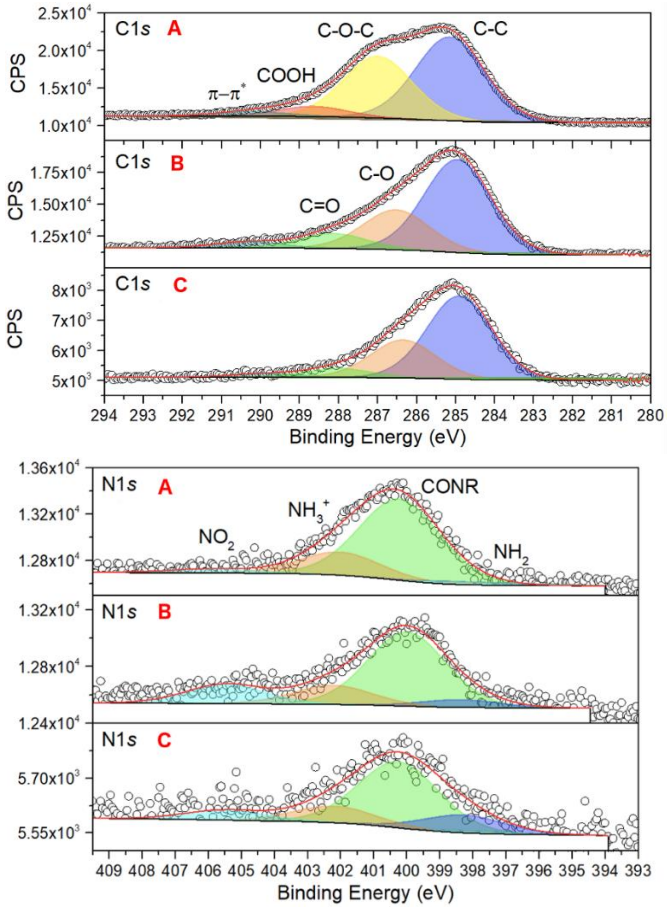

***Figure 161**. XPS spectra of rGO – N-ferrocenyl-1,2-diaminoethane*

In N1s region of spectra A, B, C we observed the presence of NH_2 (≃398 eV) and NH_3^+ (≃402 eV) groups due to molecules which have not reacted with GO. The main contribution was provided by the CN bond (≃ 400 eV), which confirmed the functionalization of GO, even after reductive processes.

In C1s region, peaks attributable to the C-O-C epoxy bonds (≃ 287 eV) and COOH of carboxylic acids (≃288.6 eV) were observed in the oxidized sample. These signals were not present in the reduced sample, where instead we can identify those of the groups C = O (≃288.5 eV) and C-O (≃286 eV). This confirmed the GO reduction.

The results therefore confirmed the data obtained from the elemental analyses and the UV-vis spectra.

7.4 CONCLUSION AND OUTLOOKS

This work showed the possibility to functionalize layers of graphene oxide with nucleophiles by using the ball milling technique. had already been obtained. Previous experiments concerning the decoration with amines via *Ball milling* demonstrated good results, but the reactivity with phenols had not been investigated. Despite the lower nucleophilicity compared to amines, it was possible to bind oxygenated nucleophiles onto GO.

The results regarding the reduction of GO samples evidenced the success of reaction proved by elemental analyses, UV-vis and IR. The reductions occurred without loss of nucleophiles covalent bund to GO, thus maintaining the functionalization.

Future investigations could introduce several phenols and amines on GO, furthermore different methods to reduce substrates may be investigated. In addition the characterization of materials could proceed by XPS; TEM or AFM to achieve additional information about the new modifications of material.

7.5 MATERIAL AND METHODS

SYNTHESIS OF GO – 8-Hydroxyquinoline **101**

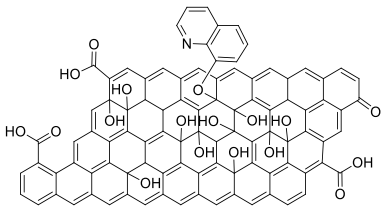

101

80 mg of graphene oxide, 80 mg of 8-Hydroxyquinoline and 100 mg of NaCl were placed into a 10 mL steel jar containing a steel sphere. The jar was put in a ball mill and subjected to mechanical stirring for 40 'at a frequency of 25 Hz. The product was recovered, dispersed in 80 mL of MilliQ water and divided into 4 50 mL Falcon tubes. It was centrifuged at 8000 rpm for 15 '. The process was repeated 7 times using a 1: 1 water / methanol mixture as solvent.

The product was subsequently dialyzed in a 4: 1 water / methanol solution in order to completely remove the excess of unreacted phenol.

The product was finally filtered on a polycarbonate membrane with 0.4 µm pores, dispersed in 80 mL of MilliQ water and freeze-dried.

Elemental analyses CHN: N 0.83 %, C 52.92 %, H 2.58 %

Nitrogen loading degree: 0.06 mmol/100 mg of material

UV-vis: the material was dispersed in methanol to achieve a 50 ppm solution, maximum absorption at 240 nm (8-Hydroxyquinoline).

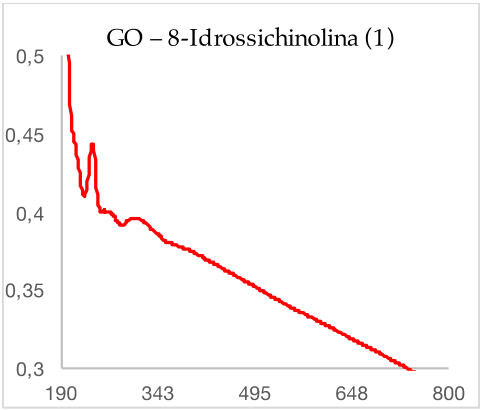

Figure162*. UV spectrum of compound 101*

IR spectrum (KBr): 3700-3000 (str. OH), 1620 (str. C=C aromatic groups), 1377 (str. C-O), 1060 (str. C-OH) cm^{-1}

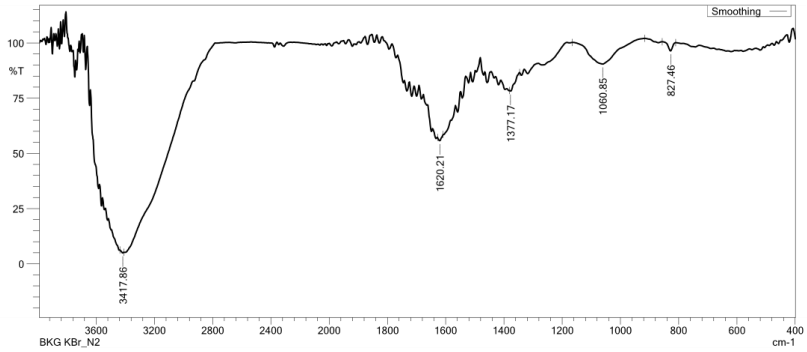

Figure 163*. IR spectrum of compound 101.*

SYNTHESIS OF GO – 8-Hydroxyquinoline with Na_2CO_3 **102**

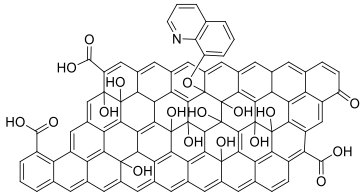

102

80 mg of graphene oxide, 80 mg of 8-Hydroxyquinoline, 100 mg of NaCl, 80 mg of Na_2CO_3 were placed into a 5 mL steel jar containing a steel sphere. The jar was put in a ball mill and subjected to mechanical stirring for 40 'at a frequency of 25 Hz. The product was recovered, dispersed in 80 mL of MilliQ water

and divided into 4 50 mL Falcon tubes. It was centrifuged at 8000 rpm for 15 '. The process was repeated 7 times using a 1: 1 water / methanol mixture as solvent.

The product was subsequently dialyzed in a 4: 1 water / methanol solution in order to completely remove the excess of unreacted phenol.

The product was finally filtered on a polycarbonate membrane with 0.4 µm pores, dispersed in 80 mL of MilliQ water and freeze-dried.

Elemental analyses: nitrogen loading degree: 0.14 mmol/100 mg of material

UV-vis: the material was dispersed in methanol to achieve a 50 ppm solution, maximum absorption at 240 nm (8-Hydroxyquinoline).

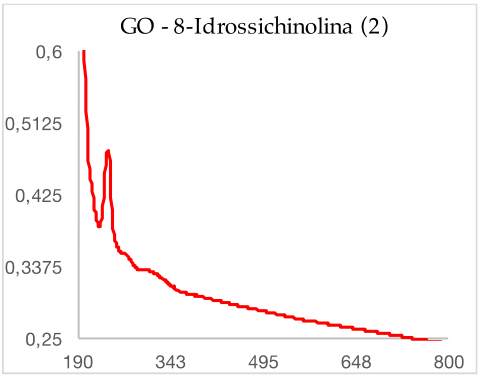

Figure 164**. UV spectrum of compound **102

IR spectrum (KBr): 3194 (str. OH), 1589 (str. C=C aromatic groups), 1375 (str. C-O), 1242 (str. C-O) cm^{-1}

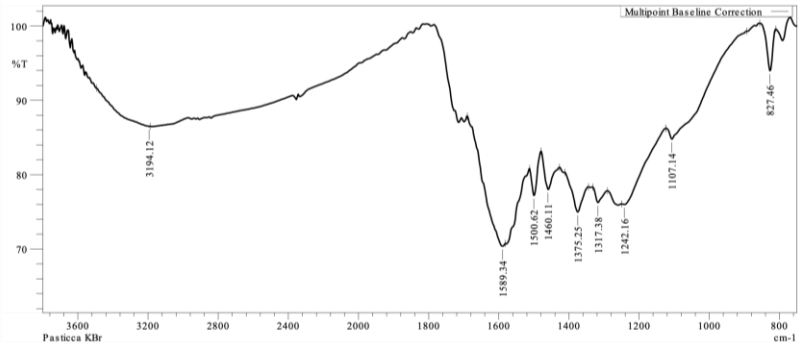

Figure 165**. IR spectrum of compound **102

Hydrothermal reduction of GO – 8-Hydroxyquinoline **103**

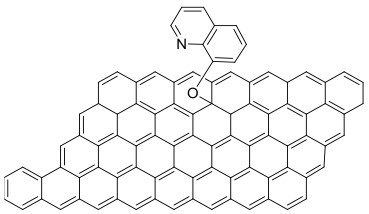

103

14 mg of GO - 8-Hydroxyquinoline were dispersed in 20 mL of MilliQ water and the suspension was brought to pH 12 with the addition of 0.1 M NaOH water solution. The mixture was placed into an autoclave which was heated to 180 ° C for 6 h, under stirring.

The product was recovered and finally filtered on a nylon membrane with 0.4 µm pore. The product was washed several times until neutral pH of washing water, then it was freeze-dried.

Elemental analyses: N 2.29 %, C 60.20 %, H 2.18 %

Nitrogen loading degree: 0.16 mmol/100 mg of material

UV-vis: the material was dispersed with difficulty in methanol, the identification of a clear peck was not possible.

IR spectrum (KBr): 3500-3000 (str. OH), 1579 (str. C=C), 1238 (str. C-O) cm^{-1}

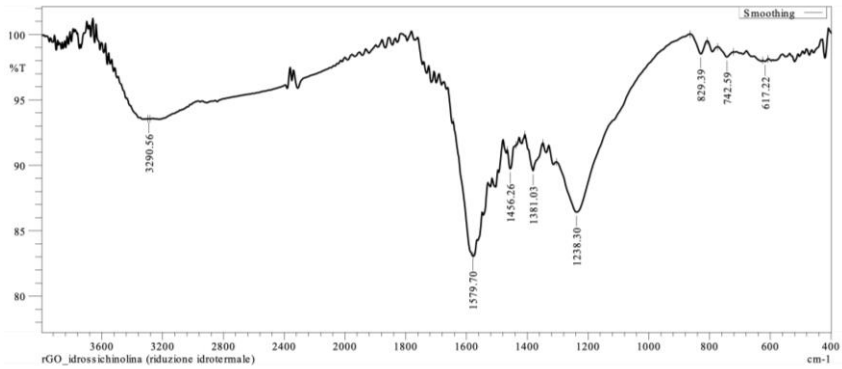

Figure 166**. IR spectrum of compound **103

Chemical reduction of GO – 8-Hydroxyquinoline **104**

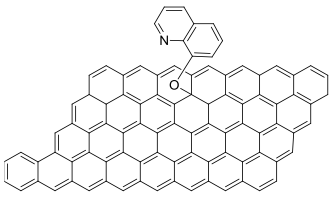

104

20 mg of GO - 8-Hydroxyquinoline were dispersed in22 mL of MilliQ water, of $NaBH_4$ were added. The reaction was reflux (100° C) for 3 h, under stirring. After 3 h a UV spectrum was performed to confirm the reduction.

The product rGO - 8-Hydroxyquinoline was recovered by vacuum filtration on a polycarbonate membrane with 0.4 µm pores, washed with MilliQ water and dried on vacuum.

Elemental analyses: N 1.41%, C 52.25%, H 2.82%

Nitrogen loading degree: 0.05 mmol/100 mg of material

UV-vis: the material was dispersed with difficulty in methanol, the identification of a clear peck was not possible.

IR Spectrum (KBr): 3700-3200 (str. OH), 1560 (str. C=C), 1236 (str. C-O) cm^{-1}

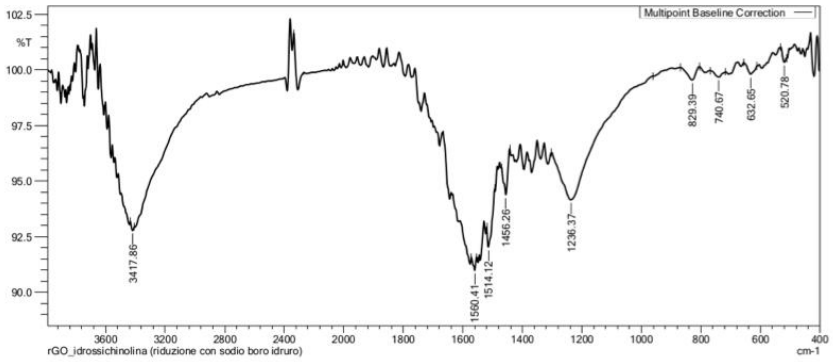

Figure 167*. IR spectrum of compound* ***104***

SYNTHESIS OF GO-4-Nitro phenol **105**

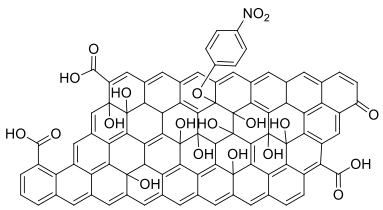

105

80 mg of graphene oxide, 80 mg of 4-Nitro phenol and 100 mg of NaCl were placed into a 10 mL steel jar containing a steel sphere. The jar was put in a ball mill and subjected to mechanical stirring for 40 'at a frequency of 25 Hz. The product was recovered, dispersed in 80 mL of MilliQ water and divided into 4 50 mL Falcon tubes. It was centrifuged at 8000 rpm for 15 '. The process was repeated 5 times using MilliQ water as solvent.

The functionalized material was filtered on a polycarbonate membrane with 0.4 µm pores, then dispersed in 80 mL of water and freeze-dried

Elemental analyses CHN: N 0.00 %, C 39.32 %, H 1.54 %

Nitrogen loading degree: 0.00 mmol/100 mg of material

UV-vis: the material was dispersed in MilliQ water to achieve a solution at 50 ppm, maximum absorption at 238 nm (GO).

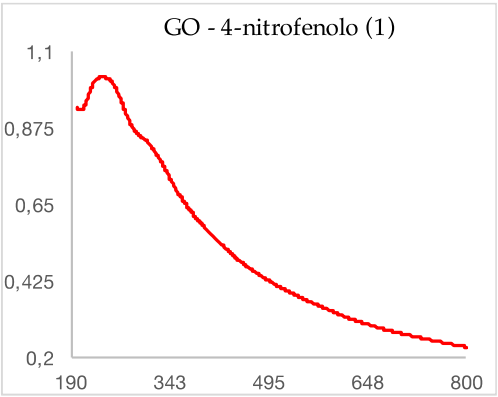

Figure 168*. UV spectrum of compound* ***105***

IR spectrum (KBr): 3600 – 3000 (str. OH), 1624 (str. C=C), 1230 (str. C-O), 1074 (str. C-OH) cm^{-1}

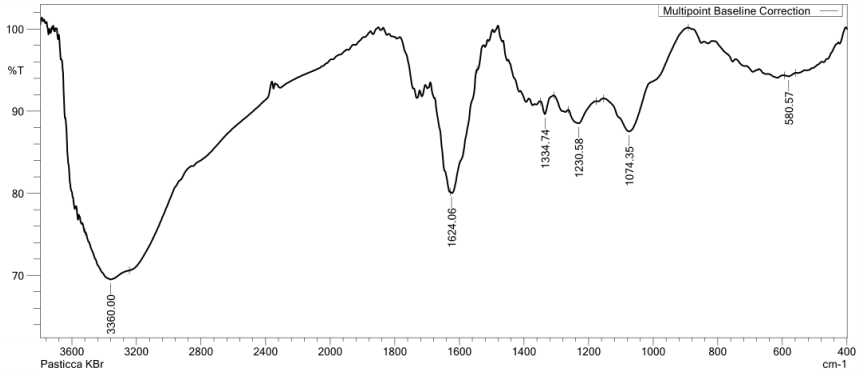

Figure 169**. IR spectrum of compound **105

SYNTHESIS OFGO – 4-Nitro phenol with Na_2CO_3

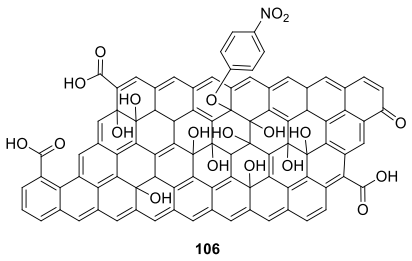

106

80 mg of graphene oxide, 80 mg of 8-Hydroxyquinoline, 100 mg of NaCl and 80 mg of Na_2CO_3 were placed into a 5 mL agate jar containing an agate sphere. The jar was put in a ball mill and subjected to mechanical stirring for 40 'at a frequency of 25 Hz. The product was recovered, dispersed in 80 mL of MilliQ water and divided into 4 50 mL Falcon tubes. It was centrifuged at 8000 rpm for 15 '. The process was repeated 5 times using a MilliQ wate as solvent.

The product was finally filtered on a polycarbonate membrane with 0.4 µm pores, dispersed in 80 mL of MilliQ water and freeze-dried.

Elemental analyses CHN: N 0.00 %, C 33.60 %, H 1.51 %

Nitrogen loading degree: 0.00 mmol/100 mg of material

UV-vis: the material was dispersed in MilliQ water to achieve a solution at 50 ppm, maximum absorption at 245 nm (GO).

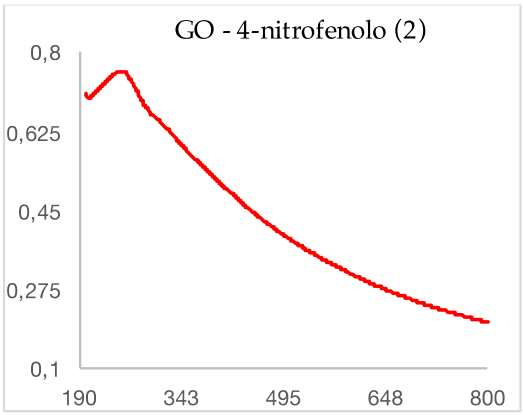

Figure 170**. UV spectrum of compound **106

IR spectrum (KBr): 3700 – 3000 (str. OH), 1631 (str. C=C), 1240 (str. C-O), 1072 (str. C-OH) cm^{-1}

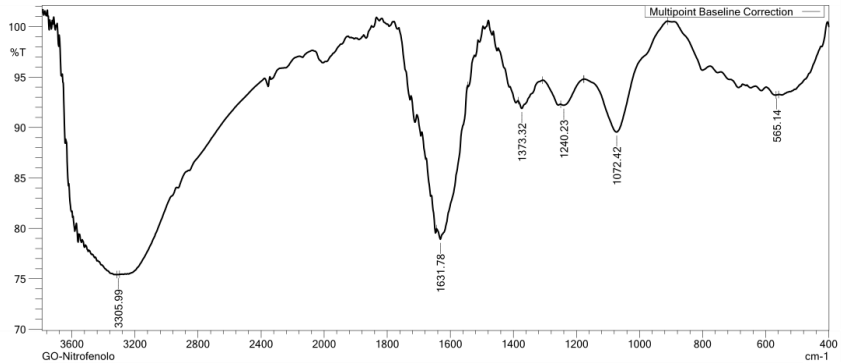

Figure 171**. IR spectrum of compound **106

SYNTHESIS OF GO-4-Hydroxyacetanilide **107**

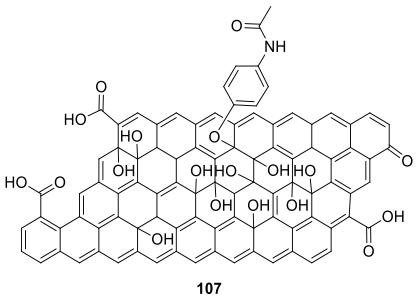

107

80 mg of graphene oxide, 80 mg of 4-Hydroxyacetanilide and 100 mg of NaCl were placed into a 10 mL agate jar containing an agate sphere. The jar was put in a ball mill and subjected to mechanical stirring for 40 'at a frequency of 25 Hz. The product was recovered, dispersed in 80 mL of MilliQ water and divided into 4 50 mL Falcon tubes. It was centrifuged at 8000 rpm for 15 '. The process was repeated 5 times using 2-propanol as solvent.

The functionalized material was filtered on a polycarbonate membrane with 0.4 µm pores, then dispersed in 80 mL of water and freeze-dried

Elemental analyses CHN: N 0.23 %, C 48.27 %, H 2.40 %

Nitrogen loading degree: 0.02 mmol/100 mg of material

UV-vis: the material was dispersed in MilliQ water to achieve a solution at 50 ppm, maximum absorption at 243 nm, peck overlapped to GO.

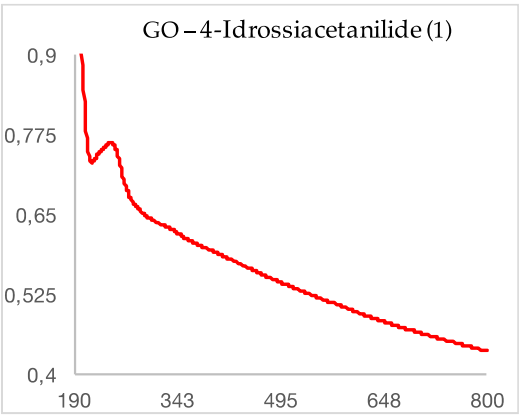

Figure 172**. UV spectrum of compound **107

IR spectrum (KBr): 3400-2500 (str. OH), 1728 (str. C=O), 1610 (str. C=C), 1234 (str. C-O), 1070 (str. C-OH) cm^{1}

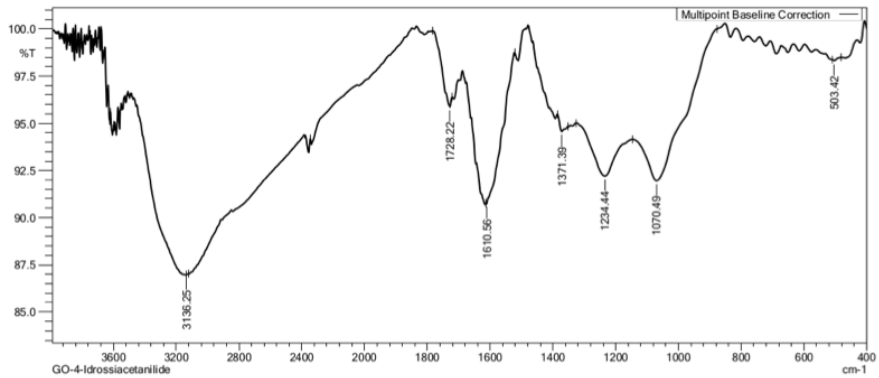

Figure 173**. IR spectrum of compound **107

SYNTHESIS OF GO-4-Hydroxyacetanilide with Na_2CO_3 **108**

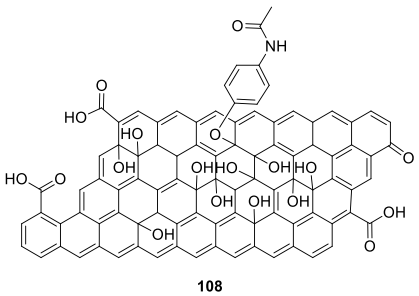

108

80 mg of graphene oxide, 80 mg of 4-Hydroxyacetanilide, 100 mg of NaCl and 80 mg of Na_2CO_3 were placed into a 10 mL agate jar containing an agate sphere. The jar was put in a ball mill and subjected to mechanical stirring for 40 'at a frequency of 25 Hz. The product was recovered, dispersed in 80 mL of MilliQ water and divided into 4 50 mL Falcon tubes. It was centrifuged at 8000 rpm for 15 '. The process was repeated 5 times using a 2-propanol as solvent.

The product was finally filtered on a polycarbonate membrane with 0.4 µm pores, dispersed in 50 mL of MilliQ water and freeze-dried.

Elemental analyses CHN: N 0.44 %, C 45.46 %, H 2.07 %

Nitrogen loading degree: 0.03 mmol/100 mg of material

UV-vis: the material was dispersed in MilliQ water to achieve a solution at 50 ppm, maximum absorption at 239 nm, peck overlapped to GO.

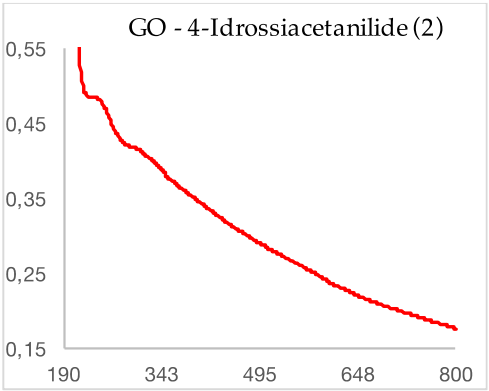

Figure 174**. UV spectrum of compound **108

IR spectrum (KBr): 3600-3000 (str. OH), 1629 (str. C=C and str. C=O), 1240 (str. C-O), 1068 (str. C-OH) cm^{-1}

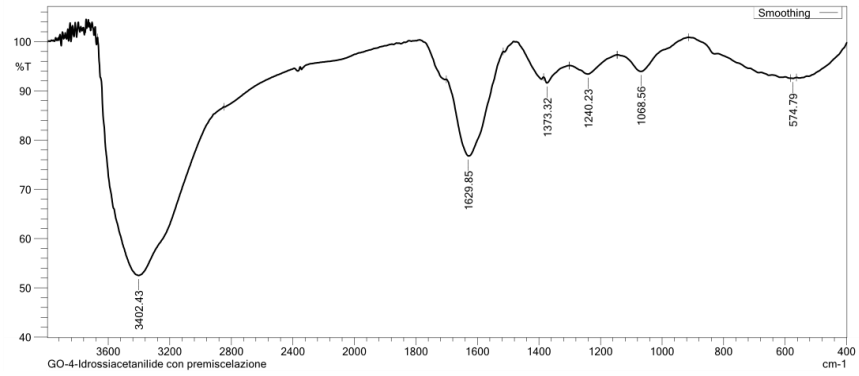

Figure 175**. IR spectrum of compound **108

Chemical reduction of GO-4-Hydroxyacetanilide WITH $NaBH_4$ **108**

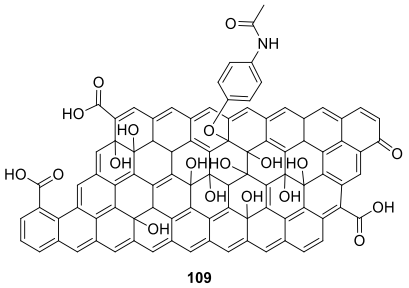

109

20 mg of GO - 4-Hydroxyacetanilide were dispersed in22 mL of MilliQ water, x of $NaBH_4$ were added. The reaction was reflux (100° C) for 3 h, under stirring. After 3 h a UV spectrum was performed to confirm the reduction.

The product rGO - 8-Hydroxyacetanilide was recovered by vacuum filtration on a polycarbonate membrane with 0.4 µm pores, washed with MilliQ water and dried on vacuum.

Elemental analyses: N 0.56%, C 56.90%, H 1.78%

Nitrogen loading degree: 0.04 mmol/100 mg of material

UV-vis: the material was dispersed with difficulty in methanol, the identification of a clear peck was not possible.

IR Spectrum (KBr): 3500 – 2500 (str. OH e str. NH), 1689 str. C=O, 1548-1514 (str. C=C), 1207 (str. C-O) cm^{1-}. A decrement in the intensity of OH signal was shawed.

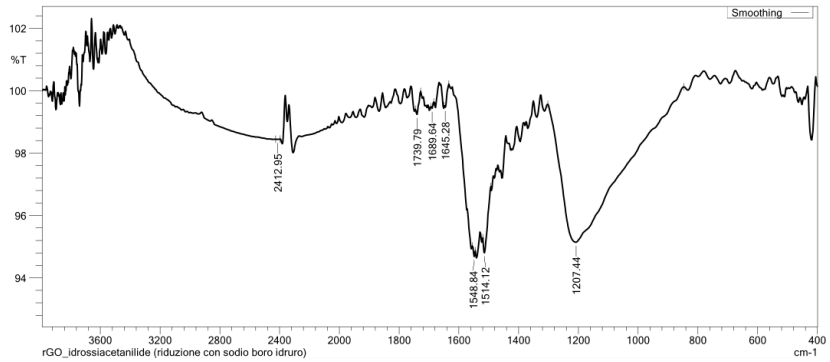

Figure 176. IR spectrum of compound **109**

SYNTHESIS OF GO-4-Chloro-2-Nitro phenol

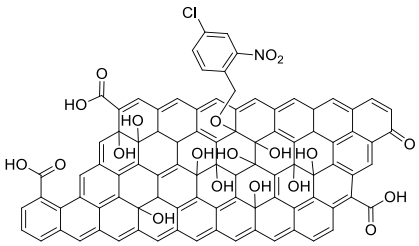

110

80 mg of graphene oxide, 80 mg of 4-Chloro-2-Nitro phenol and 100 mg of NaCl were placed into a 10 mL agate jar containing an agate sphere. The jar was put in a ball mill and subjected to mechanical stirring for 40 'at a frequency of 25 Hz. The product was recovered, dispersed in 80 mL of MilliQ water and divided into 4 50 mL Falcon tubes. It was centrifuged at 8000 rpm for 15 '. The process was repeated 5 times using 2-propanol as solvent.

The functionalized material was filtered on a polycarbonate membrane with 0.4 µm pores, then dispersed in 50 mL of water and freeze-dried

Elemental analyses CHN: N 0.00 %, C 43.55 %, H 2.15 %

Nitrogen loading degree: 0.00 mmol/100 mg of material

UV-vis: the material was dispersed in MilliQ water to achieve a solution at 50 ppm, maximum absorption at 230 nm (GO).

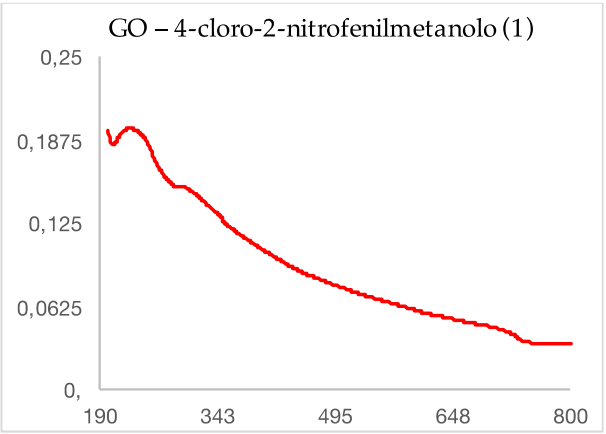

Figure 177. UV spectrum of compound **110**

IR spectrum (KBr): 3600-3000 (str. OH), 1622 (str. C=C), 1240 (str. C-O), 1066 (str. C-OH) cm^{-1}

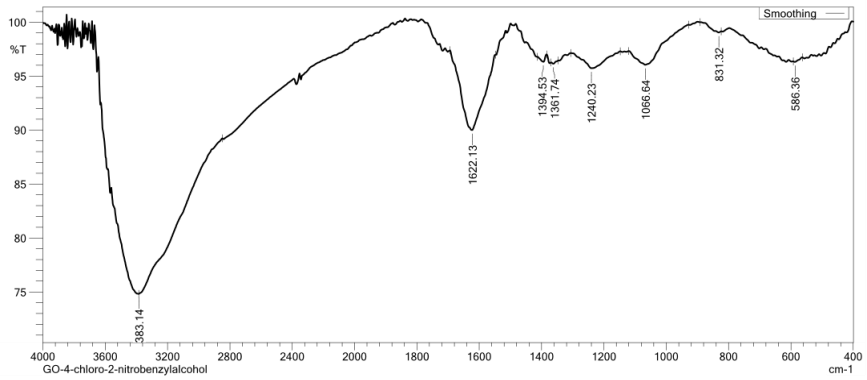

Figure 178**. IR spectrum of compound **110

SYNTHESIS OF GO-4-Chloro-2-Nitro phenol with Na_2CO_3 **111**

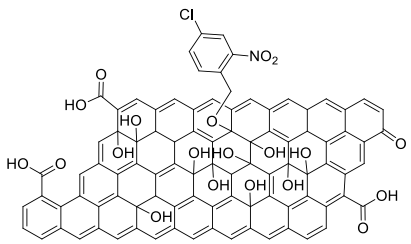

111

80 mg of graphene oxide, 80 mg of 4-Chloro-2-nitro phenol, 100 mg of NaCl and 80 mg of Na_2CO_3 were placed into a 10 mL agate jar containing an agate sphere. The jar was put in a ball mill and subjected to mechanical stirring for 40 'at a frequency of 25 Hz. The product was recovered, dispersed in 80 mL of MilliQ water and divided into 4 50 mL Falcon tubes. It was centrifuged at 8000 rpm for 15 '. The process was repeated 5 times using a 2-propanol as solvent.

The product was finally filtered on a polycarbonate membrane with 0.4 µm pores, dispersed in 80 mL of MilliQ water and freeze-dried.

Elemental analyses CHN: N 0.00 %, C 37.87 %, H 1.97 %

Nitrogen loading degree: 0.00 mmol/100 mg of material

UV-vis: the material was dispersed in MilliQ water to achieve a solution at 50 ppm, maximum absorption at 240 nm (GO).

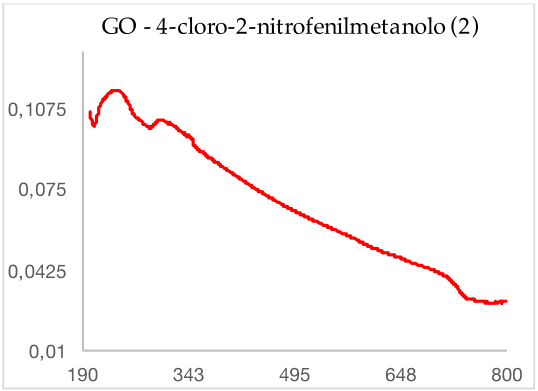

Figure 179**. UV spectrum of compound **111

IR spectrum (KBr): 3600-3000 (str. OH), 1631 (str. C=C), 1244 (str. C-O), 1072 (str. C-OH) cm^{-1}

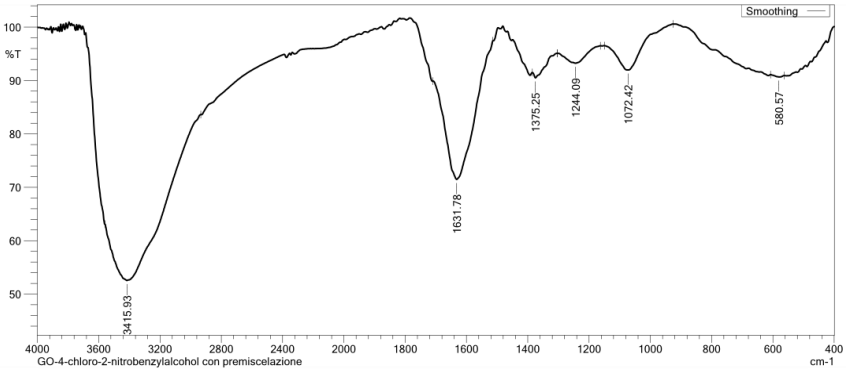

Figure 180**. IR spectrum of compound **111

SYNTHESIS OF compound **100**

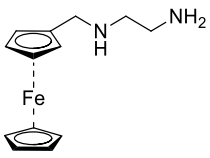

500 mg of ferrocene carboxhaldeyde (FcA) and 0.78 mL of ethylenediamine in 12.5 mL of anhydrous methanol were transferred into a 25 mL flask.

An excess (880 mg) of $NaBH_4$ was subsequently added to reduce the imine and the stirring was maintained for another 2 hours at room temperature. A control TLC was carried out to confirm the reaction occurred.

Finally, 12.5 mL of HCl and 12.5 mL of H_2O were added to the mixture and extracted with EtOAc (2 x 12.5 mL) to remove the unreacted FcA. The aqueous phases were trited with a saturated solution of $NaHCO_3$ and extracted with EtOAc three times (3 x 12.5 mL). The organic phase was dried over Na_2SO_4 and the solvent was removed.

The crude was purified by flash chromatographic column using as eluent first DCM: MeOH (9: 1) and then DCM: MeOH: NH_3 (4: 1: 0.1).

Yield: 413 mg (68%) of a yellow oil.

The product was characterized by ^{1}H NMR spectroscopy.

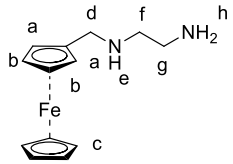

^{1}H NMR (200 MHz, $CDCl_3$): δ 4.15 (m, 9 H, Ha, Hb, Hc), 3.53 (s, 2 H, Hd), 2.75 (m, 4 H, Hf, Hg), 2.12 (s, 3 He, Hh) ppm

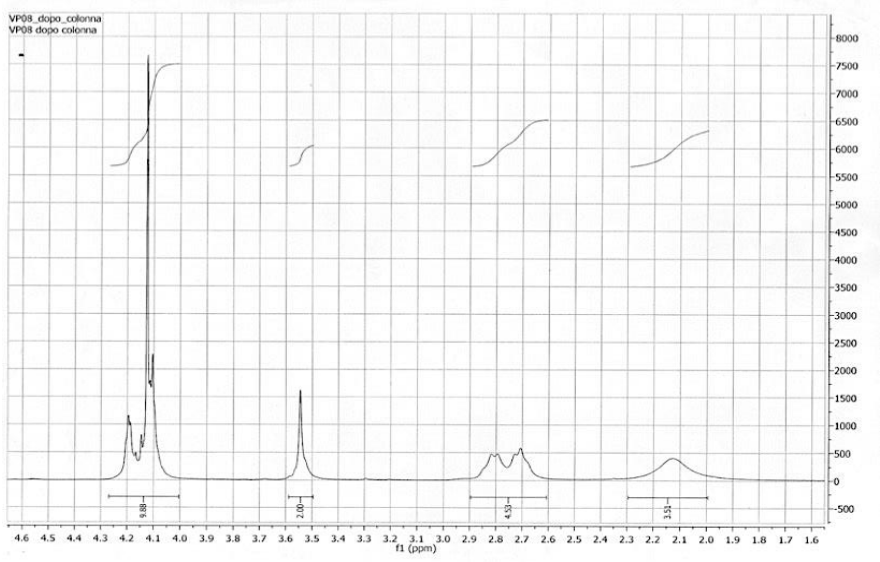

Figure 181**. ^{1}H spectrum of compound **100

SYNTHESIS OF GO-N-Ferrocenyl-1,2-diaminoethane **112**

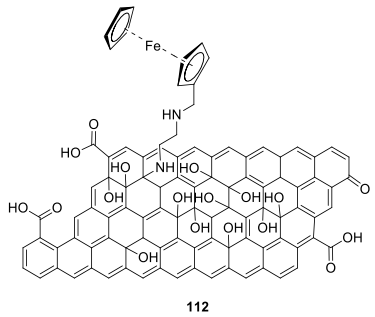

112

80 mg of graphene oxide, 80 mg of 4-N-ferrocenyl-1,2-diaminoethane and 100 mg of NaCl were placed into a 10 mL agate jar containing an agate sphere. The jar was put in a ball mill and subjected to mechanical stirring for 40 'at a frequency of 25 Hz. The product was recovered and dispersed in 80 mL of slightly acid MilliQ water and divided into 4 50 mL Falcon tubes. It was centrifuged at 8000 rpm for 15 '. The process was repeated 5 times using 2-propanol as solvent.

The functionalized material was filtered on a polycarbonate membrane with 0.4 µm pores, then dispersed in 80 mL of water and freeze-dried

Elemental analyses CHN: N 1.20 %, C 43.50 %, H 2.39 %

Nitrogen loading degree: 0.04 mmol/100 mg of material

ICP analyses: 0,02 µg/mg, Cr 0,08 µg/mg, Fe 33,82 µg/mg, S 40,1 µg/mg

IR spectrum (KBr): 3600-3000 (str. OH e str. NH), 1620 (str. C=C), 1236 (str. C-O), 1066 (str. C-OH and stretching C-N) cm^{-1}

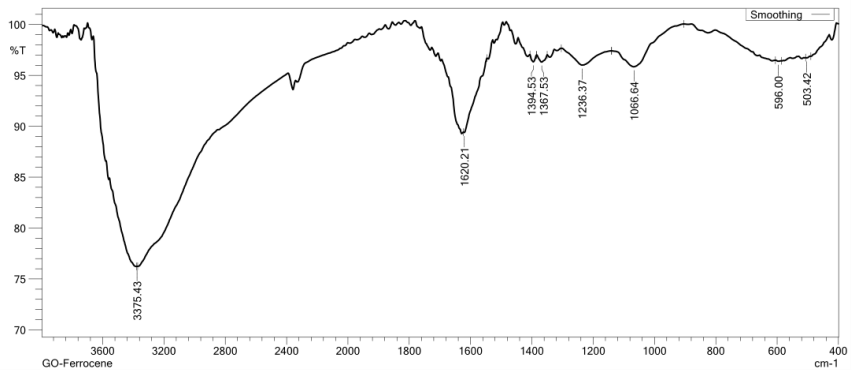

***Figure 182**. IR spectrum of compound **112**.*

Hydrothermal reduction of GO-N-Ferrocenyl-1,2-diaminoethane **113**

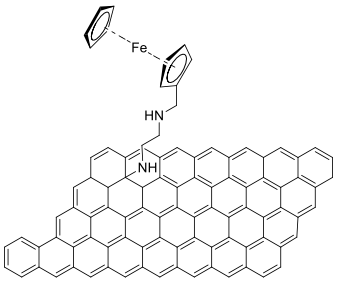

113

14 mg of GO – N-Ferrocenyl-1,2-diaminoethane were dispersed in 20 mL of MilliQ water and the suspension was brought to pH 11 with the addition of 0.1 M NaOH water solution. The mixture was placed into an autoclave which was heated to 180 ° C for 6 h, under stirring.

The product was recovered and finally filtered on a nylon membrane with 0.2 µm pores. The product was washed several times until neutral pH of washing water, then the material was freeze-dried.

Elemental analyses: N 1.03 %, C 60.23 %, H 1.44 %

Nitrogen loading degree: 0.04 mmol/100 mg of material

IR spectrum (KBr): 3500-3000 (banda slargata relativa a str. OH e NH), 1570 (str. C=C), 1185-1082 (str. C-O sovrapposto a str. C-N) cm^{-1}

A reduction in the intensity of OH stretching was observed due to the reduction process.

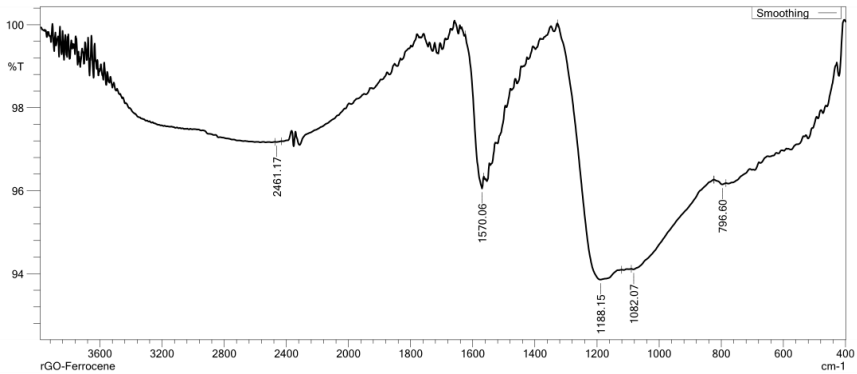

Figure 183**. IR spectrum of compound **113

Chemical reduction of GO-N-Ferrocenyl-1,2-diamino ethane with $NaBH_4$ **114**

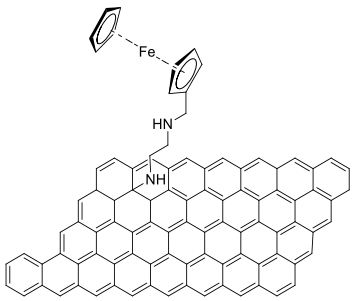

114

20 mg of GO – Ferrocenyl-1,2-diaminoethane were dispersed in22 mL of MilliQ water, x of $NaBH_4$ were added. The reaction was reflux (100° C) for 3 h, under stirring. After 3 h a UV spectrum was performed to confirm the reduction.

The product rGO - Ferrocenyl-1,2-diaminoethane was recovered by vacuum filtration on a polycarbonate membrane with 0.4 µm pores, washed with MilliQ water and dried on vacuum.

Elemental analyses: N 1.41%, C 52.25%, H 2.82%

Nitrogen loading degree: 0.05 mmol/100 mg of material

UV-vis analysis of a 50 ppm suspension in MilliQ water: absorbance maximum at 260 nm (N-ferrocenyl-1,2-diaminoethane molecule does not absorb in the UV, only the peak relative to the reduced GO was observed

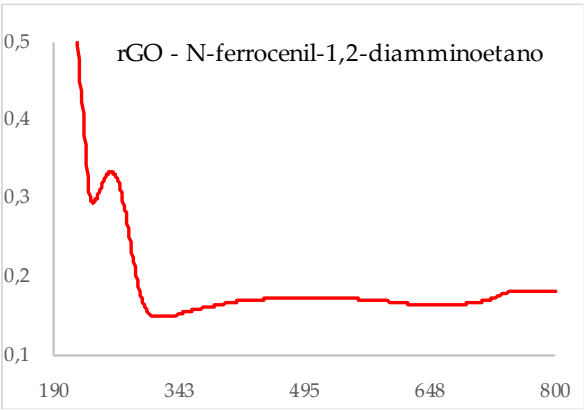

Figure 184*. UV spectrum of compound* ***114***

IR spectrum (KBr): 3500-3000 (str. OH e NH), 1575 (str. C=C overlapped to a aend. N-H), 1220 (str. C-O overlapping to str. C-N) cm^{-1}

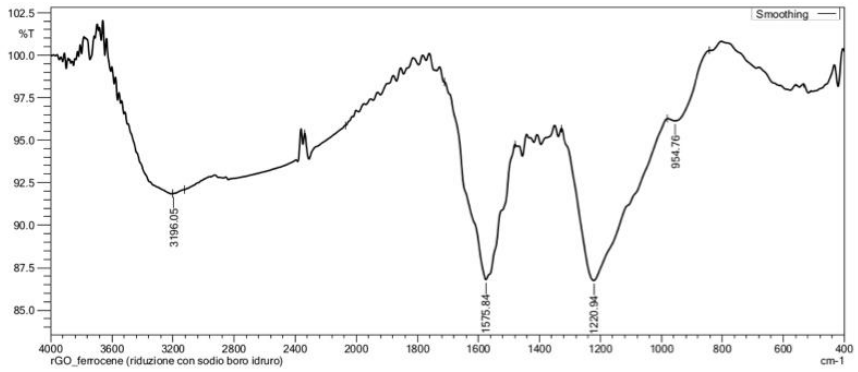

Figure 185 *IR spectrum of compound* ***114***

7.6 REFERENCES

1. Biagiotti, G. *et al.* Multiwalled carbon nanotubes for combination therapy: A biodistribution and efficacy pilot study. *J. Mater. Chem. B* **7**, 2678–2687 (2019).

2. Kostarelos, K. *et al.* Cellular uptake of functionalized carbon nanotubes is independent of functional group and cell type. *Nat. Nanotechnol.* **2**, 108–113 (2007).

3. Liu & Speranza. Functionalization of Carbon Nanomaterials for Biomedical Applications. *C — J. Carbon Res.* **5**, 72 (2019).

4. Curcio, M. *et al.* Functionalized carbon nanostructures versus drug resistance: Promising scenarios in cancer treatment. *Molecules* **25**, 1–31 (2020).

5. Perkins, B. L. & Naderi, N. Carbon Nanostructures in Bone Tissue Engineering. *Open Orthop. J.* **10**, 877–899 (2017).

6. Erol, O. *et al.* Recent advances in bioactive 1D and 2D carbon nanomaterials for biomedical applications. *Nanomedicine Nanotechnology, Biol. Med.* **14**, 2433–2454 (2018).

7. Tasis, D., Tagmatarchis, N., Bianco, A. & Prato, M. Chemistry of carbon nanotubes. *Chem. Rev.* **106**, 1105–1136 (2006).

8. Kumar, S., Rani, R., Dilbaghi, N., Tankeshwar, K. & Kim, K. H. Carbon nanotubes: A novel material for multifaceted applications in human healthcare. *Chem. Soc. Rev.* **46**, 158–196 (2017).

9. Hong, S. Y. *et al.* Filled and glycosylated carbon nanotubes for in vivo radioemitter localization and imaging. *Nat. Mater.* **9**, 485–490 (2010).

10. Wohlstadter, J. N. *et al.* Carbon nanotube-based biosensor. *Adv. Mater.* **15**, 1184–1187 (2003).

11. Fedeli, S. *et al.* Azido-Substituted BODIPY Dyes for the Production of Fluorescent Carbon Nanotubes. *Chem. - A Eur. J.* **21**, 15349–15353 (2015).

12. Mooney, E., Dockery, P., Greiser, U., Murphy, M. & Barron, V. Carbon nanotubes and mesenchymal stem cells: Biocompatibility, proliferation and differentiation. *Nano Lett.* **8**, 2137–2143 (2008).

13. Guo, J., Wang, Y. & Zhao, M. Target-directed functionalized ferrous phosphate-carbon dots fluorescent nanostructures as peroxidase mimetics for cancer cell detection and ROS-mediated therapy. *Sensors Actuators, B Chem.* **297**, 126739 (2019).

14. Janyasupab, M. & Promptmas, C. Development of non-enzymatic N-doped graphene supported cobalt/iron amperometric based sensor for glucose detection in urine. *2018 IEEE EMBS Conf. Biomed. Eng. Sci. IECBES 2018 - Proc.* 577–582 (2019) doi:10.1109/IECBES.2018.8626693.

15. Chiang, Y. C., Lin, W. H. & Chang, Y. C. The influence of treatment duration on multi-walled carbon nanotubes functionalized by H 2 SO 4 /HNO 3 oxidation. *Appl. Surf. Sci.* **257**, 2401–2410 (2011).

16. Chattopadhyay, D., Lastella, S., Kim, S. & Papadimitrakopoulos, F. Length separation of zwitterion-functionalized single wall carbon nanotubes by GPC. *J. Am. Chem. Soc.* **124**, 728–729 (2002).

17. Li, J. & Zhang, Y. Large-scale aligned carbon nanotubes films. *Phys. E Low-Dimensional Syst. Nanostructures* **33**, 235–239 (2006).

18. submitted to Nature on Feb 5, 2004. (2004).

19. Allen, M. J., Tung, V. C. & Kaner, R. B. Honeycomb carbon: A review of graphene. *Chem. Rev.* **110**, 132–145 (2010).

20. Park, S. & Ruoff, R. S. Chemical methods for the production of graphenes. *Nat. Nanotechnol.* **4**, 217–224 (2009).

21. Reina, A. *et al.* Growth of large-area single- and Bi-layer graphene by controlled carbon precipitation on polycrystalline Ni surfaces. *Nano Res.* **2**, 509–516 (2009).

22. Jiao, L., Wang, X., Diankov, G., Wang, H. & Dai, H. Facile synthesis of high-quality graphene nanoribbons. *Nat. Nanotechnol.* **5**, 321–325 (2010).

23. Coliman, J. P. *et al.* "Picket Fence Porphyrins". Synthetic Models for Oxygen Binding Hemoproteins. *J. Am. Chem. Soc.* **97**, 1427–1439 (1975).

24. Brinker, C. J., Lu, Y., Sellinger, A. & Fan, H. ChemInform Abstract: Evaporation-Induced Self-Assembly: Nanostructures Made Easy. *ChemInform* **30**, no-no (2010).

25. Sutter, P., Sadowski, J. T. & Sutter, E. Graphene on Pt(111): Growth and substrate interaction. *Phys. Rev. B - Condens. Matter Mater. Phys.* **80**, 1–10 (2009).

26. Staudenmaier, L. Method for the preparation of the graphite acid. *Eur. J. Inorg. Chem.* **31**, 1481–1487 (1898).

27. Zhang, X. *et al.* Distribution and biocompatibility studies of graphene oxide in mice after intravenous administration. *Carbon N. Y.* **49**, 986–995 (2011).

28. Pan, S. & Aksay, I. A. Factors controlling the size of graphene oxide sheets produced via the graphite oxide route. *ACS Nano* **5**, 4073–4083 (2011).

29. Gonçalves, P. A. D. & Peres, N. M. R. An Introduction to Graphene Plasmonics. *An Introd. to Graphene Plasmon.* 1–431 (2016) doi:10.1142/9948.

30. Pan, Y., Sahoo, N. G. & Li, L. The application of graphene oxide in drug delivery. *Expert Opin. Drug Deliv.* **9**, 1365–1376 (2012).

31. Li, Q.-Y., Zu, Y.-G., Shi, R.-Z. & Yao, L.-P. Review Camptothecin: Current Perspectives. *Curr. Med. Chem.* **13**, 2021–2039 (2006).

32. Liu, Z., Robinson, J. T., Sun, X. & Dai, H. PEGylated nanographene oxide for delivery of water-insoluble cancer drugs. *J. Am. Chem. Soc.* **130**, 10876–10877 (2008).

33. Rana, V. K. *et al.* Synthesis and drug-delivery behavior of chitosan-functionalized graphene oxide hybrid nanosheets. *Macromol. Mater. Eng.* **296**, 131–140 (2011).

34. Eigler, S., Grimm, S., Enzelberger-Heim, M., Müller, P. & Hirscha, A. Graphene oxide: Efficiency of reducing agents. *Chem. Commun.* **49**, 7391–7393 (2013).

35. Hunt, A. *et al.* Epoxide speciation and functional group distribution in graphene oxide paper-like materials. *Adv. Funct. Mater.* **22**, 3950–3957 (2012).

36. Szabó, T. *et al.* Evolution of surface functional groups in a series of progressively oxidized graphite oxides. *Chem. Mater.* **18**, 2740–2749 (2006).

37. Dimiev, A. M., Alemany, L. B. & Tour, J. M. Graphene oxide. Origin of acidity, its instability in water, and a new dynamic structural model. *ACS Nano* **7**, 576–588 (2013).

38. Liu, Y., Yu, D., Zeng, C., Miao, Z. & Dai, L. Biocompatible graphene oxide-based glucose biosensors. *Langmuir* **26**, 6158–6160 (2010).

39. Paquin, F., Rivnay, J., Salleo, A., Stingelin, N. & Silva, C. Multi-phase semicrystalline microstructures drive exciton dissociation in neat plastic semiconductors. *J. Mater. Chem. C* **3**, 10715–10722 (2015).

40. Yu, R. *et al.* Synthetic possibility of polystyrene functionalization based on hydroxyl groups of graphene oxide as nucleophiles. *New J. Chem.* **39**, 5096–5099 (2015).

41. Chen, H. *et al.* Phosphorylation of graphehe oxide to improve adsorption of U(VI) from aquaeous solutions. *J. Radioanal. Nucl. Chem.* **313**, 175–189 (2017).

42. De Leon, A. C., Alonso, L., Mangadlao, J. D., Advincula, R. C. & Pentzer, E. Simultaneous Reduction and Functionalization of Graphene Oxide via Ritter Reaction. *ACS Appl. Mater. Interfaces* **9**, 14265–14272 (2017).

43. Liao, K. H., Lin, Y. S., MacOsko, C. W. & Haynes, C. L. Cytotoxicity of graphene oxide and graphene in human erythrocytes and skin fibroblasts. *ACS Appl. Mater. Interfaces* **3**, 2607–2615 (2011).

44. Lu, C. H. *et al.* Using graphene to protect DNA from cleavage during cellular delivery. *Chem. Commun.* **46**, 3116–3118 (2010).

45. Wojtoniszak, M. *et al.* Synthesis, dispersion, and cytocompatibility of graphene oxide and reduced graphene oxide. *Colloids Surfaces B Biointerfaces* **89**, 79–85 (2012).

46. Yuan, J. *et al.* Cytotoxicity evaluation of oxidized single-walled carbon nanotubes and graphene oxide on human hepatoma HepG2 cells: An iTRAQ-coupled 2D LC-MS/MS proteome analysis. *Toxicol. Sci.* **126**, 149–161 (2012).

47. Chang, Y. *et al.* In vitro toxicity evaluation of graphene oxide on A549 cells. *Toxicol. Lett.* **200**, 201–210 (2011).

48. Bhattacharya, K. *et al.* Biological interactions of carbon-based nanomaterials: From coronation to degradation. *Nanomedicine Nanotechnology, Biol. Med.* **12**, 333–351 (2016).

49. Kurapati, R. *et al.* Dispersibility-Dependent Biodegradation of Graphene Oxide by Myeloperoxidase. *Small* **11**, 3985–3994 (2015).

50. Chen, S. *et al.* Mechanism-based tumor-targeting drug delivery system. Validation of efficient vitamin receptor-mediated endocytosis and drug release. *Bioconjug. Chem.* **21**, 979–987 (2010).

51. Lee, J. S. *et al.* Synthesis of a BODIPY library and its application to the development of live cell glucagon imaging probe. *J. Am. Chem. Soc.* **131**, 10077–10082 (2009).

52. Kaur, P. & Singh, K. Recent advances in the application of BODIPY in bioimaging and chemosensing. *J. Mater. Chem. C* **7**, 11361–11405 (2019).

53. Moss, G. P. Nomenclature of tetrapyrroles (Recommendations 1986). *Pure Appl. Chem.* **59**, 779–832 (1987).

54. van Koeveringe, J. A. & Lugtenburg, J. Novel pyrromethenes 1-Oxygen and 1-sulfur analogues; evidence for photochemical. *Recueil, J. R. Netherlands Chem. Soc.* **96**, 55–57 (1977).

55. Solomonov, A. V., Marfin, Y. S. & Rumyantsev, E. V. Design and applications of dipyrrin-based fluorescent dyes and related organic luminophores: From individual compounds to supramolecular self-assembled systems. *Dye. Pigment.* **162**, 517–542 (2019).

56. Li, Z., Mintzer, E. & Bittman, R. First synthesis of free cholesterol-BODIPY conjugates. *J. Org. Chem.* **71**, 1718–1721 (2006).

57. Wagner, R. W. & Lindsey, J. S. Boron-dipyrromethene dyes for incorporation in synthetic multi-pigment light-harvesting arrays. *Pure Appl. Chem.* **68**, 1373–1380 (1996).

58. Thivierge, C., Bandichhor, R. & Burgess, K. Spectral dispersion and water solubilization of BODIPY dyes via palladium-catalyzed C-H functionalization. *Org. Lett.* **9**, 2135–2138 (2007).

59. Shah, M. *et al.* Pyrromethene–BF2 complexes as laser dyes:1. *Heteroat. Chem.* **1**, 389–399 (1990).

60. Yogo, T., Urano, Y., Ishitsuka, Y., Maniwa, F. & Nagano, T. Highly efficient and photostable photosensitizer based on BODIPY chromophore. *J. Am. Chem. Soc.* **127**, 12162–12163 (2005).

61. Scheibe, B., Borowiak-Palen, E. & Kalenczuk, R. J. Oxidation and reduction of multiwalled carbon nanotubes - preparation and characterization. *Mater. Charact.* **61**, 185–191 (2010).

62. Jameson, L. P. & Dzyuba, S. V. Expeditious, mechanochemical synthesis of BODIPY dyes. *Beilstein J. Org. Chem.* **9**, 786–790 (2013).

63. Andersen, J., Madsen, U., Björkling, F. & Liang, X. Rapid synthesis of aryl azides from aryl halides under mild conditions. *Synlett* 2209–2213 (2005) doi:10.1055/s-2005-872248.

64. Ménard-Moyon, C., Fabbro, C., Prato, M. & Bianco, A. One-pot triple functionalization of carbon nanotubes. *Chem. - A Eur. J.* **17**, 3222–3227 (2011).

65. Lin, H. B., Cooper, S. L., Zhao, Z. C., Garcia-Echeverria, C. & Rich, D. H. Synthesis of a novel polyurethane co-polymer containing covalently attached RGD peptide. *J. Biomater. Sci. Polym. Ed.* **3**, 217–227 (1992).

66. Van Agthoven, J. F. *et al.* Structural Basis of the Differential Binding of Engineered Knottins to Integrins αVβ3 and α5β1. *Structure* **27**, 1443-1451.e6 (2019).

67. Sheldrake, H. M. & Patterson, L. H. Strategies to inhibit tumor associated integrin receptors: Rationale for dual and multi-antagonists. *J. Med. Chem.* **57**, 6301–6315 (2014).

68. Maligaspe, E. *et al.* Photosynthetic antenna-reaction center mimicry: Sequential energy- and electron transfer in a self-assembled supramolecular triad composed of boron dipyrrin, zinc porphyrin and fullerene. *J. Phys. Chem. A* **113**, 8478–8489 (2009).

69. Mori, H. *et al.* In silico and pharmacological screenings identify novel serine racemase inhibitors. *Bioorganic Med. Chem. Lett.* **24**, 3732–3735 (2014).

70. Hishikawa, K. *et al.* Photoinduced nitric oxide release from a hindered nitrobenzene derivative by two-photon excitation. *J. Am. Chem. Soc.* **131**, 7488–7489 (2009).

71. Mallesha, N., Prahlada Rao, S., Suhas, R. & Channe Gowda, D. An efficient synthesis of tert-butyl ethers/esters of alcohols/amino acids using methyl tert-butyl ether. *Tetrahedron Lett.* **53**, 641–645 (2012).

72. Mock, J. N. *et al.* Haloenol pyranones and morpholinones as antineoplastic agents of prostate cancer. *Bioorganic Med. Chem. Lett.* **22**, 4854–4858 (2012).

73. König, W. & Geiger, R. Eine neue Methode zur Synthese von Peptiden: Aktivierung der Carboxylgruppe mit Dicyclohexylcarbodiimid unter Zusatz von 1-Hydroxy-benzotriazolen. *Chem. Ber.* **103**, 788–798 (1970).

74. Pérez-Picaso, L., Escalante, J., Olivo, H. F. & Rios, M. Y. Efficient microwave assisted syntheses of 2,5-diketopiperazines in aqueous media. *Molecules* **14**, 2836–2849 (2009).

75. Styers, T. J. *et al.* Synthesis of Sansalvamide A derivatives and their cytotoxicity in the MSS colon cancer cell line HT-29. *Bioorganic Med. Chem.* **14**, 5625–5631 (2006).

76. Lundt, B. F., Johansen, N. L., Vølund, A. & Markussen, J. REMOVAL OF t-BUTYL AND t-BUTOXYCARBONYL PROTECTING GROUPS WITH TRIFLUOROACETIC ACID: Mechanisms, Biproduct Formation and Evaluation of Scavengers. *Int. J. Pept. Protein Res.* **12**, 258–268 (1978).

77. Hughes, A. B. Amino Acids, Peptides and Proteins in Organic Chemistry. *Amin. Acids, Pept. Proteins Org. Chem.* **2**, (2010).

78. Vardhan, D. M. S., Kumara, H. K., Kumar, H. P. & Gowda, D. C. Inhibition of Urease Enzyme Activity By Urea and Thiourea Derivatives of Dipeptides Conjugated 2, 3-Dichlorophenyl Piperazine. *Int. J. Pharm. Pharm. Sci.* **9**, 92 (2017).

79. Kaur, A., Poonam, Patil, M. T., Mehta, S. K. & Salunke, D. B. An efficient and scalable synthesis of potent TLR2 agonistic PAM2CSK4. *RSC Adv.* **8**, 9587–9596 (2018).

80. Brough, P., Klumpp, C., Bianco, A., Campidelli, S. & Prato, M. [60]fullerene-pyrrolidine-N-oxides. *J. Org. Chem.* **71**, 2014–2020 (2006).

81. Saini, N. & Yang, X. Metformin as an anti-cancer agent: Actions and mechanisms targeting cancer stem cells. *Acta Biochim. Biophys. Sin. (Shanghai).* **50**, 133–143 (2018).

82. Pierotti, M. A. *et al.* Targeting metabolism for cancer treatment and prevention: Metformin, an old drug with multi-faceted effects. *Oncogene* **32**, 1475–1487 (2013).

83. Alimova, I. N. *et al.* Metformin inhibits breast cancer cell growth, colony formation and induces cell cycle arrest in vitro. *Cell Cycle* **8**, 909–915 (2009).

84. Morales, D. R. & Morris, A. D. Metformin in cancer treatment and prevention. *Annu. Rev. Med.* **66**, 17–29 (2015).

85. Jaune, E. & Rocchi, S. Metformin: Focus on melanoma. *Front. Endocrinol. (Lausanne).* **9**, 1–9 (2018).

86. Tseng, H. W., Li, S. C. & Tsai, K. W. Metformin treatment suppresses melanoma cell growth and motility through modulation of microRNA expression. *Cancers (Basel).* **11**, (2019).

87. Vancura, A., Bu, P., Bhagwat, M., Zeng, J. & Vancurova, I. Metformin as an Anticancer Agent. *Trends Pharmacol. Sci.* **39**, 867–878 (2018).

88. Mallik, R. & Chowdhury, T. A. Metformin in cancer. *Diabetes Res. Clin. Pract.* **143**, 409–419 (2018).

89. Saraei, P., Asadi, I., Kakar, M. A. & Moradi-Kor, N. The beneficial effects of metformin on cancer prevention and therapy: A comprehensive review of recent advances. *Cancer Manag. Res.* **11**, 3295–3313 (2019).

90. Fedeli, S. *et al.* The 'click-on-tube' approach for the production of efficient drug carriers based on oxidized multi-walled carbon nanotubes. *J. Mater. Chem. B* **4**, 3823–3831 (2016).

91. Baghayeri, M., Tehrani, M. B., Amiri, A., Maleki, B. & Farhadi, S. A novel way for detection of antiparkinsonism drug entacapone via electrodeposition of silver nanoparticles/functionalized multi-walled carbon nanotubes as an amperometric sensor. *Mater. Sci. Eng. C* **66**, 77–83 (2016).

92. Mirazi, N., Shoaei, J., Khazaei, A. & Hosseini, A. A comparative study on effect of metformin and metformin-conjugated nanotubes on blood glucose homeostasis in diabetic rats. *Eur. J. Drug Metab. Pharmacokinet.* **40**, 343–348 (2015).

93. Yoo, S. *et al.* Enhanced Response of Metformin towards the Cancer Cells due to Synergism

with Multi-walled Carbon Nanotubes in Photothermal Therapy. *Sci. Rep.* 1–9 (2017) doi:10.1038/s41598-017-01118-3.

94. Denise, C. *et al.* 5-Fluorouracil resistant colon cancer cells are addicted to OXPHOS to survive and enhance stem-like traits. *Oncotarget* **6**, 41706–41721 (2015).

95. Ota, S. *et al.* Metformin suppresses glucose-6-phosphatase expression by a complex I inhibition and AMPK activation-independent mechanism. *Biochem. Biophys. Res. Commun.* **388**, 311–316 (2009).

96. Chen, Z. *et al.* The Advances of Carbon Nanotubes in Cancer Diagnostics and Therapeutics. *J. Nanomater.* **2017**, (2017).

97. Cui, X., Wan, B., Yang, Y., Ren, X. & Guo, L. H. Length effects on the dynamic process of cellular uptake and exocytosis of single-walled carbon nanotubes in murine macrophage cells /631/80 /704/172 /82/29 /14/19 /14/34 /123 article. *Sci. Rep.* **7**, 1–13 (2017).

98. Yuan, Y. M. & He, C. The glial scar in spinal cord injury and repair. *Neurosci. Bull.* **29**, 421–435 (2013).

99. Su, Z. *et al.* Reactive astrocytes inhibit the survival and differentiation of oligodendrocyte precursor cells by secreted TNF-α. *J. Neurotrauma* **28**, 1089–1100 (2011).

100. Liu, W. *et al.* Folic acid conjugated magnetic iron oxide nanoparticles for nondestructive separation and detection of ovarian cancer cells from whole blood. *Biomater. Sci.* **4**, 159–166 (2016).

101. Stichel, C. C. & Müller, H. W. The CNS lesion scar: New vistas on an old regeneration barrier. *Cell Tissue Res.* **294**, 1–9 (1998).

102. Galtrey, C. M. & Fawcett, J. W. The role of chondroitin sulfate proteoglycans in regeneration and plasticity in the central nervous system. *Brain Res. Rev.* **54**, 1–18 (2007).

103. Bradbury, E. J. & Carter, L. M. Manipulating the glial scar: Chondroitinase ABC as a therapy for spinal cord injury. *Brain Res. Bull.* **84**, 306–316 (2011).

104. Silver, J. & Miller, J. H. Regeneration beyond the glial scar. *Nat. Rev. Neurosci.* **5**, 146–156 (2004).

105. Place, L. W., Sekyi, M. & Kipper, M. J. Aggrecan-mimetic, glycosaminoglycan-containing nanoparticles for growth factor stabilization and delivery. *Biomacromolecules* **15**, 680–689 (2014).

106. Marchesan, S., Kostarelos, K., Bianco, A. & Prato, M. The winding road for carbon nanotubes in nanomedicine. *Mater. Today* **18**, 12–19 (2015).

107. Pinillos-Madrid, J. F. & Gallardo, C. Carbon nanotubes: A viable drug delivery platform for the treatment of cancer. *J. Appl. Pharm. Sci.* **5**, 143–152 (2015).

108. Moradian, H., Fasehee, H., Keshvari, H. & Faghihi, S. Poly(ethyleneimine) functionalized carbon nanotubes as efficient nano-vector for transfecting mesenchymal stem cells. *Colloids Surfaces B Biointerfaces* **122**, 115–125 (2014).

109. Herrero, M. A. *et al.* Synthesis and characterization of a carbon nanotube-dendron series for efficient siRNA delivery. *J. Am. Chem. Soc.* **131**, 9843–9848 (2009).

110. Zhou, M., Peng, Z., Liao, S., Li, P. & Li, S. Design of microencapsulated carbon nanotube-based microspheres and its application in colon targeted drug delivery. *Drug Deliv.* **21**, 101–109 (2014).

111. Zhang, W., Zuo, X. D. & Wu, C. W. Synthesis and magnetic properties of carbon nanotube-iron oxide nanoparticle composites for hyperthermia: A review. *Rev. Adv. Mater. Sci.* **40**, 165–176 (2015).

112. Jones, L. L., Margolis, R. U. & Tuszynski, M. H. The chondroitin sulfate proteoglycans neurocan, brevican, phosphacan, and versican are differentially regulated following spinal cord injury. *Exp. Neurol.* **182**, 399–411 (2003).

113. Tom, V. J., Steinmetz, M. P., Miller, J. H., Doller, C. M. & Silver, J. Studies on the development and behavior of the dystrophic growth cone, the hallmark of regeneration failure, in an in vitro model of the glial scar and after spinal cord injury. *J. Neurosci.* **24**, 6531–6539 (2004).

114. Matthews, R. T. *et al.* Aggrecan glycoforms contribute to the molecular heterogeneity of perineuronal nets. *J. Neurosci.* **22**, 7536–7547 (2002).

115. Sandvig, A., Berry, M., Barrett, L. B., Butt, A. & Logan, A. Myelin-, reactive glia-, and scar-derived CNS axon growth inhibitors: Expression, receptor signaling, and correlation with axon regeneration. *Glia* **46**, 225–251 (2004).

116. Yiu, G. & He, Z. Glial inhibition of CNS axon regeneration. *Nat. Rev. Neurosci.* **7**, 617–627 (2006).

117. Rhodes, K. E. & Fawcett, J. W. Chondroitin sulphate proteoglycans: Preventing plasticity or protecting the CNS? *J. Anat.* **204**, 33–48 (2004).

118. Gilbert, R. J. *et al.* CS-4,6 is differentially upregulated in glial scar and is a potent inhibitor of neurite extension. *Mol. Cell. Neurosci.* **29**, 545–558 (2005).

119. Zuo, J., Neubauer, D., Dyess, K., Ferguson, T. A. & Muir, D. Degradation of chondroitin sulfate proteoglycan enhances the neurite- promoting potential of spinal cord tissue. *Exp. Neurol.* **154**, 654–662 (1998).

120. McKeon, R. J., Schreiber, R. C., Rudge, J. S. & Silver, J. Reduction of neurite outgrowth in a model of glial scarring following CNS injury is correlated with the expression of inhibitory molecules on reactive astrocytes. *J. Neurosci.* **11**, 3398–3411 (1991).

121. Preston, E., Webster, J. & Small, D. Characteristics of sustained blood-brain barrier opening and tissue injury in a model for focal trauma in the rat. *J. Neurotrauma* **18**, 83–92 (2001).

122. Fitch, M. T., Doller, C., Combs, C. K., Landreth, G. E. & Silver, J. Cellular and molecular mechanisms of glial scarring and progressive cavitation: In vivo and in vitro analysis of inflammation-induced secondary injury after CNS trauma. *J. Neurosci.* **19**, 8182–8198 (1999).

123. Faulkner, J. R. *et al.* Reactive Astrocytes Protect Tissue and Preserve Function after Spinal Cord Injury. *J. Neurosci.* **24**, 2143–2155 (2004).

124. Jones, L. L., Sajed, D. & Tuszynski, M. H. Axonal Regeneration through Regions of Chondroitin Sulfate Proteoglycan Deposition after Spinal Cord Injury: A Balance of Permissiveness and Inhibition. *J. Neurosci.* **23**, 9276–9288 (2003).

125. Levine, J. M., Reynolds, R. & Fawcett, J. W. The oligodendrocyte precursor cell in health and disease. *Trends Neurosci.* **24**, 39–47 (2001).

126. Tan, A. M., Zhang, W. & Levine, J. M. NG2: A component of the glial scar that inhibits axon growth. *J. Anat.* **207**, 717–725 (2005).

127. Yang, L. J. S. *et al.* Sialidase enhances spinal axon outgrowth in vivo. *Proc. Natl. Acad. Sci. U. S. A.* **103**, 11057–11062 (2006).

128. Rhodes, K. E., Raivich, G. & Fawcett, J. W. The injury response of oligodendrocyte precursor cells is induced by platelets, macrophages and inflammation-associated cytokines. *Neuroscience* **140**, 87–100 (2006).

129. Davies, S. J. A., Goucher, D. R., Doller, C. & Silver, J. Robust regeneration of adult sensory axons in degenerating white matter of the adult rat spinal cord. *J. Neurosci.* **19**, 5810–5822 (1999).

130. Dyck, S. M. & Karimi-Abdolrezaee, S. Chondroitin sulfate proteoglycans: Key modulators in the developing and pathologic central nervous system. *Exp. Neurol.* **269**, 169–187 (2015).

131. Muleja, A. A., Mbianda, X. Y., Krause, R. W. & Pillay, K. Synthesis, characterization and thermal decomposition behaviour of triphenylphosphine-linked multiwalled carbon nanotubes. *Carbon N. Y.* **50**, 2741–2751 (2012).

132. Bonini, M., Wiedenmann, A. & Baglioni, P. Small angle polarized neutrons (SANSPOL) investigation of surfactant free magnetic fluid of uncoated and silica-coated cobalt-ferrite nanoparticles. *J. Phys. Chem. B* **108**, 14901–14906 (2004).

133. Chitosan, P. O. F. on the Structure and Properties of Chitosan. **33**, 1899–1904 (1992).

134. Coulson-Thomas, V. & Gesteira, T. Dimethylmethylene Blue Assay (DMMB). *Bio-Protocol* **4**, 1–7 (2014).

135. Shin, H. J. *et al.* Efficient reduction of graphite oxide by sodium borohydride and its effect on electrical conductance. *Adv. Funct. Mater.* **19**, 1987–1992 (2009).

136. Pei, S. & Cheng, H. M. The reduction of graphene oxide. *Carbon N. Y.* **50**, 3210–3228 (2012).

137. Gao, W., Alemany, L. B., Ci, L. & Ajayan, P. M. New insights into the structure and reduction of graphite oxide. *Nat. Chem.* **1**, 403–408 (2009).

138. Pei, S., Zhao, J., Du, J., Ren, W. & Cheng, H. M. Direct reduction of graphene oxide films into highly conductive and flexible graphene films by hydrohalic acids. *Carbon N. Y.* **48**, 4466–4474 (2010).

139. Moon, I. K., Lee, J., Ruoff, R. S. & Lee, H. Reduced graphene oxide by chemical graphitization. *Nat. Commun.* **1**, (2010).

140. Schniepp, H. C. *et al.* Functionalized single graphene sheets derived from splitting graphite oxide. *J. Phys. Chem. B* **110**, 8535–8539 (2006).

141. Fernández-Merino, M. J. *et al.* Vitamin C is an ideal substitute for hydrazine in the reduction of graphene oxide suspensions. *J. Phys. Chem. C* **114**, 6426–6432 (2010).

142. Bosch-Navarro, C., Coronado, E., Martí-Gastaldo, C., Sánchez-Royo, J. F. & Gómez, M. G. Influence of the pH on the synthesis of reduced graphene oxide under hydrothermal conditions. *Nanoscale* **4**, 3977–3982 (2012).

143. Stolle, A., Szuppa, T., Leonhardt, S. E. S. & Ondruschka, B. Ball milling in organic synthesis: Solutions and challenges. *Chem. Soc. Rev.* **40**, 2317–2329 (2011).

144. Szuppa, T., Stolle, A., Ondruschka, B. & Hopfe, W. An alternative solvent-free synthesis of nopinone under ball-milling conditions: Investigation of reaction parameters. *ChemSusChem* **3**, 1181–1191 (2010).

145. Fulmer, D. A., Shearouse, W. C., Medonza, S. T. & Mack, J. Solvent-free Sonogashira coupling reaction via high speed ball milling. *Green Chem.* **11**, 1821–1825 (2009).

146. Schneider, F., Stolle, A., Ondruschka, B. & Hopf, H. The Suzuki-Miyaura reaction under

mechanochemical conditions. *Org. Process Res. Dev.* **13**, 44–48 (2009).

147. Lee, H. C. *et al.* Review of the synthesis, transfer, characterization and growth mechanisms of single and multilayer graphene. *RSC Adv.* **7**, 15644–15693 (2017).

148. Hummers, W. S. & Offeman, R. E. Preparation of Graphitic Oxide. *J. Am. Chem. Soc.* **80**, 1339 (1958).